Magnetic X-Ray Spectroscopy and FMR Spin-Pumping Studies of PLD Amorphous YIG

Daniel Matthew Cheshire

PhD

University of York
Physics

September 2022

Abstract

In this thesis, the magnon diffusion length in amorphous YIG (a-YIG) has been studied in a series of YIG(45nm)/a-YIG/Pt(5nm) trilayer structures, fabricated on Gadolinium Gallium Garnet (GGG) substrates by pulsed laser deposition (PLD). VNA-FMR spectroscopy shows a large change in Gilbert damping with the addition of either Pt, or a-YIG plus Pt; indicating spin-pumping through the a-YIG spacer into the Pt. No significant enhancement in damping is observed when only a-YIG is grown on YIG for thicknesses between 0 and 30nm, without the Pt layer. As the thickness of the a-YIG layer is increased, the additional damping due to spin pumping into the Pt is reduced. The relationship between damping and a-YIG thickness resembles one described by diffusive magnon transport. However, a significantly longer magnon diffusion length of (16±2)nm for a-YIG is observed; approximately four times larger than that observed in previous spin-pumping studies.

Additionally, spectroscopic magnetometry offered by XMCD has been performed on a series of a-YIG thin films to study magnetization at the two Fe^{3+} sites. The Fe environment near the surface of the amorphous material is shown to be different to that in the crystalline state. Atomic multiplet calculations using Cowan's ab initio Hartree-Fock method suggest a-YIG magnetism is 80% dominated by O_h-coordinated Fe species, compared to the crystalline YIG which approaches the expected Fe^{3+} T_d:O_h ratio of 3:2, with no Fe^{2+}. Ratios of Fe^{2+}:Fe^{3+} in a-YIG could not be determined with certainty from fits of the XMCD by atomic multiplet calculations. O_h-dominated magnetism from a-YIG XMCD is shown to be weak and stable with thermal annealing, only changing significantly with recrystallisation of the YIG at 650°C, where Fe^{3+} T_d dominates over O_h Fe species. Bulk-sensitive Fe K-edge XAS and XANES provides experimental evidence for a Fe^{3+}/Fe ratio approaching 1 in both a-YIG and YIG films.

Contents

List of Figures

List of Tables

This thesis is dedicated to my parents,
Mark and Helen, for their unwavering love,
support and encouragement.

Acknowledgements

First and foremost, I would like to express my sincere gratitude to my academic supervisor, Dr Stuart Cavill, for his continued supervision and support over the past four years, without which this project would not have been possible. His guidance has proved invaluable throughout both the research and writing of this thesis.

My thanks go to Dr Leonardo Lari, Dr Adam Kerrigan and Prof Vlado Lazarov, who performed the HAADF-STEM microscopy for this project, and aided in its interpretation. I am also grateful to Connor Murrill for their assistance in preparing samples for TEM via FIB-milling. I wish to thank the team on Beamline I10 (BLADE) at the Diamond Light Source, for their assistance in acquiring VSM-SQUID and XMCD data. Similarly, my thanks go to Dr Giannantonio Cibin and Dr Diego Gianolio on Beamline B18 for their assistance in acquiring the XANES/EXAFS data.

I would also like to thank alumni of the Condensed Matter group, Dr James Beevers and Dr Chris Love, for their knowledge, insights and construction of the PLD and FMR apparatus respectively: both of which formed the experimental basis for this project. Additional thanks to Irena Azaceta, Ohoud Alsaquer and Harvey Brown for discussions of physics, sharing their experiences and doing their best to encourage me.

Last, but by no means least, a massive thank you to my parents and brother, who have provided constant support and encouragement through both the best and worst of times over the last few years. Your love truly means the world to me.

This project was supported by the EPSRC Grant No. 2106595, and by beamtime awarded by Diamond Light Source (Session No. MM22550-1 and SP24930-1).

Author's Declaration

I declare that this thesis titled *"Magnetic X-Ray Spectroscopy and FMR Spin-Pumping Studies of PLD Amorphous YIG"* is a presentation of original work and I am the sole author. This work has not previously been presented for an award at this, or any other, University. All sources are acknowledged as References. Where the thesis is based on work done jointly with others, I have made clear exactly what was done by others and what I have contributed myself.

Daniel Matthew Cheshire

Publications

The following list details original articles published, and contributions to conference proceedings, using results presented in this thesis:

- D. Cheshire, P. Bencok, D. Gianolio, G. Cibin, V. K. Lazarov, G. van der Laan and S. A. Cavill. "Absence of Spin-Mixed States in Ferrimagnet Yttrium Iron Garnet", ***J. Appl. Phys.* 132, 103902 (2022).**

Conference Attendance

- D. Cheshire, P. Bencok, R. Fan, P. Steadman, G. Cibin, G. van der Laan and S.A. Cavill. "Magnetic X-ray Spectroscopy Study of PLD-Grown Amorphous YIG Films" (poster presentation). York-Tohoku-Kaiserslauten Symposium 2019, University of York, June 2019.
- D. Cheshire and S.A. Cavill. "Enhanced diffusive magnon transport through an amorphous magnetic insulator" (oral presentation). IOP Magnetism 2022, University of York, March 2022.

Chapter 1

Introduction

1.1 Project Motivation

For the past half-century, the field of spintronics has aimed to exploit the spin of the electron to heighten the power of computational and communication devices, as well as improve storage. Magnonics is a growing sub-field of this research seeking to implement circuits that use spin waves in existing charge-based technologies. Spin waves are excitations of the local magnetic ordering of a material. These excitations can propagate through such materials as a wavelike disturbance. The corresponding quanta of spin waves are referred to as magnons and are observed in most ferromagnets, ferrimagnets and antiferromagnets [1, 2, 3].

Significant potential lies in using magnon-currents (analogous to electric currents) to transport and process information encoded on spin waves rather than the physical motion of electrons [4]. Implementing magnon-currents in computational circuits is envisaged to eliminate drawbacks inherent to modern electronics, such as energy dissipation due to Ohmic losses. Exploiting the wave-like properties of magnons such as phase could also offer additional degrees of freedom for data processing, dramatically increasing computing speeds [1, 4]. Able to operate with frequencies above GHz and wavelengths below 10nm, spin-waves also offer potential for nanoscale miniaturisation of computing technologies.

The key constituent in producing magnonic devices for use in circuits or microwave signal processors are magnetic films that can sustain and propagate spin-waves with minimal attenuation or damping. Since spin-waves do not transfer electric charge, magnetic insulators can be used [5]. On this basis, low spin-relaxation garnet films are considered some of the most promising materials in this field. Of these, the ferrimagnet yttrium iron garnet (YIG) has emerged as the material of choice, possessing uniquely low spin-wave damping. Such damping is described by a dimensionless damping coefficient, α, with a value of 3×10^{-5} in bulk YIG [6, 7]. This is the lowest damping coefficient known for any material and two orders of magnitude smaller than most metallic ferromagnets (on the order of 1×10^{-3} [8, 9, 10]), even in thin-films.

Ultra-low damping allows for long spin-wave lifetimes and magnon propagation lengths. The propagation of magnons in YIG films has been studied for many years due to their extensive application in communication, microwave and magnetic detection devices, plus their envisioned role in future technologies [1, 2, 5]. Significant research is focused on improving YIG thin-film fabrication techniques - aiming to produce nanometre films with damping (α) as low as that of bulk YIG – and incorporate these films into novel spintronic devices. Recent work in the field has shown that amorphous YIG (a-YIG) can be recrystallised by annealing to give exceptionally low damping and near bulk magnetisations, even in films below 20nm in thickness [11, 12]. This recrystallisation technique is currently unrivalled in reported YIG thin film quality.

Another emerging area of interest in magnonics is the use of antiferromagnetic insulators to mediate spin waves. Antiferromagnets are considered to be the ideal magnonic material for device applications. Unlike ferromagnets, antiferromagnets can support higher THz frequencies of magnons and have no net magnetic moment, making them impervious to external fields [13, 14]. However, antiferromagnetic materials typically have short magnon diffusion and propagation lengths. Studies of spin transport in hematite have shown that magnons are transported in α-Fe_2O_3 thin films over very small lengths of a few nm via diffusion. However, magnon diffusion lengths in α-Fe_2O_3 single crystals were instead observed to be very large, in excess of 10 microns [15]. Further investigations using magnetic imaging techniques such as XMLD-PEEM revealed that the magnon diffusion length in antiferromagnetic α-Fe_2O_3 was ultimately limited by domain walls. Thin films were concluded to produce shorter magnon diffusion lengths as a result of having multi-domain magnetic configurations [16]. This has put significant focus into *amorphous* magnetic insulators being an answer to integrating antiferromagnets into magnonic devices. The high disorder of amorphous insulators means they should have a very low domain wall density: potentially eliminating the problem. Current work suggests spin transport through these disordered magnetic insulators seems to rely only on magnetic correlations [17]. The magnon spectrum of disordered magnets has been under-explored in the past, although one may consider an analogy to phonons in glassy systems where heat transport can be surprisingly efficient, with long mean free paths despite the disorder.

This has motivated work into amorphous YIG (a-YIG) being a candidate material in this field: ideally utilising the uniquely low damping of YIG with an amorphous phase. This body of work is discussed in more detail in Section 2.6.2. New research has also been stimulated by the observation of exceptionally long magnon propagation lengths in a-YIG at room temperature between Pt electrical contacts separated by over 100 microns, rivalling propagation lengths measured in crystalline YIG films [18]. This is a surprising result, given a-YIG has no long-range structural order or ferrimagnetic order (effectively zero magnetisation), behaving instead as a frustrated antiferromagnet. However, similar repeat experiments have failed to observed this magnon transport at all [19]. Alternative experiments relying on a spin pumping geometry either suggest magnon diffusion lengths in a-YIG are significantly smaller (only 3.9nm) [20],

or also fail to observe any spin transport for any thickness of a-YIG investigated [21]. The nature and existence of spin transport in a-YIG is an ongoing debate in the literature, and one of significant importance to the outlook of amorphous magnonics. Inconsistencies in magnon diffusion lengths and observed spin transport between these studies suggest more complex issues may be present. The structure of the a-YIG examined by each group may differ slightly despite notionally similar preparation techniques; transport studies cited above [18, 19, 20, 21] all produced a-YIG layers using RF-sputtering at room temperature. Furthermore, a rigorous structural analysis or definition of what constitutes 'amorphous' YIG is especially lacking in the available literature. It can be hypothesised that samples of a-YIG may, in fact, have differing levels of 'amorphousness' and Fe cation distributions which are highly dependent on growth conditions, leading to differences in the reported behaviour.

1.2 Summary of Results and Achievements

Work presented in this thesis concerns the characterisation of, and spin-pumping through amorphous YIG grown following a room temperature pulsed laser deposition (PLD) technique. Firstly, the structural and magnetic properties of our PLD-grown amorphous YIG thin films have been characterised. The subsequent recrystallisation of these a-YIG films grown on GGG (Gadolinium Gallium Garnet) and YAG (Yttrium Aluminium Garnet) (111) substrates was also studied. Characterisation was performed via various techniques such as x-ray diffraction (XRD), vibrating sample magnetometry (VSM), ferromagnetic resonance spectroscopy (FMR) and transmission electron microscopy (TEM). A recipe for attaining high quality YIG/GGG and YIG/YAG films via recrystallisation-PLD has been established and used for additional experiments presented later in this thesis. This recipe may also be used for future research.

Secondly, amorphous YIG thin films on YAG(111) grown by PLD and subjected to different ex-situ annealing temperatures have been characterised via soft polarised x-ray spectroscopy (XMCD) and hard x-ray absorption (XANES). Theoretical fits to the XMCD data show a-YIG magnetism is ≈80% dominated by O_h-coordinated Fe^{2+} and Fe^{3+} species, compared to crystalline YIG films grown for comparison which approach the expected Fe^{3+} T_d:O_h ratio of 3:2, with no Fe^{2+}. However, hard x-ray XAS and XANES measured from all a-YIG/YIG films shows pre-edge features tending to a single Gaussian with an Fe^{3+}/Fe ratio approaching 1. This provides experimental evidence for the presence of Fe^{3+} species only in a-YIG. The weak O_h-dominated magnetism in a-YIG is observed to be stable with annealing temperature, until YIG recrystallisation occurs.

Finally, YIG/a-YIG/Pt trilayers have been grown by PLD and characterised with particular emphasis on FMR. FMR-driven spin-pumping has been observed through the a-YIG spacer into the Pt, with a large increase in Gilbert damping and spin mixing conductance. The

relationship between trilayer Gilbert damping and a-YIG thickness (t) was found to follow an exponential thickness dependence: a clear signature of diffusive magnon transport through the a-YIG. However, a notably longer magnon diffusion length of (16 ± 2)nm for a-YIG is observed. This is approximately four times larger than that observed in previous spin-pumping studies. Surprisingly, no change in Gilbert damping is observed with the addition of a-YIG alone to YIG, indicating that spin is only propagated with the addition of Pt thereafter.

1.3 Structure of the Thesis

This thesis is separated into seven chapters, including this introduction. Following **Chapter 1** which outlines the project motivation and achievements, **Chapter 2** focuses on the theoretical framework and physics which gives rise to the presented work. This section discusses principles of magnetism, and the physics required to understand the data presented in the later chapters. Additionally, the current known properties of YIG are summarised and a brief literature review surrounding amorphous YIG is given.

Chapter 3 provides details on all of the experimental and analytical techniques performed throughout the work of this thesis. Details on the experimental set ups and equipment used are stated as are the methods and theory used in order to analyse the data obtained.

The thesis then contains three separate results chapters. **Chapter 4** provides a characterisation and discussion of the magnetic and structural properties of amorphous YIG thin films, and of recrystallised YIG thin films grown on GGG and YAG substrates. The differences between the two are compared both in the as-grown amorphous state and after ex-situ annealing in air at 850°C.

Chapter 5 presents results of a polarised soft x-ray study and subsequent hard x-ray study of amorphous YIG thin films on YAG(111), grown via PLD and subjected to varying ex-situ annealing temperatures. The films are characterised structurally and magnetically, while both the valence and coordination of Fe sites responsible for (surface) magnetism in the a-YIG films is determined using polarised X-ray spectroscopy. Bulk-sensitive hard x-ray absorption results are presented to supplement this, and their meaning discussed.

Chapter 6 presents results of an FMR spin-pumping study of YIG/a-YIG/Pt thin-film trilayer structures. The trilayers are structurally and magnetically characterised, with particular attention to FMR and measurement of Gilbert damping of the YIG layer. Results showing spin transport through the a-YIG are presented, and dependence on the a-YIG thickness is analysed and discussed.

Finally, **Chapter 7** summarises the accomplished work and results obtained in the thesis, with discussion of the outcomes of each results chapter. A discussion of further work is presented, considering where the project might be taken next and possible follow-up experiments.

Chapter 2

Background Theory

In this chapter, a discussion of the background theory behind this project is presented. Particular focus is given to ferromagnetism and magnetisation dynamics, and their role in Ferromagnetic Resonance. A brief literature review surrounding YIG and amorphous YIG is also provided. Ultimately, this section will outline the key theoretical concepts used as motivation and as a basis for the interpretation of the results presented within this thesis.

2.1 Ferromagnetism

The magnetic behaviour of any material is fundamentally governed by its electron configuration. Atoms with unpaired electrons possess an intrinsic magnetic dipole moment ($\vec{\mu}$), arising from their unpaired electrons' orbital and spin angular momenta [22]. This magnetic spin dipole moment is quantum mechanical in origin, however a semi-classical analogy is that the electron rotates with a quantifiable 'spin' and thus behaves as a rotating current moment [23].

Any isolated atom or ion that contains an unpaired electron is paramagnetic. In most paramagnetic materials, the magnetic moments from these unpaired electrons are randomly oriented as a result of thermal effects, unless an external magnetic field is applied. This causes an alignment of the electron moments parallel to the field, creating an induced magnetisation. This means that paramagnetic materials, despite having unpaired electrons, possess zero magnetisation without an applied field to align them [24].

However, in certain materials, a purely quantum mechanical interaction known as exchange occurs between the unpaired electrons in neighbouring atoms, enabling their spin moments to align. This creates a non-zero spontaneous magnetisation, even in the absence of an applied magnetic field. This behaviour is known as Ferromagnetism. Ferromagnetism only occurs in a small number of elements: most strongly in iron, cobalt and nickel, plus some of the rare earth elements such as gadolinium [22, 25].

2.1.1 The Exchange Interaction

Unpaired electrons of identical neighbouring magnetic atoms interact via the exchange interaction. Due to exchange, electrons can move further apart and ultimately minimise their energy by aligning their spins [23]. This minimisation of energy is what allows the spin moments of electrons in a ferromagnet to remain aligned parallel to each other, without an applied field.

Exchange coupling is a quantum mechanical effect that arises from a combination of the Pauli exclusion principle and the Coulomb interaction. Two electrons can be considered, with spins S_1 and S_2, and individual spatial wavefunctions $\psi_1(\mathbf{r}_1)$ and $\psi_2(\mathbf{r}_2)$. The wavefunction for the joint state can be expressed as a product of the single electron states [24, 26, 27]. However, exchange symmetry must hold true between the two individual electrons. As a result, only symmetric or antisymmetric spatial product states are allowed. For fermions, the overall wave function (Ψ) must be antisymmetric. Therefore, the spin part of the wave function must either be: an antisymmetric singlet state χ_S (S = 0) in the case of a symmetric (additive) spatial state, or a symmetric triplet state χ_T (S = 1) in the case of an antisymmetric (subtractive) spatial state [24]. The overall joint state wavefunction (Ψ), including both spatial and spin components, for the singlet case Ψ_S and triplet case Ψ_T can be written as:

$$\Psi_S \propto \left[\psi_1(\mathbf{r}_1)\psi_2(\mathbf{r}_2) + \psi_2(\mathbf{r}_1)\psi_1(\mathbf{r}_2)\right]\chi_S \tag{2.1}$$

$$\Psi_T \propto \left[\psi_1(\mathbf{r}_1)\psi_2(\mathbf{r}_2) - \psi_2(\mathbf{r}_1)\psi_1(\mathbf{r}_2)\right]\chi_T \tag{2.2}$$

The electrons each induce a Coulomb repulsion as a result of their negative charges, and the two joint states above (Ψ_S and Ψ_T) are not degenerate due to the Pauli exclusion principle. The energies of the two possible states (assuming the spin parts of the wavefunctions χ_S and χ_T are normalised) are:

$$E_{\mathrm{S}} = \int \Psi_{\mathrm{S}}^{*}\hat{\mathcal{H}}\Psi_{\mathrm{S}}\mathrm{d}\mathbf{r}_1\ \mathrm{d}\mathbf{r}_2 \tag{2.3}$$

$$E_{\mathrm{T}} = \int \Psi_{\mathrm{T}}^{*}\hat{\mathcal{H}}\Psi_{\mathrm{T}}\mathrm{d}\mathbf{r}_1\ \mathrm{d}\mathbf{r}_2 \tag{2.4}$$

The effective Hamiltonian for this system is given as the sum of a constant term, plus an additional term which is dependent on spin:

$$\hat{\mathcal{H}} = \frac{1}{4}\left(E_{\mathrm{S}} + 3E_{\mathrm{T}}\right) - \left(E_{\mathrm{S}} - E_{\mathrm{T}}\right)\mathbf{S}_1 \cdot \mathbf{S}_2 \tag{2.5}$$

where $\mathbf{S}_1 \cdot \mathbf{S}_2$ are spins of the two electrons. For a singlet state (S = 0), $\mathbf{S}_1 \cdot \mathbf{S}_2 = -\frac{3}{4}$, and for a triplet state (S = 1) $\mathbf{S}_1 \cdot \mathbf{S}_2 = \frac{1}{4}$. The energy difference between the singlet and triplet

states is known as the exchange energy [28, 24], from which an exchange constant (or exchange integral) J is defined by:

$$\mathrm{J} = \frac{E_\mathrm{S} - E_\mathrm{T}}{2} \tag{2.6}$$

Factoring the exchange integral back into the effective Hamiltonian (Equation 2.5), the spin-dependent term can be written as an effective spin-spin interaction, such that electron exchange energy is given by 2.7:

$$U_{\text{Exchange}} = -2\mathrm{J}\hat{\boldsymbol{S}}_1 \cdot \hat{\boldsymbol{S}}_2 \tag{2.7}$$

where $\hat{S}_1$ and $\hat{S}_2$ are spin operators of the two electrons. In a system consisting of multiple nearby atoms with overlapping electron wavefunctions, exchange coupling can be generalised using the Heisenberg model (where J_{ij} is the exchange integral between two interacting spins, i and j respectively). [28].

$$U_{Exchange} = -\sum_{i,j} \mathrm{J}_{ij}\hat{\boldsymbol{S}}_1 \cdot \hat{\boldsymbol{S}}_2 \tag{2.8}$$

If we assume an isotropic exchange strength and only interactions between nearest neighbours are significant, the Heisenberg model in Equation 2.8 simplifies further to:

$$U_{Exchange} = -\mathrm{J}\sum_{i,j} \hat{\boldsymbol{S}}_1 \cdot \hat{\boldsymbol{S}}_2 \tag{2.9}$$

The effect of each exchange interaction is local, however each exchange pair will have an effect on their nearest neighbours, resulting in a long-range ordering of all of the spin moments throughout a crystalline material.

Ferromagnetism and Exchange

In ferromagnetic materials, the exchange integral is positive ($\mathrm{J} > 0$), $\mathrm{E_S} > \mathrm{E_T}$ and the triplet state $\mathrm{S} = 1$ is favoured. From Equation 2.7, it follows that, in order to minimise the resultant exchange energy, parallel alignment of the electron spins and thus magnetic moments is favoured. This is illustrated in Figure 2.1. This exchange-induced spin alignment ultimately produces the non-zero spontaneous magnetisation observed in ferromagnets, unlike paramagnetic materials as discussed in Section 2.1.

Exchange interactions are fundamentally a short-range phenomenon. In ferromagnets, the coexistence of short-range exchange and long-range magnetostatic attractions between individual electrons can make exact descriptions of magnetic behaviour difficult. It is more convenient to employ a continuum model, using a single vector to represent the sum total of magnetic moments. The magnetisation of a material is defined as its magnetic moment per unit volume, and in this regime is considered a continuous field:

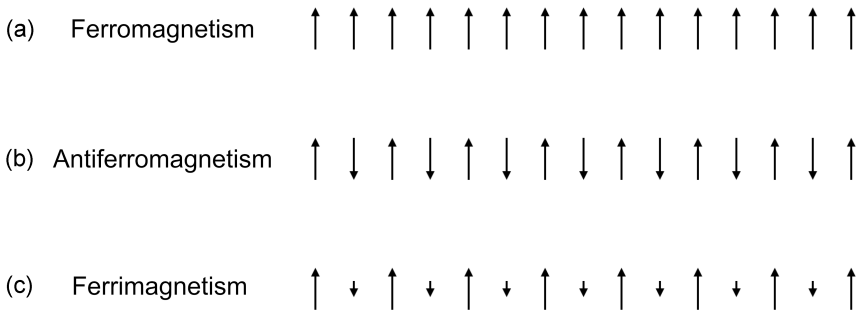

Figure 2.1: Electron spin moments in (a) ferromagnetic, (b) antiferromagnetic, and (c) ferrimagnetic ordering. The magnitude of the spin moment is related to the size of the arrow, in each of these three cases.

$$\mathbf{M}(\mathbf{r}) = M_s \hat{\boldsymbol{m}}(\mathbf{r}) \tag{2.10}$$

In Equation 2.10, $\hat{\boldsymbol{m}}$ is a unit vector in the direction of the magnetisation (known as the reduced magnetisation) and $\mathbf{r}$ notes the position vector within the crystal structure. If all spins are oriented perfectly parallel, the magnetisation (M) takes the value of the saturation magnetisation (M_s). In ferromagnetic materials, the parallel alignment of all the spin moments throughout the material gives a uniform alignment across the whole sample [26]. In real ferromagnets, large external fields must be provided to fully saturate magnetisation in the applied field direction. This is due to the formation of magnetic domains, and movement of domain walls which can be affected by the presence of defects in the crystal structure. Magnetocrystalline anisotropy (discussed in Section 2.2.2) also contributes, where larger saturation fields are required to overcome a magnetic hard axis. Nevertheless, the continuum model still works well in these conditions.

All ferromagnets have a maximum temperature, above which they no longer exhibit ferromagnetic behaviour, known as the Curie temperature ($\mathrm{T_C}$). This occurs when thermal agitation of atoms overcomes exchange between electrons, destroying ferromagnetic ordering and causing the electron spins to orient randomly. The material is rendered paramagnetic in nature, above the Curie temperature [25]. In the Weiss model of magnetism, the Curie temperature is defined as:

$$T_{\mathrm{C}} = \frac{g_J \mu_{\mathrm{B}} (J+1) \lambda M_{\mathrm{s}}}{3 k_{\mathrm{B}}} \tag{2.11}$$

where λM_S is an effective molecular field maintaining FM alignment, z is the number of nearest neighbour atoms, μ_B is the Bohr magneton, g_J is the Landé g-factor (discussed further in Section 2.3) and k_B is the Boltzmann constant. The molecular field constant can instead be related to the exchange integral, J. The Curie temperature can then be written, for a system

of atoms with angular momentum J, as [24]:

$$T_{\mathrm{C}} = \frac{2z\mathrm{J}J(J+1)}{3k_B} \tag{2.12}$$

From Equation 2.12, ferromagnets with a higher Curie temperature have either strong exchange coupling, and/or higher atomic coordination. A high T_c is essential to the application of ferromagnetic materials in devices in order to preserve spin moment alignment during device operation. All of the materials examined in this thesis have a $T_c >> 300$K.

2.1.2 Antiferromagnetism and Ferrimagnetism

A variation of exchange coupling can occur when the exchange integral is negative ($\mathrm{J} < 0$), $\mathrm{E_S} < \mathrm{E_T}$ and the singlet state $\mathrm{S} = 0$ is favoured. Following Equation 2.7, for negative J, an antiparallel alignment of the two spin moments is preferred and minimises the exchange energy. Unlike parallel alignment, antiparallel alignment of spin moments generally acts to reduce the total magnetisation within a magnetic material, with neighbouring spins opposing one another. For a two site system, an antiparallel alignment of spin moments can have one of two possible outcomes.

If the opposing moments are equal in magnitude, they will cancel each other out and no net magnetic moment is observed in the system. This is known as antiferromagnetism, shown in Figure 2.1(b). Most antiferromagnets exist as materials composed of two sublattices of oppositely oriented magnetisation, where the magnetisation within each sublattice almost cancels out that of the other sublattice. Strictly speaking, cancellation is not fully complete until T= 0K due to defects, thermal effects and effects like spin canting. As a result, antiferromagnets exhibit a very small positive susceptibility at all temperatures above 0K. Many antiferromagnetic materials are insulators and contain no free electrons. Therefore, the electrons responsible for their magnetic properties are localized to certain ions in the crystal structure. All antiferromagnets have a maximum temperature above which they no longer exhibit antiferromagnetic behaviour, known as the Néel temperature ($\mathrm{T_N}$). Above the Néel temperature, spontaneous spin alignment by exchange is overcome by thermal effects, and antiferromagnetic ordering is destroyed (analogous to the Curie temperature in ferromagnets) [22]

Alternatively, the moment on one site can be larger in magnitude than on the other site, meaning there is an observable net magnetisation at zero applied field, much like a ferromagnet. However, this net magnetisation is notably smaller than it would be if both spin sites were aligned in parallel. This is known as ferrimagnetism, shown in Figure 2.1(c). In most cases, a ferrimagnetic system can be approximated as being a ferromagnet with a small net magnetisation, displaying all of their characteristic properties such as magnetic saturation, hysteresis and coercivity. Ferrimagnetism is seen in some ionic compounds, such as magnetic oxides which

tend to have a very high electrical resistivity. This makes ferrimagnetic oxides useful for applications that typically metallic ferromagnets are unsuitable for, such as inductive circuits or filters [24, 29, 30].

Distinguishing Ferromagnetism and Antiferromagnetism

The spin alignment that is favoured for minimising exchange energy is fundamentally determined by the value of the exchange integral, J, of the material. Calculations performed in the 1930s illustrated that the sign of the exchange interaction in 3d elements is correlated to the ratio of inter-atomic distance (r_{ab}) to the radii of the partially filled 3d-subshell (r_{3d}) [31, 32]. This correlation is given by the Bethe-Slater curve, illustrated in Figure 2.2, and distinguishes the magnetism of elements possessing a 3d-electron subshell configuration. Iron, cobalt and nickel are ferromagnetic (J $>$ 0), whereas manganese and chromium are antiferromagnetic (J $<$ 0). For large values of r_{ab}/r_{3d}, exchange is positive, proceeding through a maximum before becoming negative for small values of r_{ab}/r_{3d}. Thus, the sign and value of the exchange integral, J, depends only on the separation of nearest neighbour spins. Importantly, this means a regular crystalline structure and arrangement of spin-sites is **not** required for ferromagnetism or antiferromagnetism to exist in a magnetic material [33]. This is discussed further in Section 2.1.6.

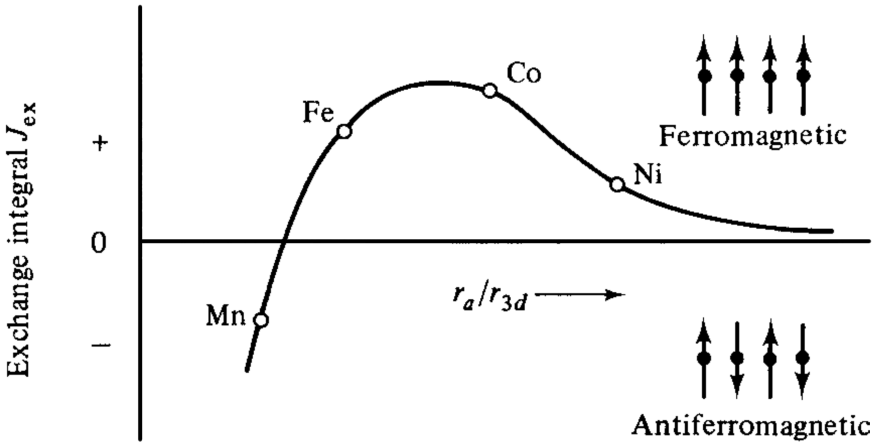

Figure 2.2: The Bethe-Slater curve. Adapted from [34]

As mentioned in Section 2.1, in a Curie paramagnet, an applied magnetic field attempts to align moments against thermal agitations that try to randomise their orientation. The magnetic susceptibility (magnetisation induced per unit applied field) of a paramagnet, χ, varies with its temperature (T) according to Curie's law, $\chi = C/T$. The value of C, the Curie constant, provides temperature-independent information on the magnetic moment μ of the paramagnetic atom or ion: if the law holds true. However, few paramagnetic solids obey this law, which is only a special case of the more general Curie-Weiss Law [24, 26]:

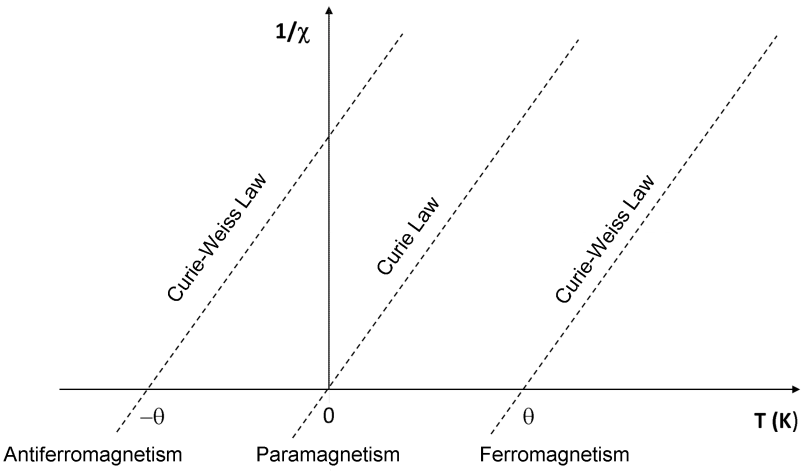

Figure 2.3: Reciprocal of magnetic susceptibility against sample temperature for paramagnetic, ferromagnetic and antiferromagnetic materials.

$$\chi = \frac{C}{T - \Theta} \tag{2.13}$$

This law instead allows the interactions between individual moments to be considered, and can therefore be applied to materials that are not perfectly paramagnetic. Θ is the Weiss constant (with dimensions of T), the value of which is used as a rationale to measure the nature and strength of interactions between neighbouring magnetic moments, if there are any. However, this does not offer an indication of whether any magnetic ordering resulting from these interactions is long-range or instead localised [22]. If a Curie-Weiss law holds true in a material, a plot of the reciprocal susceptibility $(1/\chi)$ as a function of temperature follows a straight line with gradient of 1/C and a temperature-axis intercept of $-\Theta/C$. The various magnetic ordering that may apply are shown in Figure 2.3. Note, negative temperatures observed on the antiferromagnetic plot arise from extrapolation of the Curie-Weiss plot and are not physical.

2.1.3 Superexchange

In anti-ferromagnetic and ferrimagnetic oxides, exchange interactions between magnetic iron ions are often mediated through oxygen ions that separate them, due to an overlap of electron orbital wavefunctions. This process known as superexchange, or indirect exchange. A detailed description of the theory behind superexchange is given by Anderson (1959) [35], but a brief overview is given below.

A typical system that undergoes superexchange consists of two transition metal ions, such as Fe^{3+}, separated by a non-magnetic ion, such as O^{2-}. This is illustrated in Figure 2.4. The non-magnetic oxygen ion has two p-electrons in its valence shell, whereas the two Fe ions have 5 unpaired d-shell electrons. There is little direct 3d-3d orbital overlap between the Fe ions,

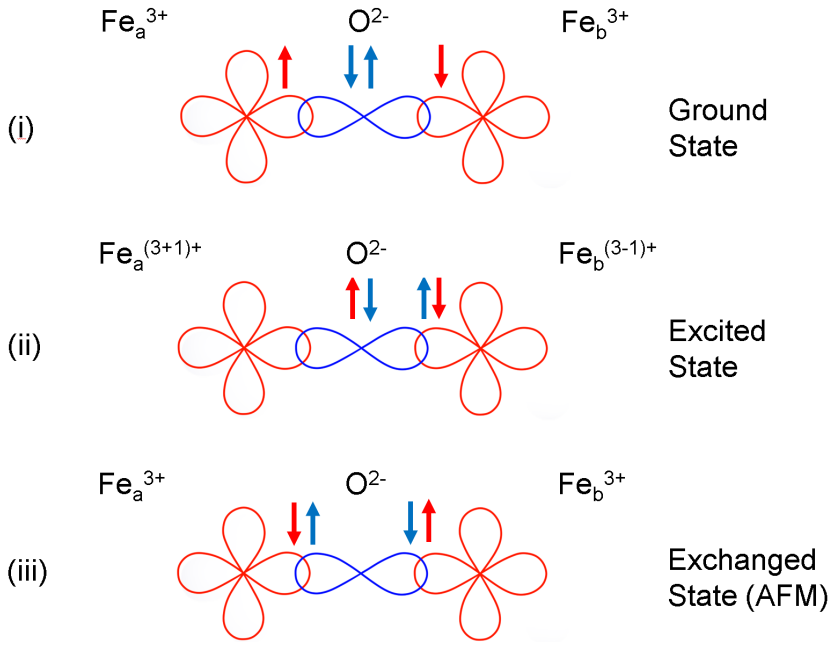

Figure 2.4: Schematic representation of Fe-O-Fe superexchange bonding, showing virtual spin transfer producing stable antiferromagnetic coupling. Adapted from [27].

but the Fe 3d-orbitals are instead hybridised with the oxygen 2p-orbital. The kinetic energy of this system is lowered by delocalising and sharing electrons between the Fe and oxygen ions, to ultimately form an antiferromagnetic coupling between the two Fe ions (with their spins oriented antiparallel) [24]. The overlap of local electron wavefunctions allows one of the p-electrons from the O^{2-} to move to one of the Fe ions, into an unoccupied 3d-orbital. Consequently, the remaining unpaired p-electron on the O^{2-} becomes directly exchanged with the other Fe ion, with the shared (exchanged) electron state shown in Figure 2.4(iii). This allows the magnetic Fe ion to interact with the Fe ion on the other side of the oxygen, via an indirect exchange interaction mediated through the oxygen's valence shell. Thus, magnetic behaviour between the two Fe ions is not suppressed.

The superexchange interaction involves the simultaneous *virtual* transfer of two electrons, causing the instantaneous formation of a $3d^{n+1}2p^5$ excited state [22, 27]. The virtual transfer of spin from Fe_a^{3+} to an equivalent orbital state in Fe_b^{3+} can be expressed as the following reaction: $Fe_a^{3+} + Fe_b^{3+} \rightarrow Fe_a^{(3+1)+} + Fe_b^{(3-1)+} + U_{Coulomb}$; $U_{Coulomb}$ is the energy cost of the excited state, effectively an on-site 3d Coulomb interaction. This transfer is illustrated in Figure 2.4. The ground state (i) is able to mix with excited states (ii) and (iii), delocalising the magnetic electrons over the Fe-O-Fe system and lowering the kinetic energy of the system. However, this electron delocalisation is limited by the potential energy cost, $U_{Coulomb}$, where Coulomb repulsion favours the reverse reaction. A balancing between kinetic energy reduction

and potential energy cost ultimately completes the virtual spin transfer and produces a stabilised antiferromagnetic Fe-Fe alignment (in the exchanged state shown in Figure 2.4(iii)) [22, 24, 27]. Expressions for exchange energy must be modified to account for this charge transfer between the ions. Thus, a new expression for the exchange energy between two magnetic d-electrons, of Fe ions i and j respectively, is given as:

$$U_{Superexchange} = -2J_{Super}\hat{\boldsymbol{S}}_i \cdot \hat{\boldsymbol{S}}_j \tag{2.14}$$

An effective superexchange constant is defined on the order of $J_{Super} \approx -\frac{t^2}{\mathrm{U_{Coulomb}}}$ [24, 27]. Here, t is a p-d hopping integral, proportional to the energy width of the conduction band [24]. Superexchange also occurs across other magnetic and neighbouring non-magnetic ion species: such as Co or Fe sites, separated by Al or Si, in Heusler alloys like CFAS. Superexchange can become more complicated with the introduction of more Fe atoms bonding to a single oxygen atom with multiple overlapping orbitals (common in the crystal lattices of magnetic oxides), but the underlying principle is the same.

2.1.4 Goodenough-Kanamori-Anderson Rules

Superexchange can result in either antiferromagnetic or ferromagnetic coupling between the two cations depending on atomic bond angles, bond lengths, and whether the ions have filled, half-filled or vacant electron orbitals. The Goodenough-Kanamori-Anderson (GKA) rules ultimately determine which of the two types of coupling is present between two magnetic ions undergoing superexchange [36]. They are based on symmetry relations and electron occupancy of the overlapping orbitals [24, 37]. The GKA rules dictate whether the exchange coupling is positive or negative in sign, and hence whether ions involved couple ferromagnetically or antiferromagnetically, respectively. The GKA rules can be summarised as follows:

1. Superexchange coupling between two half-filled d-orbitals via the same O^{2-} p-orbital is strong and antiferromagnetic for a 180° bond angle.

2. Superexchange coupling between half-filled and empty (or filled) orbitals via the same O^{2-} p-orbital is weak and ferromagnetic for a 180° bond angle

3. Superexchange coupling between two half-filled d-orbitals via different O^{2-} p-orbitals is weak and ferromagnetic.

Each of these three cases is shown in Figure 2.5. The simple case considered in Section 2.1.3 refers to the first GKA rule (strong antiferromagnetic coupling). A detailed description of the theory behind the GKA rules is given in [27, 36].

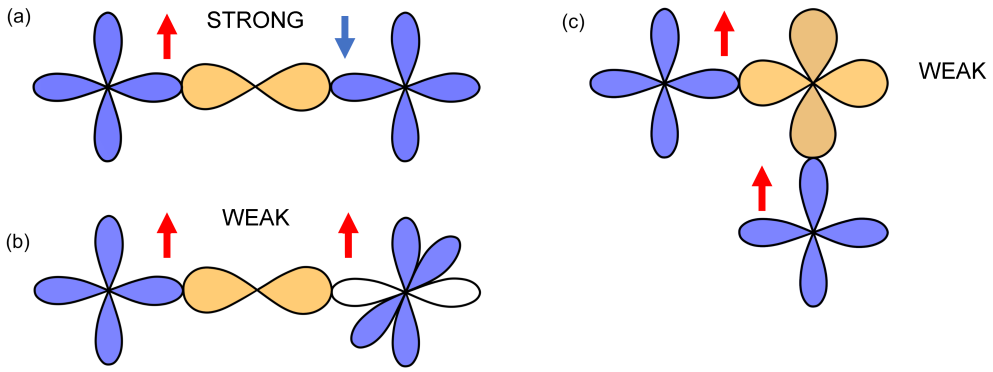

Figure 2.5: Three main types of the superexchange interaction: (a) anti-ferromagnetic superexchange between two half-filled d-orbitals via the same p-orbital; (b) ferromagnetic superexchange between half-filled and empty d-orbitals via the same p-orbital; and (c) ferromagnetic superexchange between two half-filled d-orbitals via different p orbitals.

2.1.5 Double Exchange

In magnetic materials that contain a mixed valency of ions (e.g. Fe^{3+} and Fe^{2+} in magnetite, Fe_3O_4), a secondary exchange interaction known as double exchange is able to emerge. Double exchange occurs between magnetic ions in a material that are the same element but have different valence [24, 38]. Electrons can be shared between neighbouring ion sites by hopping, but only if the available empty site possesses the same corresponding spin to the electron that will hop into it. The hopping mechanism for double exchange operates, similarly to superexchange, through a non-magnetic ligand ion such as O^{2-}. If the oxygen ion donates its spin-up electron to Fe^{3+}, the vacant oxygen orbital can then be filled by an electron from Fe^{2+}. The net result is the movement of an electron between the neighbouring Fe ions, with its spin preserved. Spin-flipping cannot occur during this double exchange process, and thus neighbouring Fe sites must be ferromagnetically aligned for hopping to occur. The hopping of electrons between sites acts as a form of charge transfer, and therefore allows electron hopping conduction to occur through the material, propagating electrical current via the different valence ions in the crystal structure [39].

2.1.6 Amorphous Magnets

Most magnetic materials showing ferromagnetic, ferrimagnetic or antiferromagnetic order have long-range structural order in the form of a crystal lattice. Amorphous magnets have no overall crystal lattice order and instead exist in a disordered liquid-like state, wherein bond disorder and/or topological disorder is present throughout. However, short-range ordering or coupling can exist between individual and groups of atoms. Such coupling can be structural

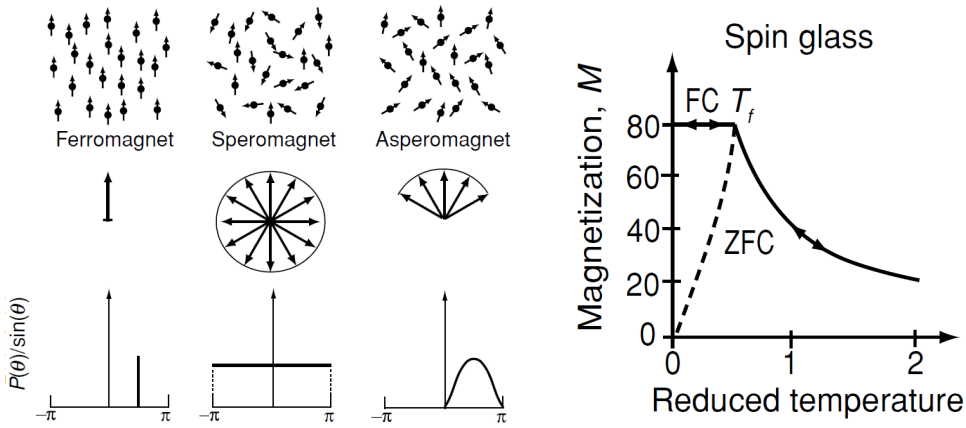

(a) (b)

Figure 2.6: (a) Experimentally observed spin configurations in amorphous magnets. (b) Temperature-dependent magnetisation in systems with spin-glass behaviour. Adapted from [33][22]

(i.e. nanocrystals or bonds with neighbouring atoms) or magnetic, mediated by local exchange or super-exchange interactions [33, 22].

In general, the behaviour of magnetic materials when amorphous depends on the nature of the exchange interaction. If exchange is ferromagnetic, magnetism in the amorphous phase is straightforwardly ferromagnetic as well. However, if exchange is antiferromagnetic, the lack of a crystal lattice has more dramatic and complicated effects. The structural disorder causes frustration of the individual exchange or superexchange bonds in magnetic oxides like YIG. 'Frustration' refers to how it is not possible to satisfy all interactions in a system to find a lowest possible ground energy. This means there is no single unique ground state, but instead several possible spin configurations with similarly low degenerate energy exist [22].

Disordered frustrated magnets like these are labelled spin glasses. A spin glass is defined as a non-magnetic matrix populated with a random distribution of magnetic atoms/spins. Spin glasses are characterised by a random, yet cooperative, freezing of spins at a well-defined spin-freezing temperature T_F. This spin freezing temperature T_F is much smaller in magnitude than the Curie temperature T_C. Spin freezing approximates to a magnetic phase transition from a high temperature disordered state to a low temperature 'ordered' state. Below T_F, spins freeze irreversibly but randomly into one of the possible degenerate ground states, appearing without the usual magnetic long-range ordering [33]. Spin glass configurations are either speromagnetic (no net magnetisation) or asperomagnetic (local net magnetisation), illustrated in Figure 2.6. In spin glasses with negative exchange interactions such as magnetic oxides, speromagnetic ordering is generally anticipated. However, as discussed in Section 2.6.2, transitions between speromagnetic and more correlated spin-glass states in amorphous oxides are considered to be

theoretically possible [17].

2.2 Magnetic Free Energy

Exchange interactions and exchange energy explain the relative orientations between isolated pairs of electron spins, and therefore magnetic moments, in ferromagnets and ferrimagnets. However, there are several other energy contributions and factors that define preferred orientations of magnetisation along certain crystallographic directions in ferro/ferrimagnetic materials. Preferred orientations of magnetisation are called magnetic anisotropies, and the interactions that give rise to them are discussed in this section.

2.2.1 The Magnetic Free Energy Equation

The magnetic free energy of a ferromagnetic system or crystal lattice is defined by a number of interactions. These include: exchange coupling, spin-orbit (or magnetocrystalline) coupling, magnetostatic interactions, potential magnetoelastic interactions, and the Zeeman interaction. Each of these interactions has an associated energy density, and the total magnetic (Helmholtz) free energy density, U, is given by a summation of them, such that:

$$U = U_{\text{Exchange}} + U_{\text{Magnetocrystalline}} + U_{\text{Magnetostatic}} + U_{\text{Magnetoelastic}} + U_{\text{Zeeman}} \tag{2.15}$$

Each of the constituent energy density terms in Equation 2.15 represents a different contribution to the total [22, 27, 28]. The value of each energy density term varies as a function of angle and crystallographic direction. It is often convenient to convert and plot the sum of these magnetic energy densities in spherical polar coordinates, in order to create a magnetic free energy surface (energy per unit volume, given U is an energy density). This energy surface allows a visualisation of directions along which orienting magnetisation is energetically 'easy' (energy surface minima) or 'hard' (energy surface maxima). In this context, spins are treated as acting uniformly under magnetic saturation. An example of a magnetic free energy surface is illustrated in Figure 2.7(a).

2.2.2 Magnetocrystalline Anisotropy

Magnetocrystalline anisotropy (MCA) refers to the dependence of internal energy on the direction of the magnetisation vector. MCA arises from a combination of two effects: spin-orbit coupling and the crystal field. Spin-orbit coupling refers to the coupling of the spin angular momentum and orbital angular momentum of an electron. This is due to the electromagnetic interaction between the electron spin and the magnetic field generated by the electron's orbit around the nucleus [24, 27]. Additionally, any given ion within a crystal experiences an electric

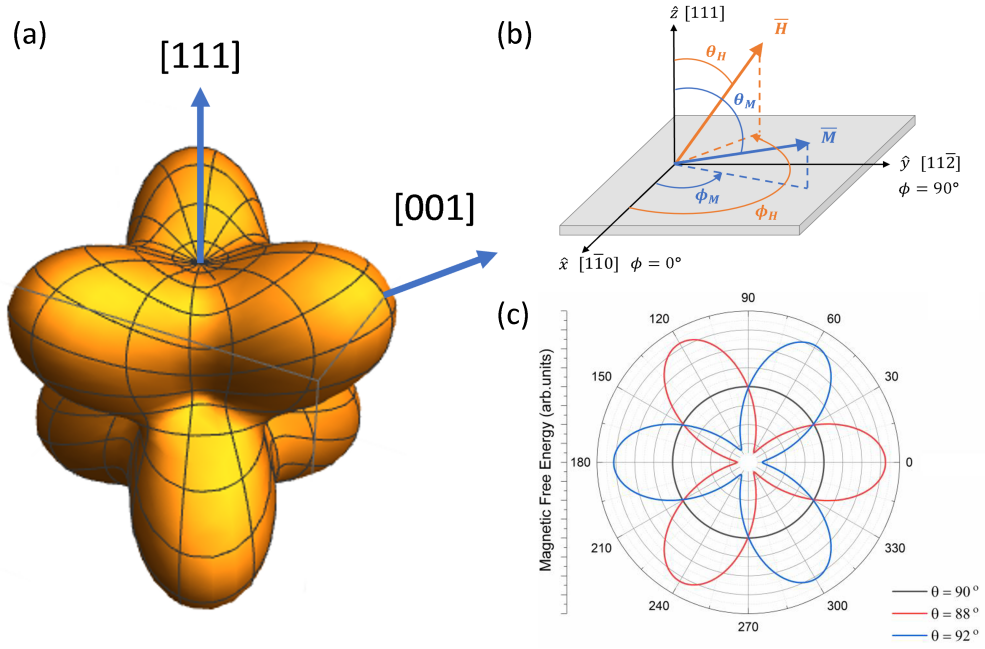

Figure 2.7: (a) Simulation of the magnetic free energy surface for a cubic crystal with a negative K_c. (b) Schematic of the magnetisation and applied magnetic field in a spherical polar coordinate geometry. (c) Azimuthal magnetic free energy for a 111-aligned cubic crystal with a negative K_c, at several polar angles.

field due to the presence of the neighbouring ions: this is known as the crystal field (discussed in Section 2.2.6). Electrons populate various orbitals in order to minimise their total energy. Due to the crystal field, these orbitals become non-degenerate, with some orbitals elevated in energy, and others lowered. This results in certain spin orientations being energetically favourable along certain crystallographic directions, known as MCA. Energetically favourable directions are referred to as easy axes [28].

The symmetry of the MCA is dependent upon the symmetry and structure of the crystal lattice. A cubic crystal structure possesses a cubic anisotropy with three easy axes. The anisotropy can be described by a corresponding energy density, U_{cubic}, expressed as a series expansion of the directional cosines α_1, α_2, and α_3 between the magnetisation and the principle crystallographic axes: $\vec{u}_1 = [100]$, $\vec{u}_2 = [010]$ and $\vec{u}_3 = [001]$ [26, 28].

$$U_{\text{cubic}} = K_{c0} + K_{c1}\left(\alpha_1^2\alpha_2^2 + \alpha_2^2\alpha_3^2 + \alpha_3^2\alpha_1^2\right) + K_{c2}\left(\alpha_1^2\alpha_2^2\alpha_3^2\right)\ldots \tag{2.16}$$

K_{ci} is the i^{th} order cubic anisotropy coefficient, which are energy density parameters with values dependent on the magnetic material. K_{c0} has no directional dependence and thus does not contribute to the overall MCA, and second order (and higher) contributions are minimal. Consequently, Equation 2.16 simplifies to:

$$U_{\text{cubic}} = K_{c1}\left(\alpha_1^2\alpha_2^2 + \alpha_2^2\alpha_3^2 + \alpha_3^2\alpha_1^2\right) \tag{2.17}$$

The sign of the cubic anisotropy constant K_{c1} determines the shape of the anisotropy. When K_{c1} is positive, the easy axes are aligned along the principle cubic axes and the hard axes along the $< 111 >$ directions. For negative values of K_{c1}, the axes invert, moving the easy axes to the $< 111 >$ directions and the hard axes to the principle cubic directions [26]. The corresponding magnetic free energy surface (considering only MCA) is shown in Figure 2.7(a).

For a (111)-oriented surface, the cubic anisotropy energy density can be written in terms of polar (θ_M) and azimuthal (ϕ_M) angles of the magnetisation, in spherical coordinates as illustrated in Figure 2.7(b). In this geometry, the first order (i.e. $K_c = K_{c1}$) cubic anisotropy term is given by Equation 2.18 [40, 24]. The azimuthal dependence of magnetic free energy density (considering only MCA) for different polar angles is illustrated in Figure 2.7(c).

$$U_{cubic}^{111} = K_c\left[\frac{1}{3}\cos^4\theta_M + \frac{1}{4}\sin^4\theta_M - \frac{\sqrt{2}}{3}\sin^3\theta_M\cos\theta_M\cos\left(3\phi_M\right)\right] \tag{2.18}$$

2.2.3 Magnetostatic Energy and Shape Anisotropy

Another free energy term arises due to magnetostatic interactions between the magnetic dipoles at each individual lattice site and the overall magnetisation of the system. In a ferromagnet, each magnetic dipole moment, $\boldsymbol{\mu}_j$, in the lattice induces a magnetic field, $\boldsymbol{h}_j$, at an atomic position $\boldsymbol{r}_j$, given by Equation 2.19 [24]:

$$\boldsymbol{h}_j = \frac{1}{4\pi}\left[-\frac{\boldsymbol{\mu_j}}{|\mathbf{r}-\mathbf{r}_j|^3} + \frac{3}{|\mathbf{r}-\mathbf{r}_j|^5}\left(\boldsymbol{\mu_j}\cdot\left(\boldsymbol{r}-\boldsymbol{r}_j\right)\right)\left(\boldsymbol{r}-\boldsymbol{r}_j\right)\right] \tag{2.19}$$

A dipole at the i$^{\text{th}}$ lattice site, $\boldsymbol{\mu}_i$, interacts with the field created by all of the other dipoles. As a summation over dipoles at all lattice sites in the system, the total magnetostatic energy E_{ms} is expressed in Equation 2.20:

$$E_{ms} = -\sum_i \boldsymbol{\mu}_i \cdot \sum_{j\neq i} \mu_0 \boldsymbol{h}_j \tag{2.20}$$

The total dipole field, $\sum_j \boldsymbol{h}_j$ is often written as the magnetostatic field, $\boldsymbol{H_d}$, allowing Equation 2.20 to be restated as:

$$E_{ms} = -\frac{\mu_0}{2}\sum_i \boldsymbol{\mu}_i \boldsymbol{H}_d \tag{2.21}$$

The magnetostatic (MS) field is referred to as the demagnetising field inside the crystal, and the stray field outside the crystal. The demagnetising field within the material acts in opposition to the local direction of magnetisation and is dependent on both the magnetisation of the material and the shape of the specimen. However, outside of the material, the stray field follows the magnetic flux lines and does not significantly affect magnetisation of the sample [26, 24]. Treating the magnetostatic field as a continuous field, $\boldsymbol{H}_d$ can be evaluated as [28]:

$$\boldsymbol{H}_d = \frac{1}{4\pi}\left[\int_V \frac{\rho_V\left(\boldsymbol{r}'\right)\left(\boldsymbol{r}-\boldsymbol{r}'\right)}{\left|\boldsymbol{r}-\boldsymbol{r}'\right|^3}dV + \int_S \frac{\rho_S\left(\boldsymbol{r}'\right)\left(\boldsymbol{r}-\boldsymbol{r}'\right)}{\left|\boldsymbol{r}-\boldsymbol{r}'\right|^3}dS\right] \tag{2.22}$$

where ρ_V and ρ_S are the charge densities of the volume and surface, respectively [24]. Where magnetisation is uniform across the whole sample, the volume integral term in Equation 2.22 goes to zero, leaving the second term only; this term (and thus $\boldsymbol{H_d}$) is entirely dependent on the shape of the sample, bounded by a surface, S. This leads to an expression for the magnetostatic energy density:

$$U_{Magnetostatic} = -\frac{\mu_0 M_s}{2}\mathbf{m}\cdot\mathbf{H}_d \tag{2.23}$$

$$U_{Magnetostatic} \approx \frac{1}{2}\mu_0 M_s^2 \cos^2\theta_M \tag{2.24}$$

Equation 2.23 illustrates a form of dipolar energy density with uniaxial anisotropy, which depends only on the magnetisation direction (unit vector $\mathbf{m}$) and the magnetostatic field $\mathbf{H}_d$ (resulting from the shape of the sample) as a dot product. This is referred to as shape anisotropy [24, 26]. In thin films, the shape anisotropy often results in the magnetisation being confined within the film plane to minimise the magnetostatic energy density, and is approximated in spherical polar coordinates by Equation 2.24.

2.2.4 Magnetoelastic Energy

Magnetoelastic (ME) interactions refer to coupling between the magnetisation of a magnetic material and mechanical strains applied to it. If mechanical strain is applied, the relative distances between magnetic moments change and the crystal lattice is distorted. This causes the spin configuration and magnetisation of the system to be modified. The reverse process is also observed, wherein applying a magnetic field results in the material experiencing a mechanical strain or change in its length (parallel to the applied field direction). This phenomenon is called magnetostriction [24, 7]. The magnetoelastic energy density associated with these effects in the (111) direction is approximated as [27]:

$$U_{Magnetoelastic} \approx \epsilon_{111}\lambda_{111}C_{44} \tag{2.25}$$

Where ϵ_{111} is the strain along [111], λ_{111} is a magnetostriction constant and C_{44} is the appropriate elastic constant. The λ_{111} constant for bulk YIG crystals at room temperature λ_{YIG} is -2.40×10^{-6} [41], with a bulk elastic constant C_{44} of 0.764×10^{12} erg/cc [42]. For materials with both very small strain and magnetostriction constants, the corresponding ME energy density term is treated as a small effect and has negligible impact on the free energy surface. However, for a strain along (111) of -0.6% (discussed for YIG/YAG in Chapter 4), an approximate $U_{Magnetoelastic}$ for YIG of 11000 erg/cc is calculated from Equation 2.25. This is only an estimation, as λ_{111} and C_{44} in YIG thin films may not necessarily have the same values as in bulk YIG, and values of λ_{111} and C_{44} are also strain dependent [7]. Nevertheless, this magnetoelastic energy density is the same order of magnitude as the first order cubic anisotropy constant for YIG, K_{c1} = -6100 erg/cc (which is itself small compared to oxides like Fe_3O_4 where K_{c1} = -1.1x10^5 erg/cc [43]). Therefore, ME energy effects require consideration in YIG where strain is significant.

2.2.5 Zeeman Energy

If an external magnetic field ($\boldsymbol{H}_{\mathbf{ext}}$) is applied to a ferromagnetic system, the magnetic moments inside are driven to align in parallel with the applied field (also called the Zeeman or bias field). The corresponding energy density is called the Zeeman energy, given by Equation 2.26. Alternatively, the Zeeman energy density may be defined in spherical polar coordinates for magnetisation and magnetic field vectors, as defined in Figure 2.7(c). For an in-plane magnetic field ($\theta_H \rightarrow \frac{\pi}{2}$), such that a factor of $\sin\theta_H \rightarrow 1$, the Zeeman energy density is given by Equation 2.27 [44, 28]:

$$U_{Zeeman} = -\mu_0 M_s \mathbf{m} \cdot \boldsymbol{H}_{\mathbf{ext}} \tag{2.26}$$

$$U_{Zeeman} = -\mu_0 H M_s \sin\theta_M \cos\left(\phi_M - \phi_H\right) \tag{2.27}$$

The Zeeman energy density is minimised when the magnetisation and the applied field vectors are parallel. As the magnitude of the applied field increases, the Zeeman term dominates the magnetic free energy surface. This results in the deformation of the free energy surface, forcing a free energy minimum along the direction of the bias field.

2.2.6 Crystal Field Effects

Different electron environments within a crystal can cause distortions to local electronic structure. Electrons in non-spherically symmetric orbitals exert Coulomb repulsion on one another in order to minimise local electrostatic energy. The additional electric field produced as a result is called the crystal field [45]. The crystal field acts to eliminate degeneracy by introducing

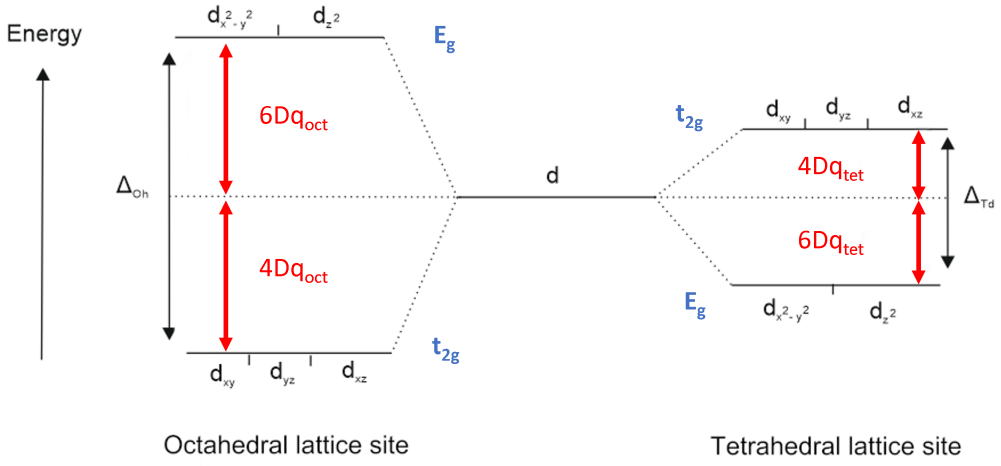

Figure 2.8: A schematic of the energy level splitting of d-orbitals in tetrahedral and octahedral lattice sites, arising from the crystal field.

an energy gap between electron orbitals whose charge cloud points in directions of differing electron density. This is illustrated in Figure 2.8, for d-orbitals in a tetrahedral or octahedral crystal field. The crystal field removes the degeneracy of the five d-orbitals by introducing an energy gap of 10Dq between orbitals of different character: defined as a doublet of E_g (degenerate $d_{x^2-y^2}$ and d_{z^2} orbitals) and a triplet of t_{2g} (degenerate d_{xy}, d_{xz} and d_{yz} orbitals). Dq is a parameter derived from crystal field theory, defined in Equation 2.28: where $\overline{r^4}$ is the mean fourth power radius of the d electrons of a central ion (with octahedral coordination) and a is the distance to one of the six surrounding negative anions of charge Ze, located at ±a on the z,y,z axes. Crystal field theory predicts that the energy splitting of an tetrahedral field is 4/9 that of an octahedral field, and reversed [46, 27]. The energy splitting is lower for tetrahedral coordination because the four surrounding anions and their ligand electrons are not oriented parallel towards any d-orbitals (unlike octahedral anions oriented along orthogonal x,y,z axes). Crystal lattice distortions due to strain can also cause shifts to the crystal field and can lift this degeneracy further. Crystal field effects are accounted for in the MCA of a material (discussed in Section 2.2.2), with respect to defining the magnetic free energy surface.

$$Dq_{\text{oct}} = \frac{Ze^2\overline{r^4}}{6a^5} \tag{2.28}$$

$$Dq_{\text{tet}} = -\frac{4}{9}Dq_{\text{oct}} \tag{2.29}$$

For transition metal ions, the crystal field eliminates orbital degeneracy and quenches the orbital angular momentum [24]. A non-degenerate ground state may exist as a real wavefunc-

tion, $|\psi\rangle$. The expectation value of the total orbital angular momentum operator, $\langle\psi|\,\hat{\boldsymbol{L}}\,|\psi\rangle$ must also be purely real. However, the operator $\hat{\boldsymbol{L}}$ is purely imaginary. The only value to satisfy these conditions is $\mathbf{L} = 0$. In real crystals, however, spin-orbit coupling occurs meaning the orbital moment is not entirely quenched. Consequently, discussed in Section 2.3, a g-factor with a spin contribution of g = 2 can be enlarged with an extra contribution proportional to the orbital angular momentum, in some materials. The first-order cubic anisotropy constant, K_1 can be defined in terms of the crystal field and spin-orbit coupling following Equation 2.30 [47]:

$$K_1 \simeq \frac{1}{V_T}\left(\sqrt{A^2 + 4\lambda^2} - A\right) \tag{2.30}$$

$$K_1 = \frac{2\lambda^2}{AV_T} \tag{2.31}$$

Where V_T is a unit volume, λ is the spin-orbit coupling constant, and 2A is the crystal field splitting. In the limit that $\lambda << 2A$, K_1 is given by Equation 2.31, and the crystal field acts to reduce K_1 [47, 26].

2.3 Magnetisation Dynamics

In addition to magnetostatic properties of materials, the dynamical motion of magnetic moments in materials is very important to consider. Dynamic magnetic behaviour can be both measured and exploited in the design of novel spintronic and magnonic devices.

The magnetic moment of an individual electron ($\boldsymbol{\mu}$) is related to its total angular momentum ($\boldsymbol{J}$) by Equation 2.32:

$$\boldsymbol{\mu} = \gamma \boldsymbol{J} \tag{2.32}$$

where $\boldsymbol{J}$ is the sum of the electron's orbital and spin angular momentum ($\boldsymbol{L}$ and $\boldsymbol{S}$) respectively. The constant γ is known as the gyromagnetic ratio, defined as the ratio of a particle's magnetic moment to its angular momentum or angular frequency [24, 26]. The gyromagnetic ratio governs the precessional motion of magnetisation in a material, and is an important value to extract in order to understand its dynamic properties. The gyromagnetic ratio is given by Equation 2.33, in terms of the Bohr magneton (μ_B) and the reduced Planck constant ($\hbar$):

$$\gamma = \left|\frac{g\mu_B}{\hbar}\right| \tag{2.33}$$

g represents the spectroscopic g-factor of the electron, which relates the electron's magnetic moment to its angular momentum. For a known gyromagnetic ratio, a value for g can be

extracted from Equation 2.33, or vice versa for a known g. For free electrons, the g-factor has a value of approximately 2, and this is measured in most materials. This is also true where $\boldsymbol{L} = 0$, such as in materials containing half-filled $3d^5$ electron shells. However, the value of the g-factor can vary if electronic angular momentum is coupled to the crystal lattice [48, 49]. Determination of g allows the relative spin and orbital moments in a magnetic material to be evaluated using Equation 2.34. Here, μ_L is the orbital moment per spin, and μ_S is the spin moment [48, 50]. The spectroscopic g-factor is measured by either ferromagnetic resonance (FMR) spectroscopy or by x-ray magnetic spectroscopy techniques [50, 51].

$$g = 2\left(1 + \frac{\mu_L}{\mu_S}\right) \tag{2.34}$$

In magnetic materials, a separation in electron energies can arise based on their alignment either parallel or antiparallel to an external applied magnetic field. This produces two discrete energy levels which are occupied by spin-down and spin-up electrons respectively, and is known as Zeeman splitting. The Zeeman splitting energy (i.e. energy gap) between the two levels is defined in part by a splitting factor called the Landé g-factor. For a given electron level in an isolated atom, the Landé g-factor (g_J) is defined by quantum numbers of the total orbital moment (L), total spin moment (S) and their sum (J) [24]:

$$g_J = g_L \frac{J(J+1) - S(S+1) + L(L+1)}{2J(J+1)} + g_S \frac{J(J+1) + S(S+1) - L(L+1)}{2J(J+1)} \tag{2.35}$$

where g_L and g_S are g-factors for orbital and spin angular momentum respectively. g_L is equal to 1, and in the approximation that $g_S = 2$, this expression reduces to give:

$$g_J = 1 + \frac{J(J+1) + S(S+1) - L(L+1)}{2J(J+1)} \tag{2.36}$$

For a purely orbital moment (S = 0, J = L), the Landé g-factor is equal to 1, and for a purely spin moment (L = 0, J = S), it is equal to 2. The Zeeman energy splitting for an electron state, resulting from a non-zero magnetic field, is given by Equation 2.37. Here, the magnetic quantum number, m_j, is a projection of total angular momentum (J) along the z-axis, either parallel or antiparallel to the field, B. For electrons, characterised by a spin quantum number ($s = \frac{1}{2}$), $m_j = m_s = \pm\frac{1}{2}$ [24].

$$E = g_J \mu_B m_j B \tag{2.37}$$

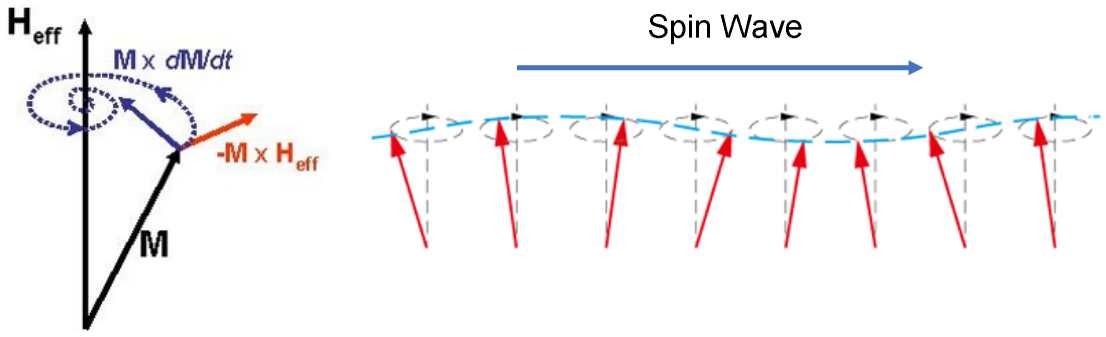

(a) (b)

Figure 2.9: (a) Larmor precession of magnetisation M about an effective H-field vector, with finite damping. [53]. (b) Phase-coherent precession of neighbouring moments as a propagating magnon/spin-wave with a finite wave-vector.

2.3.1 Landau-Lifshitz-Gilbert (LLG) Equation

Magnetisation dynamics originate from the collective precession of electron spins in a magnetically ordered medium. The magnetisation, $\mathbf{M}$, wants to align with the direction of the effective magnetic field, $\mathbf{H}_{\text{eff}}$, in a material. $\mathbf{H}_{\text{eff}}$ is considered the effective vector sum of any internal fields, anisotropy fields, demagnetising fields in the film and external applied fields. Shown in Figure 2.9(a), $\mathbf{H}_{\text{eff}}$ exerts a perpendicular torque on magnetisation $\mathbf{M}$ as a cross product: $-\mathbf{M}$ x $\mathbf{H}_{\text{eff}}$. This causes the magnetisation to precess around the direction of the total effective or applied field [26, 6]. The motion of precessing magnetisation is governed by the Landau-Lifshitz-Gilbert (LLG) equation, given in Equation 2.38, wherein γ is the gyromagnetic ratio and α is a dimensionless coefficient known as the intrinsic Gilbert damping constant [52].

$$\frac{\mathrm{d}\mathbf{M}}{\mathrm{dt}} = \underbrace{-\gamma(\mathbf{M} \times \mathbf{H}_{\text{eff}})}_{\text{Precession}} + \underbrace{\frac{\alpha}{\mathrm{M_s}}\left(\mathbf{M} \times \frac{\mathrm{d}\mathbf{M}}{\mathrm{dt}}\right)}_{\text{Damping}} \tag{2.38}$$

The LLG equation consists of two terms: a constant precessional cross-product and a damping term. For a constant $\mathbf{H}_{\text{eff}}$ and no damping ($\alpha = 0$), the magnetisation continues to precess around the effective field vector at a Lamor frequency of $\omega = \gamma\mathbf{H}_{\text{eff}}$. However, all known materials possess an intrinsic damping constant, α, greater than zero. This consequently causes the precessing magnetisation to spiral towards and align with the direction of $\mathbf{H}_{\text{eff}}$ in a timescale of $1/\alpha\omega$. This limits the length scales across which excitations such as spin waves can be sustained in a magnetic material.

Spin waves (or magnons) arise due to a coherence in phase between the precessions of neighbouring moments, shown in Figure 2.9(b). The phase difference defines the wavelength of the resultant spin-wave. Spin-wave behaviour is primarily determined by the dominant

type of interaction between the magnetic moments: either exchange interaction or dipole-dipole interaction. The exchange interaction favours the alignment of magnetic moments of neighbouring atoms to be either parallel or antiparallel. Deviations from such alignment incur an increase in the exchange energy of the system. The range of the exchange interaction is defined by the exchange length l_{ex}, expressed in terms of the exchange coupling constant A, and saturation magnetisation of a material M_S: $l_{ex} = \sqrt{\frac{A}{2\pi M_S^2}}$ in CGS units [54]. Although strong, the exchange interaction is short-ranged and only dominates for spin-waves with short wavelengths (less than 100 nm), and frequencies in the high GHz to THz regime. Longer wavelength spin-waves (1 μm or above) operate in low GHz regimes and are governed by weak, but long-ranged dipole interactions. These spin-waves are termed magnetostatic spin-waves (MSW), as they represent solutions to Maxwell's equations in the magnetostatic approximation [1][5].

2.4 Ferromagnetic Resonance

Ferromagnetic resonance (FMR) refers to the resonance precession of a material's magnetisation about a preferred equilibrium position, due to a resonant absorption of electromagnetic radiation. Physical descriptions of the FMR effect follow one of two treatments: classical or quantum.

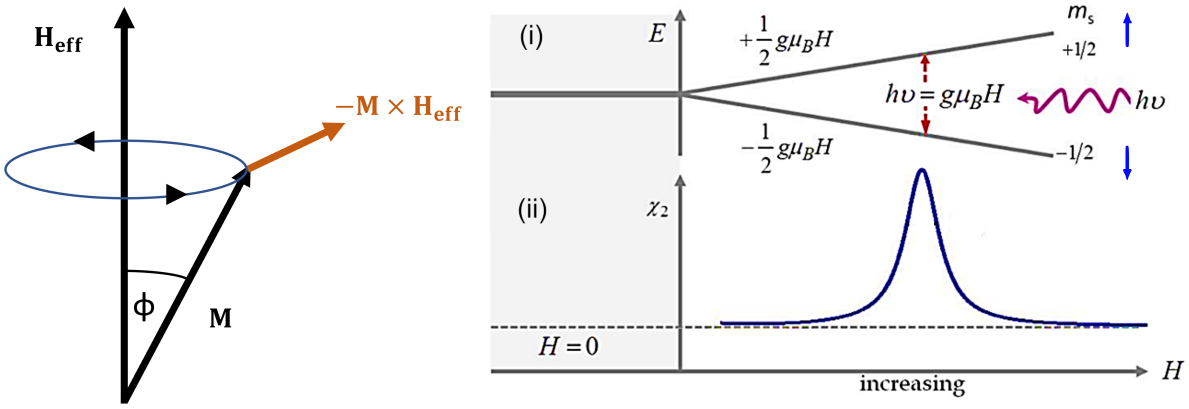

(a) (b)

Figure 2.10: (a) Classical FMR: Larmor precession of magnetisation M about an effective H-field vector, at a coning angle ϕ. (b) Quantum FMR: (i) Zeeman splitting of electron energies with applied magnetic field. (ii) FMR absorption signal, showing an increase in susceptibility for absorption, χ. Adapted from [4].

The classical treatment of FMR was first formulated by Kittel [55], and follows the dynamics described in Section 2.3 and the LLG equation (Equation 2.38). In this model, magnetic moments in a material are considered as a single magnetisation vector. In equilibrium, the

magnetisation aligns parallel to the effective field ($\mathbf{H}_{\text{eff}}$) in order to minimise magnetostatic energy. If the magnetisation is pulled from equilibrium by a field perpendicular to the effective field, the magnetisation will attempt to reach equilibrium via the torque: $-\mathbf{M}$ x $\mathbf{H}_{\text{eff}}$. If the perturbing field is applied at a frequency matching the Lamor frequency of the magnetisation ($\omega = \gamma \mathbf{H}_{\text{eff}}$), the magnetisation is driven to precess resonantly about the effective field. This is illustrated in Figure 2.10(a). Such a perturbing field would be an RF excitation, at the resonant frequency. The LLG equation describes the time-evolution of the magnetisation vector, and while the resonant RF is present, it precesses indefinitely. When the RF is no longer present, the precessing magnetisation spirals towards and realigns with the effective field. This relaxation is described by the additional damping term of the LLG equation.

Alternatively, the quantum treatment of FMR concerns the separation in electron energies arising due to the Zeeman effect. Illustrated in Figure 2.10(b), electron energy is based on the alignment of the electron spins with the effective field (with spins antiparallel to the field being a lower energy configuration) [56]. If the applied RF excitations have a photon energy ($\hbar\omega$) to match the Zeeman splitting energy (Equation 2.37), resonance occurs. This results in an excitation from low to high energy spin-states, due to magnetic dipole transitions and the RF photon being absorbed. Re-emission of the RF photon allows the spin to decay back to its ground state. [6][56].

2.4.1 The Kittel Equation

The Kittel equation describes how the resonant-RF frequency varies with the applied magnetic field. In frequency-field space, this field dependence follows a characteristic shape known as a Kittel curve. An example of a Kittel curve measured in YIG is shown in Figure 2.11(a). At low applied field, the FMR frequency follows a dominant $\sqrt{H}$ dependence, before transitioning into a more linear dependence as applied field increases in magnitude. The Kittel equation is fundamentally derived by solving the Smit-Beljers equation for FMR [57]. This resonance condition equation is given by the partial differentials of the magnetic free energy (U), with respect to polar (θ) and azimuthal (ϕ) angles of the magnetisation, such that:

$$\left(\frac{\omega}{\gamma}\right)^2 = \frac{1}{M_s^2 \sin^2\theta_M}\left[\frac{\partial^2 U}{\partial\theta_M^2}\frac{\partial^2 U}{\partial\phi_M^2} - \left(\frac{\partial^2 U}{\partial\theta_M \partial\phi_M}\right)^2\right] \tag{2.39}$$

Kittel derived that the condition for FMR for a plane surface is given by Equation 2.40. Here, H_{eff} is the strength of the static (applied) magnetic field, and B_{eff} is the magnetic induction respectively, within a magnetic material [55]. For a given crystal structure, the full expression of $H_{\text{eff}}B_{\text{eff}}$ is acquired from the Smit-Beljers equation, by obtaining a resonance condition resolved for all angular cosines [44].

$$\omega_0 = \gamma\sqrt{H_{\text{eff}}B_{\text{eff}}} \tag{2.40}$$

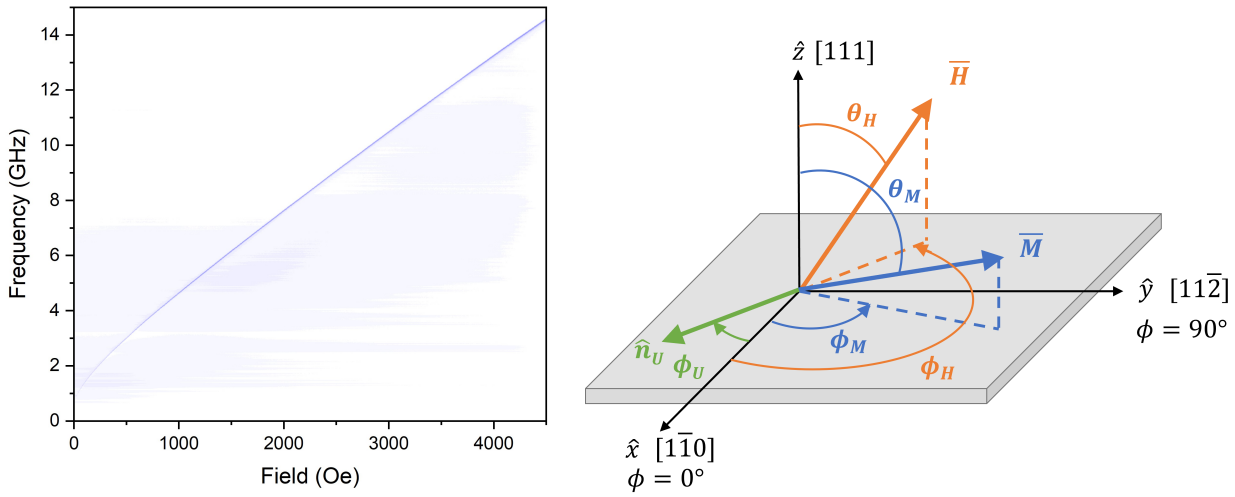

(a) (b)

Figure 2.11: (a) Kittel curve of YIG in frequency-field space, measured using VNA-FMR as described in Chapter 3. The blue shading is a background signal resulting from the co-planar waveguide (CPW) of the FMR apparatus. (b) Schematic of the magnetisation and applied magnetic field in a spherical polar coordinate geometry, with a generalised uniaxial anisotropy.

The magnetic free energy density for a (111)-oriented surface is given as the sum of the Zeeman, demagnetisation and cubic anisotropy terms (all defined in Section 2.2). A uniaxial anisotropy can be considered here with two additional terms. This uniaxial anisotropy is resolved into two components: one perpendicular, $U^u_\perp$, and the other parallel to the sample plane, $U^u_\parallel$. These two terms have corresponding anisotropy constants, $K^u_\perp$ and $K^u_\parallel$ respectively.

$$U^u_\perp = -K^u_\perp \cos^2\theta_M \tag{2.41}$$

$$U^u_\parallel = -K^u_\parallel \sin^2\theta_M \cos^2(\phi_M - \phi_U) \tag{2.42}$$

Relevant angles of the magnetisation and applied field vectors in spherical coordinates, in addition to a generalised uniaxial anisotropy, are illustrated in Figure 2.11(b). The magnetic free energy density for (111) can be written as $U_{111} = U_{Zeeman} + U_{Cubic} + U_{Magnetostatic} + U_{Uniaxial}$, or in full as (in cgs units):

$$U_{111} = -HM_s \sin\theta_M \cos(\phi_M - \phi_H) + K_c \left[\frac{1}{3}\cos^4\theta_M + \frac{1}{4}\sin^4\theta_M - \frac{\sqrt{2}}{3}\sin^3\theta_M \cos\theta_M \cos(3\phi_M)\right] + 2\pi M_s^2 \cos^2\theta_M - K_\perp^u \cos^2\theta_M - K_\parallel^u \sin^2\theta_M \cos^2(\phi_M - \phi_U) \tag{2.43}$$

Substituting this into the Smit-Beljers Equation, and in the limit that $\theta_M \to \frac{\pi}{2}$ (magnetisation is aligned in-plane), the FMR resonance condition becomes:

$$\left(\frac{\omega}{\gamma}\right)^2_{111} = \frac{1}{M_s^2}\left(\left[HM_s\cos(\phi_M - \phi_H) + 4\pi M_s^2 - K_c - 2K_\perp^u + 2K_\parallel^u \cos^2(\phi_M - \phi_U)\right]\cdot \left[HM_s\cos(\phi_M - \phi_H) + 2K_\parallel^u \cos\left[2(\phi_M - \phi_U)\right]\right] - 2K_c^2 \sin^2(3\phi_M)\right) \tag{2.44}$$

In the limit of high field, such that magnetisation aligns completely with the field ($\phi_M \to \phi_H = \phi$), further simplifications can be made to the FMR resonance condition:

$$\left(\frac{\omega}{\gamma}\right)^2_{111} = \frac{1}{M_s^2}\left(\left[HM_s + 4\pi M_s^2 - K_c - 2K_\perp^u + 2K_\parallel^u \cos^2(\phi - \phi_U)\right]\cdot \left[HM_s + 2K_\parallel^u \cos\left[2(\phi - \phi_U)\right]\right] - 2K_c^2 \sin^2(3\phi)\right) \tag{2.45}$$

Cubic and uniaxial anisotropy terms can be combined to create a single out-of-plane anisotropy field term, provided the cubic and out-of-plane uniaxial components are parallel; an in-plane easy axis Kittel equation can be obtained thereafter. However, if uniaxial anisotropy is considered negligible compared to cubic anisotropy, the FMR resonance condition simplifies further. In the limit that $K_\perp^u \to 0$ and $K_\parallel^u \to 0$:

$$\left(\frac{\omega}{\gamma}\right)^2_{111} = \frac{1}{M_s^2}([HM_s]\cdot[HM_s + 4\pi M_s^2 - K_c] - 2K_c^2\sin^2(3\phi)) \tag{2.46}$$

$$\left(\frac{\omega}{\gamma}\right)^2_{111} = H(H + 4\pi M_{\text{eff}}) - \frac{2K_c^2}{M_s^2}\sin^2(3\phi) \tag{2.47}$$

A maxima in $\left(\frac{\omega}{\gamma}\right)^2_{111}$ is observed in the limit $\phi \to 0$, due to the $-\frac{2K_c^2}{M_s^2}\sin^2(3\phi)$ term. From this FMR resonance condition, an in-plane easy axis Kittel equation can obtained. The FMR resonant frequency, ω, as a function of applied field, H, for a (111)-oriented film is given by Equation 2.48:

$$\omega = \gamma\sqrt{H(H + 4\pi M_{\text{eff}})} \tag{2.48}$$

Here, an effective magnetisation M_{eff} is defined as $4\pi M_{\text{eff}} = 4\pi M_s - \frac{K_c}{M_s}$. The effective magnetisation is composed of the saturation magnetisation, M_s, and the (first order) magnetocrystalline anisotropy constant, K_c, of the material.

Fitting of the easy-axis Kittel curve is particularly useful in characterising the magnetisation dynamics of a sample, with an extraction of the gyromagnetic ratio γ. Other useful magnetic parameters such as the saturation magnetisation can be inferred, as well as relative changes in them due to sample treatments such as annealing. For a fixed FMR frequency and γ, if the resonant field increases, the effective magnetisation must correspondingly decrease (whether due to changes to magnetisation or potential anisotropy fields), and vice versa. Varying the relative angle between the bias field and the sample's crystal structure also allows in-plane anisotropy to be mapped, as the position of the Kittel curve will shift based on the field direction relative to easy or hard axes. For an easy axis, the resonant field is minimised for a constant frequency, whereas for hard axes it is maximised. Relative changes in resonant field allow values of the additional in-plane anisotropy field to be inferred.

2.4.2 FMR Damping

Magnetic damping refers to resistance met by the precessional motion of the magnetisation. The damping of a given magnetic material is strongly dependent on its crystal structure, and plays a crucial role in the magnetisation dynamics. Magnetic damping effects in metallic ferromagnets fall under two broad categories, distinguished by their origin. Intrinsic damping (or Gilbert damping) effects arise due to interactions between the precessing magnetisation and the crystal lattice, such as from non-spherical charge distributions or non-zero orbital angular momentum [58, 59]. Alternatively, extrinsic damping can arise due to the interactions between precession and defects or dislocations within the crystal structure. Intrinsic damping effects are governed by three major mechanisms: eddy currents [60], magnon-phonon coupling (phonon drag) [61], and itinerant electron relaxation [62, 63, 64]. The relevance of each mechanism in ferromagnetic films is highly dependent on both the material of interest and the chosen film thickness.

Eddy Currents

The precession of the magnetisation leads to the induction of eddy currents by conduction electrons, and the dissipation of them is proportional to the electrical conductivity of the sample. Consequently, damping effects due to eddy current induction is more significant in metallic ferromagnets, than in magnetic insulators [60]. In metallic films, contributions of eddy currents to intrinsic damping are proportional to the square of the film thickness and are ultimately negligible in films below 50nm [65]. All materials in this thesis are insulating, in addition to being thin, and thus eddy currents are neglected.

Magnon-Phonon Coupling (Phonon Drag)

Magnon-phonon coupling effects are described using the relaxation of the electrons by phonon drag [62]. If magnetisation and lattice strain are assumed to be homogeneous in a sample, the Gilbert damping arising from phonon interactions can be described in small geometries by Equation 2.49, derived as a result of the LLG equation and lattice strain equations [66].

$$\alpha_{\text{phonon}} = \frac{2\eta\gamma}{M_S}\left(\frac{B_2(1+\nu)}{E}\right)^2 \tag{2.49}$$

where, η is the phonon viscosity, γ is the gyromagnetic ratio, B_2 is the magneto-elastic shear constant, ν is the Poisson ratio and E is the Young's modulus. While η is historically difficult to obtain, it can be found empirically for a material in the microwave frequency range using transmission experiments [67], or calculated theoretically [68]. The remaining parameters can be obtained more easily by other methods.

Itinerant Electron Relaxation

Itinerant electron relaxation is the primary intrinsic damping mechanism in metallic ferromagnetic materials. However, the exact mechanism behind this damping is still debated [69]. Currently, the most accepted model is Kambersky's breathing Fermi surface model: describing the transfer of angular momentum from Fermi level electrons to the crystal lattice due to spin-orbit coupling effects [70, 71]. The Bloch state of Fermi electrons is dependent on the electrons' magnetic moment (μ) [72]. Changing the direction of magnetisation ($\mathbf{M}$) changes the energy of the Fermi electrons, due to spin-orbit coupling. This causes the Fermi surface to distort and shift over time, 'breathing' as the magnetisation precesses. The Fermi electrons then repopulate newly-generated low-energy states at the Fermi surface via intraband transitions. This relaxation of Fermi electrons occurs over a non-zero momentum relaxation time (τ_m) and lag behind the instantaneous magnetisation. The spins relax towards $\mathbf{M}$ and transfer angular momentum to the d-electrons, leading to damping of the spin-moments. The phase lag (and resulting Gilbert damping) is proportional to the angular frequency (ω), and thus the applied RF frequency [72, 73]. A more complete review of itinerant electron relaxation (including Kambersky's torque correlation model and interband transitions) is given by Eriksson [72], and in theoretical work by Gilmore and Stiles [74].

General Form of FMR Damping

A ferromagnetic resonance may be characterised by its FMR linewidth (ΔH). Throughout this work, the FMR linewidth is taken as the HWHM of the resonance lineshape (discussed further in Section 3.3.3). In a crystal structure, the general form of the FMR damping is described by the resonance linewidth as a function of angular frequency. If intrinsic damping effects are dominant, the FMR linewidth (ΔH) is linear in ω. The FMR linewidth is then

related to the relaxation of precessing magnetisation in the material, such that for a HWHM ΔH [75]:

$$\Delta H(\omega) = \Delta H(0) + \alpha\frac{\omega}{\gamma} \tag{2.50}$$

$$\Delta H(f) = \Delta H(0) + \frac{2\pi\alpha}{\gamma}f \tag{2.51}$$

where **H** is the magnetic field strength, γ is the gyromagnetic ratio, and α is the Gilbert damping parameter. The gradient, given by $\frac{2\pi\alpha}{\gamma}$ for $\Delta H(f)$, describes the intrinsic damping behaviour of the crystal structure, while the intercept $\Delta H(0)$ describes the extrinsic damping effects arising from structural defects. Extrinsic damping effects come from two general sources. One major source is any mosaicity in the crystallographic texture of a sample, which can produce a range of spin alignments and broadens the FMR linewidth. Alternatively, any magnetic inhomogeneity in the film can cause neighbouring spins to become de-phased in incoherent precession, due to variations in local effective field [59]. However, other relaxation modes also exist, including two-magnon scattering occurring off defects in the film.

Two-Magnon Scattering

Non-linear FMR damping in ω (particularly at higher frequencies) is primarily due to two-magnon scattering in a sample. Two-magnon scattering is another extrinsic damping effect, adding a third term to the general linewidth expression from Equation 2.50. This occurs when a uniform mode magnon (k = 0, also known as FMR mode) scatters into two or more non-zero k magnons with the same frequency, due to energy conservation ($\omega(0) = \omega(\mathrm{k})$). The value of k is governed by the magnon-dispersion relation, examples of which are given in [5]. Two-magnon scattering increases with the density of defects in a sample's structure [76, 77]. The magnitude of the scattering effect is proportional to the Fourier transform of magnetic inhomogeneities in the sample, shown in the additional linewidth term:

$$\Delta \boldsymbol{H}_{2-mag} = \Gamma \sin^{-1}\sqrt{\frac{\sqrt{\omega^2 + (\omega_0/2)^2} - \omega_0/2}{\sqrt{\omega^2 + (\omega_0/2)^2} + \omega_0/2}} \tag{2.52}$$

where Γ describes the magnitude of the 2-magnon scattering, ω is the angular frequency and ω_0 is given as:

$$\omega_0 = 4\pi\gamma M_{\text{eff}} \tag{2.53}$$

Two-magnon scattering behaviour causes non-linearity in the FMR linewidth in ω, particularly at higher frequencies [59]. If two-magnon scattering dominates damping instead of the

intrinsic terms, the trend in $\Delta H(\omega)$ turns from linear to a unique two-magnon dependence. This trend in FMR linewidth and total damping is better described by Equation 2.54.

$$\Delta \boldsymbol{H}(\omega) = \Delta \boldsymbol{H}(0) + \alpha \frac{\omega}{\gamma} + \Delta \boldsymbol{H}_{2-mag} \tag{2.54}$$

2.5 Spin Pumping

2.5.1 Spin Transport Basics: SHE and STT/SOT

A brief overview of effects that concern spin transport in spintronic devices and heterostructures follows. These effects include the spin Hall effect, spin-orbit torque and spin pumping. These effects form the basis by which pure spin currents are injected into and out of magnetic insulators such as YIG.

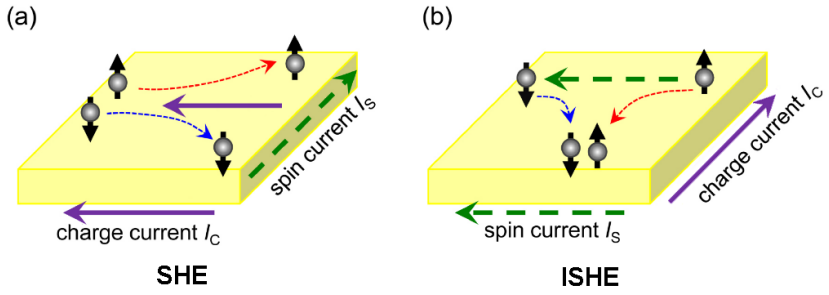

Figure 2.12: Spin Hall effect (SHE) and inverse spin Hall effect (ISHE), showing directions of charge current and perpendicular spin-current.

The spin Hall effect (SHE) is a charge-current to spin-current conversion process. The SHE occurs when materials carrying a charge current develop an accumulation of electron spins on perpendicular surfaces: possessing spins of opposite sign. The deflection of electrons based on their spin-polarisation consequently gives rise to a perpendicular spin 'current', illustrated in Figure 2.12(a). It is important to note that this spin 'current' does not result in a net electron transfer, as spin-up and spin-down electrons are deflected equally. Unlike the classical Hall effect, no applied magnetic field is necessary for the SHE to occur. The SHE often occurs in heavy metals with strong spin-orbit coupling such as platinum [78]. The effect is also observed in ferro/ferrimagnetic materials where it exhibits an added dependence on the material's magnetisation, referred to as an Anomalous Spin Hall effect [79]. The inverse spin Hall effect (ISHE) refers to when the reverse occurs: the conversion of a pure spin current into a perpendicular charge current. The ISHE is a dynamically equivalent process to the SHE (following Onsager reciprocity) and shown in Figure 2.12(b) [80].

Spin transfer torque (STT) is defined as a torque due to the absorption of an incident spin current with a polarisation component perpendicular to the magnetisation, **M**. Such spin torques cause the displacement of a magnetisation vector away from its equilibrium position. STT can be expressed as a triple cross-product between the magnetisation and an incident spin current $\mathbf{I}_s$, as $\frac{\gamma}{\mathrm{M_s}V}\mathbf{m} \times (\mathbf{I}_s \times \mathbf{m})$ [64]. Here, the unit vector of magnetisation $\mathbf{m}$ is considered, such that $\mathbf{m} = \mathbf{M}/\mathrm{M_s}$ where $\mathrm{M_s}$ is the saturation magnetisation. Adding this STT term to the LLG equation, the magnetisation dynamics are described by the Landau-Lifshitz-Gilbert-Slonczewski equation [81, 64]:

$$\frac{\mathrm{d}\mathbf{m}}{\mathrm{d}t} = \underbrace{-\gamma(\mathbf{m} \times \mathbf{H}_{\mathrm{eff}})}_{\text{Precession}} + \underbrace{\alpha\left(\mathbf{m} \times \frac{\mathrm{d}\mathbf{m}}{\mathrm{d}t}\right)}_{\text{Damping}} + \underbrace{\frac{\gamma}{\mathrm{M_s}V}\mathbf{m} \times (\mathbf{I}_s \times \mathbf{m})}_{\text{Spin Transfer Torque}} \tag{2.55}$$

The LLGS equation and Figure 2.13(a) illustrate that, depending on the direction of the spin current, STT can be antiparallel (or parallel) to the Gilbert damping term. This reduces (or reinforces) the relaxation of magnetisation back to equilibrium, and enables (or further dampens) magnetisation precession.

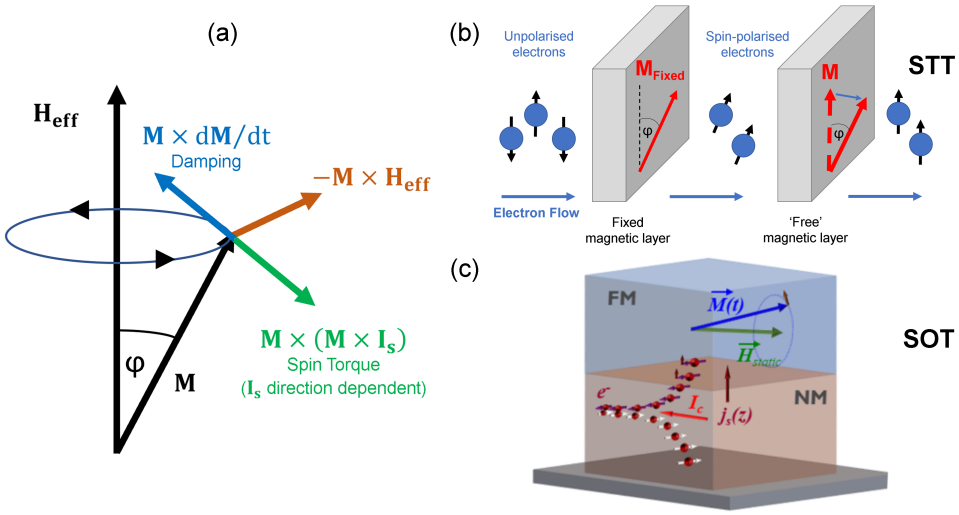

Figure 2.13: (a) Precession of magnetisation M about an effective H-field vector, with finite damping and a finite spin torque. (b) Schematic diagram of the STT process and (c) the SOT process for inducing magnetisation dynamics. Adapted from [82].

Spin-orbit torque (SOT) is another spin-torque effect, but distinct from STT. Illustrated in Figure 2.13(b), STT relies on a spin-polarised electron current in order to change the magnetisation in an isolated 'free' magnetic layer. SOT, however, results from pure spin currents with no net charge flow (generated from the SHE). SOT refers to an injection of spin across the interface of a non-magnetic heavy metal (such as platinum) and an adjacent magnetic layer, shown in Figure 2.13(c). Spin angular momentum is transferred from the conduction electrons

in the platinum to the magnetisation of the magnetic layer; this produces a spin-torque on the magnetisation, causing magnetisation precession as a spin-wave or magnon. SOT is a common method for exciting spin waves in YIG/Pt bilayers and heterostructures [3, 18, 19].

2.5.2 Spin Pumping

Spin pumping, in contrast, is the dynamically equivalent reverse process to SOT. Spin pumping is a method of generating a spin current (or spin accumulation) from a ferromagnetic (FM) layer into an adjacent normal metal (NM) or semiconductor layer in a hetero-structure. The electronic band structure of a spin-pumped FM/NM bilayer is shown in Figure 2.14(a). When the magnetisation of the FM layer is excited to precess (usually by FMR), a net angular momentum is transferred to the NM layer across the FM/NM interface [83]. The local $\frac{d\mathbf{M}}{dt}$ is enough to cause an imbalance in the chemical potentials of spin-up and spin-down electrons in the NM layer, producing a spin accumulation and thus spin current in the NM layer [84, 85, 86]. Shown in Figure 2.14(b), the spin accumulation/spin current generated at the interface in the NM layer can in turn be converted to measurable charge current and voltage via the ISHE.

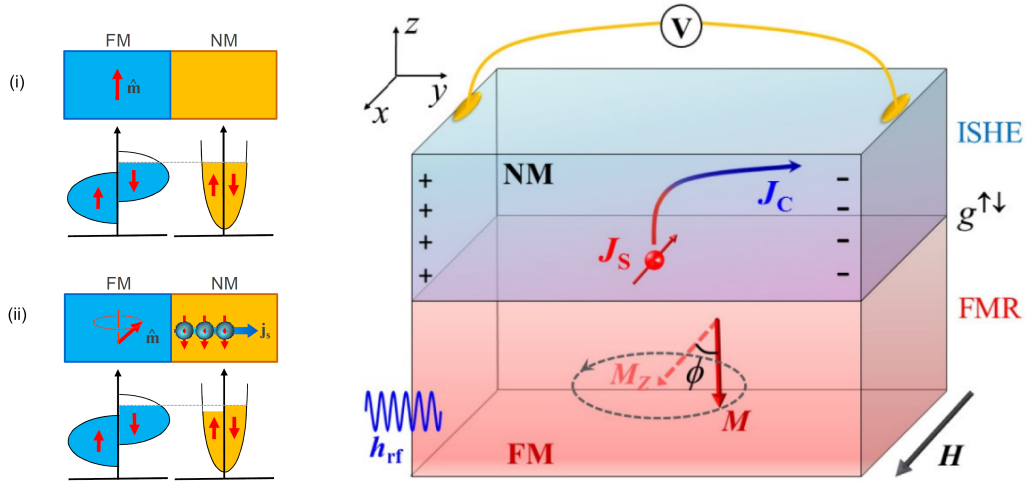

Figure 2.14: (a) Spin pumping across a ferromagnetic/normal metal (FM/NM) interface, with (i) static FM magnetisation and (ii) precessing FM magnetisation. Adapted from [87] (b) FMR-driven spin pumping, and detection via ISHE in a non-magnetic (NM)/ferromagnetic (FM) bilayer. Adapted from [83].

If the NM layer (called a spin reservoir) is a good spin sink or spin conductor, then almost no spin accumulation occurs and spin current is propagated across the FM/NM interface almost immediately. However, in more resistive spin reservoirs, spin pumping from the FM can create a build-up of spin accumulation in the NM. This spin accumulation can relax by spin-flip scattering, or a spin current backflow back into the FM can occur. In this case, the overall spin

current is a net flow into the NM, such that $\mathbf{I}_S = \mathbf{I}_S^{\text{pump}} - \mathbf{I}_S^{\text{back}}$. For an ideal spin sink and an infinite spin-flip scattering rate [88], the backflow current into the FM is zero [85]. Heavy metals ($Z \geq 50$) with p or d electrons in their conduction band, such as Pt and Pd, are near-perfect spin sinks on account of strong spin-orbit coupling [85].

The efficiency with which spins are pumped across the FM/NM interface is defined by the theoretical spin mixing conductance, $G^{\uparrow\downarrow}$ (Ω^{-1}). More commonly, the intrinsic spin mixing conductance per unit area (A) per conductance channel, $g^{\uparrow\downarrow} = G^{\uparrow\downarrow}/(Ae^2/h)$, is used [89]. $g^{\uparrow\downarrow}$ is a complex quantity expressed as $g^{\uparrow\downarrow} = g_r^{\uparrow\downarrow} + ig_i^{\uparrow\downarrow}$. $g_r^{\uparrow\downarrow}$ represents the transmitted part of the pumped spin current (aligned with the transverse component of the spin accumulation), and $g_i^{\uparrow\downarrow}$ reflects the de-phasing of spins (due to precession about the direction of the FM magnetisation) as they cross the interface [88]. Theory surrounding quantitative analysis of $g^{\uparrow\downarrow}$ is given by Tserkovnyak *et al.*, provided the real part dominates (i.e. $g^{\uparrow\downarrow} \approx g_r^{\uparrow\downarrow}$) [85, 64]. First principle calculations of $g^{\uparrow\downarrow}$ for various FM/NM interfaces show the imaginary part is negligibly small [90, 91]. DFT calculations of band structure, STTs and $g^{\uparrow\downarrow}$ for YIG/NM interfaces [92] also confirm this approximation to be valid.

For an ideal spin sink, the spin current pumped into the NM layer, by a precessing FM magnetisation, is given by Equation 2.56. For non-ideal conductors, an additional term is needed to account for potential spin-current backflow (perpendicular to the magnetisation) due to spin accumulation, $\vec{\mu_s}$ (aligned with $\mathbf{m} \times \frac{d\mathbf{m}}{dt}$) [64]:

$$\mathbf{I}_S^{\text{pump}} = \frac{\hbar}{4\pi} g_{\text{r}}^{\uparrow\downarrow} \mathbf{m} \times \frac{d\mathbf{m}}{dt} - \underbrace{\frac{g_{\text{r}}^{\uparrow\downarrow}}{4\pi} \mathbf{m} \times \vec{\mu_s} \times \mathbf{m}}_{\text{Non-ideal/backflow}} \tag{2.56}$$

A direct consequence of angular momentum transfer via spin pumping is a significant increase in the Gilbert damping constant of the FM layer. The spin current out of the FM layer carries angular momentum perpendicular to the magnetisation direction. From conservation of angular momentum, the spins ejected as a spin current $\mathbf{I}_S^{pump}$ correspond to a torque of $-\mathbf{I}_S^{pump}$ on the magnetisation. This produces an additional term in the LLG equation, accounting for the effect of spin-pumping on the FM magnetisation dynamics (shown in Equation 2.57) [85]; M_s is the saturation magnetisation and V is the volume of the FM layer. Substituting in the expression for $\mathbf{I}_S^{pump}$ (for an ideal spin sink) from Equation 2.56, the enhancement to the Gilbert damping is shown in Equation 2.58 [88]:

$$\frac{\text{d}\mathbf{m}}{\text{dt}} = -\gamma(\mathbf{m} \times \mathbf{H}_{\text{eff}}) + \alpha_{\text{FM}} \left(\mathbf{m} \times \frac{\text{dm}}{\text{dt}} \right) + \underbrace{\frac{\gamma}{\text{M}_\text{s} V} \mathbf{I}_S^{pump}}_{\text{Spin Pumping}} \tag{2.57}$$

$$\frac{\text{d}\mathbf{m}}{\text{dt}} = -\gamma(\mathbf{m} \times \mathbf{H}_{\text{eff}}) + \left(\alpha_{\text{FM}} + \frac{\hbar\gamma}{4\pi \text{M}_\text{s} \text{t}_{\text{FM}}} \text{g}_{\text{r}}^{\uparrow\downarrow} \right) \mathbf{m} \times \frac{\text{dm}}{\text{dt}} \tag{2.58}$$

This enhanced Gilbert damping for the FM/NM bilayer is defined as $\alpha_{\mathrm{FM/NM}} = \alpha_{\mathrm{FM}} + \alpha_{\mathrm{SP}}$, where α_{SP} is the increase in damping due to spin pumping, and α_{FM} is the intrinsic FM damping. The enhancement in Gilbert damping due to spin-pumping can be directly measured using FMR spectroscopy techniques, and is defined as [85, 64]:

$$\alpha_{\mathrm{SP}} = \frac{\mathrm{g}\mu_{\mathrm{B}}}{4\pi \mathrm{M_s t_{FM}}} g_{\mathrm{eff}}^{\uparrow\downarrow} \tag{2.59}$$

where $\mathrm{t_{FM}}$ is the thickness of the FM layer. g and μ_{B} represent the spectroscopic g-factor and Bohr magneton respectively. $g_{\mathrm{eff}}^{\uparrow\downarrow}$ is referred to as the *effective* spin-mixing conductance. $g_{\mathrm{eff}}^{\uparrow\downarrow}$ is another proportionality parameter that represents the availability of conduction channels (per unit area, per unit time) across the FM/NM interface. For α_{SP} to be accurate, the intrinsic ability of the NM to absorb spin current must be accounted for, as well as interfacial effects (for which no separate terms currently exist in theory). In Equation 2.59, both of these factors are included in $g_{\mathrm{eff}}^{\uparrow\downarrow}$ on an empirical basis instead. $g_{\mathrm{eff}}^{\uparrow\downarrow}$ can be determined directly from FMR measurements, and accounts for variations in NM layer properties. For a NM layer of a known thickness, $g_{\mathrm{eff}}^{\uparrow\downarrow}$ is related to the *intrinsic* spin-mixing conductance, $g^{\uparrow\downarrow}$, by [85, 64]:

$$\mathrm{g}_{\mathrm{eff}}^{\uparrow\downarrow} = \frac{\mathrm{g}^{\uparrow\downarrow}}{1 + \mathrm{g}^{\uparrow\downarrow}\left(\frac{h}{e^2}\frac{\sigma}{\lambda_{\mathrm{SD}}}\tanh\left(\frac{t}{\lambda_{\mathrm{SD}}}\right)\right)^{-1}} \tag{2.60}$$

where σ, t and λ_{SD} are the conductivity, thickness and spin diffusion length of the NM layer, respectively. From Equation 2.59, the enhancement in Gilbert damping is directly proportional to $g_{\mathrm{eff}}^{\uparrow\downarrow}$. The reciprocal thickness of the FM layer is also an important factor, wherein a larger increase in Gilbert damping is observed for thinner FM layers [93]. However, the use of $g_{\mathrm{eff}}^{\uparrow\downarrow}$ in characterising spin-pumping efficiency requires careful consideration. It is important to note that the effective spin mixing conductance, $g_{\mathrm{eff}}^{\uparrow\downarrow}$, has a dependence on the thickness of the NM layer as well. $g_{\mathrm{eff}}^{\uparrow\downarrow}$ is additionally dependent on both the spin diffusion length (λ_{SD}) and the spin-flip probability (ϵ) intrinsic to the NM material, such that:

$$g_{\mathrm{eff}}^{\uparrow\downarrow}\left(\mathrm{t_{NM}}\right) = \frac{g_{\infty}^{\uparrow\downarrow}\sqrt{\epsilon}}{\sqrt{\epsilon} + \coth\left(\frac{\mathrm{t_{NM}}}{\lambda_{\mathrm{SD}}}\right)} \tag{2.61}$$

where $g_{\infty}^{\uparrow\downarrow}$ is the spin mixing conductance assuming the NM is a perfect spin sink. Spin diffusion lengths, determined by spin pumping analysis for a given NM, can also vary by over an order of magnitude: depending on measurement technique. FMR measurements typically produce lower λ_{SD} values for Pt (1-2nm) than from other methods (over 10nm), for analysis performed on structures with a single NM thickness [94, 95]. Attempts to resolve this issue involve considering that the NM layer λ_{SD} may also have an explicit thickness dependence [96]; interfacial scattering may also play an important role. This is a topic of ongoing research in

the field.

2.5.3 Gilbert Damping in FM/N_1/N_2 Metallic Trilayers

This section provides an overview of first-principle calculations from Tserkovnyak *et al.* [85, 64] applied to spin pumping experiments by Mizukami *et al.* [97], measuring the thickness dependence of Gilbert damping in permalloy(Py)/Cu/Pt trilayers. The trilayer system considered is illustrated in Figure 2.15(a); crucially, all layers are metallic. Precessing magnetisation pumps spin into the N_1 metal layer of thickness L, as $\mathbf{I}_S^{\text{pump}}$. Spin accumulation in N_1 can then do one of three things: flow further as a spin current $\mathbf{I}_{S2}^{\text{back}}$ into the metal layer N_2, relax in N_1, or backflow into the ferromagnet (F) as $\mathbf{I}_{S1}^{\text{back}}$. N_2 is assumed to be a perfect spin sink, with any spin accumulation disregarded.

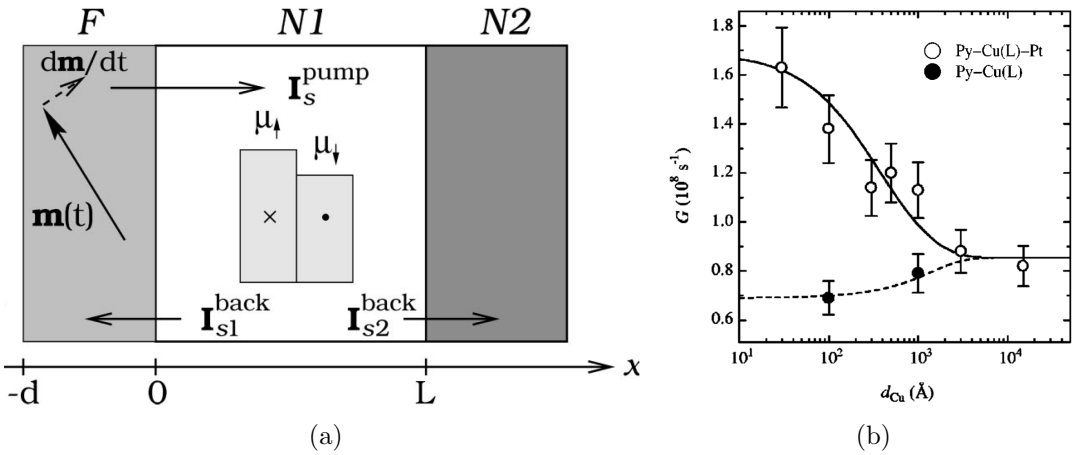

(a) (b)

Figure 2.15: (a) Ferromagnetic spin pumping from a ferromagnetic layer (F) into a N_1/N_2 metallic bilayer: forming a F/N_1/N_2 trilayer. Adapted from [85]. (b) Gilbert damping in Py-Cu-Pt trilayer and Py-Cu bilayer as a function of the Cu spacer thickness L. Solid line is theoretical prediction from Equation 2.64, dashed line from Equation 2.65 respectively. Adapted from [97]

The dependence of the FM Gilbert damping with spacer layer (N_1) thickness is evaluated by considering the spin accumulation throughout the trilayer. Spin accumulation $\boldsymbol{\mu}_s$ diffuses from the FM into the metallic N_1 layer following Equation 2.62, where D is a diffusion constant, ω is the magnetisation precession frequency and τ_{SF}^{-1} is the spin flip rate in metal N_1. This equation is valid in the regime that $\omega < \tau_{\text{SF}}^{-1}$.

$$i\omega\boldsymbol{\mu}_s = D\partial_x^2\boldsymbol{\mu}_s - \tau_{\text{SF}}^{-1}\boldsymbol{\mu}_s \tag{2.62}$$

This equation is solved with boundary conditions which maintain continuity of the spin currents, $\mathbf{I}_{S1}$ and $\mathbf{I}_{S2}$ through the FM/N_1 (x=0) and N_1/N_2 (x=L) interfaces respectively. $\mathbf{I}_{S1}$

is the net flow of the pumped spin-current and spin-accumulation driven backflow, whereas $\mathbf{I}_{S2}$ is solely based on spin-accumulation based spin-current flow into N_2. The boundary conditions are:

$$\begin{aligned} x = 0: &\quad \partial_x \boldsymbol{\mu}_s = -2(\hbar \mathcal{N} SD)^{-1} \mathbf{I}_{S1} \\ x = L: &\quad \partial_x \boldsymbol{\mu}_s = -2(\hbar \mathcal{N} SD)^{-1} \mathbf{I}_{S2} \end{aligned} \tag{2.63}$$

where $\mathcal{N}$ is the single-spin density of states in the N_1, and S is the cross-sectional area of the interface. Solutions to the diffusion equation with these conditions allow expressions for $\mathbf{I}_{S1}$ and $\mathbf{I}_{S2}$ to be found. With these, and the spin-pumping LLG term in Equation 2.57, the Gilbert damping enhancement due to spin relaxation in N_1 can be calculated as a function of N_1 thickness (with a complete derivation given in [85]); this is shown in Equations 2.64 for the FM/N_1/N_2 trilayer, and Equation 2.65 for the FM/N_1 bilayer respectively. Gilbert damping is expressed as a damping parameter, $G = \gamma M_S \alpha$, with Py/Cu(L)/Pt measurements by Mizukami *et al.* [97] shown in Figure 2.15(b).

$$G(L) = G_0 + \left[1 + g^{\uparrow\downarrow} \frac{\tau_{\mathrm{SF}} \delta_{\mathrm{SD}}}{h} \frac{1 + \tanh\left(L/\lambda_{\mathrm{SD}}\right) g \tau_{\mathrm{SF}} \delta_{\mathrm{SD}}/h}{\tanh\left(L/\lambda_{\mathrm{SD}}\right) + g \tau_{\mathrm{SF}} \delta_{\mathrm{SD}}/h}\right]^{-1} \times \frac{\left(g_L \mu_B\right)^2}{2h} \frac{g^{\uparrow\downarrow} S^{-1}}{d} \tag{2.64}$$

$$G(L) = G_0 + \left[1 + \frac{g^{\uparrow\downarrow} \tau_{\mathrm{SF}} \delta_{\mathrm{SD}}/h}{\tanh\left(L/\lambda_{\mathrm{SD}}\right)}\right]^{-1} \times \frac{\left(g_L \mu_B\right)^2}{2h} \frac{g^{\uparrow\downarrow} S^{-1}}{d} \tag{2.65}$$

Equations 2.64 and 2.65 show G(L) for the trilayer and bilayer systems respectively; the bilayer G(L) is obtained by setting the conductance per spin across the N_1/N_2 interface (g) to zero. The following parameters are used by Tserkovnyak *et al.* [85] in Figure 2.15(b) to model Py/Cu(L)/Pt; G_0 = 0.7x10^8 s^{-1} is the Py damping, for a Py thickness d of 30Å; λ_{SD} = 2500Å spin diffusion length for Cu; $g^{\uparrow\downarrow} S^{-1}$ = 1.6x10^{15} cm^{-2} and gS^{-1} = 3.5x10^{15} cm^{-2} for the Cu/Pt interface; and a Landé g-factor (g_L) of 2.1 for Py. $\tau_{\mathrm{sf}} \delta_{\mathrm{sd}}/h$ represents a dimensionless spin resistance (R_{sd}) for the Cu (at a thickness of λ_{SD}, measured in units of $(e^2/h)^{-1}$).

The trends in Figure 2.15(b) are explained on the basis of N_1 (Cu) being a poor spin sink, compared to N_2 (assumed an ideal spin sink material such as Pt). The addition of N_1 alone only produces a minor increase in damping, saturating for L $\gg \lambda_{SD}$; the majority of spins pumped into N_1 are scattered back into and relax in the FM layer. However, the addition of spin sink N_2 thereafter allows substantially larger spin transmission through N_1 to occur: dependent on the N_1 spacer thickness, L. For L$\leq \lambda_{el}$ (the elastic mean free path in N_1), spin accumulation through N_1 is mostly uniform, and only a minor fraction of spins are reflected into the FM; the remainder are transmitted into and relax in N_2. As L increases, the backflow fraction increases until the influence of ideal spin sink N_2 is diminished in the limit L $\gg \lambda_{SD}$: tending to the bilayer case [85, 64, 97]. G(L) drops off algebraically in the λ_{el} regime, and

exponentially in the λ_{SD} regime. G(L) has also been observed to be temperature dependent, with longer spin diffusion lengths being observed for lower trilayer temperatures: with Gilbert damping enhancements vanishing at a higher Cu spacer thickness, L [98].

2.6 Materials

2.6.1 Yttrium Iron Garnet (YIG)

Iron garnets (or garnet ferrites) are a class of crystalline oxide compound, characterised as cubic ferrimagnetic insulators that possess a general composition of $M_3Fe_5O_{12}$, where M is a trivalent metal ion. One such oxide is yttrium iron garnet (YIG), with the formula unit $Y_3Fe_5O_{12}$: discovered by Bertaut and Forrat in 1956 [99] and considered the "fruit fly of magnetism" by Kittel [100]. YIG is considered the main material of choice for magnonics as it possesses a cubic symmetry (Ia3d space group), contains only trivalent Fe^{3+} ions, and possesses extremely low Gilbert damping for microwave frequency spin waves [26]. Single-crystal YIG has the narrowest known FMR linewidths of approximately 0.2 Oe at 10 GHz. With the lowest known intrinsic Gilbert damping constant (α) of 0.3×10^{-4}, magnon lifetimes in YIG crystals are on the order of hundreds of nanoseconds [5]. Spin waves are observed to propagate with spin-coherence lengths of up to a millimetre in bulk YIG. The high Curie temperature of YIG (559 K) also allows spin-propagation and magnonic experiments to be performed at room temperature [101]. Important structural and magnetic properties of bulk YIG are summarised in Table 2.1.

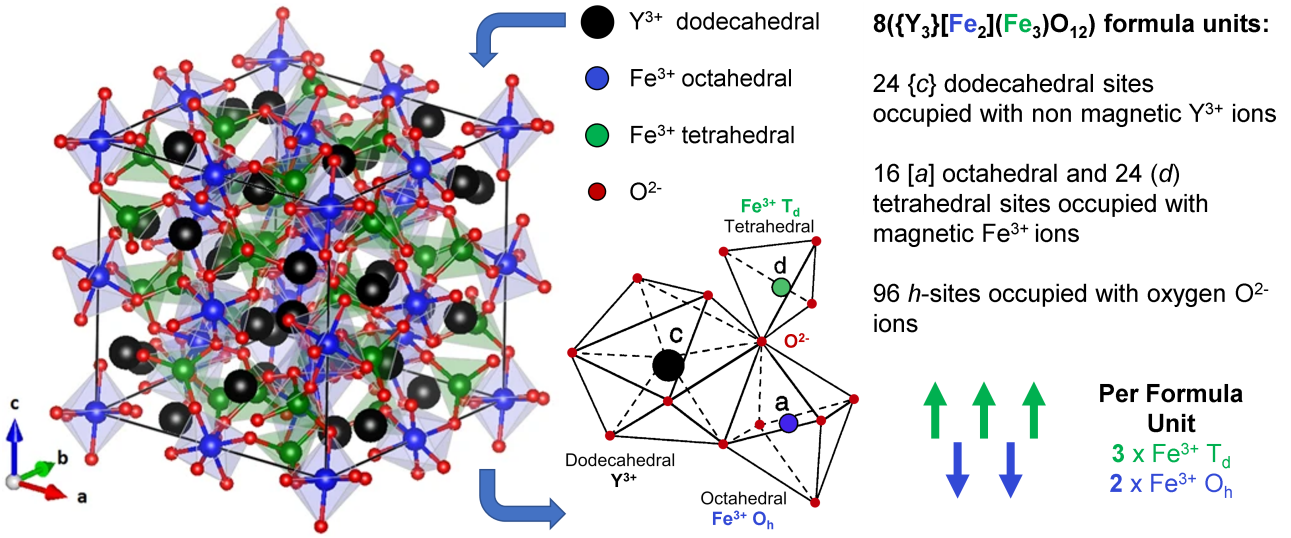

Figure 2.16: Crystal structure and Fe cations of Yttrium Iron Garnet (YIG). Adapted from [27] and [102].

Iron garnets like YIG possess a complicated crystal structure. The unit cell of YIG has a

Property	Value	Ref
Lattice Constant	12.376 ± 0.004 Å	[106, 107, 108]
Density	5.17 gcm^{-3}	[52, 106]
Thermal Expansion Coefficient	$(10.0 \pm 0.6) \times 10^{-6}$	[101, 109, 110]
Poisson Ratio	0.29	[111, 112]
Band Gap, E_g	2.85 eV	[113, 114]
Curie Temperature, T_c	559K	[52, 105]
Saturation magnetisation, $4\pi M_s$ (298K)	1750 Gauss or 140 emu/cc	[101, 105]
Intrinsic Damping Constant, α (benchmark α for YIG films)	0.3×10^{-4} $\leq 0.5 \times 10^{-4}$	[6] [7, 75]
1^{st} Order Cubic Anisotropy Constant, K_1	- 6100 erg/cc	[52, 106]
2^{nd} Order Cubic Anisotropy Constant, K_2	- 260 erg/cc	[52, 106]

Table 2.1: Summary of structural and magnetic properties of single crystal YIG (at 298K)

cubic structure and each unit cell of YIG consists of 8 chemical formula units, meaning one unit cell contains 160 ions. The positive cations in YIG are situated in three types of sub-lattice site. Y^{3+} cations are situated in *c* sites (8 surrounding O^{2-} ions). Fe^{3+} cations, however, can be either on tetrahedral *d* sites (4 surrounding O^{2-} ions) or octahedral *a* sites (6 surrounding O^{2-} ions) [26, 103]. The crystal structure of YIG is illustrated in Figure 2.16.

In stoichiometric YIG, yttrium ions (Y^{3+}) are diamagnetic and contribute little towards magnetisation. The magnetisation of YIG arises from the net moment from two oppositely magnetised Fe^{3+} sublattices (i.e. *d* sites and *a* sites). This is due to superexchange interactions between neighbouring d-site/a-site Fe^{3+} ions mediated across a O^{2-} bond, at a bond angle of 126.6° [104]. Each Fe^{3+} ion contributes $5\mu_B$ to total magnetisation at absolute zero, where μ_B denotes the Bohr magneton. In YIG's formula unit, three Fe^{3+} ions reside on *d* sites and two on *a* sites, giving a formula unit magnetisation of $5\mu_B$ at 0K and a net unit cell magnetisation of $40\mu_B$ [105]. In addition, Fe^{3+} ions exist in YIG with angular momentum L=0 and spherical charge distributions. This weakens their interaction with phonons in the crystal lattice and contributes to very narrow FMR linewidths [26, 103]. Furthermore, because YIG is a magnetic insulator, precessing magnetisation does not induce eddy currents to contribute to intrinsic spin-wave damping, owing to a lack of conduction electrons [5].

The unit cell magnetisation of $40\mu_B$ corresponds to a theoretical saturation magnetisation of 197 emu/cc at 0K: in broad agreement with films measured below 5K (196emu/cc). Room temperature saturation magnetisation has an agreed value of 140 emu/cc. The first and second order cubic anisotropy constants of YIG are K_1 = -6100 erg/cc and K_2 = -260 erg/cc respectively. From K_1, a first-order effective anisotropy field (K_1/M_s) of 44Oe is predicted for YIG(111) films, if K_2 is negligible [52]. A three-fold symmetric in-plane effective anisotropy field $\ll$ 44Oe is also expected, based on simulations of the magnetic free energy surface. As

$K_1 < 0$, YIG has a cubic magnetocrystalline anisotropy with an easy axis oriented along the (111) direction. Indeed, most reported YIG growth is performed on (111)-oriented gadolinium gallium garnet (GGG). This is a substrate of choice due to its very small lattice mismatch of 0.06% with YIG, producing epitaxial films with high magnetisation [4, 5].

YIG has seen extensive use in insulator spintronics since the 1950s, and continues to be used in spin pumping and spin-torque experiments. However, some drawbacks inherent to iron garnets have motivated recent research into alternative spintronic materials. The complex structure of YIG - with 3 sublattices, 160 ions and a huge unit cell - can make stoichiometric growth challenging in comparison to other materials. Most growths of YIG also require a high thermal budget (annealing at temperatures over 700°C) to optimise crystalline film quality. Interfacing of YIG with other classes of crystalline material is also known to be difficult, potentially forming magnetic dead layers [115, 116]. Furthermore, substrates for epitaxial growth such as GGG are prohibitively expensive for mass device production. Current front-runner alternatives include ferrimagnets such as spinel ferrites or hexaferrites, and recent reports have directed interest towards the potential use of YIG in its amorphous phase [18].

2.6.2 Amorphous YIG (a-YIG)

Much of the existing literature on a-YIG concerns various studies of 'disordered YIG' performed several decades ago. Various preparations of disordered YIG - not often in thin-film form – all showed a broad peak in temperature-dependent magnetisation (M vs T) between 50K and 100K. At this peak, splitting of M vs T curves obtained in zero field cooled (ZFC) and field cooled (FC) conditions is also observed. Such curves are shown in Figure 2.17(c). Above this splitting temperature, M vs T shows agreement with a Curie-Weiss Law, whereby the M(T) dependence follows Equation 2.13. Large negative values of Θ measured on the order of -100K indicate strong antiferromagnetic exchange (AF) interactions in a-YIG. This is reasonable given the nearest neighbour environment of crystalline YIG is also antiferromagnetic (resulting from superexchange). AF interactions and a lack of long-range order heavily suggests a-YIG may exhibit spin glass or possibly more complex behaviour, as magnetic frustrations are likely to occur. Strong AF correlations between neighbouring spins are expected up to temperatures near the Curie temperature of YIG (560K). Spin freezing temperatures likely depend on the disorder or interactions present in a particular a-YIG structure. Table 2.2 suggests the magnetic properties of amorphous YIG of notionally similar composition may greatly differ based on their preparation or local structure.

Non-local transport in a-YIG

Recent studies of a-YIG show surprising behaviour. Wesenberg *et al.* (2017) observed exceptionally long spin lifetimes in room-temperature argon-sputtered a-YIG films, despite having no long range structural or ferrimagnetic order (such that the magnetisation is essentially zero). As

a-YIG [Ref]	Preparation Technique	Fe Moment (μ_B/Fe)	T_{Peak} (K)	Weiss,Θ (K)
Gyorgy, 1979 [117]	Twin roller quenching melt	4.4	40	-500
Simpson, 1970 [118]	Anodic oxidation	2.9	40-50	-250
Chukalkin, 1991 [119]	Neutron irradiation	2.3	50	-155
Wesenberg, 2017 [18]	Room-temperature sputtering	–	50	-100
Gomez-Perez, 2020 [19]	Room-temperature sputtering	–	70	–

Table 2.2: Summary of measured magnetic properties of different preparations of amorphous YIG.

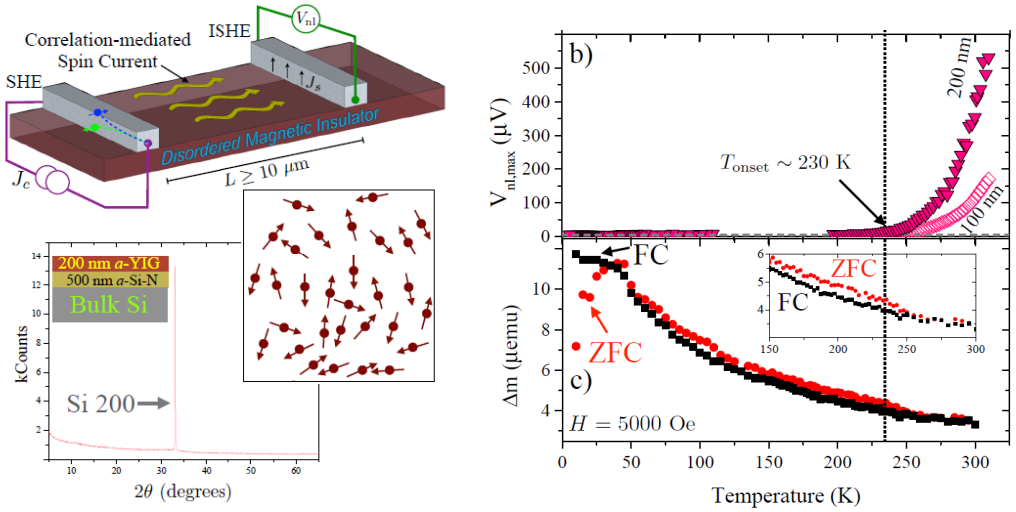

Figure 2.17: (a) Spin-transport through a disordered magnetic insulator. XRD of sputtered a-YIG layer showing no long-range order. (b) Non-local voltage (V_{nl}) vs temperature, indicating spin-transport. (c) Magnetisation of a-YIG against temperature showing a spin-glass (spin freezing) signature at 50K. Inset shows an additional ZFC/FC curve splitting at near 230K. Adapted from [18].

illustrated in Figure 2.17(a), spin transport in a-YIG was measured to propagate over distances exceeding 10 microns between lithographed platinum contacts (using SHE for spin injection and ISHE for detection). Spin signals were detectable even beyond a 100-micron separation. Comparatively, spin transport via magnons in crystalline YIG films can be measured up to a few millimetres. Even more surprisingly, the non-local ISHE voltages measured from spin-transport in a-YIG – shown in Figure 2.17(b) - were many orders of magnitude larger than seen in magnon spin-currents in crystalline YIG: hundreds of μV rather than a few nV [3]. This was observed in both 100nm and 200nm thick a-YIG films. Spin-transport in the a-YIG was observed to be enhanced with the introduction of an in-plane thermal gradient [18]. Wesenberg *et al.* (2017) argue spin transport through the a-YIG must rely on magnetic correlations mediated by strong local exchange interactions and not long-range magnetic order.

Correlation-mediated spin transport is also examined by Ochoa *et al.* (2018). The authors

consider structural disorder in two limiting cases for amorphous magnetic insulators like a-YIG. In Figure 2.18(a), spins remain pinned to the anisotropy axes defined locally at atomic sites. The spins are correlated among a few atomic sites within a grain of size R_a. This is the case of a speromagnet where collective rotations of the spins cost energy. Alternatively, in Figure 2.18(b), if the spins have a correlation length greater than R_a, the exchange interaction stabilises a smooth spin texture on the scale of the grain size. This state, known as a correlated spin glass, is smooth on the scale of a correlation length $R_c > R_a$ and, for spin transport, a collective rotation of the spins connects distinguishable states with approximately the same energy [17]. Wesenberg *et al.* (2017) provides potential evidence of a-YIG being a correlated spin glass. Like previous studies, M vs T measurements in Figure 2.17(c) show the expected broad peak in magnetisation at 50K with splitting between curves measured in ZFC and FC. Importantly, a previously unseen additional splitting near 230K was measured [18]. This temperature correlated to the onset of observed long-range spin transport effects in the a-YIG – a potential signature for correlated spin-glass behaviour. This strongly suggests that spin-correlation lengths in a-YIG are temperature dependent whereby a transition between the speromagnetic and correlated spin glass states can occur. No further investigations into such a transition have been published to date.

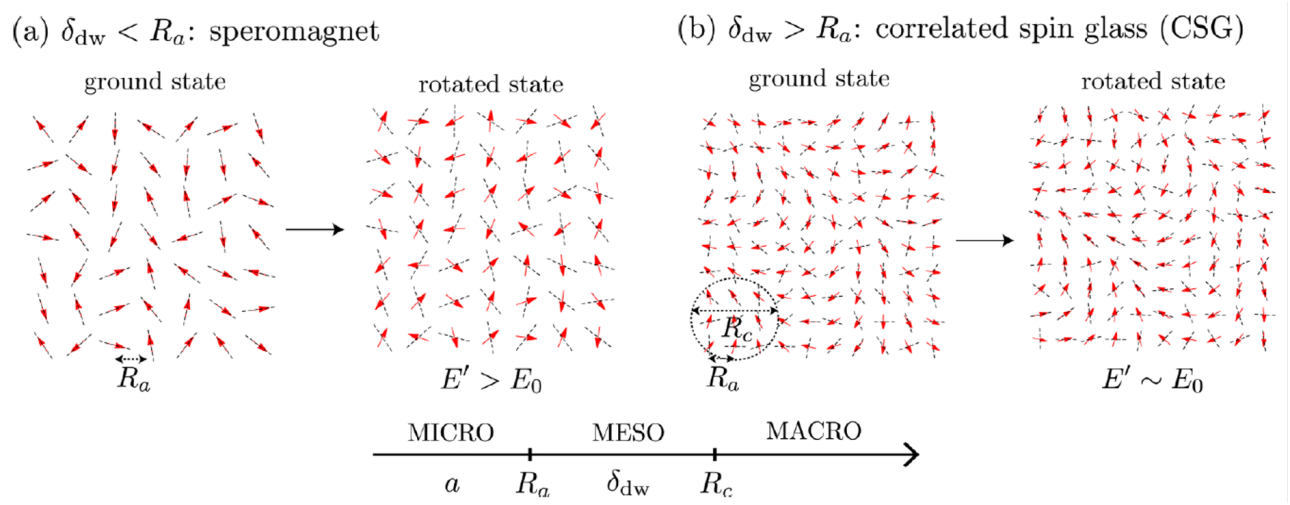

Figure 2.18: Spin textures in amorphous magnets with local anisotropy axes (dashed lines) defined by atomic arrangement. Length scales in this phase relative to domain wall width, δ_{dw}, are shown. Adapted from [17].

However, similar non-local transport experiments performed since Wesenberg *et al.* (2017) [18] have failed to observe magnon transport. Gomez-Perez *et al.* (2020) [19] performed a near identical experiment, with the use of an additional copper detector contact. Shown in Figure 2.19(b) and (c), spin transport signal similar to that observed between the platinum injector and detector contacts was also detected in the copper contact (though an order of magnitude

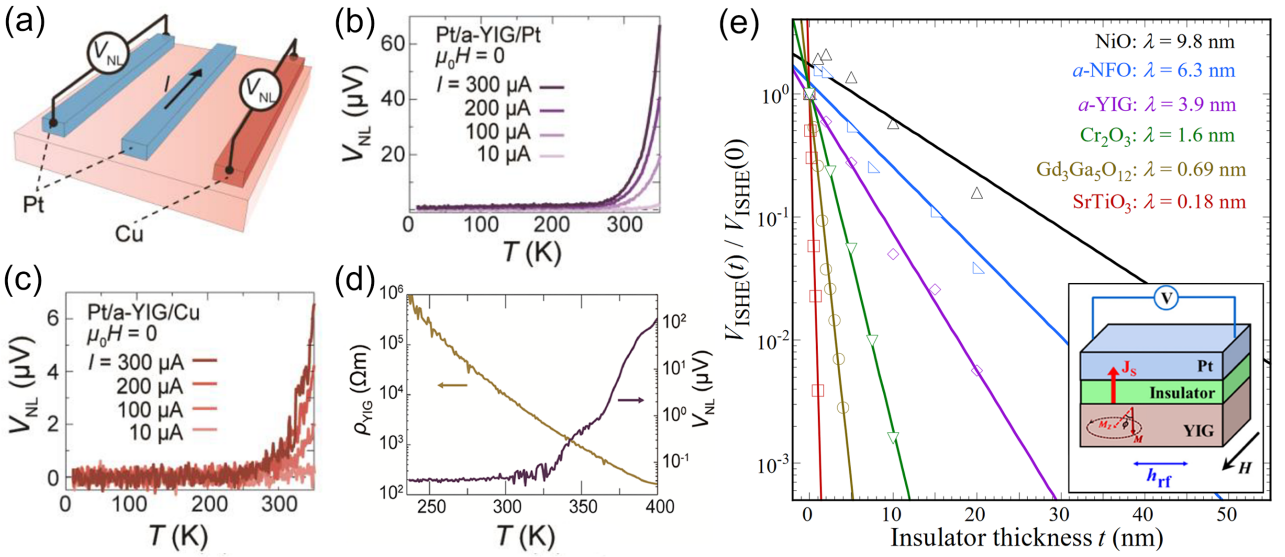

Figure 2.19: (a) Lateral spin transport geometry used by Gomez-Perez *et al.* (2020) with Pt and Cu detector contacts. (b) Non-local voltage (V_{nl}) vs temperature measured from Pt contact and (c) Cu contact. (d) a-YIG resistivity and V_{nl} against temperature (measured by Pt). Adapted from [19] (e) FMR-driven spin-pumping through amorphous insulators measured by ISHE, from Wang *et al.* (2015). Inset shows the measurement geometry. Adapted from [20].

smaller than from the platinum). The authors argue this should not be possible if the signal is truly propagated by spins or magnons, due to copper having a very low spin-orbit coupling (compared to platinum). Furthermore, temperature-dependent measurements of the a-YIG resistivity showed a drop in resistivity of two orders of magnitude across the same temperature range where the non-local signal was detected. Gomez-Perez *et al.* (2020) concluded that spin-transport was ultimately absent in a-YIG. Non-local signals were instead considered the result of a resistivity drop caused by Joule heating from the electrical contacts [19]. This conclusion has since lead other groups to suspect Wesenberg *et al.* (2017) was observing a similar effect, instead of long-range magnon transport.

Other studies of correlation-mediated spin transport in antiferromagnetic insulators have been performed via an FMR-driven spin pumping technique. Wang *et al.* (2015) [20] injected spin from crystalline YIG-on-GGG into various insulators – most notably a-YIG and NiO - in the form of YIG/insulator/platinum trilayers. Like Wesenberg *et al.* (2017), insulator layers were deposited using off-axis room-temperature sputtering to a thickness of 20nm. A blocking temperature of 45K was inferred for the a-YIG from temperature dependent measurements of exchange bias. While considerable spin transport into the platinum was measured via ISHE, spin decay lengths in a-YIG were inferred to be approximately 3.9nm from Figure 2.19(e). This is surprisingly small compared to the vast propagation distances from Wesenberg *et al.* (2017), and in fact inferior to NiO with a 9.8nm decay length [20]. However, more recent studies

have failed to observe spin transport in a-YIG with this technique too. Yang *et al.* (2021) [21] observed that, despite significant spin pumping in YIG/Pt bilayers, the addition of any thickness of a-YIG between these layers caused spin mixing conductance to drop immediately to zero, with no spin pumping being observed [21]. It is noted that the different means of spin-excitation used (electrical contact SHE versus FMR-driven pumping) also makes a direct comparison of magnon diffusion length between studies more difficult.

Recrystallisation of a-YIG

Recent work has shown that amorphous YIG grown by PLD at room temperature can be post-annealed in oxygen or air and completely recrystallised to form high quality epitaxial films. Hauser *et al.* (2016) report recrystallised YIG films of extremely high structural and magnetic quality, with high-resolution TEM images shown in Figure 2.20(a). Exceptionally low damping of $(7 \pm 2)\text{x}10^{-5}$ was measured for films as thin as 20nm, representing the lowest reported for all PLD grown films so far, following ex-situ recrystallisation in oxygen [11]. Similar recrystallisation has also been observed in 22nm sputtered YIG films by Chang *et al.* (2014), achieving damping of $(8.6 \pm 0.2)\text{x}10^{-5}$ following recrystallisation in oxygen [12]. Given the deposition of amorphous material at room-temperature is trivial compared to ensuring epitaxial and stoichiometric in-situ film-growth at high temperature, this recrystallisation-PLD approach presents an exciting new prospect for high quality nm YIG film growth.

Nevertheless, few studies of the recrystallisation process itself exist in literature. A recent study of recrystallised YIG on SiO_2-on-silicon by Gage *et al.* (2017) shows that one-step rapid thermal annealing (800°C, 3 min) causes incomplete recrystallisation in YIG. Through TEM imaging, such annealing was seen to produce films containing YIG crystallites within a nanocrystalline non-garnet matrix, shown in Figure 2.20(b)(i). This non-garnet matrix restricts the size of magnetic YIG grains and forms antiphase boundaries that reduce overall film magnetisation. In contrast, a two-step annealing procedure (400°C for 3 minutes, followed by 800°C for 3 minutes) led to the formation of phase-pure garnet YIG films, increasing magnetisation by 30emu/cc (from 100emu/cc for one-step annealed YIG). This unexpected growth behaviour suggests that a low-temperature anneal produces seed nanocrystals, enabling the rapid formation of YIG during the subsequent high-temperature anneal. Yet TEM diffraction suggests the YIG remains largely amorphous after a pre-anneal at 400°C [120]. Gage et al. (2017) also demonstrate highly localised recrystallisation was achievable through in-situ TEM laser annealing; 50µm dots of YIG were formed using a 343nm UV laser with powers up to 82.6mW. Similarly to thermal annealing, a two-step laser anneal (25.2mW, 32.0mW) was seen to improve the crystallinity of final YIG features. To date, no other rigorous studies of the YIG recrystallisation process have been reported.

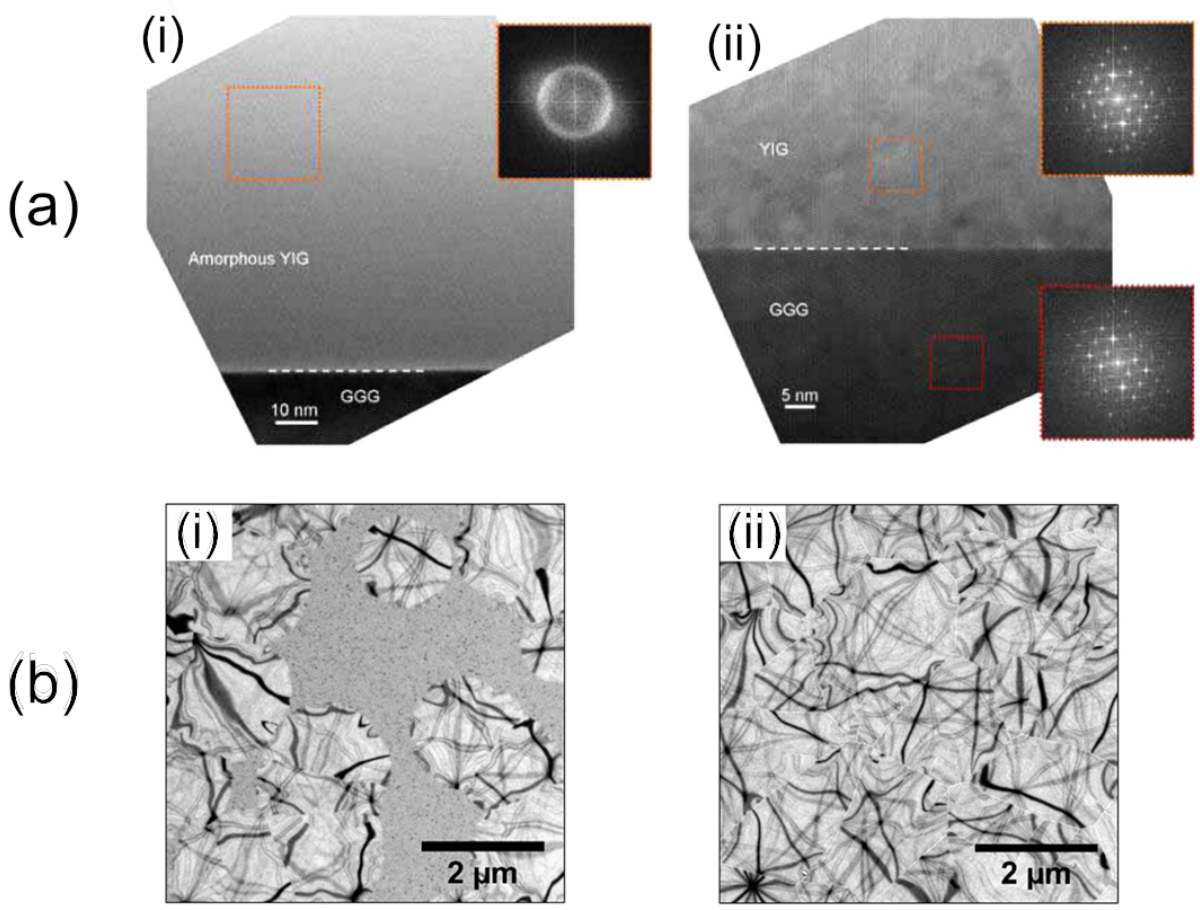

Figure 2.20: (a) High Resolution TEM (HR-TEM) images of an (i) amorphous YIG film, and (ii) YIG film on a GGG substrate after annealing (800°C, 3hrs, ambient oxygen). Insets show FFT patterns. Adapted from [11]. (b) BF-TEM images of YIG films on SiO_2, in-situ annealed at (i) 800°C and (ii) 400°C for 3 minutes, followed by 800°C for 3 minutes. Adapted from [120].

Chapter 3

Experimental Fabrication and Characterisation Techniques

The experimental techniques used to both fabricate and then characterise various thin films of YIG and a-YIG are discussed in this chapter. Fabrication techniques cover both thin film deposition and subsequent treatments such as annealing. Characterisation techniques fall under two distinct categories: techniques used to characterise the structure of samples, and those to investigate magnetic behaviour. Synchrotron-based X-ray spectroscopy techniques are also discussed separately.

3.1 Thin Film Fabrication

3.1.1 Pulsed Laser Deposition (PLD)

This research made use of a multi-target PLD growth system established in the University of York's magnetic spectroscopy laboratory. The design of this PLD system was specifically oriented towards the stoichiometric growth of complex oxides such as hexaferrite films, enabling the growth of YIG thin-films to be performed with this apparatus. A schematic of the system is shown in Figure 3.1(a). PLD allows for versatile control over film growth, due to the large number of variable deposition conditions which can change the resultant film properties [121]. The main advantage of PLD is the stoichiometric transfer of material from target to substrate.

The PLD growth system consisted of a central vacuum chamber with numerous external ports for mounting additional instruments. Inside, a sample cradle and shutter were situated directly above the target manipulator. Samples were mounted with the surface of the substrate facing down towards the target. The sample cradle was attached to an x-y-z and ϕ manipulation stage, allowing the position and height of the sample relative to the target to be adjusted, and the sample to be rotated about its azimuth. The shutter was used to shield the sample from

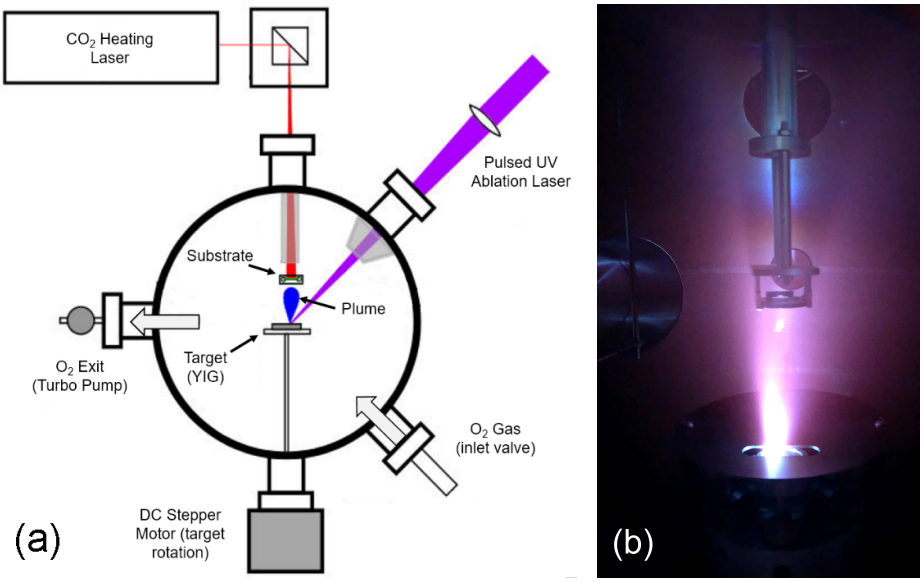

Figure 3.1: (a) Diagram of the PLD growth system illustrating laser setup and oxygen flow in the vacuum chamber. (b) Plume of material from ablating a $Y_3Fe_5O_{12}$ target inside the chamber: laser-pulse energy of 100mJ at 266nm, partial O_2 pressure of 2.5×10^{-3} mbar.

plumes if needed, for instance when pre-ablating a target before use in deposition. A load-lock transfer mechanism established in the chamber rear allowed quick sample transfer in and out without breaking vacuum. The vacuum chamber and load-lock were evacuated using two turbo pumps to a base pressure of 1×10^{-7} mbar.

Substrates were housed and transported throughout the PLD with a 2.5mm thick titanium sample cartridge. Shown in Figure 3.2(a), within the cartridge is a 12mm square hole, with a 17mm square recess around it, into which insets were fixed and designed to hold a substrate of a desired size. The cartridge insets were made from Macor ceramic, chosen due to its good thermal insulating properties: minimising conduction of heat away from the sample through the substrate cartridge. For 5mm x 5mm substrates used throughout this research, an inset with a 5.5mm square indent was used, into which a substrate is placed face down. The corners of the square are left to prevent the substrate falling through, but thin enough to prevent significant shadowing of the substrate from the PLD plume. Discussed further in Section 4.2, an alternative cartridge inset was developed to house and allow PLD deposition on 3mm x 3mm TEM windows. Shown in Figure 3.2(b), this inset consisted of a central 5.5mm x 5.5mm square indent, inside of which a smaller 3.5mm x 3.5mm deeper indent was located. This was centred with a hole 1.5mm in diameter (located over the TEM window) where material could be deposited locally. The larger 5.5mm x 5.5mm indent was used to place a substrate above the TEM window to secure it in place.

A stoichiometric polycrystalline YIG PLD target was used to grow the films. To ablate this target, a frequency quadrupled neodymium-doped yttrium aluminium garnet (Nd:YAG)

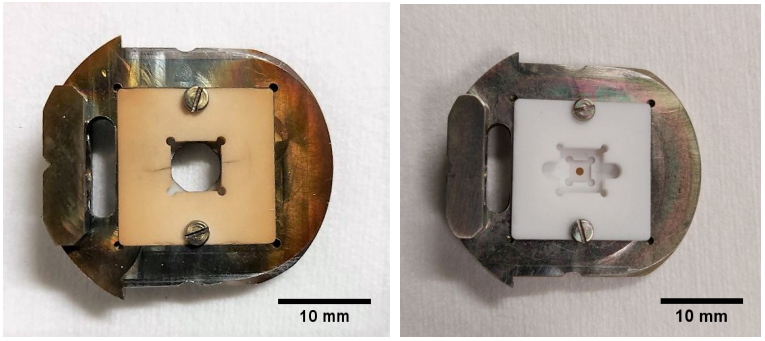

Figure 3.2: Photographs showing the top view of the PLD sample cartridge for (a) 5mmx5mm substrates, taken after several hours of deposition and heating, and (b) 3mmx3mm TEM windows.

laser was used: a LPY674-10 model by Litron Lasers. This ultraviolet laser operated with a lasing wavelength of 266nm, with a repetition frequency of 10Hz and pulses of 2ns duration. A laser energy of 100mJ per pulse was used, as this was deemed optimal in previous PLD growths for producing a consistent deposition rate. The laser operated in a tracking mode where the second frequency doubling crystal was adjusted continuously to maintain a constant output power. PLD targets were mounted on a motorised manipulator which allowed for target rotation and rastering. This ensured the entire target surface was being ablated and avoided degradation of a single point. A photograph of a YIG ablation plume is shown in Figure 3.1(b).

A controllable oxygen partial pressure in the chamber was necessary for the PLD growth of oxides. Oxygen was required to maintain deposited oxide stoichiometry, replacing any lost from the ablated target [122, 123, 124]. Control over partial oxygen pressure also provided control over the deposition rate, if necessary. The growth system utilised a gas inlet with a mass flow controller (MFC) connected to a source of 99.9% purity oxygen. A flow rate of 0.1sscm was used to provide fine control of oxygen leakage into the chamber. For additional pressure control, a PLD throttling system was used to control the rate at which a turbo pump evacuated oxygen from the chamber. This was used at high pressure to achieve a constant oxygen flow by balancing gas inlet and turbo evacuation, measured using a mounted Pirani gauge.

Substrate heating was possible using a carbon dioxide laser setup. A pulsed 35W 48-2 series SYNRAD CO_2 laser, operating at 10.6μm infrared wavelength, was directed onto the back of substrates cradled in the PLD chamber [125]. These wavelengths are absorbed strongly by oxide substrates such as GGG and YAG, allowing substrate temperature to be controlled by varying the duty cycle of the CO_2 laser pulses. Substrate temperature influences film crystallinity, wherein higher in-situ temperatures improve epitaxial film growth upon the substrate. In addition to this, substrate heating prior to depositions can be used to out-gas and remove moisture from substrates that have been cleaned with organic solvents: improving deposition quality. PLD samples can also be annealed post-deposition to improve both their structural

and magnetic quality; ex-situ annealing was a crucial factor following the deposition process of the thin films examined in this thesis, and is discussed further in Section 4.1.2.

3.2 Structural Characterisation

3.2.1 X-Ray Diffraction (XRD)

X-ray diffraction (XRD) is a powerful non-destructive tool used to identify the crystal structure and ordering of materials in this work: whether epitaxial, polycrystalline or amorphous. Other x-ray crystallography measurements such as x-ray reflectivity, rocking curve, pole figure and reciprocal space map measurements have also been performed to determine thin film thickness and roughness, or provide insight into thin film quality, texture and potential strain.

Crystals are composed of regular repeating arrays of atoms, which form a crystal lattice. Atoms act as scatterers to incident monochromatic X-rays, and re-radiate scattered x-rays as a spherical wave. If atoms are arranged with a regular separation (d_{hkl}), these spherical waves will be in phase and add constructively only in directions where the path difference ($2d_{hkl}\sin\theta_B$) between them equals an integer number of x-ray wavelengths. In this case, part of the incident x-ray beam is reflected by an angle of $2\theta_B$, producing a peak in x-ray intensity. For a beam of monochromatic coherent x-rays of wavelength λ, incident at an angle θ_B relative to (hkl) planes of scattering atoms, the constructive interference condition is generalised by Bragg's Law [126]:

$$2d_{hkl}\sin\theta_B = n\lambda \tag{3.1}$$

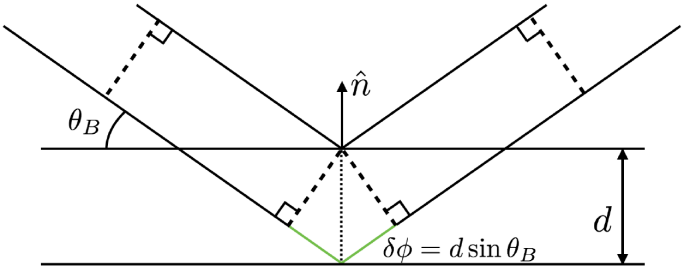

Figure 3.3: Schematic diagram of Bragg reflected x-rays from the same wavefront, scattering from two different crystal lattice planes[11].

Here, d_{hkl} is the distance between parallel (hkl) lattice planes and n an integer multiple of wavelengths (or the order of the diffracted x-ray reflection). The Bragg condition is illustrated in Figure 3.3. In a cubic crystal structure, such as YIG, inter-planar spacing is related to the lattice constant a and miller indices of the planes (hkl) by Equation 3.2 [126]. Combining

this with Bragg's law, the lattice constant of a structure can be extracted from a measured diffraction angle, θ_B using Equation 3.3. The diffraction and constructive interference of X-rays in a crystal can also be explained vectorially via the Laue formulation, or geometrically by the Ewald sphere construction: an extension of Bragg's law to 3D space [126][127].

$$\frac{1}{{d_{hkl}}^2} = \frac{h^2 + k^2 + l^2}{a^2} \tag{3.2}$$

$$a = \frac{n\lambda\sqrt{h^2 + k^2 + l^2}}{2\sin\theta_B} \tag{3.3}$$

All XRD measurements presented were performed on a Rigaku SmartLab diffractometer, with a Cu Kα_1 x-ray source (wavelength 1.5406Å). A schematic representation of the diffractometer arms, and the goniometer stage geometry is given in Figure 3.4. X-rays from the source are made parallel via a multi-layer mirror, and the incident beam width was determined by the insertion of slits; a 2mm width was chosen for 5mm-wide samples, and a 5mm width chosen for 10mm-wide samples. A Ge(220)x2 monochromator removes any additional L_α and K_β x-ray reflections, and provides a better diffractometer resolution. The x-ray beam then interacts with the sample on the goniometer stage. This stage is adjustable in x, y, z, ϕ and χ. Diffracted x-rays are then measured in the detector arm. A series of mechanical slits, and a parallel slit analyser (PSA) provide an adjustable and constant angular resolution for x-rays detected over a large area [128]. A 2D detector (HyPix) was used, eliminating the need for an x-ray attenuator.

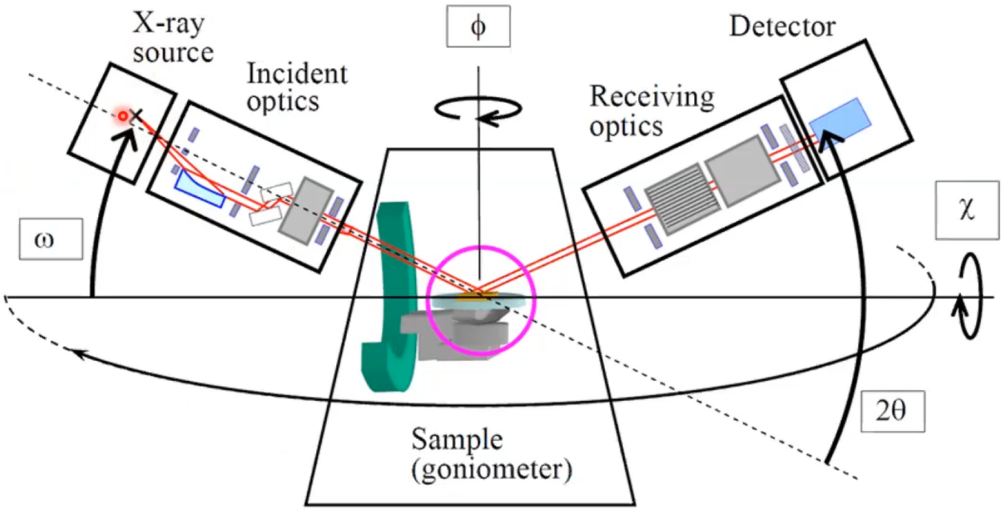

Figure 3.4: Schematic diagram of the Rigaku X-Ray diffractometer, showing the XRD angles ω and 2θ, as well as XRD angles χ and ϕ.

2θ-ω Scans

The most common measurements in XRD are 2θ-ω (2-theta/omega) scans, directly measuring the crystal structure of films [126][129]. These concern the incident angle of the X-rays (ω) and the angle of x-ray reflection (2θ). For symmetric 2θ-ω scans, 2θ and ω are programmed such that ω is always half of 2θ (i.e. $\omega = \theta$). This 2θ-ω angle is then scanned relative to the sample plane. The resulting intensity vs 2θ-ω plots show intense diffraction peaks, corresponding to allowed reflections from specific crystal planes (hkl), parallel with the face of the sample. This is equivalent to when the scattering vector (**Q**), is exactly equal to a reciprocal lattice vector (**G**), producing intense diffraction. In the case of an epitaxial crystal, a single family of planes will exist to give rise to x-ray reflections. The spacing between these planes can be extracted using Bragg's law. In the case of a symmetric 2θ-ω scan, this is the out-of-plane spacing, d_{hkl}, as illustrated in Figure 3.3. Observation of additional unpredicted diffraction peaks suggests the presence of additional phases, or indicates the sample is polycrystalline rather than an epitaxial crystal [126][130]. 2θ-ω scans can also be performed in different scan geometries to extract information of in-plane lattice constants or strain.

XRD peaks were identified using predicted values calculated by the INDX software package [131] using space group and lattice constant values from literature. Only certain (hkl) reflections will be observed from the material being investigated, based on selection rules that arise as a result of its crystal structure. Reflections that do not obey these selection rules are considered forbidden, and are excluded due to inference between reflected x-ray waves being destructive instead of constructive. Selection rules for YIG and other garnets are governed by the cubic space group (Ia3d). From this, allowed reflections satisfy the condition $h + k + l = 2n$ where n is an integer, and hkl may be mixed in being odd or even. Allowed reflections also satisfy (if $h = k$) that $h + l = 4n$, or (if $h = 0$) that $k + l = 2n$.

Rocking Curves (ω Scans)

Rocking curves are measurements of x-ray intensity as a function of incident x-ray angle ω (tilting the sample relative to $\omega = \theta$) for a fixed reflection angle 2θ, located on a diffraction peak. Rocking curves provide a quantitative measure of the out-of-plane orientation of (hkl) film planes, measuring the intensity from (hkl) planes that are not perfectly parallel. The FWHM of the resulting rocking curve is used as a figure of merit that evaluates the misalignment between crystal grains in an epitaxial thin film. This misalignment is known as mosaicity [132, 126]. Rocking curves with smaller FWHM indicate lower mosaicity, reflecting better alignment of crystal grains and plane parallelism in a thin film. A perfect crystal would produce a very narrow rocking curve, resulting from both perfectly parallel crystal planes and angular alignment with the (hkl) plane-normal. However, the peak width is finite due to crystal defects and imperfections that make planes decreasingly parallel or coherent. These can include crystal dislocations, curvature induced by strain or distortions, or mosaicity [132]. The net effect of such defects is to create an angular distribution in the atomic (hkl) planes that contribute to the

detected diffraction peak intensity. In addition, the FWHM is increased further by instrumental broadening [133, 134]. Measurements of FWHM are a useful quality indicator when compared either to similar films in literature, or as a relative comparison between different thin films grown as a series. Rocking curves can also be applied to XRD peaks in polycrystalline samples, where the size of crystallites that cause the observed peak broadening can be inferred using the Scherrer equation [126, 135].

Pole Figures

Pole figures allow the crystallographic texture of a sample to be visualised and investigated. A pole figure is obtained at a fixed 2θ, measuring the x-ray intensity as a function of two goniometer angles: sample rotation angle (ϕ) and sample tilt (χ), as shown in Figure 3.4. Effectively, a pole figure measurement maps the x-ray intensity for a diffraction peak of interest as a function of sample rotation, measured at different tilts of the sample surface normal, averaged over a large sample area. The 2D pole figure represents the distribution of a crystallographic orientation (i.e. planes) in angular space, as a 2D map projection. An examplar pole figure is given in Figure 3.5. The 2D map is a polar plot, wherein sample tilt angle χ varies with radius and sample rotation angle ϕ varies with azimuthal pole figure angle. The centre of the map represents $\chi = 0°$, with a sharp narrow x-ray intensity indicating a high degree of plane orientation parallel to the surface normal: consistent with a typical 2θ-ω scan. The axes of the pole figure are often labelled Rolling Direction (RD), Transverse Direction (TD) and Normal Direction (ND). These correspond to goniometer axes X (in-plane, parallel to x-ray beam), Y (in-plane, perpendicular to x-ray beam) and Z (out-of-plane), respectively. X and Y also correspond to $\phi = 0°$ and $\phi = 90°$ respectively [136].

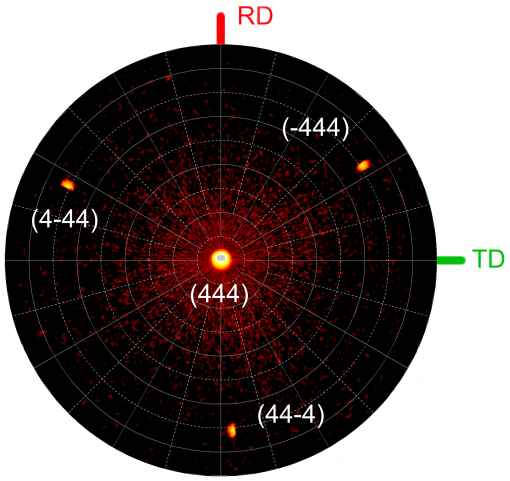

Figure 3.5: Example XRD pole figure taken from the GGG(444) peak for a blank GGG(111) substrate. The central (444) reflection is clearly observed, with other $< 444 >$ peaks observed spaced equally around the central peak

Pole figures are mainly used to measure the angular distribution of crystallographic (hkl) planes in a thin film. This is referred to as the film's crystallographic texture. In polycrystalline samples, a distribution of x-ray intensities will be observed at various angles due to a distribution of crystallites being present. Pole figures can also be used to confirm epitaxial growth in crystalline thin films. Epitaxial single crystals will show a central ($\chi = 0°$) reflection from the (hkl) plane of interest, and then be surrounded by reflections at other positions of χ and ϕ from other planes of the $<$ hkl $>$ family. The angular symmetry of these $<$ hkl $>$ reflections should reflect the expected symmetry of the crystal structure.

Reciprocal Space Mapping

Reciprocal space mapping (RSM) is a high-resolution XRD technique used to extract additional information from around reciprocal lattice spots and reflections. RSMs are constructed by taking multiple single line 2θ-ω scans with slightly different offsets of ω. This builds a two-dimensional intensity map of an XRD reflection in either angular space ($\Delta 2\theta$ vs $\Delta\omega$) or reciprocal space (Q_x vs Q_z). The conversion of angular space coordinates to reciprocal space is described by Equations 3.4 and 3.5 [132][137].

$$Q_x = \frac{2\pi}{\lambda}(cos(2\theta - \omega) - cos(\omega)) \tag{3.4}$$

$$Q_z = \frac{2\pi}{\lambda}(sin(2\theta - \omega) + sin(\omega)) \tag{3.5}$$

RSMs provide quantitative information for characterising the structure of epitaxial layers. This is particularly useful for systems with strain present. Strain shifts the lattice points of the thin film in reciprocal space (relative to those of substrate), preventing collection of data with a single scan [133]. For a normal symmetric 2θ-ω scan, ω is always half of 2θ, and the scattering vector is fully out of plane. In an RSM, this is not the case for many points (asymmetric scans), producing a scattering vector with an in-plane component. Measuring an RSM about an in-plane reflection that is accessible with a fixed sample tilt of $\chi = 0$ ensures that in-plane components of Q are oriented entirely along the Q_x direction [132]. Changes in film peak position produced by compositional change or strain can be separated and identified using asymmetric scans. The quality of the thin film layer can also be probed via asymmetric RSM scans; The shape of the film diffraction peak in an RSM provides information on gradients of strain or composition, or alternatively defects that may be present. This is illustrated in Figure 3.6 [137].

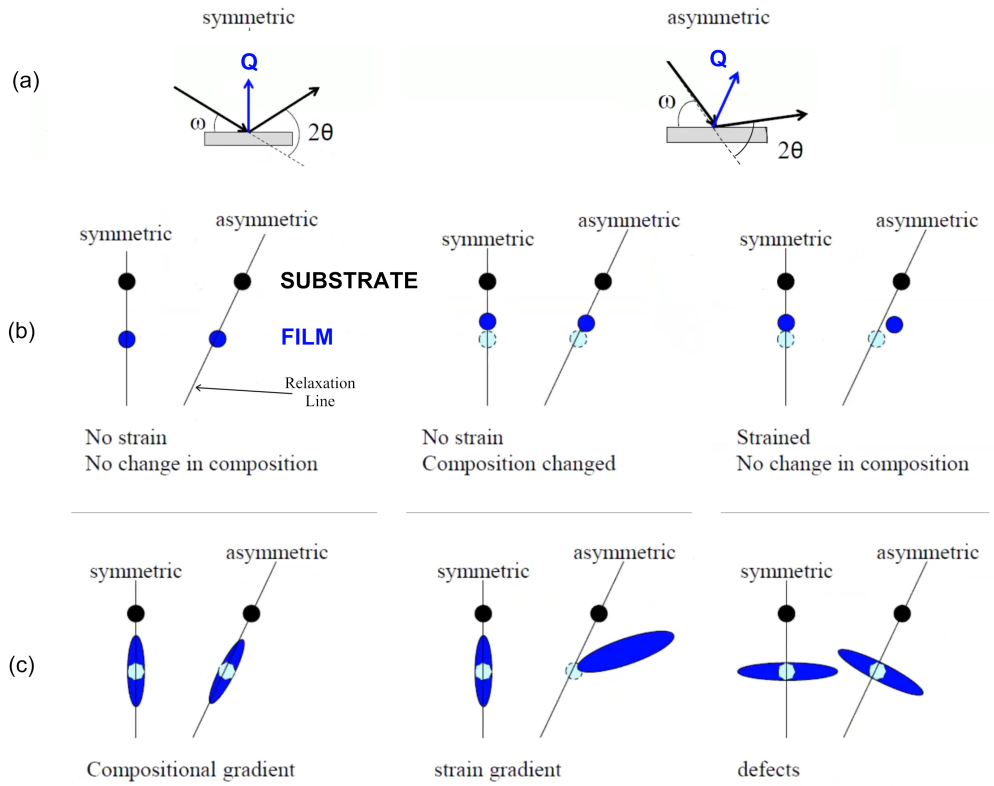

Figure 3.6: (a) Schematic of symmetric ($\omega = \theta$) and asymmetric ($\omega \neq \theta$) 2θ-ω scans used to form an RSM. (b) Asymmetric scans allow shifts in film peak due to strain and compositional change to be separated. The relaxation line from Q=0 to the substrate peak is shown. (c) Defects and gradients can produce spreading of the film peak in reciprocal space [133].

X-Ray Reflectivity

Unlike the previously discussed XRD techniques, x-ray reflectivity (XRR) is not a diffraction related phenomenon. However, XRR is an effect that can still be measured on the same XRD apparatus. XRR measurements are primarily used to measure the film thickness, surface or interfacial roughness, or density of a deposited material (or even multiple layers of materials)[138]. XRR is especially useful for determining the thicknesses of films grown on the PLD system, to determine deposition rates and evaluating overall film quality.

XRR fundamentally concerns x-rays interacting with a thin film surface and interfaces at a low incident angle. Such x-rays generate a specularly reflected wave, a refracted wave, and other diffuse reflections, as illustrated in Figure 3.7 [139]. The critical angle for total internal x-ray reflection (θ_c) is related to the refractive index of the material [138]. Below this critical angle, the x-ray beam is completely reflected by the film surface, ultimately producing a maximum in specular x-ray reflectivity when incident angle $<$ the critical angle. Cu-K_α x-rays often have a corresponding refractive index below 1 in many materials. As a result, the critical

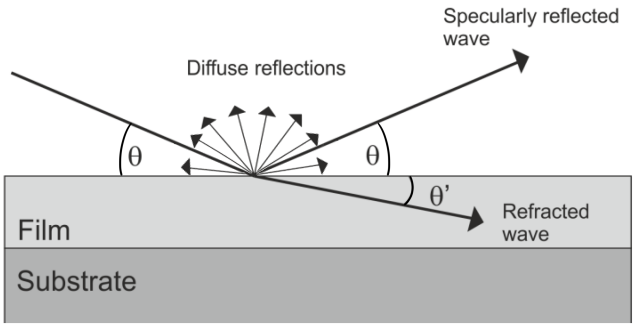

Figure 3.7: Schematic diagram of reflected and refracted x-rays incident on a thin film surface at low incident angle θ.

angle has a material density-dependence. This allows precise determination of the sample density. As the incident angle is increased above θ_c, the x-ray reflectivity decays rapidly at a rate proportional to θ^4. Even amorphous samples allow the specular reflection of x-rays and produce XRR curves, though high angle diffraction peaks are not observed [138]. Above θ_c, the phase difference between specular x-ray reflections from the film surface and the film-substrate interface produces interference fringes in the overall XRR curve. These fringes, known as Kiessig fringes, can be fitted to extract parameters such as film thickness, SLD or roughnesses.

An exemplar XRR profile with interference fringes is shown in Figure 3.8, whose shape is dependent on many factors. The periodicity of the fringes is inversely proportional to the film thickness. However, there is a limit of approximately 150nm, above which Kiessig fringes become indistinguishable and thickness cannot be reliably measured; the exact limit is strongly dependent on both the material density and film roughness [138]. When multiple layers are present, periodicities are convoluted together, making exact determination of thicknesses more challenging. The amplitude of the fringes is proportional to the difference in density between layers (i.e. film and substrate), with smaller differences in density yielding smaller fringes and more difficult thickness extraction. Surface roughness contributes to the rate of reflectivity dropoff at and above θ_c, and produces a loss of periodicity at higher angle. Roughness at the film-substrate interface also contributes to both the rate of reflectivity decay and the fringe amplitude. Generally, a rough film will have short-lived reflectivity with weak fringes, compared to a smooth film with clean interfaces. As mentioned above, material density determines critical angle, but this also contributes to the rate of reflectivity decay; XRR in denser materials extends to higher θ due to a larger critical angle and greater reflectivity overall [138].

Given these various dependencies, care must be taken when fitting XRR to ensure obtained solutions are accurate and unique. Fitting was undertaken primarily using the GenX software package [140], as well as the Rigaku GlobalFit software [141] to ensure fitting parameters independently produced were in good agreement.

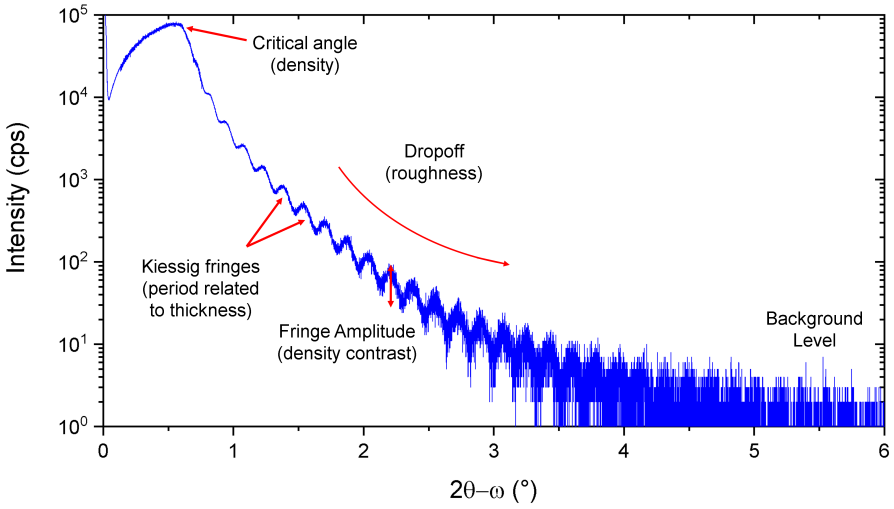

Figure 3.8: An exemplar XRR curve profile measured using an XRD diffractometer, for a YIG/GGG(111) thin film. XRR features are annotated, with general properties they inform in parentheses.

3.2.2 Transmission Electron Microscopy (TEM)

Transmission electron microscopy (TEM) is a powerful technique for imaging and structural analysis of thin films or structures at local and near-atomic scales. High energy electrons can possess wavelengths up to 10^5 times shorter than that of photons, giving electron microscopes far higher resolution than optical ones. The corresponding wavelength for an electron accelerated across a voltage, V, is given by the de Broglie wave-particle duality formula:

$$\lambda = \frac{h}{p} = \frac{h}{\sqrt{2m_0 eV\left(1 + \frac{eV}{2m_0c^2}\right)}} \tag{3.6}$$

where m_0 is the electron rest mass, and e the electron charge. A relativistic correction factor of $(1+\frac{eV}{2m_0c^2})$ is required to describe the electrons' momentum, due to electron velocities being a significant proportion of the speed of light at typical energies of 100keV or more. Corresponding wavelengths at these energies are picometers in scale: offering potential for atomic resolution sample imaging. However, resolution is ultimately limited by instrumental factors such as aberrations. In an electron microscope, a high energy beam of electrons is made incident on and scattered from a specimen under UHV conditions. This produces a large number of exit signals which may be sampled or analysed, as illustrated in Figure 3.9(b) [142]. Electrons are elastically or inelastically scattered as they both penetrate and pass through the sample. If the sample is thin enough (usually 100nm or thinner), it will be transparent to forward scattered electrons that can be used to produce transmission-based sample images. In TEM, the direct

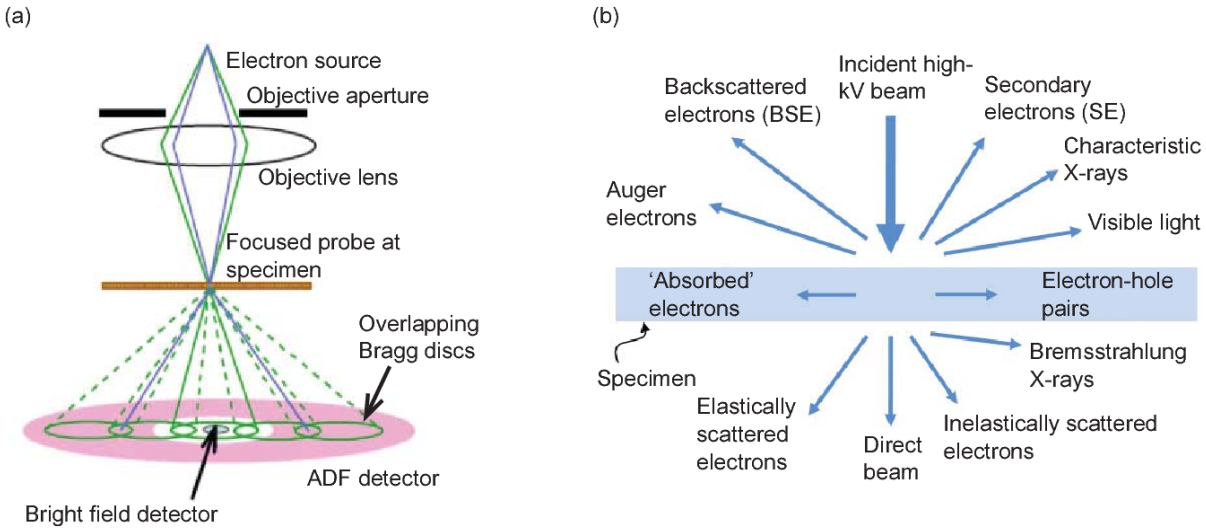

Figure 3.9: (a) Schematic diagram of a STEM microscope, showing image formation for the on-axis small bright-field detector and the larger annular dark-field detector (in pink) [143]. (b) Electron interactions with a thin specimen by an electron microscope beam, reproduced from [142].

beam and elastically scattered electrons are usually the main signals of interest.

A schematic of a basic STEM is given in Figure 3.9(a), and consists of three functional components: a source or gun where electrons are produced and accelerated, a column where electrons are focused by magnetic field 'lenses' and apertures before interacting with the specimen, and finally a detector where transmitted electrons are measured. One system of lenses manipulates electrons to be incident on the specimen as either a parallel beam (TEM) or brought to a focus (scanning TEM). A second system of lenses after the electrons have passed through the specimen magnify and record either an image or diffraction pattern [142]. There are several techniques and operating modes associated with TEM, however only those relevant to this thesis will be discussed. Specific techniques used in this work are Scanning Transmission Electron Microscopy (STEM) with High-Angle Annular Dark-Field STEM (HAADF-STEM) and Selective Area Electron Diffraction (SAED).

BF and HAADF-STEM, SAED, and EDX

Bright field STEM (BF-STEM) and HAADF-STEM are established techniques for imaging local structures of thin film lamellas, which differ based on the chosen electron detector and corresponding electrons from the sample that arrive at them. BF-STEM imaging relies on detecting electrons scattered by very small angles (below 10mrad) or electrons from the beam directly transmitted through the sample. HAADF-STEM instead is a variety of dark-field imaging that images electrons that have undergone elastic Rutherford-like scattering. These

are detected by an annular detector at higher scattering angles (typically above 50mrad) Here, incident electrons have been deflected due to Coulomb interactions and passing very close to atomic nuclei scatterers. The probability of Coulomb scattering is proportional to the scattering atom's proton number squared, Z^2. This produces an image contrast based on atomic number (known as z-contrast). However, electrons scattered at these higher angles are not coherent, and consequently Bragg scattered electrons and diffraction contrasts cannot be imaged in HAADF-STEM mode. This can be advantageous as diffraction contrast can be unwanted and mask structural information. Only detecting high-angle scattered electrons with Z-contrast allows higher-resolution TEM images to be acquired, with typical resolutions of below a nanometer.

Selected area electron diffraction (SAED) is a common STEM characterisation technique, used to infer structural information about the crystal structures being imaged. A parallel electron beam is made incident on a sample, along a given zone axis or direction in the specimen. Electrons that are elastically scattered at angles below 50mrad remain coherent and will interfere to generate an electron diffraction pattern. Similarly to XRD, this follows Bragg's Law. An SAED aperture is inserted into the image plane of the objective lens, in the path of the electron beam after it has passed through the sample. This allows Bragg electrons scattered from the sample to be selected, from which the diffraction pattern is acquired. In the limit of electron diffraction, incident angles are very small and a small angle approximation ($\sin\theta \approx \theta$) is valid; an adjustment to Bragg's law (Equation 3.1) follows such that if n=1 [142]:

$$n\lambda = 2d\theta \tag{3.7}$$

$$\frac{\lambda}{d} = 2\theta = \frac{r}{L} \tag{3.8}$$

where r is the distance between diffraction points seen in the SAED pattern and L is the imaging camera's focal length, Similarly to XRD, SAED patterns and Equation 3.7 can be used to infer values for lattice parameters and plane spacing.

Beam rastering of the STEM also made the microscope appropriate for localised energy dispersive x-ray spectroscopy (EDX) measurements on imaged TEM samples. EDX relies on inelastic collisions and excitations of atoms near the surface of a TEM specimen, due to the incident electron beam. Inelastic collisions cause the ionisation of atoms, leaving a core electron hole. Characteristic x-rays are emitted as electrons from outer orbitals fall to fill such core holes, emitting an x-ray photon corresponding to the difference in electron energy levels. An x-ray spectrometer mounted to the STEM detects characteristic x-rays emitted from the TEM sample surface, and can be used to determine relative ratios of certain elements present and perform compositional analysis.

To obtain TEM images of thin films discussed in this thesis, all samples were prepared for TEM imaging using a focused-ion beam (FIB) milling method [144], with the exception of films

grown directly onto TEM membranes. This technique allowed a narrow cross-section or lamella for imaging to be extracted, typically below 200nm in thickness to remain electron transparent for TEM imaging. All FIB milling was performed by Connor Murrill, using a FEI Nova 200 NanoLab FIB/SEM instrument. BF and HAADF-STEM images, as well as SAED patterns were acquired using a CEOS double aberration corrected JEOL 2200FS scanning transmission electron microscope at the JEOL Nanocentre at York. Imaging was performed by both Dr Leonardo Lari and Dr Adam Kerrigan, operating at an electron energy of 200keV. The JEOL 2200-TEM microscope was also fitted with a Thermo Scientific Noran 7 EDX detection system. EDX measurements were performed with the same 200keV electron beam used for imaging, at a magnification of 10000x to allow local measurements of areas approximately 250μm in diameter. The TEM zone axis of imaged lamellas was confirmed using the JEMS electron microscopy simulation software to compare electron diffraction patterns.

3.3 Magnetic Characterisation

A variety of characterisation techniques were used to assess the magnetic properties of the materials under investigation. The most important techniques used to characterise the magnetism of samples were vibrating sample magnetometry and ferromagnetic resonance spectroscopy.

3.3.1 Vibrating Sample Magnetometry (VSM)

Vibrating sample magnetometry (VSM) is a technique for measuring the magnetic moment (or magnetisation) of a sample. The sample to be investigated is placed inside a uniform magnetic field, created by an electromagnet with two pole pieces. This field magnetises the sample. The sample is then vibrated sinusoidally, through the action of a piezoelectric crystal. The changing magnetic flux due to the vibration of the magnetised sample induces a current in detection coils located close to the sample [145]. The induced current signal is measured using a lock-in amplifier, which uses the frequency of the piezoelectric oscillator as a reference signal. The magnitude of the measured voltage is proportional to the magnetic moment of the sample. The value of the magnetic moment is inferred from the signal using a known pre-measured calibration. With a known (or estimated) volume for the magnetic film or sample, the magnetisation of the material can be calculated in emu/cc, as a function of applied field M(H). This aids comparison between different magnetic materials, having normalised to a unit volume. However, such M_S estimates have large uncertainties, of at least $\pm$5emu/cc, depending on uncertainties in film area (and thickness) which can produce significant changes in volume.

Room temperature M(H) measurements for this research were performed using the LakeShore 8600 VSM at the University of York. This VSM produced a maximum saturation field of 2.5T and was able to perform M(H) loops with very small field steps (0.01Oe minimum) [146]. Both

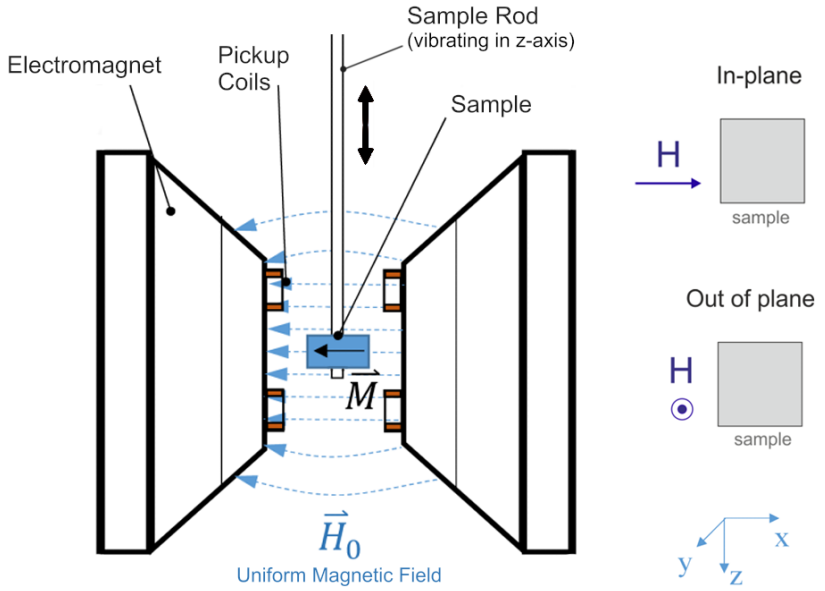

Figure 3.10: Schematic of a typical vibrating sample magnetometer setup. Adapted from [146]

of these qualities were favourable for the study of magnetically soft YIG and also a-YIG. For these measurements, the samples were mounted on a quartz rod using a small amount of GE varnish as an adhesive. The quartz rod was then mounted to the vibrating head, and the sample was centred within the magnetic pickup coils. The centering procedure (saddling) involved adjusting sample position, in X,Y,Z with micrometer screws, aiming for a minimum of the signal as a function of X, and a maxima as functions of Y and Z respectively. This improved the consistency of VSM loops measured for either separate samples or the same sample, aiding comparisons. Both in and out-of-plane measurements at room temperature were performed. These two orientations are shown in Figure 3.10, defined by the orientation of the applied field with respect to the sample. Switching between the two orientations was achieved by the rotation of the sample rod by 90°. For all measurements, point-by-point averaging was performed, opposed to a continuous sweeping of applied field. Averaging times equal to double the time required to step between field points (as a minimum) was used to achieve reasonable signal-to-noise. Background and linear contributions from substrates - either diamagnetic or paramagnetic - are removed from the M(H) data by subtraction of the linear background observed when the sample is magnetically saturated. For magnetically weak samples, background data-sets acquired from just the quartz rod or a clean substrate were acquired separately for comparison or subtraction from raw M(H).

3.3.2 Temperature Dependent Magnetometry (VSM-SQUID)

M(T) measurement provides insight into some structural behaviour of the sample, especially in the case of those materials with magnetic or structural phase transitions. Measuring M(T) can be performed either in a field-cooled (FC) scheme, where the sample is saturated in a DC magnetic field then cooled in preparation for a temperature sweep, or a zero-field cooled (ZFC) method, where the sample is cooled in zero-field and the field is set to a non-zero level for in-field measurement [147, 148]. The difference between these two methods lies in the orientation of the magnetisation: in the FC case, the magnetisation is saturated and cooled before the measurement field is applied, while the ZFC case retains any latent spin disorder in the sample that may be present, while the temperature is lowered.

Temperature dependent measurements were performed using a Quantum Design VSM-SQUID Magnetometer, located at the Diamond Light Source. A Superconducting Quantum Interference Device (SQUID) is a highly sensitive form of magnetometer and allows for the measurement of extremely small magnetisation and magnetic field changes, based on superconducting tunnel junctions. Shown in Figure 3.11(a), the VSM-SQUID magnetometer measures samples located in superconducting detector coils. Superconducting detection coils are configured as a second-order gradiometer [149, 150], with counterwound outer coils making the set of coils non-responsive to uniform fields or field gradients. The coils only generate a current in response to local flux changes from a magnetised sample's magnetic moment moving through the pick-up coils. These coils are inductively coupled to an rf-SQUID sensor and thereby induce a current in the SQUID. A SQUID sensor consists of two Josephson junctions formed into a loop between two superconducting wires. A DC SQUID is shown in Figure 3.11(b). Applying a magnetic flux to the SQUID sensor, a phase difference is introduced between opposite sides of the loop: with current from the detection coils being either supplemented or opposed by magnetically induced current. This produces a periodic net current based on magnetic flux quantisation, which provides a highly sensitive mechanism for voltage detection [149]. This is ideal for magnetometry and temperature dependent measurements, allowing for any subtle changes in magnetisation to be detected as the sample temperature is swept [150]. This was considered particularly important for studying magnetically weak materials such as a-YIG.

For each thin film sample measured, the sample was mounted onto a short quartz rod (from Quantum Design) using a small amount of GE varnish as an adhesive. GE varnish was chosen both its suitability for cryogenic anchoring and application, and its ease to remove with acetone (compared to silicon grease), minimising potential for contamination or sample damage when cleaning. Unlike the room-temperature VSM (where samples are attached to the end of a long quartz rod), samples in the VSM squid are mounted centrally on the quartz rod, as shown in Figure 3.11(a). The quartz rod plus sample is then attached to the end of a long rigid carbon-fibre sample rod. This sample rod is introduced into the VSM-SQUID chamber. The

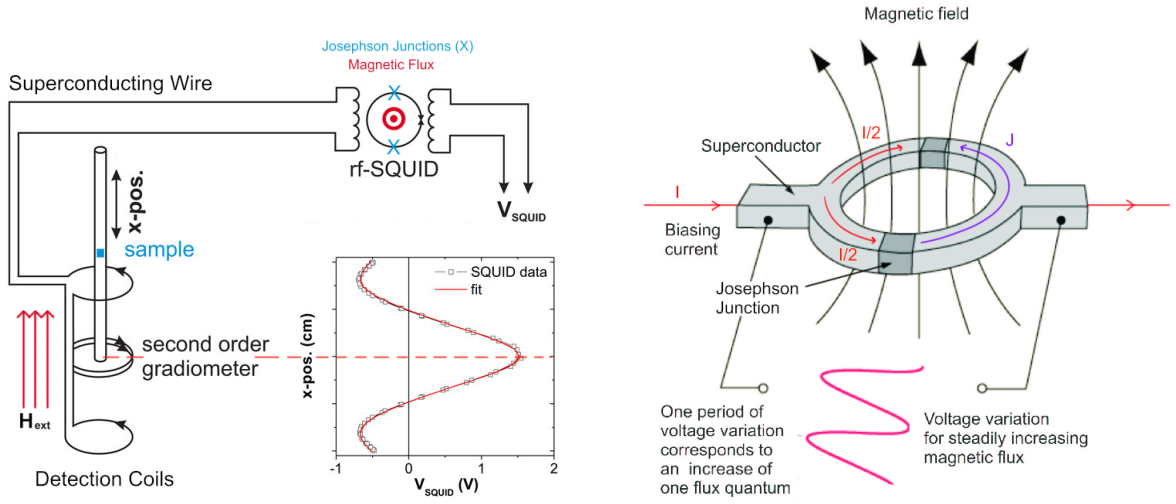

Figure 3.11: (a) Schematic of the VSM-SQUID magnetometer: showing the second order detection coils at the centre of the superconducting magnet, and the rf-SQUID sensor. (b) Diagram showing measurement of voltage from a DC SQUID sensor in the presence of magnetic flux, with a biasing current (I). Adapted from [151]

sample is then centered in the SQUID pickup coils to ensure that all coils sense the magnetic moment and that moment is measured accurately. During a centering measurement - inset in Figure 3.11(a) - the instrument scans the entire length of the quartz and the position where the magnetic moment is strongest is chosen: typically around 66mm [150].

The temperature dependence of the magnetisation, M(T), was measured following a programmed sequence of zero-field-cooling (ZFC) and field-cooling (FC) protocols. Crystalline YIG samples were first cooled from room temperature (300 K) to 10 K with no applied field. A measuring field of 1000 Oe was then applied at 10 K and the zero field cooled (ZFC) magnetisation data collected on warming to 350K. Subsequently, the samples were cooled again, now in an applied magnetic field of 1000Oe (equal to the measuring field) and field cooled (FC); magnetisation data was recorded on warming to 350K. A repeat measurement of ZFC was finally performed, cooling from 350K, as a sanity check and comparison to FC cooled from 350K. For amorphous YIG samples, this measurement sequence was the same, except cooling and measuring fields of 5000Oe were used instead, following [18]. Discussed in Section 5.3, the final ZFC scan (cooled from 350K instead of 300K) was highly important in measuring M(T) of a-YIG without the appearance of artefacts. All samples were cooled at a rate of 3K/min. M(T) was then measured at approximately 0.1K intervals, as the temperature was increased in a continuous sweep at 3K/min. For all M(T) measurements, an offset was subtracted to account for contributions of the substrate. However, for amorphous films, extra background contributions were considered. This is discussed further in Section 5.3.

3.3.3 Ferromagnetic Resonance Spectroscopy (FMR)

Ferromagnetic resonance (FMR) spectroscopy uses the principle of FMR discussed in Section 2.4 to characterise the magnetisation dynamics of ferro and ferrimagnetic thin film samples. Using FMR spectroscopy, magnetic damping parameters (Gilbert and extrinsic), anisotropies, the spectroscopic g-factor and estimates for saturation magnetisation can be obtained. FMR spectroscopy is a bulk-sensitive technique, whereby the magnetisation dynamics of the majority of the sample are shown in the FMR response. It is not usually possible to isolate effects of individual layers in a stack, or different magnetic phases throughout a sample, in single measurements; however, layers that are not coupled and have different M_S may produce multiple measurable Kittel curves. Specialised sample geometries - such as spacer layer wedges with increasing thickness - may also be used to extract thickness-dependent FMR data from single samples [152, 94]. Isolating effects of individual layers otherwise involves either growing two series of samples to compare, or a 'layer-by-layer' growth and characterisation approach. The latter is discussed further in Section 6.1. Since FMR relies on RF absorption, RF penetration depth must be considered. RF frequency photons possess an RF skin depth of below a micron in metallic samples [153]. However, all samples and trilayers studied in this thesis are below 100nm in total thickness, and thus the entire magnetic film undergoes resonance.

This research made use of an FMR spectrometer system established in the University of York's magnetic spectroscopy laboratory. The FMR apparatus consisted of a 50Ω coplanar waveguide (CPW), centred between poles of a rotatable DC electromagnet, the field from which (up to 0.5T) was aligned along the CPW with an in-plane geometry. This is illustrated in Figure 3.12. The CPW is connected to an RF source to form a two-port microwave transmission circuit. Two different methods of FMR spectroscopy have been used to collect data presented in this thesis. These are Vector Network Analyser FMR (VNA-FMR) and Modulation FMR (Mod-FMR) techniques. Both techniques are based on the same principles of RF absorption and exciting precession of magnetisation about an effective field. However, the two techniques differ in methods of RF generation and FMR signal measurement.

Vector Network Analyser FMR

VNA-FMR is an established technique for measuring ferromagnetic resonance in thin films. Figure 3.12 shows the FMR apparatus set up in VNA-FMR mode. The technique uses a vector network analyser (VNA) to provide a variable frequency RF signal to drive FMR in a magnetic sample under investigation. An RF frequency signal is compared between the input (port 1) and output (port 2) SMA microwave ports of the VNA. From this, scattering parameters - or S-parameters, S_{xy} - are measured by the VNA. The S-parameter model of a two-port VNA is illustrated in Figure 3.13. S-parameters relate the magnitude and phase of incident and reflected RF waves in a two-port VNA system, and are numbered by which port the wave propagates to (x) and which port the wave originates from (y). Conventionally, the forward

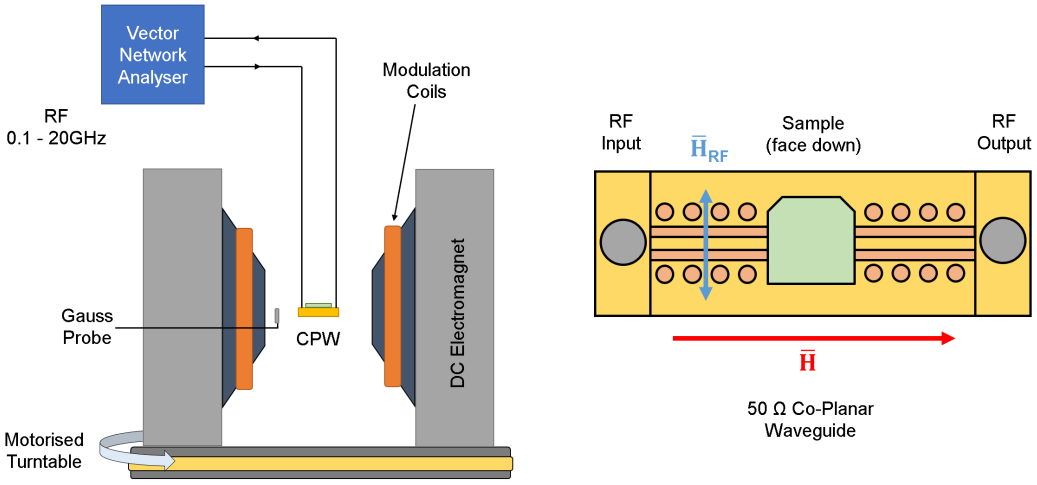

Figure 3.12: Schematic of the FMR spectrometer used to perform VNA-FMR measurements: a microwave transmission circuit, measuring RF absorption through a coplanar waveguide located in an in-plane magnetic field, H.

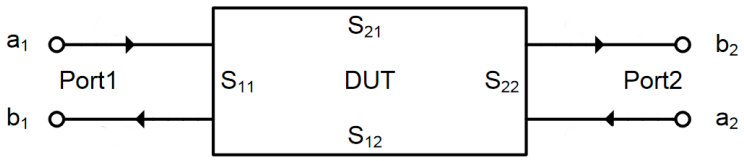

Figure 3.13: Two-port S-parameter model of a VNA, with a DUT (device under test): the CPW plus magnetic thin film. Adapted from [154].

microwave transmission coefficient for a fixed RF frequency is defined as S_{21}, for an input at port 1 and output at port 2 [154]. A two-port VNA with a DUT (device under test) has four S-parameters: two transmission coefficients (S_{21} and S_{12}) and two reflection coefficients (S_{11} and S_{22}). A wave leaving the DUT (b_1 or b_2) is a linear combination of waves entering the DUT (a_2 and a_1). These linear combinations are determined by the S-parameters, and given in Equations 3.9 and 3.10 [154]:

$$b_1 = S_{11}a_1 + S_{12}a_2 \tag{3.9}$$

$$b_2 = S_{21}a_1 + S_{22}a_2 \tag{3.10}$$

Configuring the VNA such that no waves enter the DUT from port 2 (i.e. the output port), a_2 is zero. The forward microwave transmission coefficient, S_{21}, is then given by the ratio between the RF signal input at port 1 (a_1) and output at port 2 (b_2) following Equation 3.11 [154]:

$$S_{21} = \left.\frac{b_2}{a_1}\right|_{a_2=0} \tag{3.11}$$

The VNA itself induces a RF-frequency magnetic field oscillating perpendicular to the stripline. This RF field excites the magnetisation precession in the sample, and the applied DC field from the electromagnet allows the Lamor frequency of the sample to be changed. FMR occurs when the Lamor frequency equals that of the RF field. At resonance, absorption of the RF power causes an attenuation of the RF current passing through the CPW, and a decrease in RF signal intensity at output port 2. This is observed as a drop in S_{21} as a function of frequency. The Kittel curve is 2-dimensional (varying with both applied frequency and applied magnetic field), and therefore a similar drop in S_{21} is observed as function of applied field, at a fixed frequency. An exemplar S_{21}(H) VNA-FMR spectrum for a YIG thin film in this work is shown in Figure 3.14.

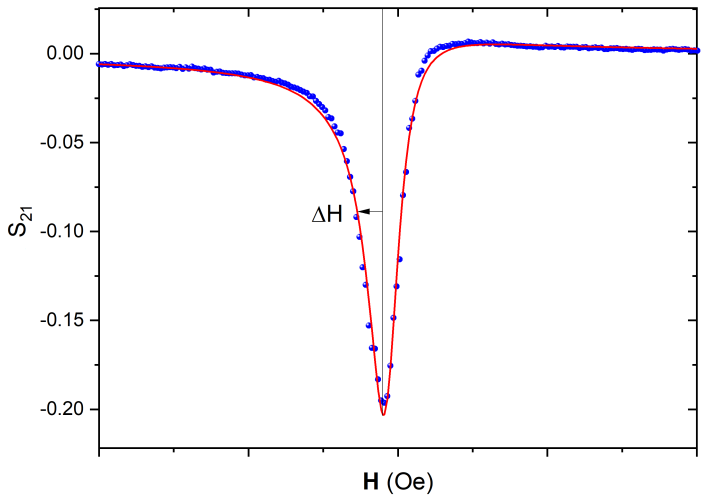

Figure 3.14: VNA-FMR linescan of S_{21} at a fixed RF frequency of 10GHz. The ferromagnetic resonance is described by resonant field H_r and FMR linewidth ΔH. An asymmetric Lorentzian fit (following Equation 3.12) is shown by the red line.

The linewidth of this resonance can be obtained by fitting to an asymmetric Lorentzian function, given by Equation 3.12:

$$\chi'' \cos\delta + \chi' \sin\delta = A\frac{\Delta H \cos\delta + (H - H_r)\sin\delta}{\Delta H^2 + (H - H_r)^2} + B \tag{3.12}$$

where A and B are constants, χ' and χ'' are the real and imaginary parts of the AC susceptibility, and δ is the mixing angle between the absorptive and dispersive components of the FMR. ΔH is the linewidth of the absorption Lorentzian lineshape defined to be the half width at half maximum (HWHM), H_r is the resonance field and H is the applied magnetic

field. Symmetric Lorentzians do not account for coupling that may occur between the sample and the transmission line, which produces asymmetry and mixing between real and imaginary parts of the susceptibility [155]. Due to losses inherent to the CPW at certain RF frequencies, the baseline for FMR Lorentzians are typically not flat. A background data set (with the resonance forced to a high field beyond the measurement range) is taken and subtracted from all subsequent data to flatten the baseline. However, environmental perturbations during measurements, such as temperature fluctuations, could produce non-linear background contributions that were manually subtracted.

By extracting the FMR linewidth, ΔH, from linescans at various fixed RF frequencies, magnetic damping within the sample can be evaluated. If the frequency dependence of the FMR linewidth ΔH(f) is linear, then fitting of the data to Equation 2.50 will yield both the intrinsic Gilbert damping parameter, α, from the gradient and extrinsic damping from any observed zero-frequency offset in linewidth, ΔH(0). However, if ΔH(f) is non-linear and curved (particularly at higher applied RF frequencies), then evaluation of two-magnon scattering parameters from Equation 2.52 can be applied to evaluate the dominant damping mechanism.

Extraction of the Kittel curve from frequency-field space at a constant applied field provides insight into other key parameters. Resonant frequency as a function of applied field, ω_r(H), can be fit to the Kittel equation discussed in Section 2.4. If magnetisation is both in-plane and aligned along an easy axis, fitting ω_r(H) to Equation 2.48 yields the effective magnetisation (M_{eff}) and gyromagnetic ratio (γ). From Equation 2.33, the spectroscopic g-factor can be extracted from the gyromagnetic ratio. From g, the ratio of spin-to-orbital magnetic moments in the sample can be obtained, μ_L/μ_S (Equation 2.34). The gyromagnetic ratio is also necessary to obtaining a value for Gilbert damping.

FMR data acquired as a function of in-plane field azimuthal angle allows in-plane anisotropy to be assessed. Measurement of resonant field H_r for different azimuthal angles effectively traces out the free energy surface in the plane of the sample. Easy axes correspond to minima in H_r, whereas hard axes correspond to maxima. For a (111)-oriented-film, a six-fold anisotropy would be expected in-plane [156, 157].

Modulation FMR

Modulation FMR (Mod-FMR) provides an alternative lock-in detection based technique for FMR measurement, the benefit of which is a higher sensitivity to weaker resonance signals. This was considered important for FMR from amorphous YIG (if any) or for crystalline films of poorer magnetic quality. Mod-FMR operates similarly to VNA-FMR, however signal detection is performed differently. Mod-FMR relies on an time-varying AC magnetic bias field - the modulation field - being applied in parallel to the bias field. The total AC susceptibility of sample plus waveguide is thus given by [158]:

$$\chi\left(\boldsymbol{H}+\boldsymbol{H}_m e^{i\omega t}\right) \tag{3.13}$$

Considering the time-dependent field in 3.13 as a Taylor expansion, where higher order terms are small enough to be ignored, the AC susceptibility can be written as:

$$\chi(\boldsymbol{H})+i\omega\boldsymbol{H}_m e^{i\omega t}\frac{d\chi}{d\boldsymbol{H}} \tag{3.14}$$

where χ is the AC susceptibility, H is the bias field, H_m is the modulation field and ω the frequency of the modulation coils. With the modulation technique, the sample absorption of the RF power is measured by a lock-in amplifier. The setup of the lock-in amplifier to the FMR spectrometer and its modulation coils is shown in Figure 3.15. The lock-in signal measured is proportional to the derivative (with respect to field) of the imaginary component of the AC susceptibility. Correspondingly, magnetic parameters are extracted from mod-FMR data using the first derivative of the asymmetric Lorentzian function (Equation 3.12) used to describe ferromagnetic resonance [155]. The derivative is given by Equation 3.15, where all fitting parameters are the same as Equation 3.12.

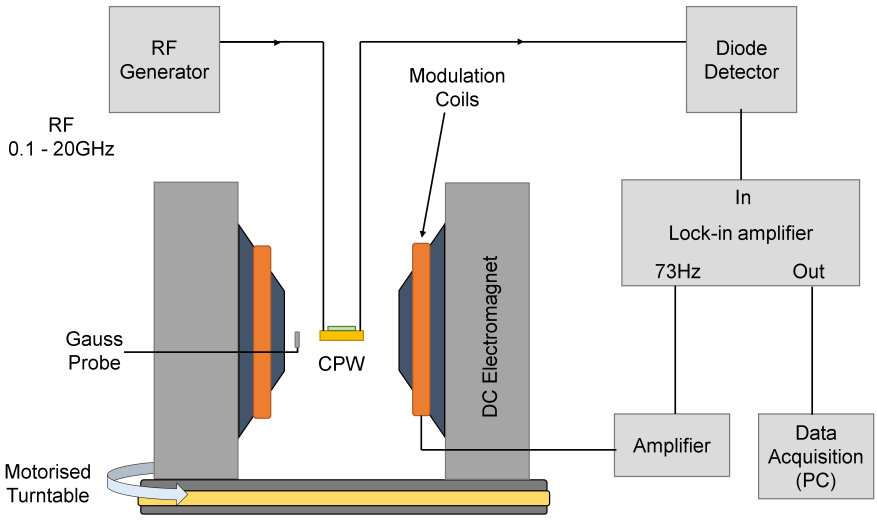

Figure 3.15: Schematic of the FMR spectrometer in Modulation-FMR measurement mode.

$$\frac{d\left(\chi''\cos(\delta)+\chi'\sin(\delta)\right)}{d\boldsymbol{H}}=A\left[-\frac{2\left(\boldsymbol{H}-\boldsymbol{H}_r\right)\Delta H\cos(\delta)}{\left[\Delta H^2+\left(\boldsymbol{H}-\boldsymbol{H}_r\right)^2\right]^2}-\frac{\left[\Delta H^2-\left(\boldsymbol{H}-\boldsymbol{H}_r\right)^2\right]\sin(\delta)}{\left[\Delta H^2+\left(\boldsymbol{H}-\boldsymbol{H}_r\right)^2\right]^2}\right]+B \tag{3.15}$$

An exemplar Mod-FMR spectrum is shown in Figure 3.16. Parameters of interest from the Lorentzian derivative are similar to the VNA-FMR technique: resonant field H_r and HWHM linewidth ΔH. The exact heights of the peaks observed in the derivative are usually not of prac-

tical interest, with the y-axis being an arbitrary amplitude. However, peak-to-peak linewidth ΔH_{PP} from the modulation FMR requires a correction factor of $\sqrt{3}/2$ to equal the HWHM of a Lorentzian (Equation 3.16) [155]. A notable disadvantage of Mod-FMR is the use of a lock-in technique and modulated magnetic field causing systematic broadening of measured FMR linewidths by approximately 5-6Oe. This is less detrimental for magnetic materials with broad ΔH, however accurate measurement of narrow ΔH as in YIG is made difficult.

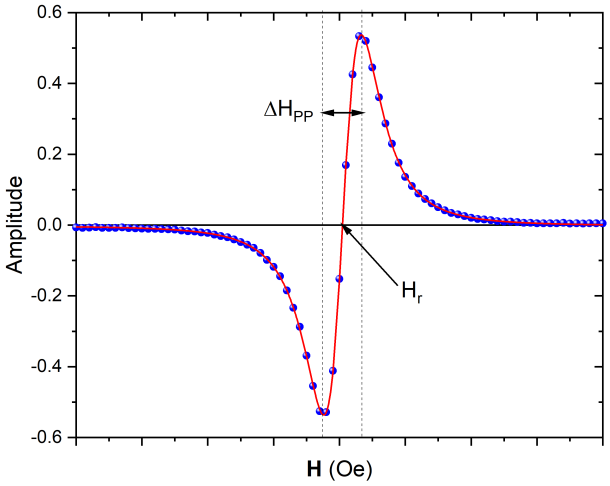

Figure 3.16: Modulation FMR linescan at a fixed RF frequency of 10GHz. The ferromagnetic resonance is described by resonant field H_r and peak-to-peak linewidth ΔH_{PP}. An asymmetric Lorentzian derivative fit (following Equation 3.15) is shown by the red line.

$$\Delta \boldsymbol{H}_{VNA} = \left(\frac{\sqrt{3}}{2}\right) \Delta \boldsymbol{H}_{PP} \tag{3.16}$$

Magnetic parameters of interest are extracted in an identical manner to VNA-FMR; extracting M_S and γ from the Kittel curve $\omega(H)$, assessing in-plane anisotropy from measuring $H_r(\phi)$, or Gilbert and extrinsic damping from $\Delta H(f)$ following scaling correction of linewidth.

3.4 X-Ray and Magnetic X-Ray Spectroscopy

X-ray absorption spectroscopy (XAS) and x-ray magnetic circular dichroism (XMCD) have been performed at the Fe K-edge and Fe L-edges respectively, on various YIG and a-YIG samples studied in this thesis. These measurements were performed on the B18 core XAS beamline and I10 BLADE at the Diamond Light Source synchrotron facility. XAS is an established technique at synchrotron facilities for assessing the local structure and oxidation states of

specific elements in various materials. XMCD is a variation of XAS, wherein the difference between absorption spectra for right and left circularly-polarised x-rays (by a sample in a magnetic field) is measured. XMCD allows analysis of magnetism in thin films to be performed with elemental specificity and coordination sensitivity [159].

3.4.1 X-Ray Absorption Spectroscopy (XAS)

XAS is obtained by measuring the x-ray absorption coefficient of a material as a function of energy. Absorption occurs when an x-ray photon energy causes a transition between a core electron level to unoccupied states above the Fermi level. Energy from the photoelectric absorption either excites the electron to a higher energy unoccupied orbital, or into a continuum being no longer associated with the atom. XAS spectra consist of sharp peaks as a function of energy corresponding to electron transitions from occupied core level states to unoccupied states in the absorbing element. These peaks are called absorption edges. The name of the edge depends upon the core electron that is excited. The principle quantum numbers (n = 1, 2 and 3) are represented by the K, L and M edges, respectively. K-edge and L-edge transitions are shown in Figure 3.17. L-edge transitions are further sub-categorised into L_1, L_2 and L_3 edges, based on the initial electron orbitals: L_1 from the 2s state, L_2 from $2p_{1/2}$ and L_3 from $2p_{3/2}$. The energy at which an absorption edge occurs is based on both the transition and the element. K-edges occur at a higher energy than the L-edge, due to the increased binding energy of electrons in the 1s orbital. In 3d transition metals like Fe, the K-edge occurs in the hard x-ray energy range (7keV and above), whereas the L-edge occurs in the soft x-ray energy range (400-1000eV).

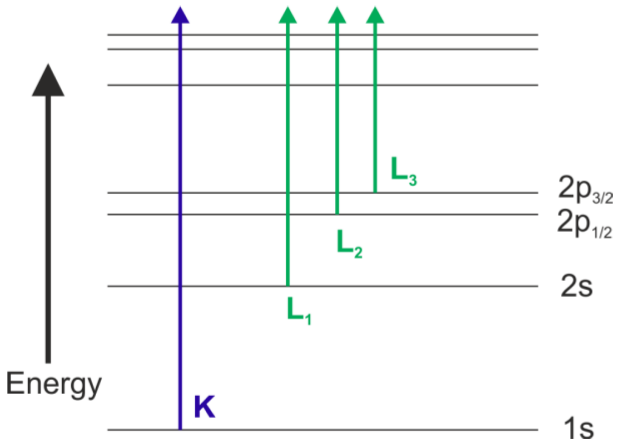

Figure 3.17: K-edge (blue) and L-edge (green) electron transitions and associated electron orbital energy levels.

Energy must be conserved following x-ray absorption for a transition to occur; the energy difference between initial and final electron states must be equal to the incident photon energy.

Angular momentum must also be conserved, transferred from the photon to the electron, by coupling the photon angular momentum with electron orbital angular momentum. In materials with spin-split core states, photon angular momentum couples to electron spin momenta as well as orbital momenta, due to spin-orbit coupling. Electron transitions must also obey quantum mechanical selection rules to occur, regarding angular momenta and spin of final electron states. The most intense absorption edges in XAS are due to electric dipole transitions, obeying the orbital (or Laporte) rule where $\Delta l = \pm 1$. Spin-flip is forbidden between initial and final electron states, following the spin rule $\Delta S = 0$ [160]. Consequently, $L_{3,2}$-edges are due to 2p $\rightarrow$ 3d transitions, and the K-edge is due to transitions from 1s $\rightarrow$ p-like final states [161]. However, it is known that x-ray transitions which violate typical dipole selection rules exist with a far weaker absorption probability, such as electric quadrupole transitions ($\Delta l = \pm 2$) [160]. These weaker absorption peaks are observed in XAS as pre-edge features to more intense Laporte-allowed dipole transitions (discussed further in Section 3.4.3).

XAS Measurement

XAS spectra are measured using either a total electron yield (TEY) or a fluorescence yield (FY) technique. The core holes created due to x-ray absorption produces an avalanche of decaying electrons, resulting in the emission of photons and Auger electrons via two different decay processes. Electrons can decay by emitting photons equal to the electron transitions, which are then detected as the FY signal. Alternatively, extra energy from an electron decay can be used to reorganise the electron distribution in atoms, causing the emission of an Auger electron from the material's valence band [162]. TEY measures the total number of electrons emitted from the sample: including Auger electrons, secondary electrons and photoelectrons. Secondary electrons here are electrons produced by primary XAS products (Auger electrons, photoelectrons, emitted photons) interacting with atoms in the sample. The number of emitted electrons is directly proportional to the number of core holes created by x-rays absorbed by the sample; thus, the TEY signal is proportional to the x-ray absorption coefficient [163]. Transmission XAS measurements are also possible, but are not appropriate for substrate-grown thin films examined in this thesis.

The type of decay product measured determines the probing depth of the XAS. TEY is measured by connecting an electron source to the sample and measuring the drain current due to XAS-induced electron emission. The drain current is proportional to the TEY, assuming that electron escape depth is significantly smaller than the absorption depth [163]. For a constant photon frequency, the TEY is given by Equation 3.17

$$I_{\mathrm{TEY}} = C \left(\frac{1}{1 + \frac{\lambda_e}{\lambda_x \cos\theta}} \right) \mu \tag{3.17}$$

where λ_x is the x-ray penetration depth, λ_e is the electron escape depth, μ is the x-ray

absorption coefficient, C is a constant, and θ is the incident angle of the x-rays relative to the surface normal. The absorption depth of x-rays at the absorption edge is on the order of 50nm. However, TEY is ultimately a surface sensitive technique as the escape depth of electrons is typically limited to 5-6nm. FY detection, in contrast, is a bulk sensitive technique due to deeper penetration of the x-rays compared to electron mean free paths. However, FY signals are weaker because of the increased probability for Auger electron emission, compared to that of photon emission at the L-edges. For hard x-rays (at the K-edge), these decay path probabilities are reversed, and FY detection is more commonly used [159].

3.4.2 X-Ray Magnetic Circular Dichroism (XMCD)

XMCD is defined as the difference arising between two XAS spectra measured with opposite circularly polarised soft x-rays, in the presence of a magnetic field. One XAS is measured with right-circularly polarised (RCP or σ^+) x-rays, and the other with left-circularly polarised (LCP or σ^-) x-rays. The XMCD is thus defined to be the difference spectrum. Conventionally, the difference is defined such that the L_3 edge in the XMCD spectrum is negative [159]. Throughout this thesis, this convention is met with XMCD being given by $\sigma^- - \sigma^+$. The XMCD effect arises from the excitation of core electrons into unoccupied conduction states. Transition metals such as Fe have partially filled 3d orbitals, with a spin-split density of states that exists near the Fermi level. Due to spin-flip being forbidden in electric dipole transitions, only spin-up photoelectrons can be excited to spin-up 3d holes (and vice versa for spin-down). The absorption probability is proportional to the number of empty d-holes that an electron of a given spin can be excited into. This consequently produces a difference in x-ray absorption probability between RCP and LCP x-rays (in a magnetically saturated sample) due to spin-up and spin-down hole imbalance, illustrated in Figure 3.18. [159].

XMCD is magnetically sensitive to magnetic moments of electrons due to the use of circularly polarised x-rays. Circularly polarised x-rays possess a photon helicity vector of either ± 1. These photons transfer angular momentum to the 2p electrons with an orbital moment parallel to the photon helicity. RCP photons transfer the opposite angular momentum to electrons as LCP photons do, allowing for selective spin-up/spin-down photoelectron excitation with these two polarisations. The $p_{3/2}$ and $p_{1/2}$ electron levels have opposite spin-orbit coupling, so the spin polarisation is opposite at the L_3 and L_2 edges. XMCD signals at each absorption edge therefore take opposite orientations [159].

XMCD allows for elemental specificity by tuning the x-ray photon energy to coincide with the absorption edges for elements in a material. The $L_{3,2}$-edges ($2p \rightarrow 3d$ transitions) are typically used for XMCD due to the fact that magnetism in transition metals like Fe are mostly due to the 3d electrons. In addition, like all XAS based techniques, binding energies of valence electrons (and therefore holes) are sensitive to the oxidation state of the absorbing ions. Thus,

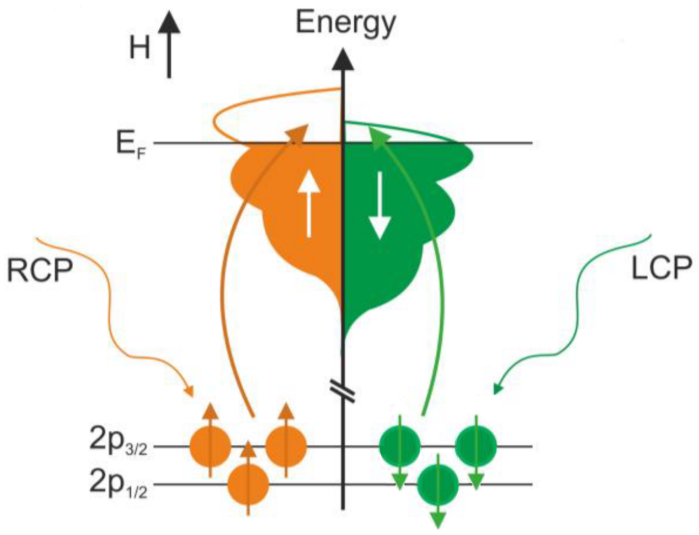

Figure 3.18: XMCD effect arising from the spin-split density of states in a partially filled 3d transition metal, in a magnetic field, H. Adapted from [159]

XMCD allows for valence specificity (i.e. between Fe^{2+} and Fe^{3+} ions). Coordination of these ions also affects the XAS/XMCD, where the crystal field causes splitting of the d-orbitals in energy. Discussed in Section 2.2.6, crystal field effects cause the d-orbitals to become non-degenerate. Consequently, Fe cations in tetrahedrally (T_d) and octahedrally (O_h) coordinated sites experience x-ray absorption at different photon energies. Magnetic contributions of Fe cations at each of these sites can be estimated by simulation and fitting of the XMCD using theoretical atomic multiplet calculations.

3.4.2.1 Atomic Multiplet Calculations

Atomic multiplet calculations can be performed to match the experimental XMCD. These simulations allow valence, coordination and crystal field energies of transition-metal elements in the sample to be determined. XMCD simulations in this thesis are generated using calculations performed by the CTM4XAS software [164]. The physical basis of the CTM4XAS software is a combination of atomic multiplet theory and crystal field theory. Atomic multiplet theory concerns models that describe the atomic structure in many-electron atoms with quantum mechanics [160]. Cowan's ab-initio Hartree-Fock method with a relativistic correction [165] is the model used by CTM4XAS to calculate the electronic structure of a given transition metal atom species (of a desired valence and coordination). [160]. Full details of this approximation are given in reference works by Cowan [165, 166]. Crystal field effects are then considered as a perturbation to the atomic result (i.e. an extra electrostatic field potential) [167]. From the final calculated electronic structure, the XAS (and XMCD) spectrum is simulated following the Fermi golden rule, applied for linearly and circularly polarised X-ray photons [164]. A linear

combination of two (or more) simulated XMCD spectra is then used to match experimental data for a sample.

This technique can be used to estimate the stoichiometry of iron oxide samples. Stoichiometric YIG has a 3:2 ratio of T_d:O_h Fe^{3+} ratio, as discussed in Section 2.6.1, with no O_h Fe^{2+} present. Using CTM4XAS to calculate theoretical XMCD for these three Fe sites, combined spectra allowed the relative occupation of each site to be estimated. However, it must be emphasised that atomic multiplet calculations reflect contributions to the magnetism observed in the XMCD only, and may not necessarily reflect the ratio of chemical species present in the material. This, and other shortcomings of atomic multiplet calculations are discussed further in Chapter 5. Multiplet calculation codes (such as CTM4XAS) are most practically used in simulating L and M edge absorption in transition metals [159]. These calculations are performed semi-empirically (based on various input parameters described below) and explicitly include important 2p-3d core-valance electron interactions. These include Coulomb interactions, exchange interactions, and the overlap of the 2p and 3d electron wavefunctions. Such interactions are neglected in single-particle and DFT-based codes, making their use for simulating 2p-3d XMCD unsuitable [163, 164].

A simulated XMCD spectrum is based on several input parameters. For a chosen element with a given valence, choice of coordination dictates the crystal field splitting parameter, 10Dq (discussed in Section 2.2.6). Slater integral reduction parameters - F_{dd}, F_{pd}, G_{pd} - describe the two-electron integrals defined by Cowan [165], with a weighting value ranging between 0 and 1; a Slater parameter reduction input of 1 indicates atomic values, which represent 80% of the Hartree-Fock values [164]. Spectral broadening effects are accounted for by both Gaussian and Lorentzian broadening factors, adjustable to match experimental peak widths; expected broadening factors may also be known for a given experimental setup. Sample temperature can also be defined, by weighting the electron population of the initial state configuration with a Boltzmann function. This controls both the magnitude of the simulated XMCD spectrum, and also the XMCD lineshape in the case of coordinations or valencies that exhibit a temperature dependence [159, 164].

3.4.2.2 XMCD Sum Rules Analysis

XMCD sum rules can be used to extract additional magnetic information from measured spectra. This is because x-rays only interact with the orbital component of the electron wavefunction, so orbital and spin contributions to magnetic moment in a material can be distinguished [168]. Parameters used in the XMCD sum rules are defined in Figure 3.19, and the XMCD sum rules themselves defined as:

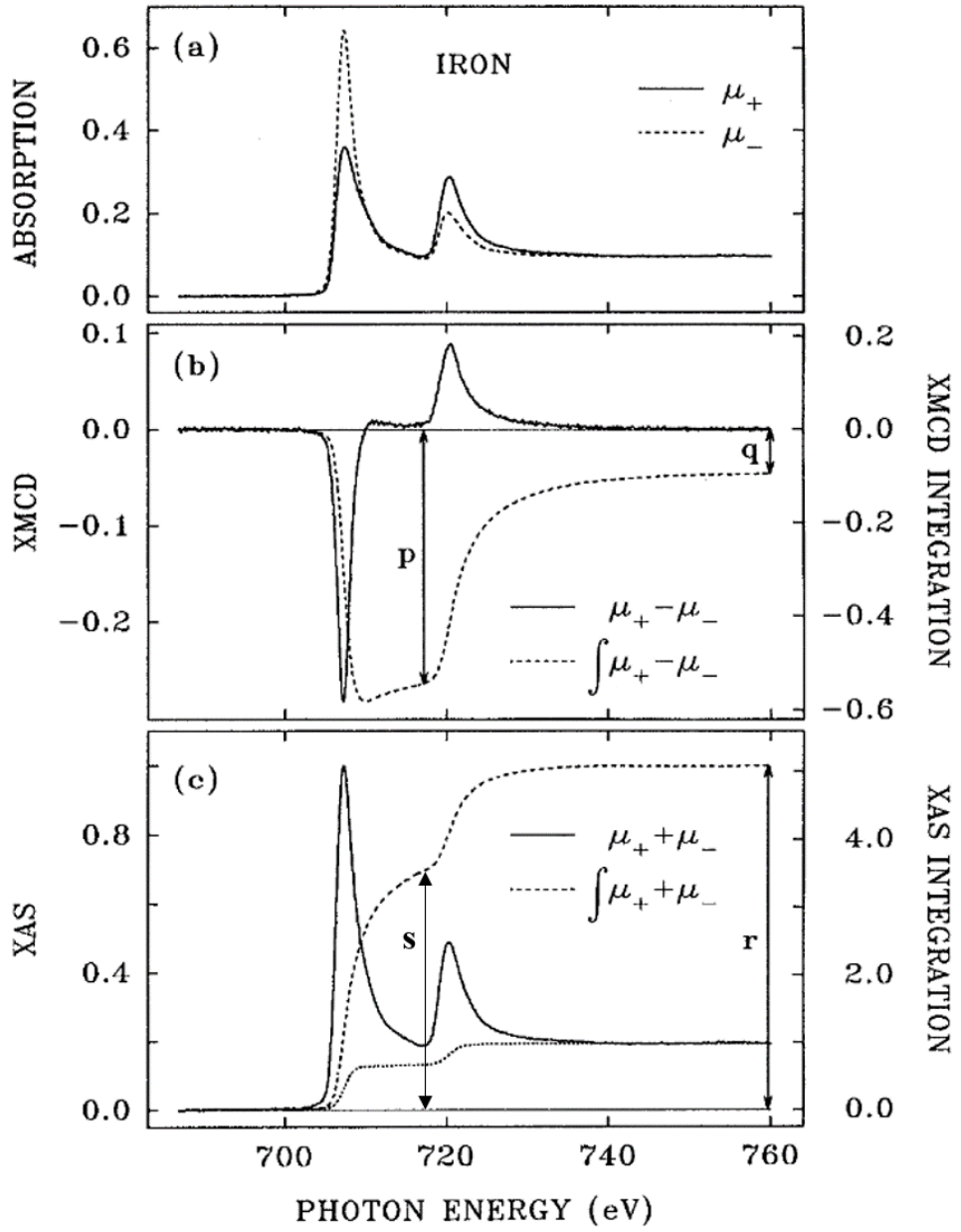

Figure 3.19: $L_{2,3}$-edge XAS/XMCD spectra of iron with integrals required for sum-rules analysis; (a) XAS spectra showing dichroism between positive and negative circular x-rays. (b) Resulting dichroism (XMCD); the integrated XMCD is shown by the dashed line, from which **p** and **q** are obtained. (c) Integrated XAS is shown by the broad dashed line, from which **r** and **s** are obtained. The finer dotted line - shown beneath the XAS lineshape in (c) - indicates a two-step function used for edge jump removal before XAS integration. Adapted from [169].

$$n_h \propto r \tag{3.18}$$

$$\frac{< l.s >}{n_h} = 2 - \frac{3s}{r} \tag{3.19}$$

$$< L >= \frac{-4qn_h}{3r} \tag{3.20}$$

$$< S > + \frac{7 < T >}{2} = \frac{-(3p - 2q)}{n_h} \tag{3.21}$$

$$\frac{< L >}{\left(< S > + \frac{7<T>}{2}\right)} = \frac{4q}{(9p - 6q)} \tag{3.22}$$

n_h is the number of d-electron holes in the material, r and s are parameters extracted from the integral over the total XAS (RCP + LCP), and $\frac{<l.s>}{n_h}$ is the branching ratio (ratio of intensities at the L_2 and L_3 edges). q and p are parameters extracted from the integrated XMCD, $< L >$ is the expectation value for the orbital angular momentum, $< S >$ is the expectation value for the spin angular momentum, and $< T >$ is the expectation value for the magnetic dipole operator[159, 170]. In bulk cubic 3d-transition metal ferromagnets, $< T >$ is vanishingly small compared to $< S >$, allowing the last two sum rules to be simplified:

$$< S > \approx \frac{-(3p - 2q)}{n_h} \tag{3.23}$$

$$\frac{< L >}{< S >} \approx \frac{4q}{(9p - 6q)} \tag{3.24}$$

An alternate notation was introduced by Chen *et al.* [169], valid on the basis that the core spin-orbit coupling is larger than the core-valence interaction. This condition is considered true for transition metals like Fe and Co [159]. Sum rules can instead be written in terms of orbital magnetic moment (μ_L) and effective spin magnetic moment (μ_S^{eff}):

$$\mu_L = -\frac{4q}{3r} n_h \tag{3.25}$$

$$\mu_S^{eff} = -\frac{(6p - 4q)}{r} n_h \tag{3.26}$$

$$\frac{\mu_L}{\mu_S^{eff}} = \frac{1}{\left(\frac{9p}{2q} - 3\right)} \equiv \frac{2q}{(9p - 6q)} \tag{3.27}$$

Equation 3.27 allows the ratio of orbital to spin magnetic moments, μ_L/μ_S to be easily extracted from integrated XMCD spectra. From this, the spectroscopic g-factor can be extracted using Equation 2.34 and additionally the gyromagnetic ratio from Equation 2.33.

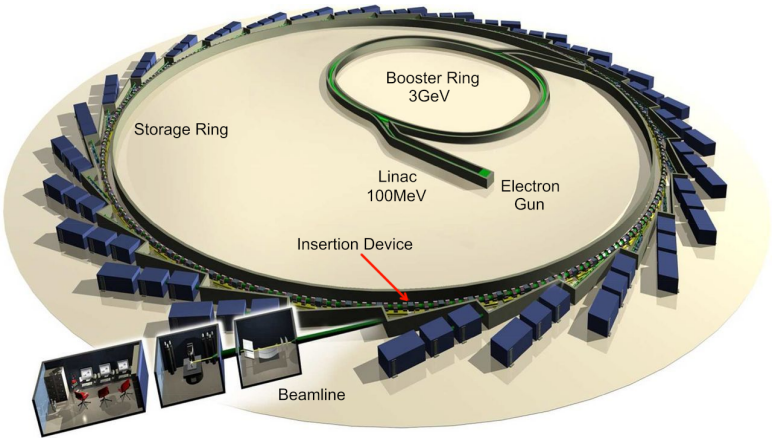

Figure 3.20: Schematic diagram of the synchrotron at the Diamond Light Source facility. Adapted from [171].

3.4.2.3 Synchrotron X-Ray Generation and Experimental Setup

Photons in the soft x-ray range of 400-1000eV are required to scan across the $L_{3,2}$ edges of iron for XMCD measurements. Hard x-ray measurements over the Fe-K edge (discussed in Section 3.4.3) require even higher x-ray energies approaching 7keV and above. For both techniques, an intense and tunable x-ray source is required. Consequently, soft and hard x-ray absorption are synchrotron based techniques. The XMCD measurements in this thesis were performed on the I10 BLADE (beamline for advanced dichroism experiments) at the Diamond Light Source (DLS) synchrotron facility.

A schematic of the DLS synchrotron is shown in Figure 3.20. Electrons are initially accelerated by a 100MeV linear accelerator, and then accelerated again in a booster ring synchrotron to energies of 3GeV under UHV conditions; the path of the electrons around the ring is not circular, but a series of straights and bend sections. The electron orbit is curved in the bend sections through the use of dipole magnets. High energy electrons are then fed into the main storage ring of the DLS, 561m in circumference. The electron beam in the storage ring is maintained with regular top ups from the booster ring, roughly every 10 minutes. Insertion devices, such as bending magnets or undulators, are located at front end of each beam-line. As the electron beam passes through the insertion device, it forces the electrons to bend or oscillate, which produces high intensity synchrotron radiation [171, 172].

The I10 beamline uses APPLE-II HU48 undulators in order to produce X-rays within an energy range of 500-1700eV [173, 174]. The undulator is composed of four independent arrays of permanent magnets, with each array producing an alternating magnetic field along its length. This alternating field forces the electron beam to repeatedly undulate, producing coherent beams of x-ray photons. The x-ray photons interfere constructively to produce a collimated, high intensity x-ray beam with a high photon flux. X-rays from undulators consist of a set of discrete harmonic energies, determined by the periodic length of the undulator magnet

array (λ_u). The x-ray wavelength can be selected by tuning the magnetic field strength of the undulator, by changing the separation of the magnet arrays. The X-ray wavelength is given by [175]:

$$\lambda = \frac{\lambda_U}{2\gamma^2}\left(1 + \frac{k^2}{2} + \gamma^2\theta^2\right) \tag{3.28}$$

where θ is the deflection angle and k is a magnetic deflection parameter, defined as $\frac{eB_0\lambda_u}{2\pi m_e c}$. Here, B_0 is the magnetic field of the undulator, and e, m_e and c are physical constants: electron charge, electron rest mass and speed of light respectively. The Lorentz factor, γ, accounts for the relativistic motion of electrons approaching the speed of light. A correction proportional to $\frac{1}{\gamma^2}$ accounts for both Lorentz contraction and relativistic Doppler shift. The APPLE-II HU48 undulators allow for variable x-ray polarisation by shifting two of the four arrays of magnets in parallel to the others. A parallel shift of $\pm\frac{\lambda_u}{4}$ changes the x-ray beam from linear horizontal polarisation to ± 1 (right or left) circular polarisation respectively, shown in Figure 3.21.

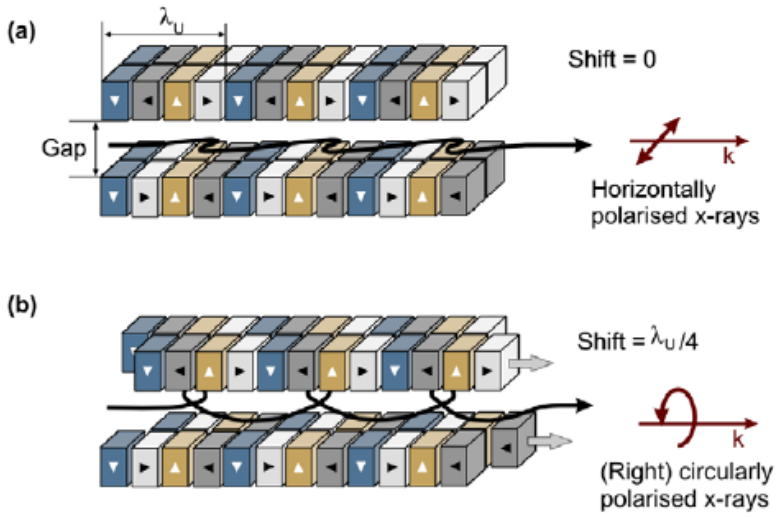

Figure 3.21: Schematic diagram of the APPLE-II undulator on the I10 beamline at the DLS, to produce either (a) horizontally (linearly) polarised or (b) right-circularly polarised X-rays. Adapted from [176].

Polarised x-rays travel from the undulator and down the beamline towards the XMCD experimental set up. Several apertures and grazing incidence mirrors along the beam line act to collimate the x-ray beam further, before being monochromated by a diffraction grating. Cylindrical and toroidal focusing mirrors then focus the x-ray beam onto the sample of interest in the XMCD chamber, reduced to a spot size of 10μm x 100μm [173]. A schematic of the XMCD experimental set up is shown in Figure 3.22.

The XMCD setup on I10 consists of a high field (14T) superconducting magnet, which the sample is placed inside under UHV conditions. The high field magnet has a split coil design,

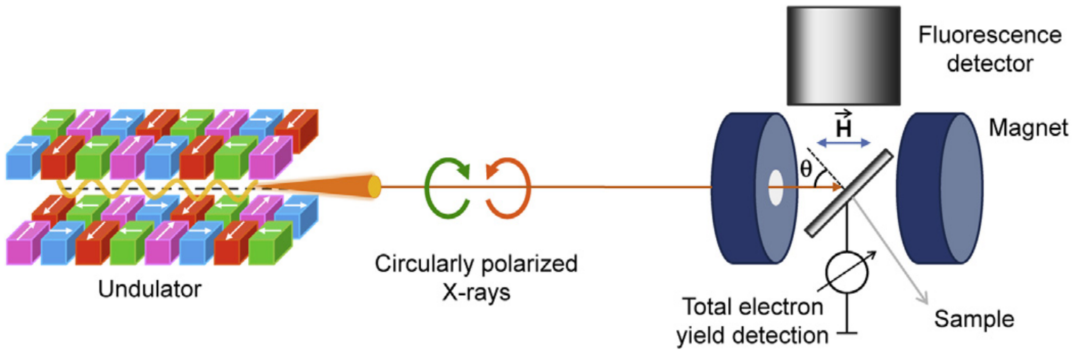

Figure 3.22: Schematic diagram of experimental XMCD setup on the I10 beamline. The beamline optics have been omitted. Adapted from [159].

where the X-ray beam passes directly through the centre of the magnet and onto the sample. A cryostat provides sample temperature control between 2K and 400K. XAS (and XMCD) is measured using both a TEY drain current for metallic samples or those capped with a metal conducting layer, and also a fluorescence detector for FY (discussed in Section 3.4.1). The sample can be rotated around the vertical axis by $\pm 90^{\circ}$ to perform XMCD with x-rays either at grazing incidence or normal incidence. XMCD is proportional to the projection of the sample magnetisation vector along the direction (helicity vector, σ) of the circular x-rays: following $\mathbf{M}.\sigma$. Use of a grazing incidence provides an increased beam footprint (proportional to $1/\sin\theta$, θ is incident beam angle with respect to the sample normal in Figure 3.22), allowing measurement of a larger sample area and a larger XAS signal. Grazing incidence also allows measurement of in-plane magnetisation, compared to normal incidence where only out-of-plane effects are observed. However, self-absorption effects are present in spectra measured in FY and TEY (independent of incident angle) which require additional corrections [177]: particularly in FY experiments.

For all samples, XMCD measurements in this thesis were performed at normal incidence, in order to reduce the effect of self-absorption on the spectra [177]. XMCD was measured in a positive saturating field of 5T applied collinear to the photon helicity vector, at a number of different sample temperatures between 10K and 300K. XAS measurements using RCP and LCP x-rays were performed over the Fe L_3 and L_2 edges. Photon energy was scanned through the L_3 and L_2 edge transitions of Fe (695-750eV). Eight sets of XAS were acquired per sample at each temperature: four with positively circular x-rays (σ^+) and four with negatively circular x-rays (σ^-). From these, sixteen XMCD subtractions (σ^- - σ^+) were acquired, from which three to four XMCD signals were averaged.

3.4.3 Hard X-Ray Absorption Techniques

3.4.3.1 XANES

Analysis of hard x-ray XANES (X-ray absorption near edge structure) is an extremely sensitive technique for probing both the oxidation state and coordination chemistry of an element in the bulk of materials. Shifts in energy of XAS edge and pre-edge features occur as a result of shielding effects, which result from changes to cation oxidation states [178]. XANES features generally shift to higher photon energy upon an increase in their oxidation number; more energy is required to excite core electrons via XAS in cations with higher oxidation states. Other shifts and screening effects can occur in covalent compounds due to bonds with neighbouring atoms influencing the local electron density.

K-edge XAS for metals that are not $3d^{10}$ configuration show pre-edge features corresponding to (typically 'dipole forbidden') electric quadrupole transitions ($\Delta l = \pm 2$) for $1s \rightarrow 3d$ [161]. Features like this are highly significant in analysing the composition of iron oxides or compounds, using XANES [179, 180]. The Fe K-edge spectral shape is more sensitive to the geometric details of the absorbing site (symmetry, distances and bond angles) than the L-edge absorption. Chemical shifts associated with the change in Fe ion oxidation state and site geometry between Fe^{3+} and Fe^{2+} species is in the photon energy range of 3–4 eV, which is easily detected experimentally. Moreover, while the L-edge absorption probes only the surface of the films 5-6nm (in TEY detection mode), K-edge absorption of hard x-rays probes the bulk of the film volume. This was considered key for allowing the relative amounts of the different oxide phases, if present, in YIG and a-YIG to be determined. Characterising oxidation states in unknown samples relies on comparison to XANES of either control samples or samples of an expected coordination.

3.4.3.2 EXAFS

The lack of an extensive regular structure in amorphous materials limits the amount of unambiguous structural information which can be gained from conventional structural techniques such as x-ray or neutron diffraction. EXAFS (Extended X-ray Absorption Fine Structure) has become a well established technique to measure amorphous materials, giving information on short range order, structural disorder and coordination combined with chemical element specificity. EXAFS refers to oscillations in the XAS spectrum above the absorption edge energy. These oscillations result from constructive and destructive interference between outgoing photoelectron waves (from the absorbing atom) and waves backscattered from neighbouring atoms. This is shown in Figure 3.23.

The EXAFS signal in energy space, χ(E), is extracted from a measured XAS spectrum as:

$$\chi(E) = \frac{\mu(E) - \mu_0(E)}{\Delta\mu_0(E)} \tag{3.29}$$

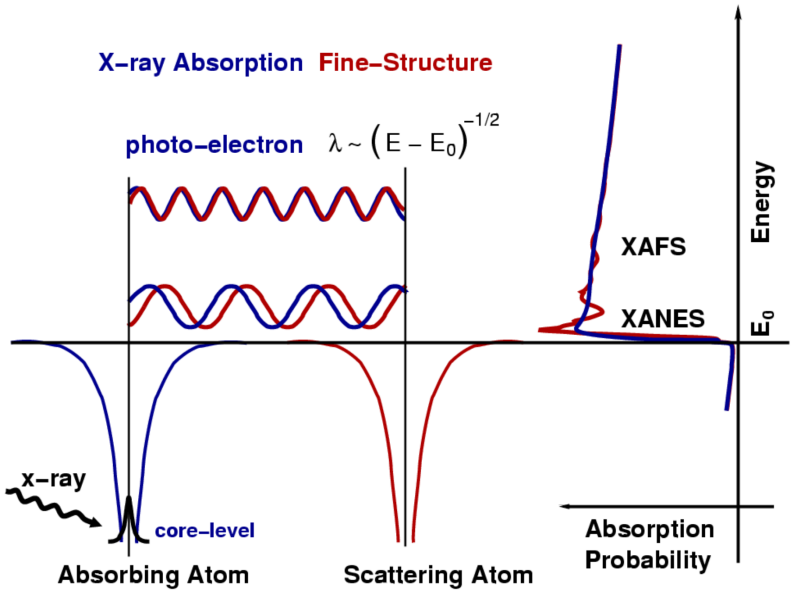

Figure 3.23: Photoelectrons emitted from x-ray absorbing atoms are backscattered by neighbouring atoms, modulating the electron wavefunction at the absorbing atom by constructive (or destructive) interference. This modulates the measured x-ray absorption coefficient $\mu(E)$, producing oscillatory EXAFS. Adapted from [181].

where μ(E) is the measured x-ray absorption coefficient, μ_0 is a smooth background function (cubic spline) reflecting absorption by an isolated atom, and $\Delta\mu_0$ is the absorption edge jump as illustrated in Figure 3.24(a) [181]. χ(E) is usually converted to χ(k) - Figure 3.24(b)(i) - based on electron wavenumber, defined as:

$$k = \sqrt{\frac{2m\left(E - E_0\right)}{\hbar^2}} \tag{3.30}$$

where E_0 is the absorption edge energy, m is the electron mass and $\hbar$ the reduced Planck constant. The full EXAFS equation for χ(k) is given by:

$$\chi(k) = \sum_j \frac{N_j f_j(k) e^{-2k^2\sigma_j^2} e^{-2R_j/\lambda(k)}}{kR_j^2} \sin\left[2kR_j + \delta_j(k)\right] \tag{3.31}$$

For an atom type j: $f(k)$ and $\delta(k)$ are the amplitude reduction function and EXAFS amplitude function, respectively, of the atoms neighbouring the excited atom. N is the number of neighbouring atoms, R is the distance to the neighbouring atom, σ^2 is the mean-square deviation (i.e. disorder in) the neighbour distance [182, 181], and $\lambda(k)$ is the photo-electron mean-free path. The EXAFS equation is essentially a product of the amplitude of the electron waves ($\frac{N_j f_j(k) e^{-2k^2\sigma_j^2} e^{-2R_j/\lambda(k)}}{kR_j^2}$) and the phase of the electron waves ($\sin\left[2kR_j + \delta_j(k)\right]$), summed

over an atom type. The EXAFS signal amplitude decays very quickly in k, due to the $e^{-2k^2\sigma_j^2}$ factor. Thus χ(k) is often multiplied by either k, k^2 or k^3 in order to emphasise oscillations at higher k-values, and produce an EXAFS spectrum with a more uniform amplitude in k-space; this is known as k-weighting. An additional factor of $e^{-2R_j/\lambda(k)}$ dampens the EXAFS signal amplitude further, accounting for inelastic scattering of the photo-electron and finite core-hole lifetimes [181].

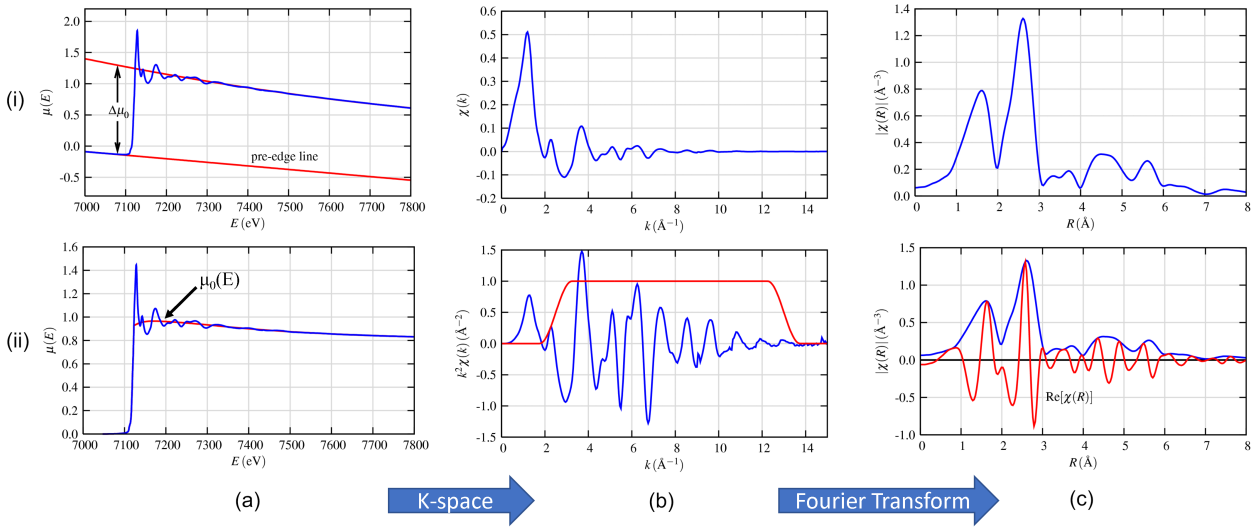

Figure 3.24: (a) Exemplar XAS signal in energy space (i) prior to subtraction/normalisation, and (ii) following normalisation to the absorption edge jump. (b) Extracted EXAFS signal (i) χ(k) and (ii) weighted by k^2. A chosen window for Fourier transform into R-space is shown in red. (c) (i) Magnitude of R-space plot obtained from Fourier transforming k^2-weighted EXAFS signal; (ii) The Fourier transform is complex, with magnitude(R) and Re(R) being shown. Adapted from [181].

A Fourier transform of the k-space EXAFS converts the data into R-space, allowing different coordination and bond lengths around an absorbing atom to be identified in a material. The choice of k-range and k-weight over which the Fourier transform is performed is the most subjective part of the analysis; in general, a range with fairly uniform k-amplitude (for a given k-weight) and free of obvious glitches/noise is preferred. K-weighting of k^2 or k^3 are also favoured to infer coordination peaks at high-R. Systematic scattering phase shift corrections on the order of 0.5Å may also be required for atomic coordination lengths values in R-space to be completely accurate. These are inferred by EXAFS simulation and fitting to a known model crystal structure [182]. However, phase correction is considered less important for measurements of relative changes between samples. Furthermore, EXAFS simulation is a complex procedure and very difficult for materials with complex unit cell stoichiometry such as YIG.

3.4.3.3 Experimental Setup

Hard x-ray absorption measurements in this thesis were performed on the B18 core XAS beamline at the Diamond Light Source synchrotron facility. As discussed in Section 3.4.2.3, the DLS storage ring maintains a 3GeV electron beam from which synchrotron radiation is produced with insertion devices. The B18 beamline uses a bending magnet as the x-ray beam source, unlike undulators used on beamline I10. The bending magnet provides a uniform dipole magnetic field which forces the electrons to travel in a circular arc (the radius of which is determined by the field strength). This produces a wide horizontal 'fan' of synchrotron radiation, but with a narrow vertical divergence of $\pm 1/\gamma$ radians [183]. The photon energy produced is a broad spectrum ranging between 2keV and 35keV. X-rays from the bending magnet (called the white beam) are incident on a collimating mirror, before being reflected onto one of two optical branches, selected by a pair of secondary slits. Beamline optics from here are summarised in Figure 3.25. The two branches enter a double crystal monochromator with two crystals - Si(111) or Si(311) - which can be translated in vacuum to the desired optical branch. The choice of Si monochromator dictates the available photon energy range. The choice of optical branch is based on having either a Cr or Pt coated toroidal mirror focus the monochromated x-ray beam; Cr coating provides better reflectivity and higher flux at lower energies, while Pt coating is preferable at higher energies. For XAS about the Fe K-edge, the Pt-mirror branch was chosen with a Si(111) monochromator, providing a photon energy range of 4-11 keV. The toroidal focusing mirror (and a high harmonic rejecting mirror) finally focuses the beam onto the sample with a spot size of 200μm x 250μm [184, 185].

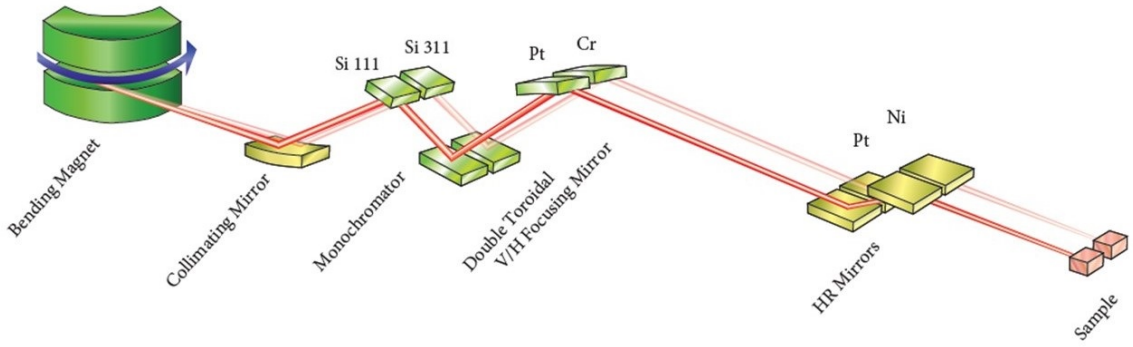

Figure 3.25: Diagram of the B18 beamline optics with a bending magnet as the x-ray source. The optical branch/optics for this work follow the strong red path: Si(111) monochromator and Pt focusing mirror. Adapted from [185].

In the XANES/EXAFS setup on B18, the sample was mounted at approximately 45° to the incident x-ray beam, and x-ray fluorescence was measured as the incident x-ray energy was swept from 6.8-7.5keV across the Fe K-edge. Fluorescence data was collected in continuous scan mode using an emission spectrometer in dispersive Von Hamos geometry and a Medipix quad chip detector. The Von Hamos geometry was chosen in order to separate the fluorescence

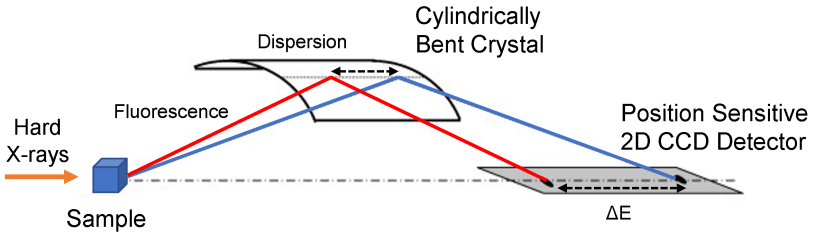

Figure 3.26: Schematic diagram for the dispersive Von Hamos geometry used to measure fluorescence.

line of Kα from the elastic substrate reflections; the principle behind this is illustrated in Figure 3.26. The spectrometer was configured to focus the Fe Kα signal (while photons of different energies were defocused) and a region of interest was defined around the focal point to extract the fluorescence counts from the images acquired for each energy point. The use of the spectrometer offered a better energy resolution with respect to a monolithic Ge detector and helped remove the interference from substrate diffraction peaks in the XAS spectrum. 16 separate scans were acquired and averaged for each sample, in order to improve signal-to-noise ratio. Acquired XAS data was then processed using the ATHENA program [182] to evaluate EXAFS and radial distribution functions, as well as analyse XANES in the form of 1s$\rightarrow$3d pre-edge features.

Chapter 4

Recrystallisation of Amorphous YIG Thin Films

In this chapter, a characterisation of both a-YIG and its recrystallisation into magnetic YIG thin films is presented. A TEM study of a-YIG deposited on silicon nitride membranes is presented, followed by both structural and magnetic characterisation of crystalline YIG thin films deposited and recrystallised on GGG(111) and YAG(111) substrates. These results form the basis for a-YIG and YIG sample preparation for experiments discussed in Chapters 5 and 6, and more generally provide a recipe for YIG film growth via a recrystallisation-PLD approach with ex-situ annealing.

4.1 Sample Growth and Annealing

4.1.1 Deposition Conditions for a-YIG

In choosing PLD conditions for amorphous YIG thin films, those from an optimisation PLD study of crystalline YIG-on-YAG thin films performed by Sposito *et al.* (2014) were used as a baseline [186]. Growth conditions used by Hauser *et al.* (2016) - first reporting the recrystallisation-PLD approach - were also compared, where emphasis was placed on a slow deposition in an adequate oxygen partial pressure [11]. Conditions reported from both of these studies, and the final conditions used for our own a-YIG films are detailed in Table 4.1. The main difference between Sposito *et al.*, and this work and Hauser *et al.* was deposition temperature. Room temperature deposition was necessary to produce an amorphous YIG layer with no long-range crystallinity prior to recrystallisation by ex-situ annealing. Compared to [186], our target-substrate distance was also increased to reduce the number of particulates reaching the substrate, attempting to improve film quality [123]. Characterisation of the recrystallised YIG films showed the crystallographic and magnetic quality was high, and suitable for further

Condition	Sposito (2014) Crystalline	Hauser (2016) Amorphous	York (2022) Amorphous
YIG Target	Single Crystal	–	Polycrystalline
Ablation Laser (λ)	KrF (248nm)	KrF (248nm)	Nd:YAG (266nm)
Repetition Frequency (Hz)	20	5	10
Laser Fluence (Jcm^{-2})	∼3.0	∼2.5	∼3.0
Target-Substrate Distance (cm)	6.0	–	8.0
O_2 Partial Pressure (mbar)	$1x10^{-2}$	$2.5x10^{-2}$	$2.5x10^{-3}$
Substrate Temperature	∼1250K (975°C)	∼298K (25°C)	∼298K (25°C)

Table 4.1: PLD growth conditions used by Sposito *et al.* [186] for YIG-on-YAG, and those used by Hauser *et al.* [11] and in this research for amorphous YIG films (to be recrystallised).

experiments.

PLD of a-YIG was performed on 5mm x 5mm x 0.5mm thick single-crystal gadolinium gallium garnet GGG(111), or yttrium aluminum garnet YAG(111) substrates, pre-cut and sourced from MTI Corp. (111)-oriented films were chosen to aid comparison to YIG(111) films in literature. Substrates were precleaned in acetone (sonicated for 5 minutes) and then in IPA (sonicated for 5 minutes). The cleaned substrates were then dried using a nitrogen gun to prevent the formation of residue. Samples were transferred to the PLD load-lock and allowed to pump down for at least an hour. In-situ outgassing of the substrate with the CO_2 laser was performed at approximately 200°C, in-vacuum at a base pressure of $1x10^{-7}$ mbar for 30 minutes to remove any residual moisture. The substrate was then allowed to cool to room temperature for at least an hour before deposition. An amorphous YIG layer was then deposited at room-temperature in a partial oxygen pressure of $2.5x10^{-3}$ mbar, with a constant flow (throttled below 1 sscm). The Nd:YAG ablation laser was operated with a repetition frequency of 10Hz and fluence of approximately 3.0 Jcm^{-2}, equating to an average incident laser power of 0.96W. This pulsed laser power ablated a stoichiometric polycrystalline YIG target. The substrate was steadily rotated during deposition at 6RPM, to promote an even distribution of a-YIG material. The a-YIG thin film was then removed from the chamber for post-deposition annealing.

4.1.2 Ex-Situ Annealing of a-YIG

PLD samples almost always require annealing to improve crystal quality. This involves heating samples either *in*-situ (inside the PLD apparatus) or *ex*-situ in a furnace: either in an open atmosphere (air), or in gas mixtures of O_2 and N_2 [121, 124]. After deposition, the room-temperature a-YIG films were annealed ex-situ in a high temperature tube furnace to recrystallise the YIG. Annealing was performed in an open-air atmosphere for 3 hours at a given temperature. Ex-situ annealing in flowing oxygen would have been preferred. This would have followed Hauser *et al.* (annealing in a 99.9% oxygen atmosphere) and potentially improved the

magnetic oxide stoichiometry, but was not available initially. Consequently, annealing in air was performed for all YIG films produced for this research. For any chosen annealing temperature, a heating and cooling rate of < 4°C/minute was used to avoid excessive thermal strain of the garnet substrate and YIG film [11]. Hauser *et al.* report YIG recrystallisation being optimum between 800-900°C, with differences in FMR considered statistical. This is corroborated by a large number of YIG FMR studies - reviewed in [75] - where YIG annealing both in-situ and ex-situ is typically performed in this temperature range.

4.2 Amorphous YIG - TEM

Prior to recrystallising a-YIG thin-films on GGG(111) and YAG(111), a preliminary characterisation of the amorphous YIG via TEM was performed. An a-YIG thin film approximately 50nm thick was deposited on a 500μm x 500μm TEM window consisting of a 35nm thick silicon nitride (SiN) membrane. The TEM chip itself was only 3mm x 3mm in size, so an alternative sample holder inset for the PLD cartridge was designed to hold it in place. This alternate 3.5mm x 3.5mm inset is shown in Figure 3.2(b). The TEM window, placed membrane-side down (towards the PLD plume) in the 3.5mm x 3.5mm inset, was secured in place with a split 5mm x 5mm piece of silicon placed above the TEM window in the 5.5mm x 5.5mm inset. The supporting silicon was deliberately split into two pieces to allow molecules in the PLD system to freely access both the front and back sides of the membrane: preventing potential rupture from a pressure build-up while pumping down or deposition. Deposition was then performed using the same conditions outlined in Section 4.1.1, without in-situ outgassing to prevent membrane damage. An optical microscope photograph of the deposited a-YIG/SiN is shown in Figure 4.1.

The a-YIG/SiN was examined with the aberration-corrected JEOL 2200 FS microscope at the JEOL Nanocentre at York. Imaging was performed by Dr Leonardo Lari, operating at an electron energy of 200keV. Figures 4.2(a) and 4.2(c) shows BF images of the as-deposited a-YIG. BF imaging confirms that the a-YIG is amorphous, showing no clear structural or nanocrystallite features, and indicating a lack of long range structural order. The inset diffraction pattern in Figure 4.2(a) measured over the a-YIG reflects an amorphous structure, with only diffuse single rings being visible. This agrees well with a similar in-situ TEM study performed by Gage *et al.* [120] into a-YIG sputtered onto SiO_2 TEM windows. The JEOL 2200 microscope allowed for in-situ annealing to be performed with current heating adjacent to the TEM membrane. The in-situ temperature of the a-YIG film was increased to 700°C while imaging, intending to observe a phase transition from a-YIG to YIG recrystallising on the SiN membrane. Temperature of the a-YIG/SiN was ramped at a rate of approximately 50°C every 10 minutes. Radial integration of diffraction patterns acquired at different temperatures during the in-situ annealing are shown in Figure 4.2(d). Between room temperature and 600°C,

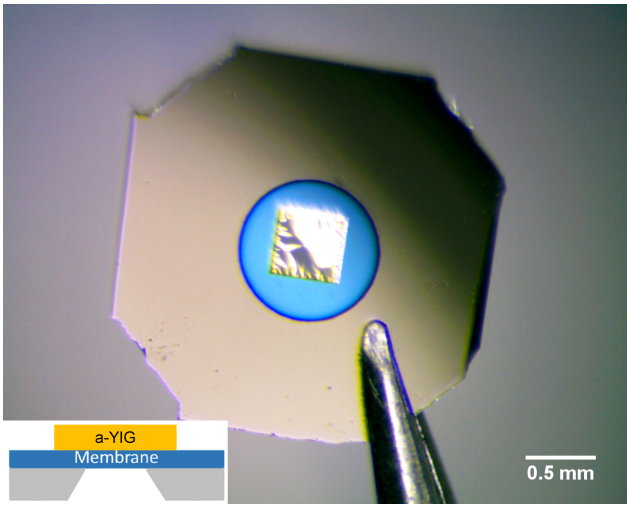

Figure 4.1: Optical microscope photograph of SiN TEM window with a-YIG locally deposited around the TEM window: appearing blue above the silicon chip, and yellow above the window. Schematic of TEM window geometry given as inset.

no significant changes to the a-YIG/SiN diffraction pattern were observed in TEM, remaining diffuse and single-ringed following Figure 4.2(a). At 650°C, a sudden transition is observed and a recrystallised YIG phase emerges on the SiN membrane. BF imaging for 650°C in Figure 4.2(b) shows a clear change in crystal microstructure compared to the as-deposited state. Electron diffraction patterns (inset) are very notably polycrystalline, showing clear sharp rings (or alternatively diffraction peaks with radial integration). Candidate (hkl) planes from YIG corresponding to the d^{-1} of each peak are annotated in Figure 4.2(d), with plane spacing in Å. These crystalline planes corresponded to an average lattice constant of (12.39 ± 0.03)Å, in agreement with bulk YIG within error. Similar diffraction peaks are observed at 700°C, though slightly sharper. Only the (024), (008) and (248) peaks agree with YIG/SiO_2 films from Gage *et al.*, ex-situ annealed at 800°C in air for 2 hours [120]. However, being annealed in air on a different membrane material for longer and at a higher temperature, direct comparisons cannot be made to this in-situ annealing study. The clear onset temperature of YIG recrystallisation at 650°C mirrors some PLD YIG films in the literature grown at similar substrate temperatures [187, 75].

Ex-situ annealing of a-YIG/SiN thin films in air at 800°C for 2 hours as described in Section 4.1.2 was also attempted, following [120]. However, this was challenging experimentally, with the SiN membranes routinely being ruptured by either the ex-situ annealing process or in transport to the TEM. Nevertheless, useful insights were gained from TEM imaging of ruptured membranes still within the TEM window region. Figure 4.3(a) shows BF imaging of a crystallisation front between a region of crystalline YIG and a-YIG. Crystalline YIG/SiN regions showed diffraction contrast features such as bend contours and grain boundaries, which

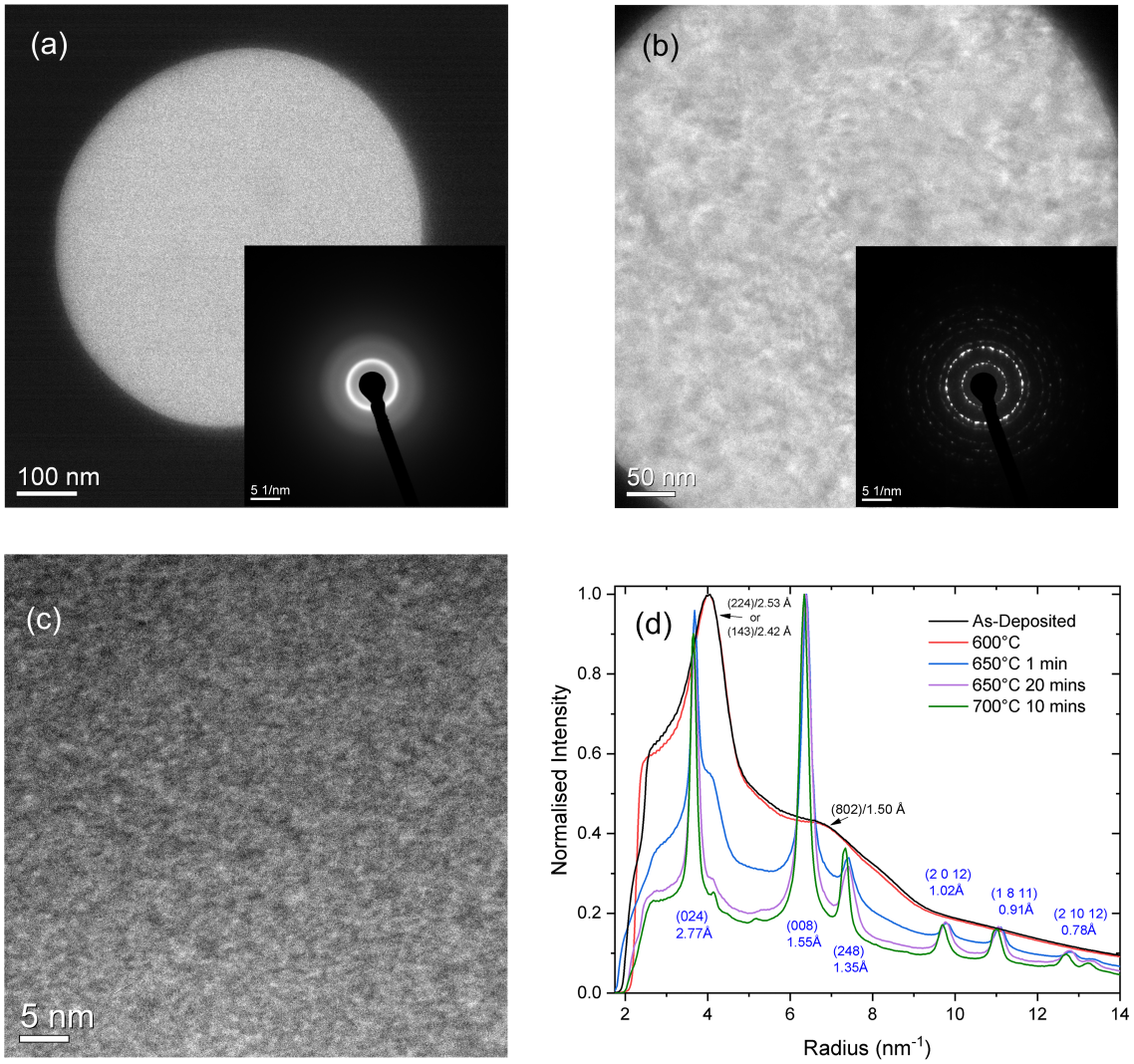

Figure 4.2: (a) SAED BF imaging of as-deposited a-YIG/SiN with amorphous diffraction pattern inset. (b) SAED BF imaging of recrystallised YIG/SiN, in-situ annealed at 650°C with polycrystalline diffraction pattern inset. (c) High magnification BF imaging of a-YIG/SiN. (d) Radially integrated electron diffraction data for as-deposited a-YIG/SiN and in-situ annealed YIG/SiN. Annotations indicate YIG (hkl) planes corresponding to observed d^{-1} for a-YIG (black text) and YIG (blue text).

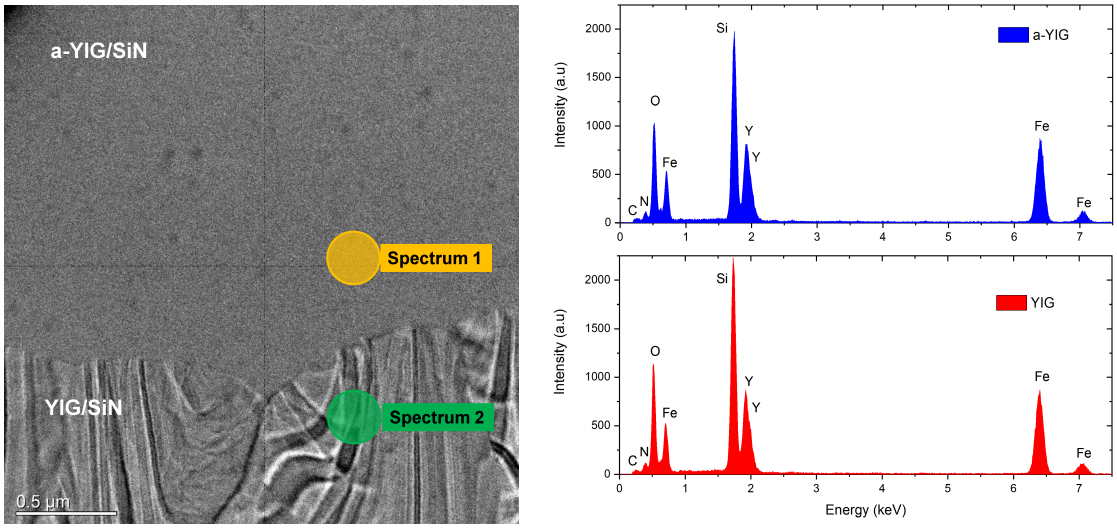

(a) (b)

Figure 4.3: (a) BF imaging of ruptured YIG/SiN membrane after ex-situ annealing at 800°C, showing a crystallisation front. Regions from which EDX spectra were acquired are marked. (b) EDX spectra acquired for a-YIG/SiN (spectrum 1) and YIG/SiN (spectrum 2) respectively.

warrant a future investigation on un-ruptured membranes. EDX measurements were performed in the crystalline and amorphous YIG regions and compared to assess chemical composition between the two. Shown in Figure 4.3(b), EDX verifies that chemical composition is the same in both a-YIG and YIG. Proportions of Y, Fe and O present in both phases are near identical in both intensity and the photon energies observed. All areas measured indicated the presence of C in the system, a potential residual contaminant from other samples measured with this instrument.

4.3 YIG/GGG(111) Thin Films

With confirmation from TEM that deposited a-YIG possesses no long range structural order, multiple thin films of YIG have been grown following a recrystallisation-PLD approach reported for producing YIG films of extremely high structural and magnetic quality [11, 12]. Recrystallisation of YIG has been performed on the highly lattice matched garnet substrate, GGG, with PLD of a-YIG thin films following Section 4.1.1. Ex-situ annealing of YIG/GGG(111) films was performed at 850°C in air for 3 hours. Figure 4.4 shows a visual comparison of an as-deposited a-YIG/GGG film, and a YIG/GGG film after ex-situ annealing. An obvious colour change from orange-red to green-yellow is observed with recrystallisation from a-YIG to YIG, reflecting a change in crystal structure and electronic configuration. This is noted for YIG films in the literature [186, 188, 189] and likely attributed to the electronic band gap (where E_g of

YIG = 2.85eV, or 435nm) [113].

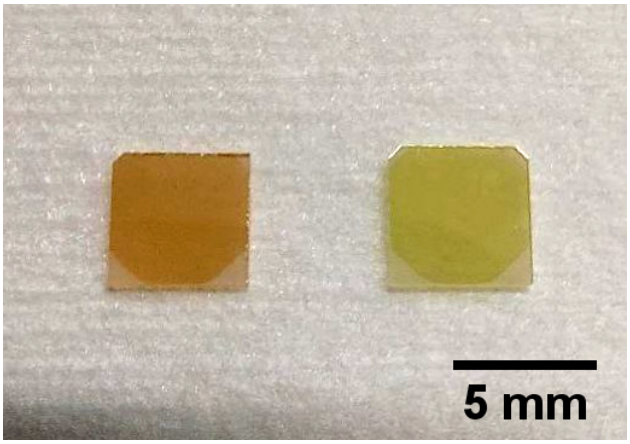

Figure 4.4: Photograph comparing (left) an as-deposited a-YIG/GGG thin film and (right) an identically prepared YIG/GGG thin film, following ex-situ annealing in air at 850°C for 3 hours.

4.3.1 Structural Characterisation

4.3.1.1 X-Ray Diffraction and Reflectivity

X-ray diffraction (XRD) was performed with a 2θ-ω scan around the (444) reflection both before and after ex-situ annealing. This was to confirm the as-deposited a-YIG was amorphous, and also confirm the epitaxial crystallisation of the YIG on the GGG substrate by annealing. 2θ-ω measurements shown in Figure 4.5 confirm both of these facts. XRD for a-YIG/GGG thin films shows only GGG substrate reflections, with no other features visible. Recrystallisation of YIG(111) on GGG(111) is shown to be highly epitaxial. As bulk materials, the lattice mismatch between YIG and GGG is minimal ($\Delta a = 0.06\%$). The corresponding overlap expected between the YIG and GGG Bragg reflections is evidenced by presence of Pendellösung oscillations in Figure 4.5 about the GGG(444) reflection in $2\theta - \omega$. The overlap is so significant that the YIG and GGG peaks cannot be individually separated. The out-of-plane spacing between YIG(444) planes, d_{444}, for YIG/GGG can only be estimated to be within $\pm 0.25\%$ of bulk YIG (1.786Å), by comparing to the largest Pendellösung fringes. The absence of a resolvable YIG peak prevents reliable measurement of a rocking curve to assess (444) plane parallelism in the YIG.

Pole figures measurements of YIG(444) were attempted by locating $2\theta - \omega$ on the largest Pendellösung fringe $(51.19 \pm 0.02)^\circ$, to avoid simply measuring the pole figure of the GGG(444) substrate peak. The YIG(444) pole figure shown in Figure 4.6 illustrates a clear three-fold crystal symmetry about (111). This, with the absence of other reflections, indicates a highly crystalline texture and matches the expected Ia3d cubic space group for GGG (and bulk YIG):

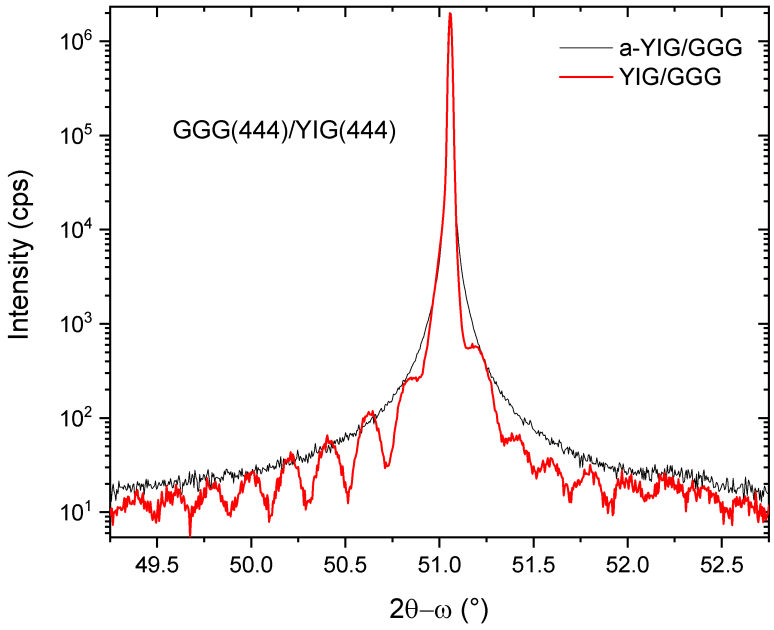

Figure 4.5: $2\theta/\omega$ XRD measurements for an a-YIG/GGG(111) thin film (black line) and then YIG/GGG(111) film following ex-situ annealing (red line).

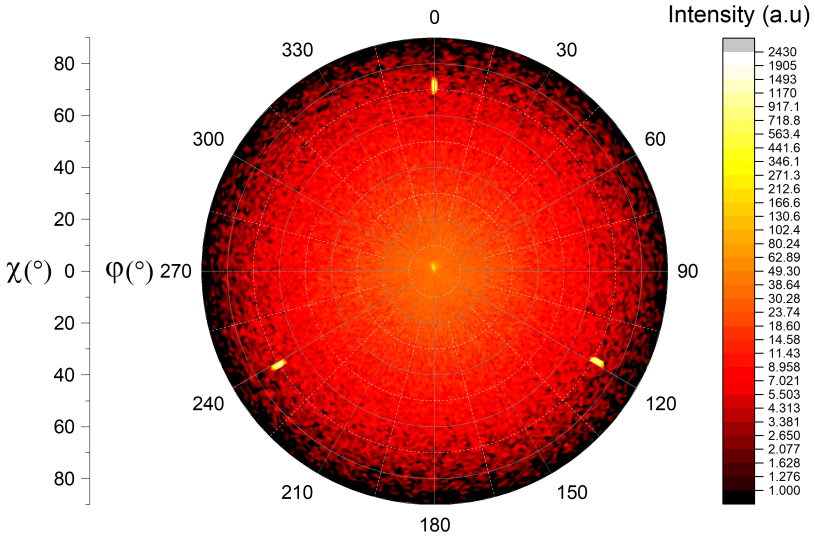

Figure 4.6: XRD pole figure taken from a Pendellösung oscillation 2θ - 51.19° - adjacent to the GGG(444) diffraction peak for the YIG/GGG(111) film.

further emphasising the high epitaxy of the YIG/GGG recrystallisation. A reciprocal space map (RSM) was measured about the off-axis (426) reflection to evaluate potential in-plane stress between the YIG film and GGG substrate. The RSM in Figure 4.7 shows that the only the GGG substrate reflection and Pendellösung oscillations are visible about the (426) reflection, with no YIG film peak being resolvable. Without an obvious YIG film peak to deviate from the connector line (relaxation line) between the substrate peak and Q=(0,0), strain is deemed minimal in the YIG film.

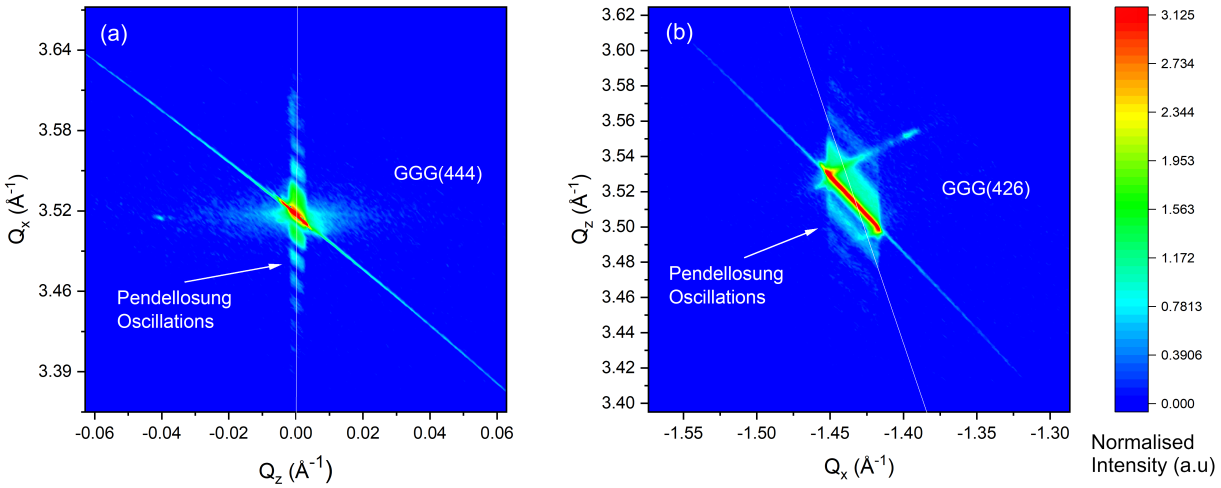

Figure 4.7: Reciprocal space maps taken about the (a) (444) and (b) (426) reflections respectively for YIG/GGG(111). Reciprocal space coordinates (Q_x,Q_z) are used. A relaxation line intersecting the substrate peak and Q = (0,0) is shown (white).

XRR measurements were performed to determine the thickness and average roughness for the YIG layer. Measurements were performed scanning 2θ-ω below 6°, and acquired reflectivity fringes were fitted to using the GlobalFit and GenX software packages. Measured and fitted Kiessig reflectivity fringes are shown in Figure 4.8, with accompanying scattering length density (SLD) simulation from extracted fitting parameters as an inset. For the fitting procedure, fixed densities of 7.08 gcm^{-3} and and 5.17 gcm^{-3} were used for the GGG and YIG respectively. From Figure 4.8, an average YIG thickness of (44.3 ± 0.2)nm was inferred with an RMS roughness of (0.6 ± 0.1)nm. The GGG substrate roughness came to a similar value at (0.7 ± 0.1)nm. Roughness of this scale is good, being approximately half of the notional unit cell length of crystalline YIG (1.23nm) and indicating the YIG layer is relatively smooth, averaging over the entire sample area.

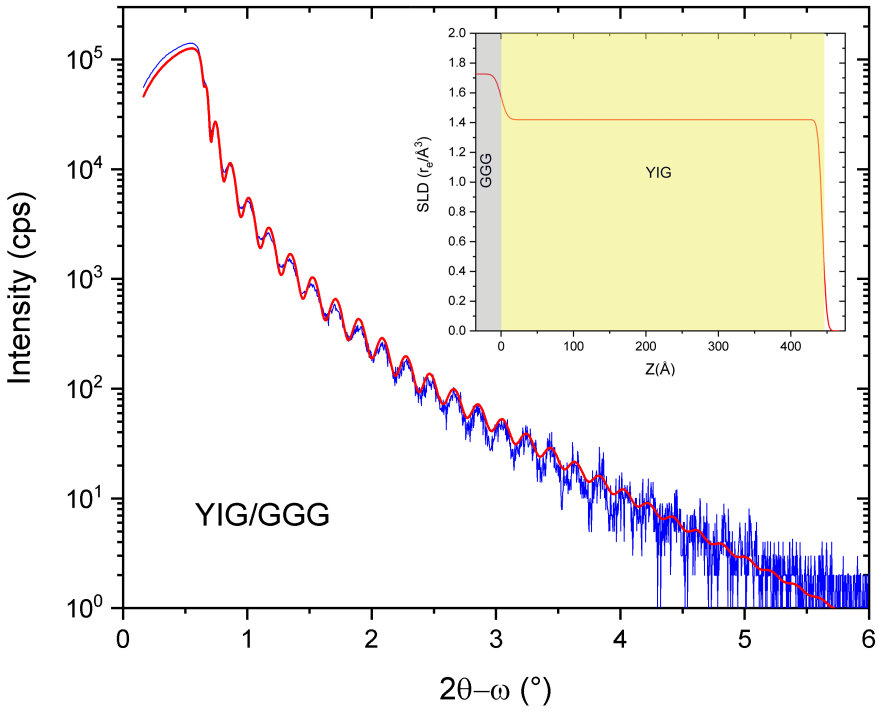

Figure 4.8: XRR measurement (blue) with fitted curve (red) for YIG/GGG(111) thin film. Simulated scattering length density (SLD) against sample depth (Z) from XRR fitting is inset.

4.3.1.2 Cross-sectional TEM

The YIG/GGG film was prepared for HAADF-STEM imaging via focused ion beam milling, to assess the epitaxy of the recrystallised YIG and the interface between the YIG/GGG. Cross-sectional TEM images shown in Figures 4.9 and 4.10 confirm a highly epitaxial recrystallisation of the YIG on the GGG substrate. From Figure 4.9, diffraction patterns taken from the YIG and GGG agree well with simulated electron diffraction patterns for a zone axis of $[\bar{1}10]$. No obvious structural mixing or defects between the YIG/GGG layers are observed that could potentially indicate magnetic dead layers (as reported by films from Mitra *et al.* [116]). The YIG/GGG interface is seen to be smooth with interfacial roughness below 1nm, and minimal lattice mismatch between the YIG and GGG; this is also apparent in TEM images taken of the $[11\bar{2}]$ zone axis in Figure 4.10. This agrees well with roughness inferred from XRR measurements and fitting. A YIG film thickness of 44nm was observed, in agreement with thickness obtained from XRR.

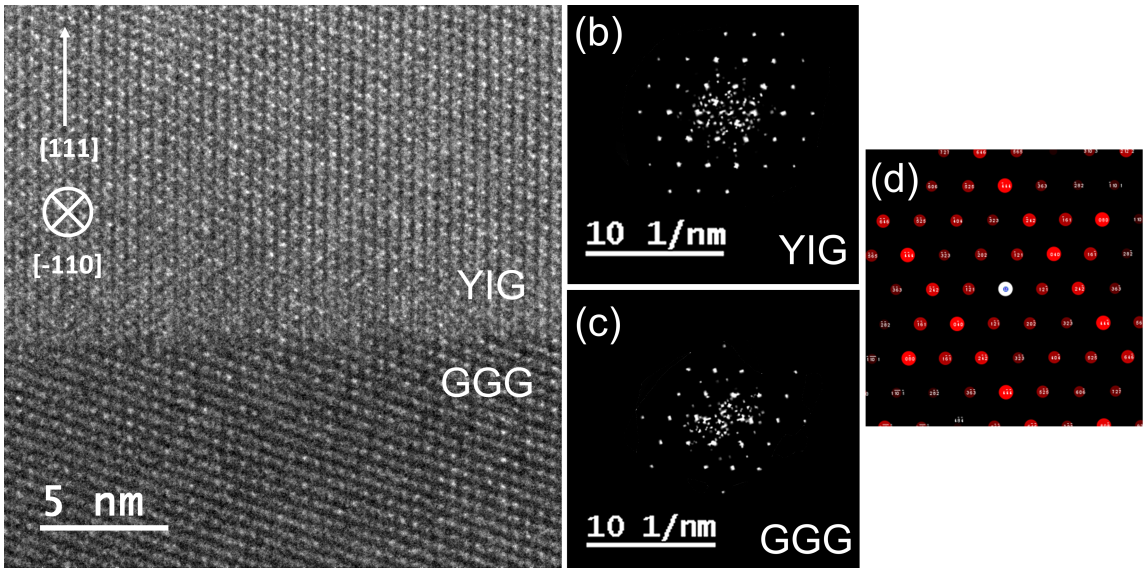

Figure 4.9: (a) Cross-sectional TEM image of the YIG/GGG interface for the recrystallised YIG film, [$\bar{1}$10] zone axis. (b) Electron diffraction pattern acquired from the YIG layer and (c) the GGG layer. (d) Diffraction pattern for YIG [$\bar{1}$10] simulated using the JEMS (Java Electron Microscopy Simulation) software [190], matching observed YIG diffraction.

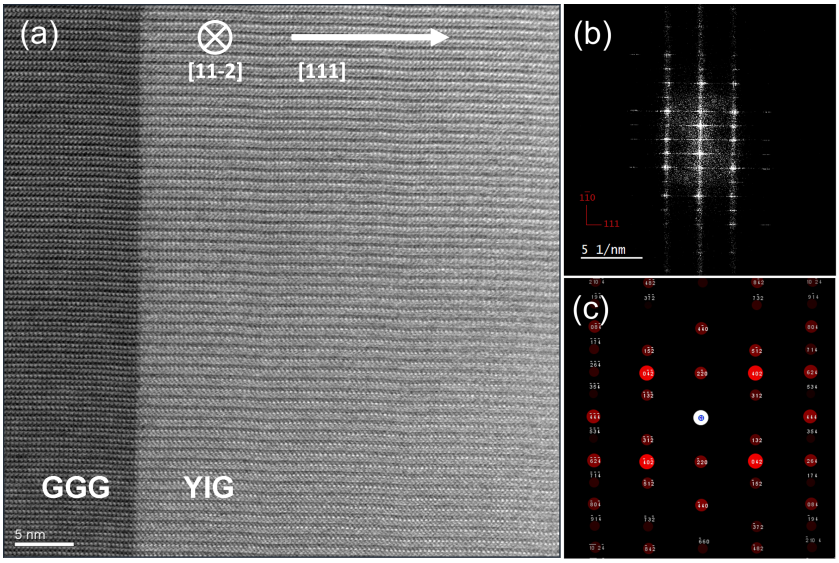

Figure 4.10: (a) Cross-sectional TEM image of the YIG/GGG interface for the recrystallised YIG film, [11$\bar{2}$] zone axis. (b) Electron diffraction pattern acquired from the YIG layer. (c) Diffraction pattern for YIG [11$\bar{2}$] simulated using the JEMS (Java Electron Microscopy Simulation) software [190], matching observed YIG diffraction.

4.3.2 Magnetic Characterisation

4.3.2.1 Vibrating Sample Magnetometry

Vibrating sample magnetometry was performed on the YIG/GGG to assess the hysteresis behaviour, magnetisation and coercivity of the YIG. In-plane VSM measurements were performed using the LakeShore 8600 VSM at room temperature. A magnetic bias field between ±100 Oe was sufficient to saturate the magnetically soft YIG and show clear hystersis. Measured in-plane M(H) loops - following removal of the paramagnetic GGG background - are shown in Figure 4.11. Measurement of the a-YIG/GGG magnetism before recrystallisation was not possible, with the magnetic signal (if any) being completely washed out by the paramagnetic GGG. YIG film volume was obtained using thickness extracted from XRR, and multiplying by the sample area. The sample area was measured using a travelling optical microscope. Using this calculated volume, raw magnetic moment (emu) was converted into magnetisation (emu/cc) in the plotted M(H) loops.

Room temperature M(H) shows a very sharp in-plane magnetic reversal occurring over 0.5Oe, and with coercivity below (0.25 ± 0.05) Oe. This magnetic reversal and coercivity is more easily observed in the inset of Figure 4.11: a higher resolution M(H) performed with 0.01Oe field step. A saturation magnetisation (M_S) is estimated to be approximately (126 ± 5) emu/cc from estimated YIG film volume. This magnetisation is below the expected value for bulk-like YIG films (140 emu/cc), at approximately 90%. However, reduced M_S is reported for YIG/GGG films produced by Hauser *et al.* following their own recrystallisation PLD approach, with M_S between 115-123 emu/cc (82-88%) being typical [11]. This observation is consistent with our own YIG/GGG within error.

Magnetism of YIG/GGG has also been measured using the VSM-SQUID at the Diamond Light Source. A comparison in M(H) data for the YIG/GGG film between the two instruments is shown in Figure 4.12(a). Good agreement in moment/magnetisation between the two data sets is observed. However, the magnetic reversal is notably offset in the VSM-SQUID response, occurring towards -25Oe instead of 0Oe. This was a direct result of the VSM-SQUID magnet having a remanent field on the order of 50Oe, producing significant offsets in H_C in magnetically soft materials like YIG. Thus, H_C measured from VSM-SQUID must be taken as an average (of positive and negative H_C values) and even then can only be an approximation. Continuous M(T) measurement of YIG/GGG was not possible due to the paramagnetic GGG contribution dominating the M(T) response. This is shown in Figure 4.12(b). Instead, several M(H) loops were measured at different sample temperatures between 10-300K. Following removal of the paramagnetic background, values of M_S and H_C were extracted from these loops and plotted as a function of temperature: shown in Figure 4.13. M_S follows the expected ferrimagnetic response. The M_S temperature response does not reflect YIG films with significant Gd^{3+} ion intermixing at the YIG/GGG interface [116], where a decrease in M_S would be observed at

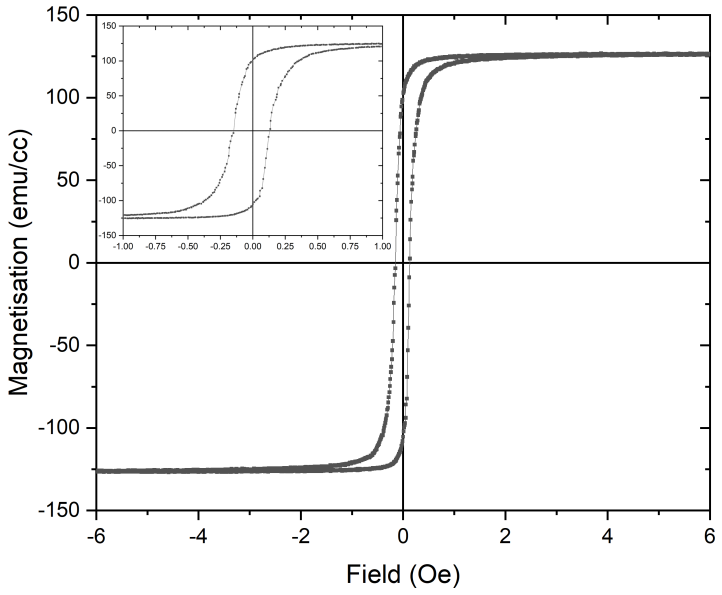

Figure 4.11: In-plane M(H) hysteresis for 44nm thick YIG/GGG(111) thin film recorded from 8600VSM at T=300K. In-plane field swept between ±100 Oe.

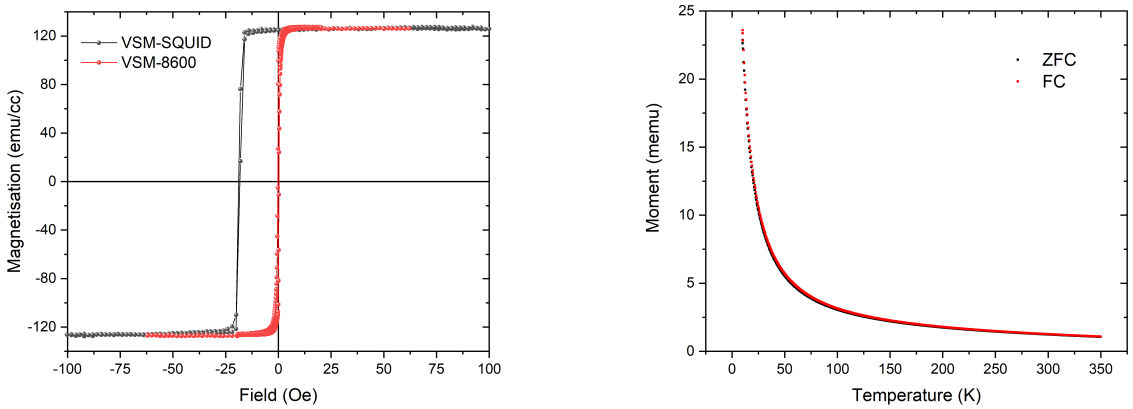

(a) (b)

Figure 4.12: (a) A comparison in M(H) for YIG/GGG(111) taken at T=300K from both 8600VSM and VSM-SQUID. (b) Continuous M(T) response measured from YIG/GGG by the VSM-SQUID: measuring field of 100Oe.

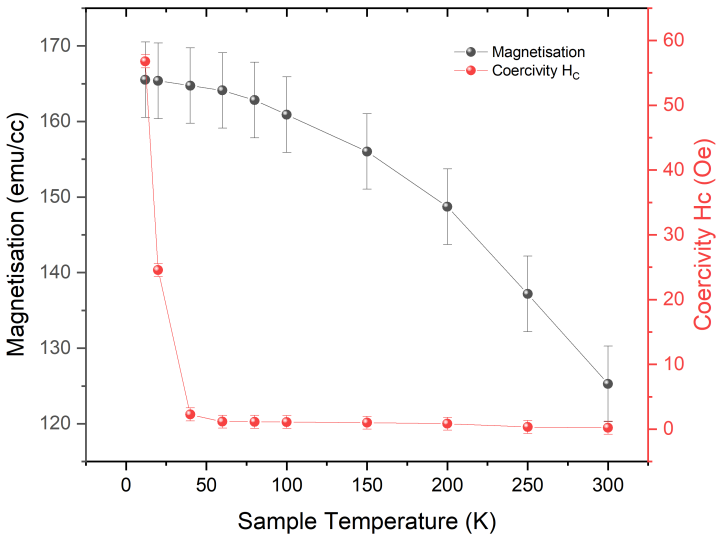

Figure 4.13: M_S and average H_C extracted from M(H) loops measured using the VSM-SQUID, as a function of sample temperature.

lower temperatures due to a compensation point. An increase in H_C from less than 1Oe to (58 ± 2)Oe is observed approaching 10K. Notably, H_C remains similarly small (near 1Oe) between 50-300K. Similar temperature dependence of coercivity is reported in YIG/GGG films by Mitra *et al.* [116], and rare-earth garnet films on GGG from Vertesy *et al.* (1995) [191]. Analysis by these authors shows that coercivity in garnets follows a piece-wise exponential dependence with temperature. Shown in Figure 4.14, a semi-logarithmic plot of $\ln(H_C)$ versus temperature data shows linear correlations, with different slopes observed in different temperature ranges. Each linear part is fitted to an exponential function: $H_c(T) = H_i \exp(-T/T_i)$, where H_i and T_i are values obtained from the i-th temperature range. From Figure 4.14, between 10-50K, H_1 = (200 ± 16)Oe and T_1 = (9.5 ± 0.5)K, and between 50-300K, H_2 = (1.7 ± 0.3)Oe and T_2 = (271 ± 6)K. The two exponential regimes are considered a result of two different types of domain wall pinning traps (defects) which dominate at different temperatures [116, 191]. However, no explicit descriptions of these types of defect (or transitions between them with temperature) currently exist in the literature. Extrapolation of the fits in Figure 4.14 shows a breaking point between the two regimes at approximately (48 ± 2)K. This is in broad agreement with breaking points from Mitra *et al.* (49K) [116] and Vertesy *et al.* (57K) [191]: all of which are near the freezing temperature of oxygen at 54.4K [192]. However, it is not possible to state whether the freezing point of oxygen is directly related to the change in domain wall pinning defects in epitaxial garnets, or instead simply coincidental. Oxygen physisorbed to the surface of YIG films in the VSM-SQUID is considered irrelevant to the increasing coercivity, given liquid and solid oxygen are paramagnetic in nature [192].

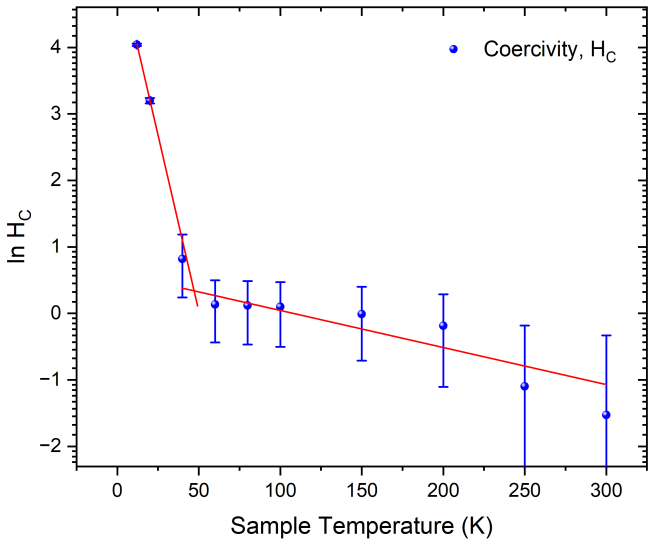

Figure 4.14: Natural logarithm of average H_C from Figure 4.13, as a function of sample temperature. Two exponential fits, between 10-50K and 50-300K respectively, are shown in red.

4.3.2.2 Ferromagnetic Resonance

Ferromagnetic resonance (FMR) spectroscopy was performed to assess information about the magnetisation dynamics and damping in YIG/GGG thin films. Vector network analyzer (VNA) based FMR spectroscopy with an in-plane geometry was used. Placing the YIG/GGG sample face down on the co-planar waveguide, the microwave transmission parameter, S_{21}, was measured over a VNA frequency range of 0.001-15GHz in 1601 equally spaced frequency steps. A magnetic field range of 0-4.5kOe was covered with a field step of 0.5Oe to measure resonance below 15GHz. All VNA-FMR measurements were performed at an RF power of +7dBm. VNA-FMR was also performed at different azimuthal angles to probe in-plane magnetic anisotropy of the YIG. For angular FMR measurements, the azimuthal angle was rotated in steps of 5° over a 180° range between -90° and 90°: centred around the 0° position (along which the $[11\bar{2}]$ direction of the YIG was oriented. However, a larger field step of 2.5Oe was used to allow azimuthal scans to proceed at a reasonable speed (compared to the 0° case). Linescans at a constant frequency of 10GHz were extracted from FMR measured at each angle and fit using an asymmetric Lorentzian function to determine the corresponding resonance field (H_r). $H_r(\phi)$ data measured over the 180° range was then mirrored to produce a full 360°. H_r was plotted as a function of azimuthal angle to measure in-plane anisotropy.

For the as-deposited a-YIG/GGG thin film, no FMR response was observed for either VNA-FMR or modulation FMR techniques: with only background being visible. This was expected, given the corresponding absence of a magnetic response in VSM and lack of structural order

observed from XRD and TEM. In contrast, following ex-situ annealing, the YIG/GGG thin film showed an extremely strong FMR response: sharp and resolvable even at low resonance field. The strong response made VNA-FMR a more suitable technique than use of modulation-FMR. An exemplar FMR field-frequency map is shown in Figure 4.15(a), with a fixed frequency linescan at 10GHz shown in Figure 4.15(b). This data was recorded with the applied field oriented along the $[11\bar{2}]$ axis. A narrow resonance of $\Delta H(10GHz) = (2.0 \pm 0.3)Oe$ was measured at an H_r of $(2827 \pm 1)Oe$. Shown in Figure 4.16(b), the frequency response of linewidth $\Delta H(f)$ is seen to be linear over the full frequency range, with non-linear two-magnon scattering like behaviour absent. This suggests that the magnetic quality of the YIG/GGG is high, with a low defect density throughout the film.

The azimuthal FMR data shown in Figure 4.16(a) showed only very minor variations in $H_r(\phi)$, effectively isotropic in-plane, with no obvious anisotropy or preferred in-plane directions and approaching the limit of our resolution. A maximal change in H_r of $(5 \pm 2)Oe$ was measured, with most H_r values in agreement within error. This agrees well with in-plane anisotropy measured for (111)-oriented YIG thin films in the literature, similarly small for entirely in-plane applied fields [193]. Additional azimuthal FMR measurements were performed at a fixed field of $(2826 \pm 1)Oe$, sweeping resonant frequency from 9.8-10.2GHz in 801 equally spaced points. This was intended to yield a higher sensitivity measurement than field-sweeping could produce. A very weak anisotropy was measured, showing a maximal change in frequency of approximately 0.015GHz. This corresponded to a change in H_r of $(4 \pm 2)Oe$ from the measured Kittel curve. However, like the $H_r(\phi)$ measured by sweeping field, this change in H_r approaches the error of the magnet power supply and is far too small to be considered significant to the Kittel curve.

Given all in-plane directions are effectively easy from the azimuthal data, the Kittel curve along the $[11\bar{2}]$ direction was extracted from Figure 4.15(a). Following [12, 194], the gyromagnetic ratio γ is determined by fitting the in-plane easy axis Kittel equation (Equation 2.48), shown in Figure 4.15(b). This yielded $\gamma = (1.74 \pm 0.01)x10^{11}rad/T$ or $(27.7 \pm 0.2)GHz/T$, and an effective magnetisation M_{eff} of $(140 \pm 5)emu/cc$ or $4\pi M_{eff}$ of $(1759 \pm 63)Oe$. M_{eff} agrees well with various YIG FMR studies [11, 194, 75]. γ is close to the free-electron value of 28.02 GHz/T, and agrees with other FMR studies of recrystallised YIG/GGG [11, 195].

Removing the magnetic anisotropy correction $(-\frac{K_1}{M_S})$ of approximately $(4 \pm 1)emu/cc$ from M_{eff}, a saturation magnetisation M_S for YIG of $(136 \pm 5)emu/cc$ is obtained from FMR. Comparing FMR to the M_S of $(126 \pm 5)emu/cc$ from VSM, a difference of 7% is observed, though accountable within experimental error. It is important to note that M_S from FMR is entirely dependent on the measured Kittel curve and not on estimations of film volume (unlike VSM or SQUID). M_S values from VSM are smaller than those from FMR for all thin films measured throughout this work: suggesting thin film volume calculated from area and XRR thickness is potentially an overestimate. This may be attributed to the accuracy of film area

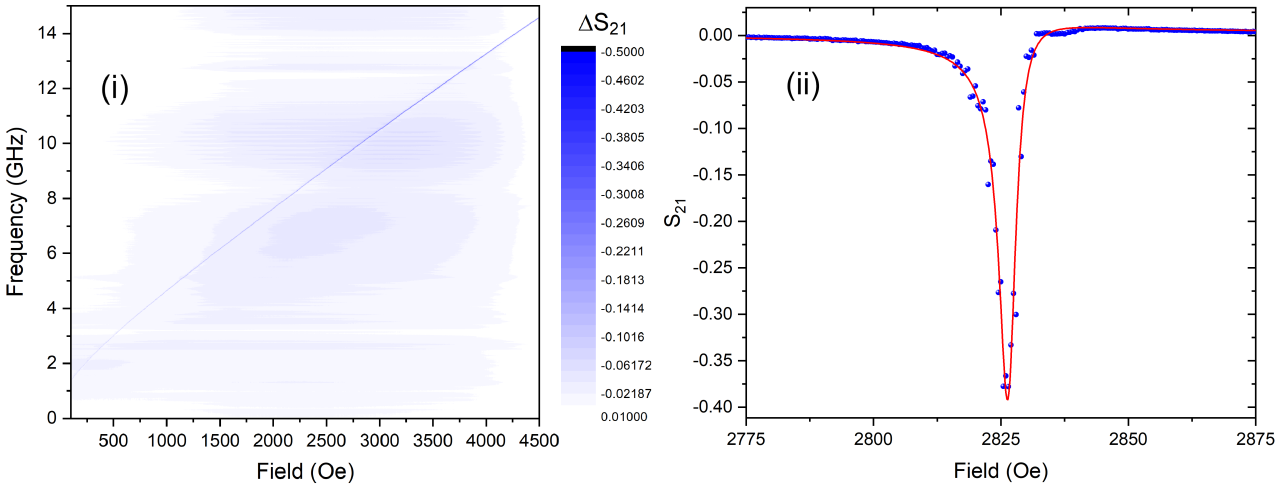

(a)

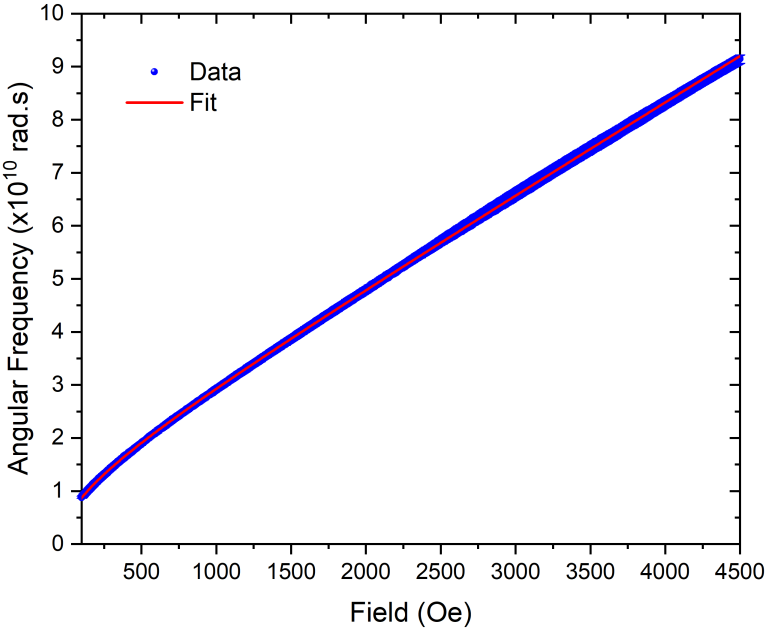

(b)

Figure 4.15: (a) (i) In-plane VNA-FMR frequency-field map for YIG/GGG. (ii) A resonance linescan taken at 10GHz, fit to an asymmetric Lorentzian function (red). The blue shading in (a)(i) is a non-linear background signal in S_{21} from the CPW. The CPW background was removed from individual linescans. (b) Kittel curve extracted from (a)(i) and fit to the in-plane easy-axis Kittel equation.

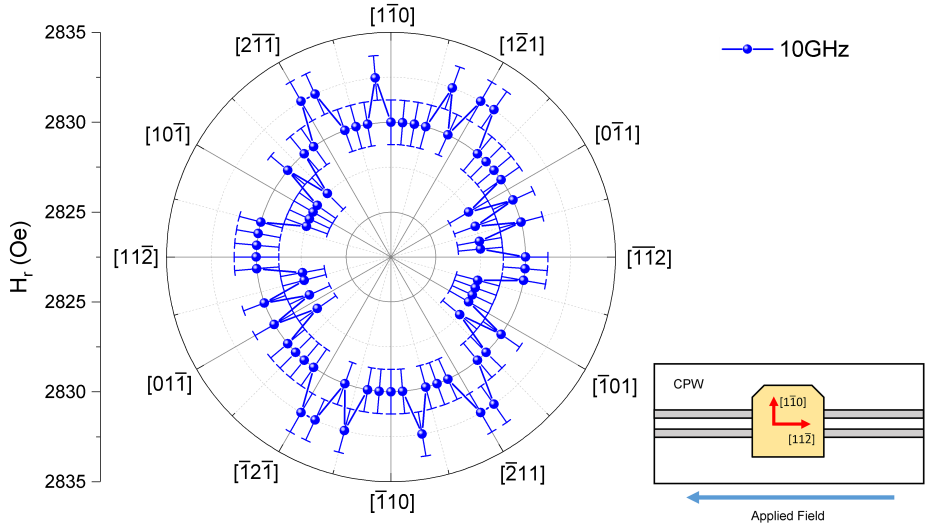

(a)

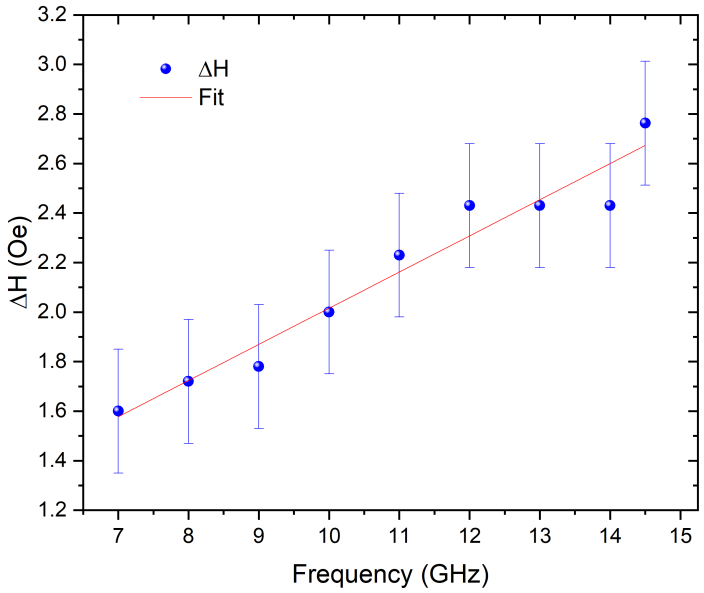

(b)

Figure 4.16: (a) $H_r(\phi)$ data extracted from azimuthal VNA-FMR of YIG/GGG at fixed resonance frequency of 10GHz. Relative orientation of the clipped corners indicating the [11$\bar{0}$] of the sample to the CPW at the '0 degrees' position is shown as an inset. (b) Measured FMR linewidth as a function of RF frequency, $\Delta H(f)$.

measurements, and that film thickness is likely to be thinner towards the film edges (compared to that in the film centre). Therefore, values of M_S of YIG estimated from VSM may be considered as a minimum bound, as minor reductions in film volume are likely to increase VSM M_S values by 3-4 emu/cc. Ideally, measurements of FMR out-of-plane would allow M_S to be obtained directly (without the need for anisotropy corrections) and compared [11]. However, this geometry was not available on our FMR apparatus.

Gilbert damping of the YIG/GGG was calculated from the frequency dependence of FMR linewidth and obtained γ to be (4.2 ± 0.5)x10^{-4}. This is notably larger - approximately seven times - than recrystallisation-PLD YIG/GGG from Hauser *et al.* [11] of a similar thickness. It is possible that ex-situ annealing in an atmosphere of pure oxygen (opposed to air) may contribute to this lower Gilbert damping. However, Gilbert damping of this size is still in keeping with many studies of YIG/GGG fabrication [196] and suitable for spin pumping experiments discussed in Chapter 6. Extrinsic damping in the YIG/GGG is also low on the order of (1.0 ± 0.3) Oe, a further indicator of YIG/GGG approaching literature quality. A range of values for Gilbert damping and extrinsic damping in YIG/GGG thin films reported in recent literature, are given in Table 4.2 for comparison. From Equation 2.33 and the obtained gyromagnetic ratio, a g-factor of (1.98 ± 0.01) is obtained, close to the free-electron value of 2. The obtained g-factor corresponds to an orbital-to-spin moment ratio of μ_L/μ_S = (-0.011 ± 0.005).

Growth Technique	Thickness (nm)	Damping (x10^{-4})	ΔH_0 (Oe)	Reference
PLD (RT)	20	0.7 ± 0.2	1.1 ± 0.1	[11]
	56	0.6 ± 0.2	1.2 ± 0.1	[11]
	44	4.2 ± 0.5	1.0 ± 0.3	(This work)
PLD (800-850°C)	40	3.5 ± 0.3	–	[197]
	23	2.0 ± 0.1	3.5 ± 0.5	[198]
	20	2.3 ± 0.2	2.4 ± 0.2	[199]
	79	2.2 ± 0.1	0.8 ± 0.1	[196]
Sputtering (RT)	22	0.86 ± 0.02	6.8 ± 0.1	[12]
	26	9.9 ± 0.1	2.0 ± 0.1	[194]
	49	2.4 ± 0.3	3.0 ± 0.1	[200]
	96	7 ± 1	1.7 ± 0.1	[201]
LPE	18	3.4 ± 0.2	2.4 ± 0.2	[202]
	100	2.8 ± 0.2	1.6 ± 0.1	[203]
	106	1.2 ± 0.1	0.6 ± 0.1	[157]
	200	2.0 ± 0.1	0.20 ± 0.05	[204]

Table 4.2: Summary of Gilbert and extrinsic damping values for YIG films grown on GGG(111), recently reported in literature using different growth techniques: PLD, sputtering and LPE (Liquid Phase Epitaxy). RT = room temperature deposition, ex-situ annealing between 800-900°C.

4.4 YIG/YAG(111) Thin Films

The recrystallisation of a-YIG on the alternative garnet substrate, YAG, has also been performed. This is both because YAG is a common alternative to GGG in literature [188, 186], and also to assess the effects of a larger lattice mismatch on the YIG recrystallisation (Δa = 3.1%). Like YIG/GGG, a characterisation of YIG/YAG(111) thin films ex-situ annealed at 850°C is presented. Additional characterisation of YIG/YAG thin films annealed at temperatures of 650°C (recrystallised) and below (amorphous) is presented in Chapter 5.

4.4.1 Structural Characterisation

4.4.1.1 X-Ray Diffraction and Reflectivity

YIG/YAG thin films were structurally characterised with XRD about the (444) reflection to confirm epitaxial recrystallisation of the YIG on the YAG substrate. A 2θ-ω scan of the (444) reflection was performed both before and after ex-situ annealing at 850°C. Shown in Figure 4.17, the XRD for a-YIG/YAG only shows YAG substrate peaks, with no other features present. Recrystallisation of YIG(111) on YAG(111) however is shown to be epitaxial, with a clear distinguishable YIG(444) diffraction peak at 2θ = (51.42 ± 0.02)°. From Bragg's law, an out-of-plane YIG(444) plane spacing d_{444} of (1.775 ± 0.001)Å is calculated for YIG/YAG, indicating a compressive strain of -(0.61 ± 0.04)% (compared to bulk cubic YIG d_{444} at 1.786Å). This reflects the larger lattice mismatch between YIG and YAG as bulk materials, with a Δa = 3.1%: significantly larger than between YIG and GGG. This is consistent with YIG/YAG(001) recrystallisation studied by [205], where out-of-plane YIG lattice constants (c) ranging between 12.31-12.33Å are measured for similar film thicknesses (compared to 12.376Å for bulk YIG). A minor peak is observed at 2θ-ω = 54.25°, not correlating to any known YIG or YAG (hkl) reflections, potentially due to fluorescence from the YAG.

Crystallographic quality was further investigated about the YIG(444) peak by performing an ω-scan or rocking curve measurement. Shown in Figure 4.18, a Lorentzian FWHM of (0.30 ± 0.01)° was measured in omega. Generally, a rocking curve FWHM below 0.5° indicates crystal films with a reasonably high degree of orientation quality [134, 133]. However, FWHM for literature YIG/GGG films typically fall below 0.1°; LPE YIG/GGG films approximately 200nm thick show rocking curve FWHM as narrow as 0.018°[196]. This suggests that despite relatively high orientation quality, curvature of atomic planes of YIG/YAG induced by strain is a limiting factor to recrystallised film quality and plane parallelism overall. Pendellösung fringes were also notably absent from the YIG(444) reflection. This likely indicates that the YIG/YAG crystal quality is inferior to that of YIG/GGG due to strain. The broadening of the YIG(444) peak in ω compared to literature YIG/GGG suggests that strain in the YIG/YAG film is inhomogeneous: with different planes being strained by different amounts. Inhomogeneous

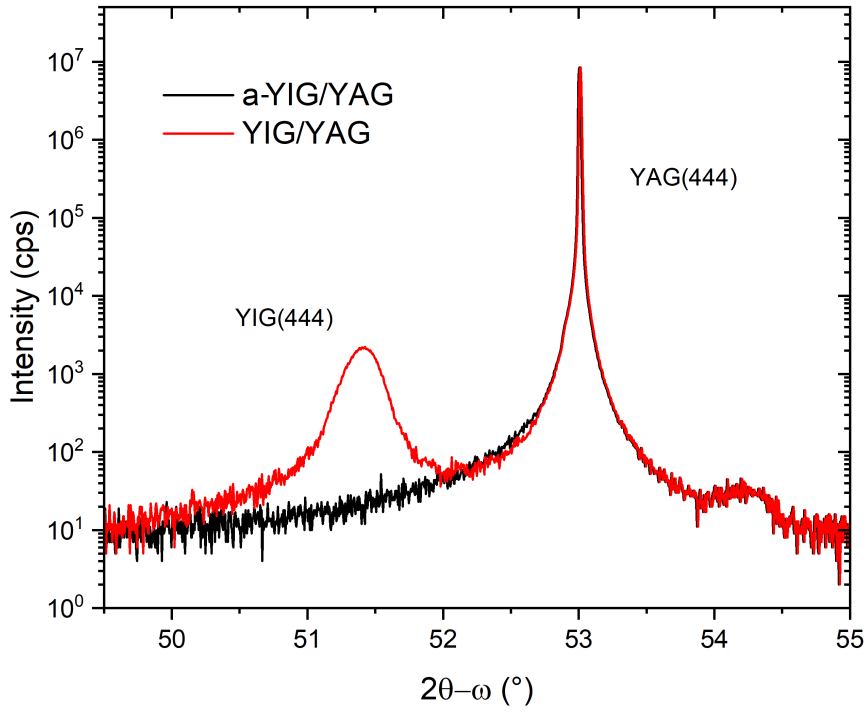

Figure 4.17: $2\theta - \omega$ XRD measurements for an a-YIG/YAG(111) thin film (black line) and then YIG/YAG(111) film following ex-situ annealing (red line).

strain in the YIG/YAG film is also indicated by the FMR data (Section 4.4.2.2).

The width of the YIG(444) reflection in ω was confirmed by obtaining reciprocal space maps of both the on-axis (444) and off-axis (426) reflections, shown in Figure 4.19. Unlike YIG/GGG, the YAG substrate and YIG film peaks are distinguishable in reciprocal space, allowing possible in-plane strain to be examined. A relaxation line from Q = (0,0) is drawn intersecting the YAG(426) substrate peak; deviation from this line in Q_x indicates tensile or compressive in-plane strain. From Figure 4.19, the YIG(426) peak shows a very small deviation from the relaxation line towards $Q_x = 0$, suggesting a minor tensile strain in-plane. This deviation in Q_x from the RSM corresponds to an in-plane tensile strain of (0.30 ± 0.06)%. This is supported by an approximation of in-plane (transverse) strain using the Poisson ratio ($\nu = -\frac{d\epsilon_{\text{Transverse}}}{d\epsilon_{\text{Axial}}}$). For $\nu_{\text{YIG}} = 0.29$, and an out-of-plane (axial) compressive strain of -0.6%, a transverse strain of 0.17% is calculated along both in-plane axes. The observation of tensile in-plane strain for the YIG/YAG is an unexpected result. Comparing bulk lattice parameters, a_{YIG} (12.376Å) > a_{YAG} (11.954Å), the in-plane lattice constant would be expected to be compressed to match the YAG substrate, and therefore forcing the out-of-plane lattice constant into tensile strain. Nevertheless, out-of-plane compression and in-plane tension measured in our YIG/YAG is in

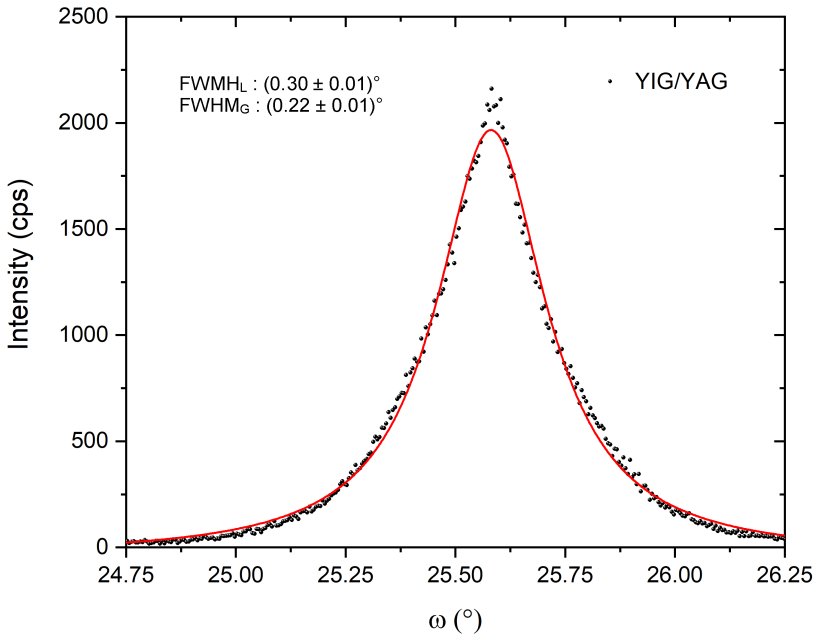

Figure 4.18: ω XRD measurements for $2\theta - \omega$ located at YIG(444), 51.42°: for the YIG/YAG(111) film. A Voigt best fit is shown (red), with Gaussian (G) and Lorentzian (L) FWHM.

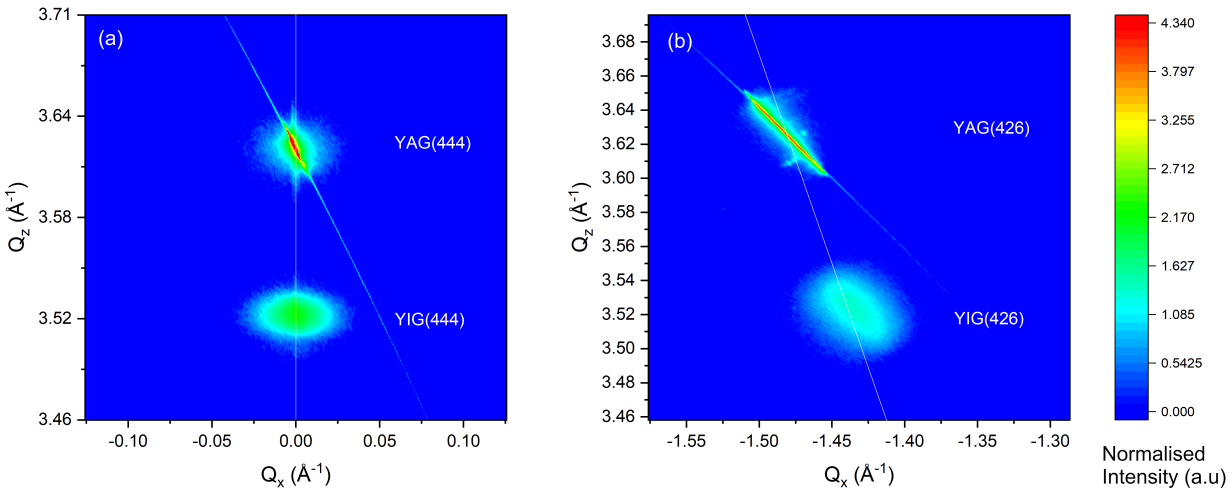

Figure 4.19: Reciprocal space maps taken about the (a) (444) and (b) (426) reflections respectively for YIG/YAG(111). Reciprocal space coordinates (Q_x,Q_z) are used. A relaxation line intersecting the substrate peak and Q = (0,0) is shown (white).

agreement with recrystallised YIG/YAG(001) films of similar thickness studied by Krysztofik *et al.* (2021) [205]. However, the mechanism behind this crystal lattice formation currently remains an open question in the field.

A pole figure was also measured about the YIG(444) reflection, shown in Figure 4.20. The YIG(444) pole figure illustrates a clear three-fold crystal symmetry about (111), with no other reflections present. This indicates, similarly to the YIG/GGG thin film, that the recrystallised YIG/YAG has both an epitaxial and crystalline texture with the expected Ia3d space group for YAG and other cubic garnets.

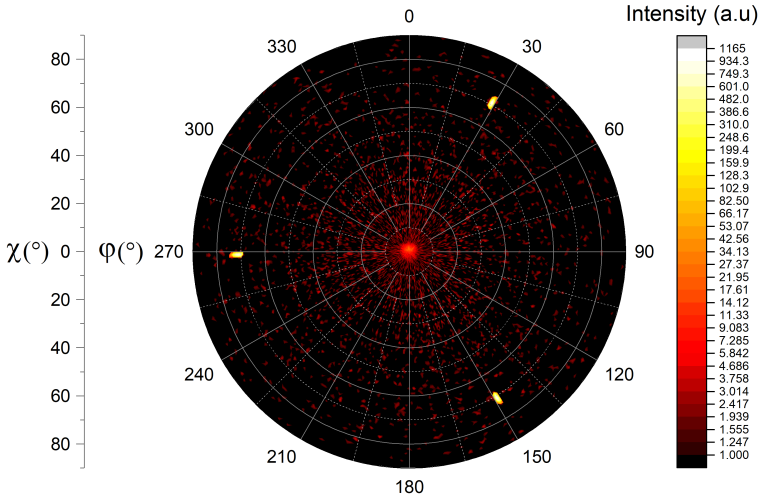

Figure 4.20: XRD pole figure taken YIG(444) diffraction peak (51.42°) for the YIG/YAG(111) film.

XRR measurements were performed to determine the thickness and average roughness for YIG/YAG. Measured and fitted Kiessig reflectivity fringes are shown in Figure 4.21, with accompanying scattering length density (SLD) simulation from the extracted fitting parameters as an inset. YAG and YIG densities were fixed at values of 4.56gcm^{-3} [206] and 5.17gcm^{-3} [52, 106] respectively for fitting. The use of a fixed YIG density was justified as preliminary XRR fits (leaving the YIG density to float) tended towards the expected YIG value of 5.17gcm^{-3}, with YIG film and thickness and roughness values being within 2% of those given below. An average YIG thickness of (48.8 ± 0.2)nm was inferred with an RMS roughness of (1.0 ± 0.1)nm. The YAG substrate roughness was observed to be slightly less, at (0.6 ± 0.1)nm. YIG/YAG roughnesses on the order of 1nm or less agree well with [205]. However, this roughness is slightly larger than that of the YIG/GGG film (at 0.6nm), potentially a result of strain producing a modified surface morphology. Cross-sectional TEM imaging was planned to investigate this further. However, this has not been possible due to instrumental problems with the FIB.

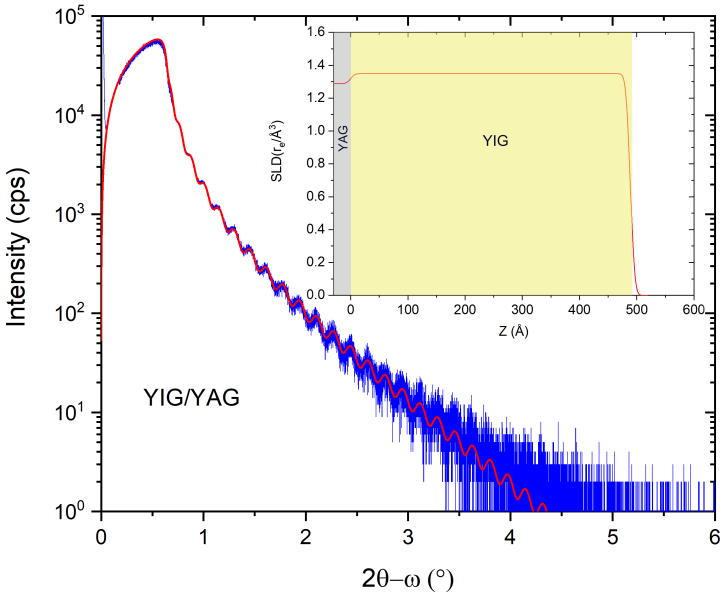

Figure 4.21: XRR measurement (blue) with fitted curve (red) for YIG/YAG(111) thin film. Simulated scattering length density (SLD) against sample Z from XRR fitting is inset.

4.4.2 Magnetic Characterisation

4.4.2.1 Vibrating Sample Magnetometry

Vibrating sample magnetometry was performed on the YIG/YAG film to assess the hysteresis behaviour, magnetisation and coercivity of the YIG. In-plane VSM measurements were performed with the LakeShore 8600VSM at room temperature. A magnetic bias field between ±16kOe was used, following [207] to saturate the YIG/YAG and show a clear hysteresis loop. Measured in-plane M(H) loops are shown in Figure 4.22, following removal of the diamagnetic YAG background. Measurement of a-YIG/YAG magnetism before recrystallisation showed apparent hysteretic behaviour; however, this was ultimately determined to be an effect of the YAG substrate, and is discussed further in Section 5.3. This substrate contribution dominated the response of the magnetically weak a-YIG. Room-temperature M(H) of YIG/YAG in contrast shows a clear hysteretic signal, with a more rounded hysteresis compared to recrystallised YIG/GGG, occurring over at least 1kOe and with larger coercivity of approximately (42 ± 3)Oe. Magnetic reversal and coercivity are more easily observed in the inset of Figure 4.22. A saturation magnetisation (M_S) is determined to be (99 ± 5)emu/cc using the film volume. This magnetisation is significantly lower than bulk-like YIG films (140emu/cc), at approximately 70%, and also smaller than seen in YIG/GGG thin films. This correlates well with most YIG/YAG films reported in literature, with M_S between 90-100 emu/cc at room temperature being typical [186, 195]. A notable exception is YIG/YAG recently reported by [207] to have a

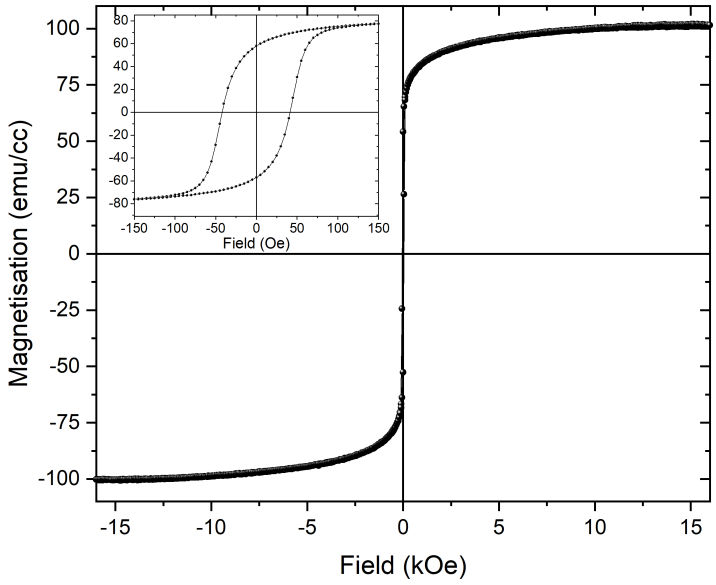

Figure 4.22: In-plane M(H) hysteresis for 48.8nm thick YIG/YAG(111) recorded from 8600VSM at T=300K. In-plane field swept between ±16 kOe.

surprisingly high M_S of 125emu/cc - despite following a similar recrystallisation-PLD approach to our own - comparable to YIG/GGG films but still below bulk YIG. Reductions in M_S across all YIG/YAG studies are considered to be due to the YIG-YAG lattice mismatch and/or oxygen and cation non-stoichiometries resulting from growth and recrystallisation processes [208].

Out-of-plane VSM measurements are shown in Figure 4.23. Large magnetic bias fields of ±16kOe were used to bring magnetisation out of plane (exceeding a bulk-YIG $4\pi M_S = 1750$G). An M_S of (102 ± 5)emu/cc is obtained from the out-plane loops. This was consistent with in-plane loops. However, the raw out-of-plane M(H) data from Figure 4.23 is arguably not entirely flat, even approaching 16kOe. This rounded saturation response of M(H) for out-of-plane reversal is typical of strained films. Antiphase boundaries caused by defects can often require very large fields to fully saturate thin films [209, 210]. Nevertheless, both M_S estimates agree within an experimental tolerance of 5emu/cc, and broadly agree with literature.

Magnetism of the YIG/YAG was also measured using the VSM-SQUID at the Diamond Light Source. Continuous M(T) measurement was possible with the diamagnetic YAG substrate (unlike paramagnetic GGG), shown in Figure 4.24, performed in a 5kOe measuring field. The expected ferrimagnetic response is observed, with an increase in M_S from approximately 98 emu/cc at room temperature (agreeing well with VSM8600 data above) to 162 emu/cc approaching 10K. The coercivity of YIG/YAG shows a much larger temperature dependence than YIG/GGG, increasing somewhat linearly across the tested temperature range, and with

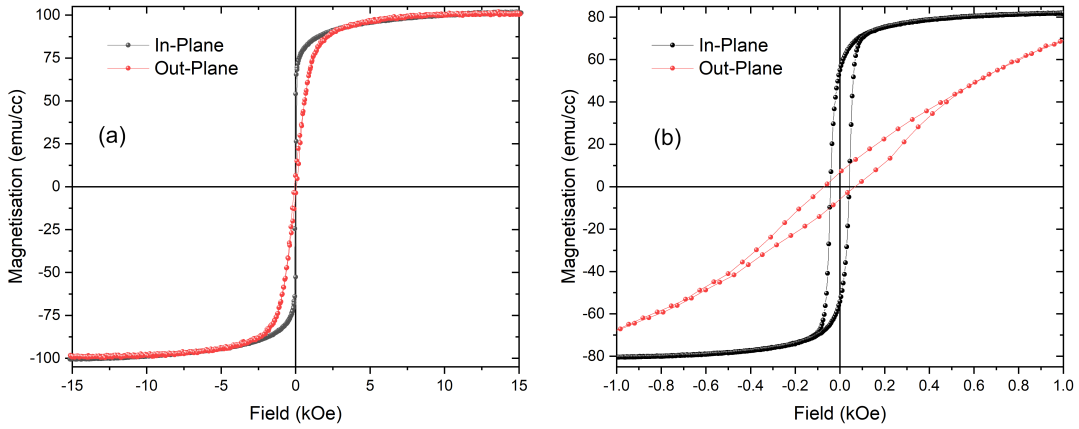

Figure 4.23: (a) Out-of-plane M(H) hysteresis for YIG/YAG(111) recorded from 8600VSM at T=300K, with in-plane hysteresis from Figure 4.22 shown for comparison. (b) Zoomed in M(H) plot at low field, highlighting the hysteresis in the out-of-plane measurement.

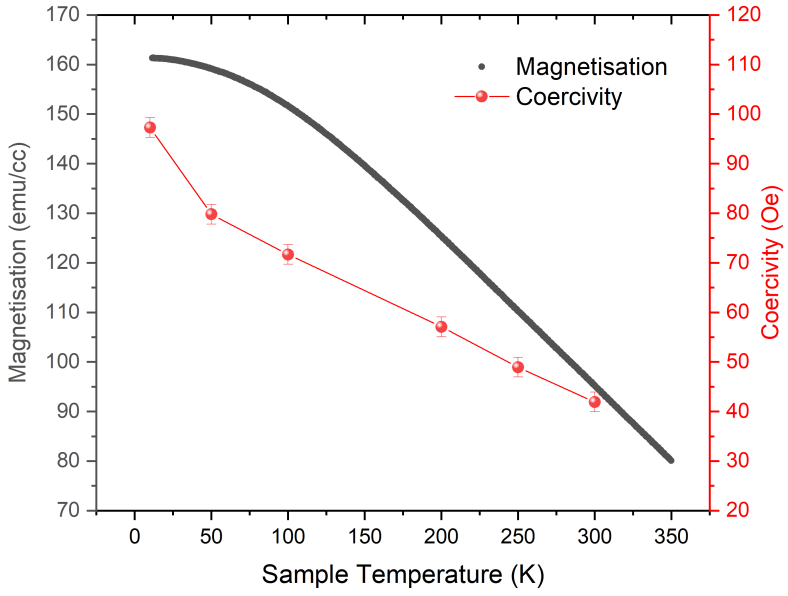

Figure 4.24: Temperature dependent M(T) for YIG/YAG(111) recorded by VSM-SQUID, and average H_C extracted from M(H) loops measured in-plane at different sample temperatures.

H_C values 15-20 times larger than YIG/GGG above 50K. Similar M(T) behaviour is reported in YIG/YAG from Mitra *et al.* [195].

4.4.2.2 Ferromagnetic Resonance Spectroscopy

Ferromagnetic resonance was performed on the YIG/YAG film to compare in-plane magnetisation dynamics to that of the YIG/GGG. Initially, the VNA-FMR technique was used, with measurements being performed identically to YIG/GGG as discussed in Section 4.3.2.2. However, the FMR response from the YIG/YAG was significantly weaker than the YIG/GGG: with ΔS_{21} being approximately an order of magnitude smaller. VNA-FMR resonances from the YIG/YAG were not clearly resolvable at low field and frequency from the background. Consequently, the lock-in based modulation-FMR technique was used instead. FMR linescans of field were measured as a function of applied RF frequency, between 0-15GHz in 0.5GHz intervals. Each linescan covered a magnetic field range swept from 0-4.5kOe, with a 5Oe field step. All mod-FMR measurements were performed at an RF power of +7dBm. Azimuthal mod-FMR data was also acquired from linescans at a fixed frequency of 10GHz, taken in 10° steps over a 180° range, from which the resonant field was extracted by fitting a asymmetric Lorentzian derivative (Equation 3.15).

For the as-deposited a-YIG/YAG thin film, no FMR response was observed from modulation-FMR that was discernable from the background: consistent with the lack of magnetism (VSM) and structure (XRD) seen in a-YIG/YAG and also a-YIG/GGG. In contrast, the YIG/YAG shows a moderately narrow FMR resonance, with a fixed frequency linescan at 10GHz shown in Figure 4.25(a). This data was recorded with the applied field along the $[11\bar{2}]$ axis. A resonance of $\Delta H(10GHz) = (37.0 \pm 0.5)$Oe was measured at an H_r of (2984 ± 3)Oe. The FMR YIG/YAG linewidth is seen to broaden by an order of magnitude (compared to YIG/GGG). The increase in H_r at constant frequency reflects a decrease in M_{eff} of YIG/YAG compared to YIG/GGG. Resonant field extracted as a function of frequency produces a Kittel curve shown in Figure 4.26(a). Fitting $H_r(f)$ to the easy axis Kittel equation produces a gyromagnetic ratio γ of $(1.72 \pm 0.01)\text{x}10^{11}$ rad/T or (27.4 ± 0.2)GHz/T, corresponding to a g-factor of (1.96 ± 0.01) and an orbital-to-spin moment ratio of $\mu_L/\mu_S = (-0.022 \pm 0.005)$. An M_{eff} of (110 ± 5)emu/cc is inferred: considerably lower than the 140emu/cc M_{eff} seen in YIG/GGG, reflecting the lower magnetisation of YIG/YAG. However, unlike YIG/GGG, M_{eff} for the YIG/YAG film contains **two** magnetic anisotropy terms. In addition to $-\frac{K_1}{M_S}$, magnetoelastic energy produces an added anisotropy out-of-plane, K_{ME}, due to the -0.6% compressive strain along the (111) axis. As discussed in Section 2.2.4, this magnetoelastic anisotropy is a similar order of magnitude to K_1. These two corrections act in the same direction, forcing the magnetisation in-plane and they cannot be distinguished. Furthermore, the YIG/YAG system is no longer cubic due to strain, meaning the $-\frac{K_1}{M_S}$ correction will also differ. Consequently, only M_{eff} measured from the Kittel curve can be given with certainty, with values of M_S being more difficult to estimate.

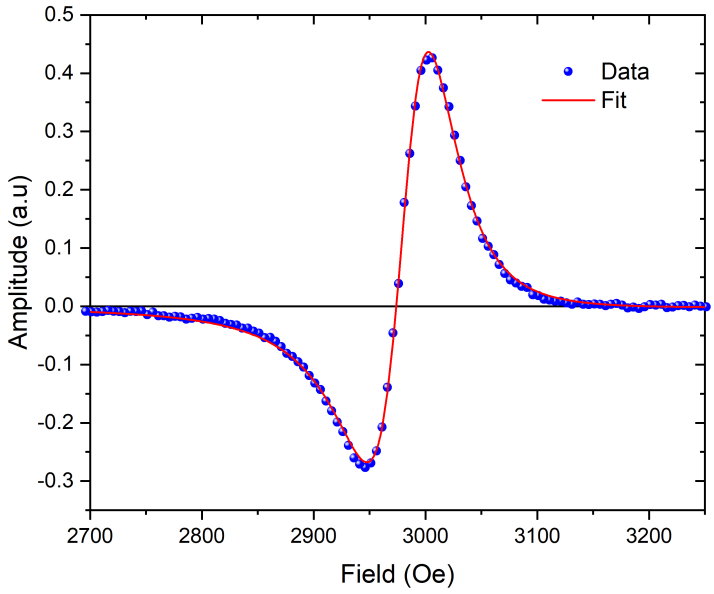

(a)

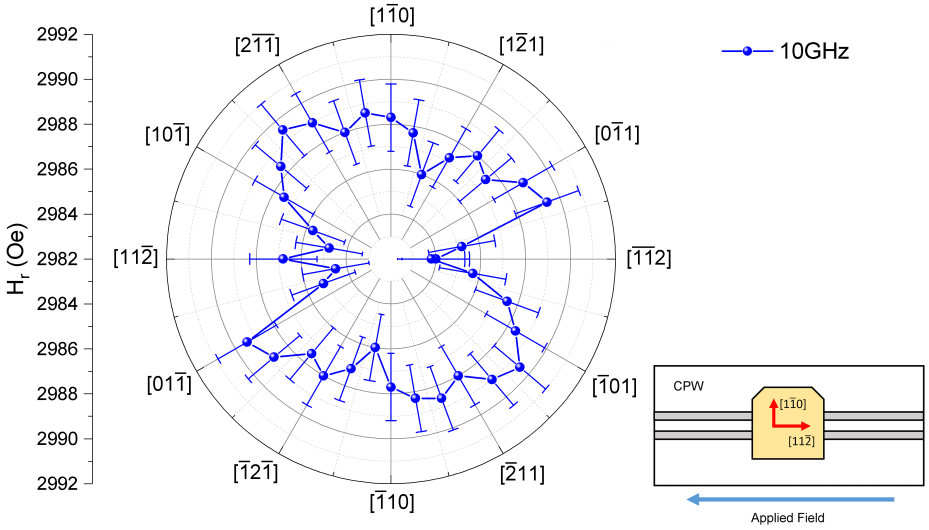

(b)

Figure 4.25: (a) In-plane modulation-FMR resonance linescan taken at fixed frequency of 10GHz for YIG/YAG, fit to an asymmetric Lorentzian derivative function. (b) $H_r(\phi)$ data extracted from azimuthal modulation-FMR of YIG/YAG at fixed resonance frequency of 10GHz. Relative orientation of the clipped corners indicating the $[11\bar{0}]$ of the sample to the CPW at the '0 degrees' position is shown as an inset.

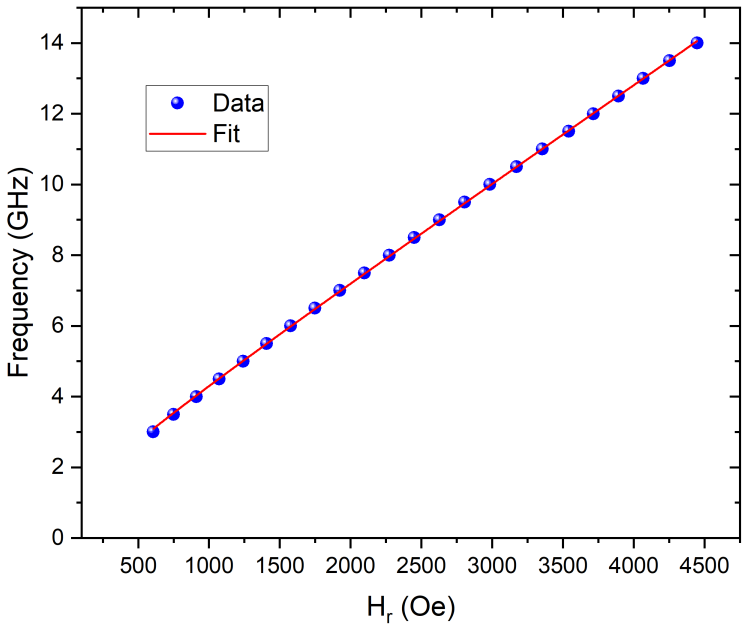

(a)

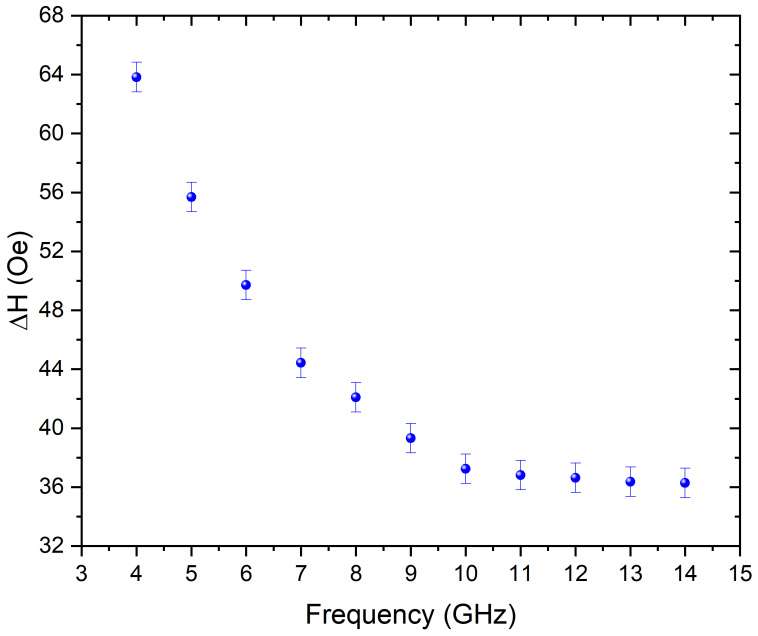

(b)

Figure 4.26: (a) In-plane Kittel curve extracted from various linescans and fit to the in-plane easy-axis Kittel equation. (b) Measured FMR linewidth as a function of RF frequency, ΔH(f).

Shown in Figure 4.25(b), the azimuthal $H_r(\phi)$ at 10GHz shows only very small deviations in H_r. A maximal change in H_r of (6 ± 2)Oe was measured from asymmetric Lorentzian fitting to 10GHz linescans, with most H_r values agreeing with each other within error. A uniaxial anisotropy along the $[1\bar{1}0]$ direction could be argued. However, the difference of (6 ± 2)Oe is considered too small to produce a significant change in the Kittel curve and Kittel curve fitting. Additional measurements of $H_r(\phi)$ were performed using a 1Oe field step, however no improvements to $H_r(\phi)$ were seen. In part, this is a result of the modulation bias-field systematically broadening the resonance, making these small changes in H_r difficult to resolve even with a 1Oe step.

The most significant difference between YIG/YAG and YIG/GGG FMR lies in the response of FMR linewidth with frequency, ΔH(f), shown in Figure 4.26(b). ΔH(f) measured in the YIG/YAG film is unexpectedly non-linear and negative, showing a **decrease** in linewidth as RF frequency increases. This non-linear behaviour contradicts the behaviour expected of dominant intrinsic damping from Equation 2.50 - a positive linear correlation with Gilbert damping and extrinsic damping measurable from gradient and offset respectively - and is not observed in the YIG/GGG film. Similar YIG/YAG ΔH(f) responses have only recently been reported in literature by Krystofik *et al.* (2021) [205], where a similar U-shaped dependence is observed in YIG/YAG(001) thin films, with RF frequencies ranging from 0-40GHz. YIG/YAG damping characteristics are typically overlooked in literature published beforehand, with YIG/YAG film quality being primarily weighted by FMR linewidth, ΔH(10GHz), instead [186]. This non-linear response is a likely reason, as evaluation of both the Gilbert damping, α, or extrinsic damping at 0GHz is not feasible following Equation 2.50. Surprisingly, ΔH(f) does not resemble two-magnon scattering behaviour following Equation 2.52 either, which is typical of thin films subject to defects or crystallographic mosaicity. Krystofik *et al.* (2021) propose strain, due to the YIG-YAG lattice mismatch, to be inhomogeneous throughout the YIG film, inducing a dispersion of anisotropy fields. This anisotropy dispersion produces a resonant frequency distribution at a constant field, and a consequently broader FMR linewidth (effectively multiple resonances over a finite RF frequency range). This frequency distribution is modelled to narrow with larger applied fields as alignment of moments to the bias field improves, producing narrower FMR linewidths and the negative Δ(H) response [205]. A complete explanation of this behaviour is an area of ongoing research.

4.5 Summary and Conclusions

In this chapter, thin films of YIG have been grown following a recrystallisation-PLD approach on both GGG(111) and YAG(111) substrates, to both characterise their structural and magnetic properties as a baseline for other experiments described in this thesis, and examine differences

in recrystallisation resulting from lattice mismatch. Structural characterisation has been performed using XRD and HAADF-STEM, and magnetic characterisation has been achieved using both in-plane FMR spectroscopy and VSM (both at room temperature and as a function of temperature).

As-deposited a-YIG has been confirmed to be amorphous without long-range structural order, following deposition on silicon nitride (SiN) TEM windows. Annealing recrystallises the film at a threshold temperature between 600°C and 650°C. A rapid amorphous to polycrystalline YIG phase transition is observed, producing clear radial electron diffraction patterns. The recrystallisation threshold temperature of 600°C is consistent across various heating methods (in-situ TEM annealing and ex-situ furnace annealing), and recrystallisation observed on SiN, as well as GGG and YAG (discussed further in Chapter 5).

Recrystallisation of YIG on GGG(111) is highly epitaxial, such that a YIG(444) film peak cannot be resolved from the substrate reflection in XRD and strong Pendellösung oscillations are produced instead. Out-of-plane YIG(444) plane spacing can only be estimated to be within 0.25% of bulk cubic YIG, and off-axis reciprocal space maps taken about the (426) reflection show no discernable in-plane strain. A crystalline film texture is inferred from both pole figures taken about the (444) reflection - showing three fold-symmetry expected from an Ia3d space group garnet - as well as cross-sectional TEM imaging. VSM magnetometry shows an extremely sharp in-plane magnetic reversal with coercivity below 0.3 Oe, and M_S estimated at (126 ± 5)emu/cc, in broad agreement with other recrystallisation PLD YIG/GGG films [11, 195]. Extremely strong FMR is observed, sharp and resolvable at low field and frequency. Linewidths of (2.0 ± 0.3)Oe at 10GHz indicate the quality of our YIG-on-GGG approaches literature [75], with extrinsic damping approaching 1Oe and intrinsic Gilbert damping of (4.2 ± 0.5)x10^{-4}. Easy axis Kittel curve fitting gives an effective magnetisation of (140 ± 5)emu/cc, and a g-factor of (1.98 ± 0.01) approaching the free electron value of 2. Angular measurements of resonant field at 10GHz indicate in-plane anisotropy for YIG/GGG is effectively isotropic within 5Oe.

The effects of larger lattice mismatch in recrystallising YIG on YAG(111) are significant. Epitaxial growth is confirmed by XRD, however YIG film and YAG substrate peaks are separable and lacking Pendellösung oscillations. Out-of-plane YIG(444) plane spacing differs from bulk YIG by -0.61%, indicative of an unexpected compressive strain out-of-plane. Reciprocal space mapping of the YIG(426) reflection shows a minor tensile strain in-plane, calculated from the deviation in Q_x to be (0.30 ± 0.06)%. Pole figures measured about the YIG(444) reflection in YIG/YAG films show similar symmetry to YIG/GGG films. However, rocking curves of YIG(444) show a Lorentzian FWHM of (0.30 ± 0.01)°, significantly broader than in literature YIG/GGG films. The broadening of the YIG(444) reflection in ω compared to YIG/GGG in literature suggests strain in the YIG/YAG film is inhomoegeneous throughout the film thickness. VSM magnetometry shows a reduction in magnetisation to (102 ± 5)emu/cc and systematic

broadening of coercivity by an order of magnitude. Magnetic hysteresis is observed to be considerably more rounded than YIG/GGG, reflecting strain in the film. Correspondingly, the FMR response is also worsened with broadened 10GHz linewidths of (37.0 $\pm$ 0.5)Oe. Most notable, however, is the emergence of a dominant extrinsic damping behaviour - both negative and non-linear in ΔH(f) - as a result of inhomogeneous strain in the YIG/YAG film.

Chapter 5

Magnetic X-Ray Spectroscopy Study of Amorphous YIG Thin Films

Detailed spectroscopic information on a-YIG is lacking in literature, begging the question "what exactly is a-YIG and is it the same from sample to sample?" Literature suggests the Fe environment in the amorphous material is different than that in the crystalline state, although existing reports disagree on this issue [117, 211]. Samples of a-YIG may, in fact, have differing 'amorphousness' and Fe environments, causing differences in reported behaviour or alternate pathways for non-local transport. Spectroscopic magnetometry offered by XMCD is essential to study magnetization at the two Fe^{3+} sites in a-YIG to attempt to confirm this theory.

In this chapter, a study of four a-YIG on YAG thin films is presented. Four a-YIG (80nm) films were fabricated on Yttrium Aluminium Garnet (YAG) substrates by room temperature PLD and annealed ex-situ in air at varying temperatures, attempting to modify the spin correlation length. Normal incidence XAS and XMCD at the Fe $L_{2,3}$ edges were performed to probe the chemical and magnetic disorder in the films and whether low temperature annealing modified this and therefore potential spin correlation. Supplementary Fe K-edge XAS (XANES and EXAFS), XRD and M(T) VSM characterisation has also been performed.

5.1 Sample Preparation and Growth

YAG was chosen as the substrate for this study due to it being a diamagnetic garnet, compared to GGG which is strongly paramagnetic. GGG would be preferred, particularly for studying ex-situ annealing effects on a-YIG (approaching recrystallisation), being highly lattice matched to YIG. However, paramagnetic background contributions from GGG in magnetic measurements are orders of magnitude larger than the a-YIG magnetism, making M(H) and M(T) measurements by VSM and VSM-SQUID of these materials extremely difficult. This is not the case for substrates such as YAG or silicon, where diamagnetic contributions are far smaller. YAG

was chosen over silicon, being a garnet (with the same Ia3d space group as GGG) and more lattice matched to YIG than silicon. This means that any changes in magnetism in a-YIG on YAG due to ex-situ annealing are more comparable to that of a-YIG on GGG. This is reflected in the M(H) and M(T) measurements shown in Section 5.3, where recrystallisation of a-YIG is observed at 650°C on YAG, but not on silicon.

Four samples of amorphous YIG were deposited by room-temperature PLD onto 5x5mm YAG(111) substrates. In all cases, the YAG substrate was pre-cleaned in acetone (sonicated for 5 minutes) and then in IPA (sonicated for 5 minutes). The cleaned substrates were then dried using a nitrogen gun to prevent the formation of solvent residue. In-situ outgassing of the YAG with the CO_2 laser was performed at approximately 200°C, in-vacuum at a base pressure of $1x10^{-7}$ mbar for 30 minutes to remove any residual moisture. The substrate was then allowed to cool to room temperature before deposition. The deposition conditions used were identical to the a-YIG/YAG thin films presented in Chapter 4, given in Table 4.1. a-YIG and YAG thin films were deposited to a nominal thickness of 80nm. This thickness (larger than the films presented in Chapter 4) was chosen to provide a significant magnetic film volume for VSM.

The four a-YIG/YAG samples were then ex-situ annealed in a tube furnace. Annealing was performed in air for 3 hours, with each sample at a different respective temperature. The first sample was annealed at 650°C to achieve long range crystalline order as a YIG-on-YAG control. The other a-YIG/YAG samples were as-grown, or annealed at 200°C and 400°C respectively without crystallising the sample. A consistent ramping rate was used - ramping at 4°C per minute - for all samples annealed in the tube furnace. At this stage, characterisation by XRD and VSM was performed on each of the a-YIG/YAG samples to confirm a lack of crystallisation in the samples annealed below 650°C.

Following this, a platinum cap layer was deposited onto each sample in preparation for magnetic soft x-ray spectroscopy (XAS/XMCD), as well as hard x-ray absorption (XANES/EXAFS) and VSM measurements. The purpose of the platinum cap was to act as a surface conductor for TEY XMCD. The a-YIG/YAG films were inspected under optical microscope for potential contamination, before being blown clean via nitrogen gun. Crucially, in-situ outgassing via CO_2 laser was **not** performed. This was decided in order to prevent modification to the a-YIG correlation length due to additional heating. Instead, the a-YIG/YAG samples were left to pump down for 3 hours under load-lock vacuum: to produce an optimal base pressure and eliminate as much moisture as possible without heating. Unlike the a-YIG, room-temperature Pt deposition was performed in-vacuum at a base pressure of $< 1x10^{-7}$ mbar. Platinum deposition by PLD is discussed further in Chapter 6. All platinum layers were deposited with a notional thickness of 2nm.

It is important to note that, after the initial four a-YIG-on-YAG samples - as-deposited or ex-situ annealed at 200°C, 400°C and 650°C respectively - three additional a-YIG-on-YAG samples were produced. These three additional samples were ex-situ annealed at 500°C, 550°C

and 600°C respectively: following the procedure outlined above. The deposition of these samples was decided upon following the outcomes of the XMCD data shown in Section 5.4. Due to these samples being produced after the awarded XMCD beam-time and ongoing maintenance on the BLADE superconducting magnet, no XMCD data for a-YIG-on-YAG annealed between 500 and 600°C has been acquired to date. However, XRD, VSM and XANES/EXAFS data has been obtained for these samples.

5.2 X-Ray Diffraction and Reflectivity

X-ray diffraction was performed on each sample to confirm no obvious recrystallisation of the a-YIG layer had occurred on the YAG substrate, following ex-situ annealing below 650°C. A series of 2θ-ω scans were performed on each sample around the YAG(444) reflection to observe if the corresponding YIG(444) reflection was present. The XRD data shown in Figure 5.1 shows that for a-YIG, either as-deposited or ex-situ annealed below 550°C, only the substrate reflection is observed. This confirms that a-YIG remains sufficiently amorphous in this temperature range to prevent coherent diffraction of x-rays. At 600°C and 650°C, an epitaxial YIG(444) reflection is observed in addition to the YAG(444) substrate. Epitaxial growth was confirmed with no other features being present in broader 2θ-ω scans. A clear shift in 2θ-ω is observed between YIG(444) annealed at 600°C and 650°C; 2θ-ω for the 850°C YIG/YAG film from Chapter 4 is included for comparison.

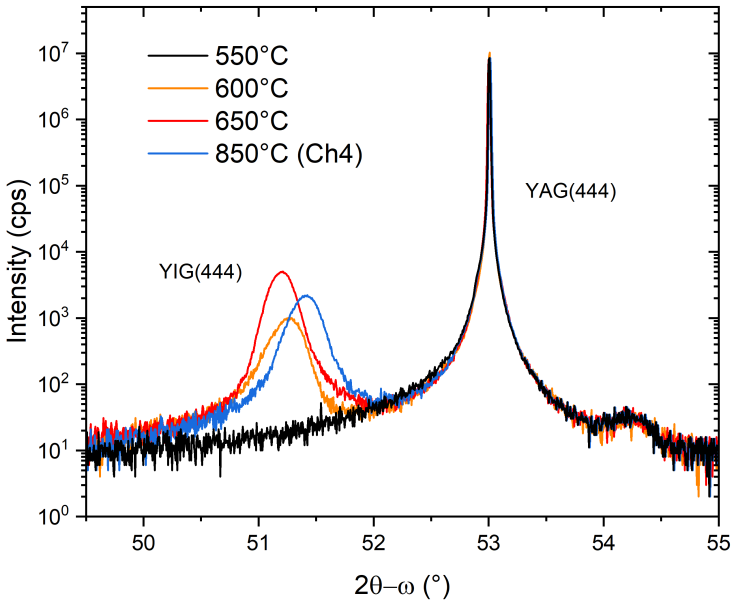

Figure 5.1: 2θ-ω XRD measurements for a-YIG/YAG(111) and YIG/YAG(111) films of different annealing temperatures, with the 850°C YIG/YAG film from Chapter 4. Spectra for all films annealed below or at 550°C are identical.

For the YIG-on-YAG, an out-of-plane YIG(444) plane spacing d_{444} was calculated from Bragg's law as (1.780 ± 0.001)Å for 600°C and (1.782 ± 0.001)Å for 650°C respectively. Compared to the bulk cubic YIG d_{444} (1.786Å) [52, 101], the YIG-on-YAG films all show a compressive out-of-plane strain. This trend agrees with compressive out-of-plane stresses observed in the YIG/YAG film recrystallised at 850°C from Chapter 4, showing only marginally larger compressive out-of-plane strain of -0.61%. High-temperature in-situ grown YIG/YAG films in literature exhibit similar out-of-plane strain on the order of -0.5% [205]. However, it is noted that the 650°C annealed YIG/YAG shows a reduction in compressive out-of-plane strain with annealing (from -0.34% at 600°C, to -0.22% at 650°C), compared to the 850°C film from Chapter 4 with -0.61% strain. It is important to note that the 600°C and 650°C YIG/YAG thin films were grown at an increased nominal thickness of 80nm (discussed in the XRR below), compared to the 48.8nm thick 850°C YIG/YAG film from Chapter 4. Therefore, a direct comparison cannot be drawn with the 850°C YIG/YAG film with respect to d_{444} and out-of-plane strain.

Improvements in structural order of the YIG/YAG between 600°C and 650°C are also evidenced by ω scans, and pole figures (measured with a 1mm slit width) taken over the YIG(444) reflection. Shown in Figure 5.2, increased intensity and reductions in the Lorentzian FWHM of YIG(444) rocking curves highlight an improvement to plane parallelism and orientation quality. Rocking curve Lorentzian and Gaussian FWHM values are summarised in Table 5.1. The Lorentzian FWHM was measured to show a minor decrease from (0.34 ± 0.01)° to (0.31 ± 0.01)° with annealing temperature between 600°C and 650°C. Obtained Gaussian FWHM values are mostly consistent between all three samples, within error.

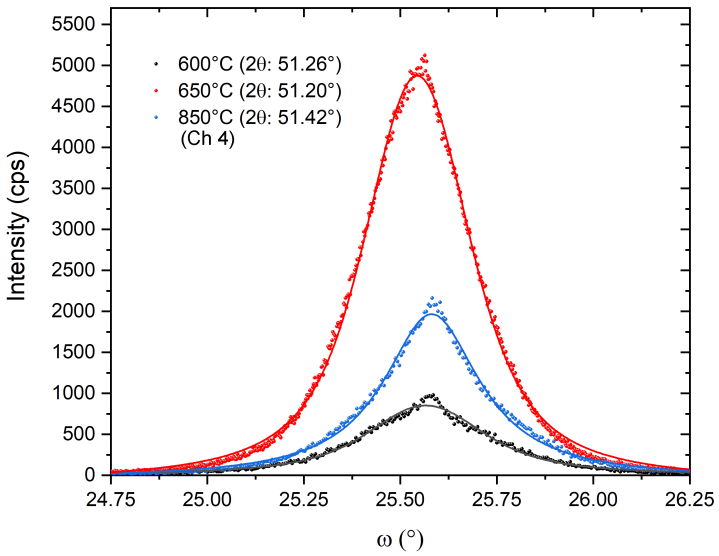

Figure 5.2: ω scans performed by rocking over the YIG(444) reflection. 850°C annealed YIG/YAG from Chapter 4 is included for comparison.

YIG/YAG Annealing Temperature (°C)	FWHM L (± 0.01°)	FWHM G (± 0.01°)
600	0.34	0.23
650	0.31	0.22
850	0.30	0.22

Table 5.1: Summary of Lorentzian (L) and Gaussian (G) FWHM from measured rocking curves in Figure 5.2 for crystalline YIG/YAG thin films.

Pole figures shown in Figure 5.3 show that for 600°C, despite the expected Ia3d symmetry of YIG(444), additional weaker reflections are observed surrounding each of the $< 444 >$ family reflections (despite measurements being performed with a narrow 1mm receiving slit size). This suggests potential in-plane mosaicity and incomplete recrystallisation. In contrast, these reflections disappear for 650°C YIG/YAG, leaving only the epitaxial Ia3d symmetric $< 444 >$ reflections. YIG/YAG pole figures below 600°C were unobtainable as there was no YIG(444) reflection to measure over (only the substrate peak).

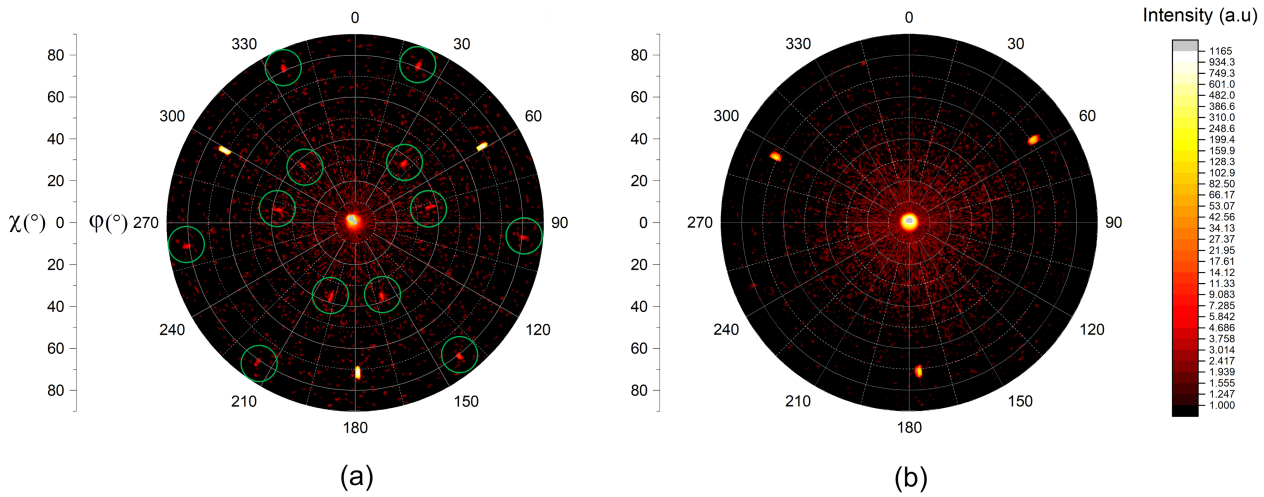

Figure 5.3: XRD pole figures from the YIG(444) diffraction peaks for (a) 600°C annealed YIG/YAG and (b) 650°C annealed YIG/YAG. Both pole figures were acquired with a 1mm receiving slit size. Additional reflections for 600°C annealed YIG/YAG are highlighted in green.

XRR measurements were performed on all samples in the series to determine the thickness and roughness of the a-YIG layer and the final platinum capping layer. Measurements were performed as described in Section 3.2.1, and reflectivity fringes were fitted using the GenX and GlobalFit software package [140]. XRR was measured before and after platinum deposition, as the platinum would dominate the XRR owing to its higher density: making the a-YIG or YIG difficult to characterise after Pt capping. XRR measurements for the as-deposited a-YIG/YAG and 650°C annealed YIG/YAG are shown in Figure 5.4 as examples, with simulated SLD. For

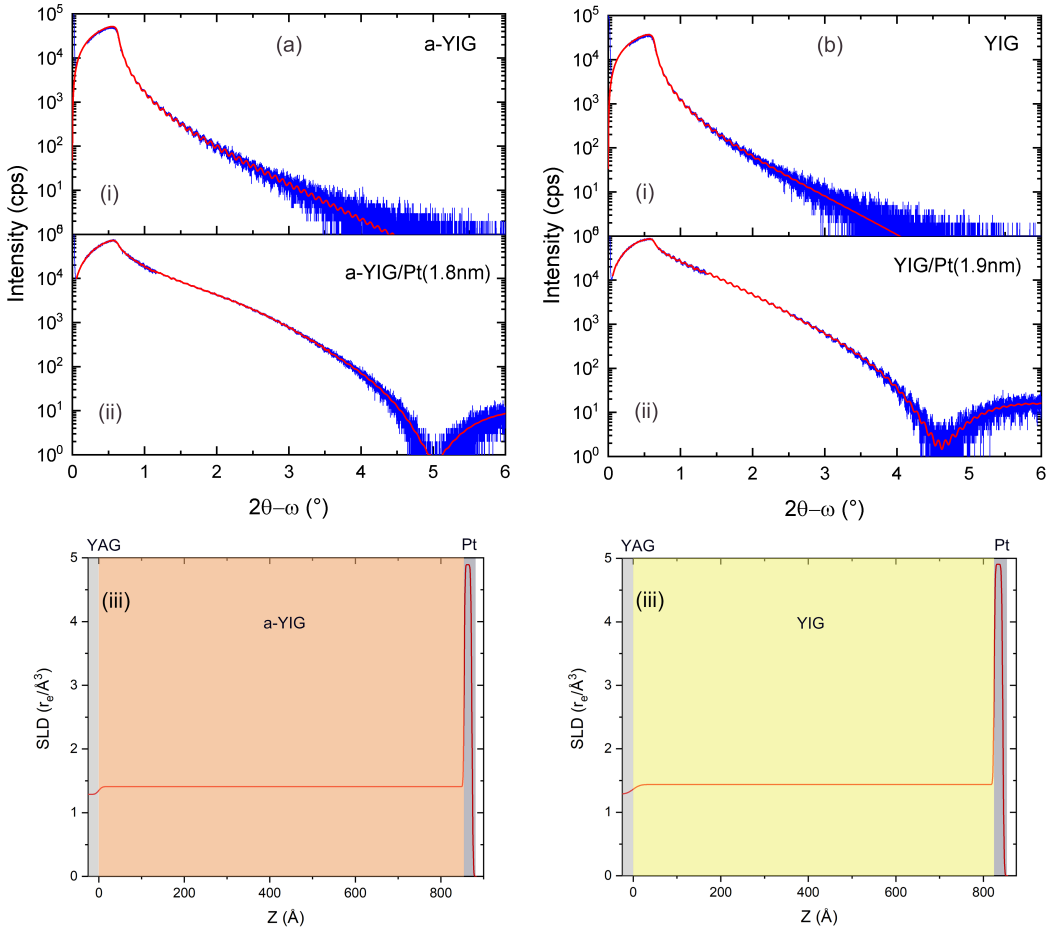

Figure 5.4: XRR measurement (blue) with fitted curve (red) for a-YIG and YIG on YAG thin films. Measured spectra for the (i) a-YIG or YIG and (ii) a-YIG or YIG plus Pt are shown for: (a) a-YIG/YAG as-deposited and (b) YIG/YAG annealed at 650°C. Simulated scattering length density (SLD) against sample Z from XRR fitting is shown in (iii) for each sample respectively.

the fitting, notional densities of 4.56gcm^{-3} for the YAG substrate and 5.17gcm^{-3} for the YIG film were used. Across all grown a-YIG/YAG layers, the fitting of the Kiessig fringes returned an average a-YIG thickness of (80 ± 5)nm, with an average RMS roughness of (0.6 ± 0.1)nm (errors quoted here given by standard deviation). This roughness, coming to approximately half the unit cell length of YIG (1.23nm) was favourable. Allowing the a-YIG density to float during fitting, a difference in scattering length density (SLD) of approximately 2% between the YIG and a-YIG was observed. This difference is more clearly seen in the XRR/SLD obtained for YIG/a-YIG/Pt trilayers discussed in Chapter 6. For the platinum capping layer, an average thickness of (1.8 ± 0.1)nm was measured with an average RMS roughness of (0.27 ± 0.09) nm. The Pt density was held constant at 21.45 gcm^{-3} for all fittings.

5.3 VSM

Vibrating sample magnetometry (VSM) was performed on all of the a-YIG/YAG samples to measure their magnetic properties: both M(H) and M(T). M(H) measurements were acquired using both the Lakeshore 8600 model VSM at the University of York, and the QuantumDesign SQUID-VSM at the Diamond Light Source; M(T) measurements were acquired exclusively from the SQUID-VSM. All VSM data illustrated was measured for a magnetic field applied in the plane of the a-YIG thin films. For all measured VSM loops, magnetisation was compared (unless stated otherwise) to account for any small differences in a-YIG film volume. a-YIG film volume was obtained using thickness extracted from XRR, and multiplying by the sample area (measured using a travelling optical microscope).

Room Temperature M(H)

Room temperature M(H) measurements of the a-YIG/YAG films are shown in Figure 5.5. A magnetic field of ±16kOe was applied to saturate the magnetically soft, yet strained YIG/YAG. YIG/YAG samples (annealed above 550°C) show clear hystersis across this field range. YIG/YAG samples crystallised at 650°C shows a magnetisation of (94 ± 5) emu/cc, and a coercivity of (47 ± 2) Oe. For a-YIG/YAG samples annealed below 550°C, M(H) measurements show that a finite hysteresis still exists, and remains similar in magnitude between as-deposited a-YIG and a-YIG annealed at 500°C. This initally suggested the a-YIG may have an asperomagnetic ordering - such that the M(H) loop is not linear, but also does not saturate as quickly or strongly as a ferromagnet [33] (Figure 2.6). However, while the magnetisation remained similarly small (and in fact decreases slightly) between as-deposited a-YIG and 500°C, the coercivity showed a sizable decrease from (345 ± 5)Oe to (33 ± 5)Oe. This is before the coercivity (as well as magnetisation) then begins to increase with the crystallisation of the YIG above 600°C.

This prompted VSM measurements to be performed on a plain 5x5mm YAG (111) substrate, as a function of identical ex-situ annealing over a similar temperature range. Shown in Figure 5.6, M(H) loops for YAG(111) show an identical shape to those for a-YIG/YAG below 500°C; the moment (rather than magnetisation) is shown. Ex-situ annealing was performed sequentially on the same YAG substrate. Shown in Figure 5.6(b), both coercivity and moment follow a similar decline to that shown for a-YIG/YAG. This magnetism is likely originated from oxygen defects present in the YAG oxide [212], explaining its reduction with increasing annealing in air as oxygen defects are filled. Given the YAG substrate volume is far larger than that of the a-YIG thin films, the resulting YAG magnetisation is estimated to be approximately $1.9\text{x}10^{-3}$ emu/cc. This is far smaller than the magnetisation estimated from the a-YIG thin film volumes below 500°C annealing in Figure 5.5; nevertheless, this produces a considerable magnetic moment overall due to considerable YAG volume: ultimately making the a-YIG magnetism very difficult

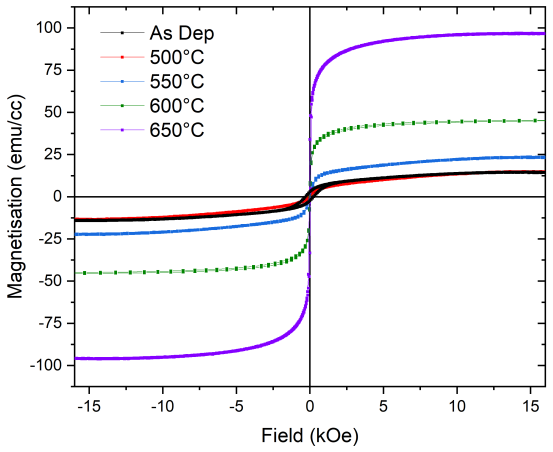

(a)

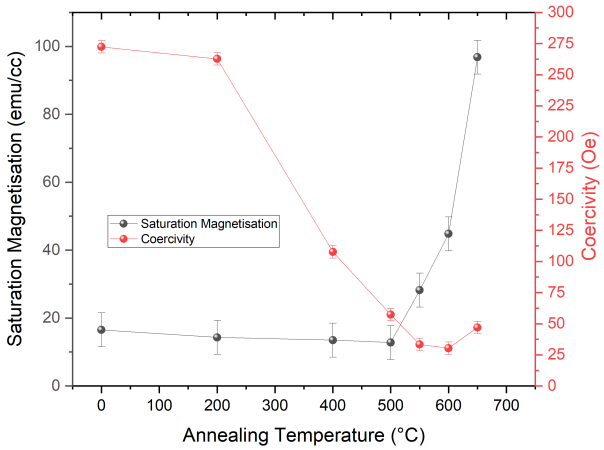

(b)

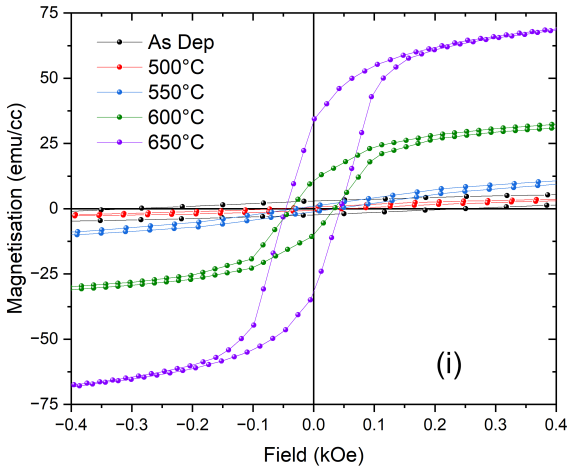

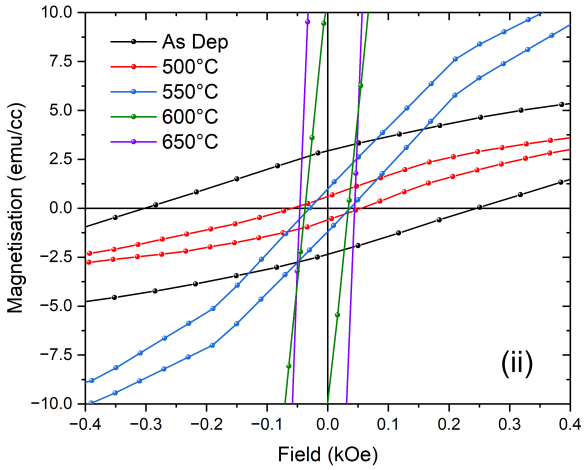

(c)

Figure 5.5: (a) In-plane M(H) hysteresis for YIG/YAG and a-YIG/YAG subject to different annealing temperatures, recorded from 8600VSM at T=300K. (b) Saturation magnetisation and coercivity extracted as a function of annealing temperature. (c) Low-field zoomed-in M(H) plots, highlighting the hysteresis of (i) more strongly magnetic YIG/YAG, and (ii) weakly magnetic samples of a-YIG/YAG.

to measure on its own. This suggests that YAG substrates require additional preparation by annealing in air above 500°C, prior to a-YIG deposition.

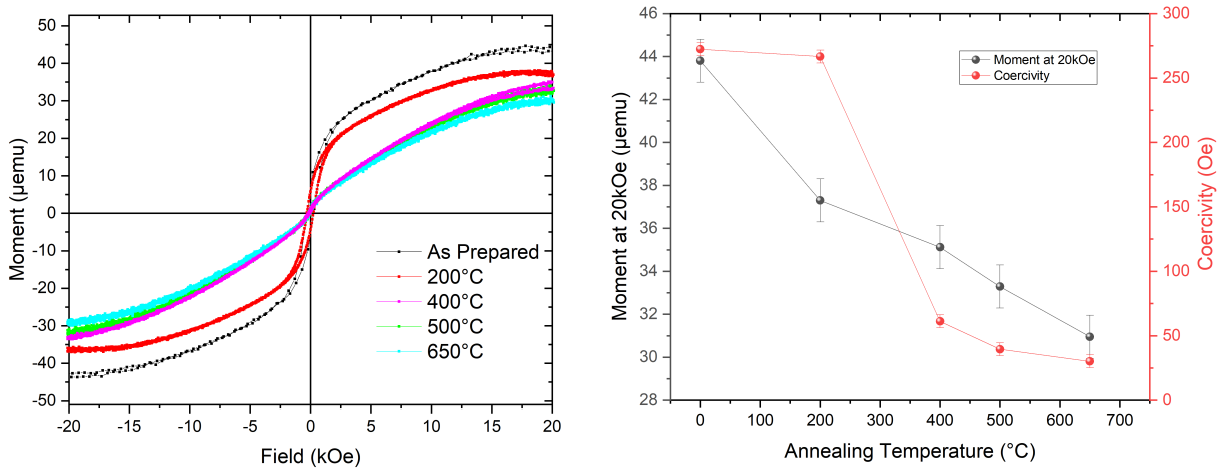

(a) (b)

Figure 5.6: (a) In-plane M(H) hysteresis (recording magnetic moment) for a 5x5mm YAG(111) substrate subject to different annealing temperatures, recorded from 8600VSM at T=300K. (b) Moment at 20kOe applied field and coercivity extracted as a function of annealing temperature.

Attempting to bypass the YAG magnetism, four more a-YIG thin films were grown on Si(111) substrates as a comparison: as-deposited, or ex-situ annealed at 200°C, 400°C and 650°C respectively to reflect the annealing temperature range of the a-YIG/YAG films. XRR measurements of the a-YIG/Si films produced an average thickness of (85 ± 2) nm and an average roughness of (0.6 ± 0.1)nm: both agreeing within standard deviation of the a-YIG/YAG films. For all four films, no YIG diffraction peaks were observed in 2θ-ω, suggesting no YIG recrystallisation. Room temperature M(H) measurements for all four films, shown in Figure 5.7(a), are similarly small in magnetisation and resembles the signal observed with the quartz rod alone (saddled to the same XYZ used to measure the a-YIG/Si films). Subtracting the quartz rod signal, the resulting M(H) in Figure 5.7(b) is extremely weak with a poor signal-to-noise ratio, with magnetisation below 2emu/cc for all a-YIG/Si films: including a-YIG/Si annealed at 650°C. This illustrates that the a-YIG has very little magnetic order, as expected, and this lack of magnetism is apparently stable across this annealing temperature range (on Si substrates). The absence of YIG recrystallisation at 650°C for a-YIG/Si likely reflects the larger lattice mismatch between Si and YIG (Δa = -56%), whereby a larger thermal budget is required to initiate recrystallisation compared to YIG and YAG (Δa = 3.1%).

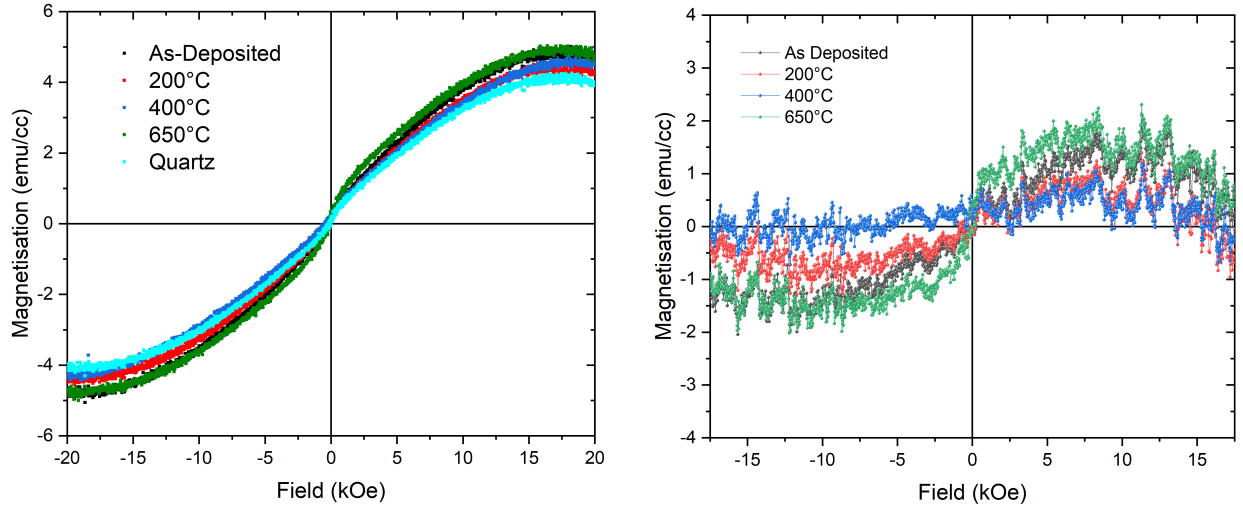

(a) (b)

Figure 5.7: (a) (a) In-plane M(H) hysteresis for a a-YIG/Si thin films subject to different annealing temperatures, recorded from 8600VSM at T=300K. M(H) response of the quartz sample rod is included. (b) M(H) hysteresis for a a-YIG/Si thin films following subtraction of the quartz rod signal, showing very weak and noisy M(H) for a-YIG/Si.

Temperature-Dependent Magnetism

M(T) was measured on the a-YIG/YAG films (and a-YIG/Si films for comparison) to observe any spin-glass signatures at low temperature, and potential changes with annealing temperature. Discussed in Section 2.1.6, disordered antiferromagnetic materials exhibit a cooperative, but random freezing of spins into one of many possible degenerate ground states at low temperature. This manifests as a splitting between zero-field cooled (ZFC) and field-cooled (FC) M(T) curves below a characteristic spin freezing temperature, T_F. Following Wesenberg *et al.* [18], a measuring field of 5kOe was used for all samples, and field-cooling was performed in the 5kOe measuring field in all cases. M(T) data above the spin-freezing temperature was fitted to a Curie-Weiss dependence with the addition of two background terms, shown in Figure 5.8(a): a constant offset in moment, and another linear in T. Linear contributions are associated with temperature-dependent Van Vleck-like paramagnetic contributions, observed in semiconducting substrates like Si (which is diamagnetic) [213, 214], whereas constant offsets are typically associated with sample mounting on the SQUID rod [215]. Subtraction of these background sources produces data for a temperature-dependent change in moment. Zero-field cooling and field-cooling were performed from 350K to 10K, and thereafter M(T) was measured with warming at 3K/min. Shown in Figure 5.8(b), cooling performed from different starting temperatures produces unexpected and non-physical divergence between the ZFC and FC datasets towards higher temperatures.

M(T) data for the as-deposited a-YIG/YAG film is shown in Figure 5.9(b). The ZFC and

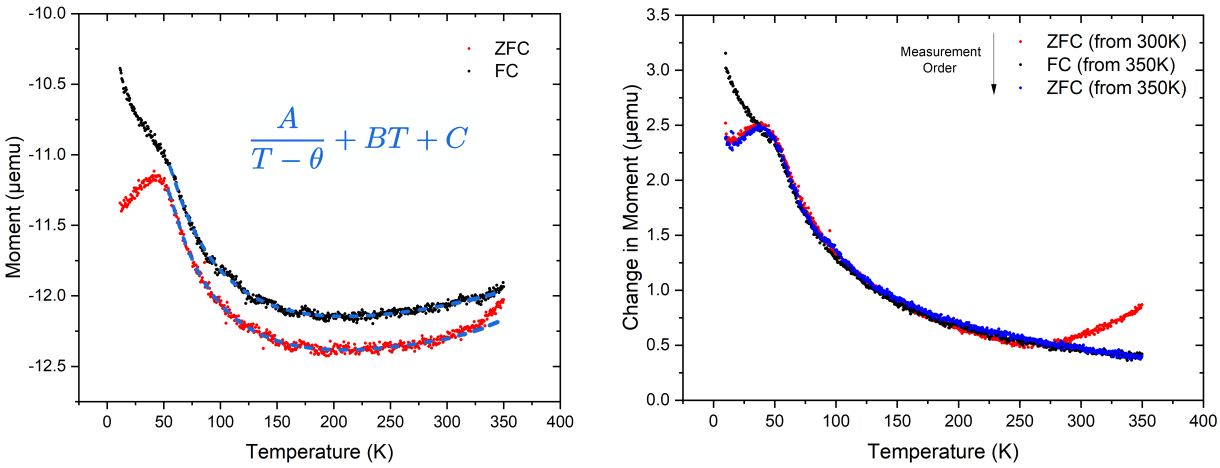

(a) (b)

Figure 5.8: (a) Raw ZFC and FC M(T) for as-deposited a-YIG/Si in 5kOe measuring field for both FC and ZFC. Each dataset is fitted with a Curie-Weiss law (blue fit lines following [18]), including two background contributions which are then subtracted. (b) ZFC and FC M(T) after subtraction for as-deposited a-YIG/Si, showing diverging artefacts approaching room-temperature, when sample is cooled down from different starting temperatures.

FC datasets diverge at a spin freezing temperature of (45 ± 2)K, indicating spin-glass like behaviour in the a-YIG. The spin-freezing transition in a-YIG/YAG forms a shoulder, rather than an isolated peak. This is likely due to oxygen generating the background signal, whereby any gaseous oxygen in the SQUID chamber begins to condense into liquid oxygen (known to be paramagnetic) below its boiling point of 90K [192, 216] . Such a paramagnetic background below 90K is absent for as-deposited a-YIG/Si, shown in Figures 5.8 and 5.10, with a distinct spin freezing peak at (44 ± 2)K. Above the freezing temperature, M(T) broadly follows the expected Curie-Weiss law dependence of 1/(T-Θ). In contrast to [18], no clear splitting between ZFC and FC is observed near 230K for a-YIG/YAG or a-YIG/Si: an onset temperature for alleged non-local spin transport. In addition, Weiss constants (Θ) on the order of -15K to -10K were obtained through fitting shown in Figure 5.8: significantly smaller than those of -100K from Wesenberg *et al.* [18], this implies our a-YIG is less strongly antiferromagnetically ordered than that of Wesenberg *et al.* Spin glass behaviour (with a spin-freezing 'shoulder') is also observed for a-YIG/YAG samples annealed at 200°C, 400°C and 500°C. With increased annealing temperature below 500°C, the rate of decrease in M(T) following the spin-freezing temperature is faster. Smaller absolute moments are also observed at the spin-freezing shoulder, suggesting the a-YIG is magnetically weaker. Both ZFC and FC for the 500°C annealed sample show an apparent increase in moment above 200K. However, this is likely non-physical and a result of the background subtraction/fitting (Figure 5.8(a)) being worse at higher sample temperatures for weaker magnetic signals; a similar increase is also seen for the weak YAG substrate M(T)

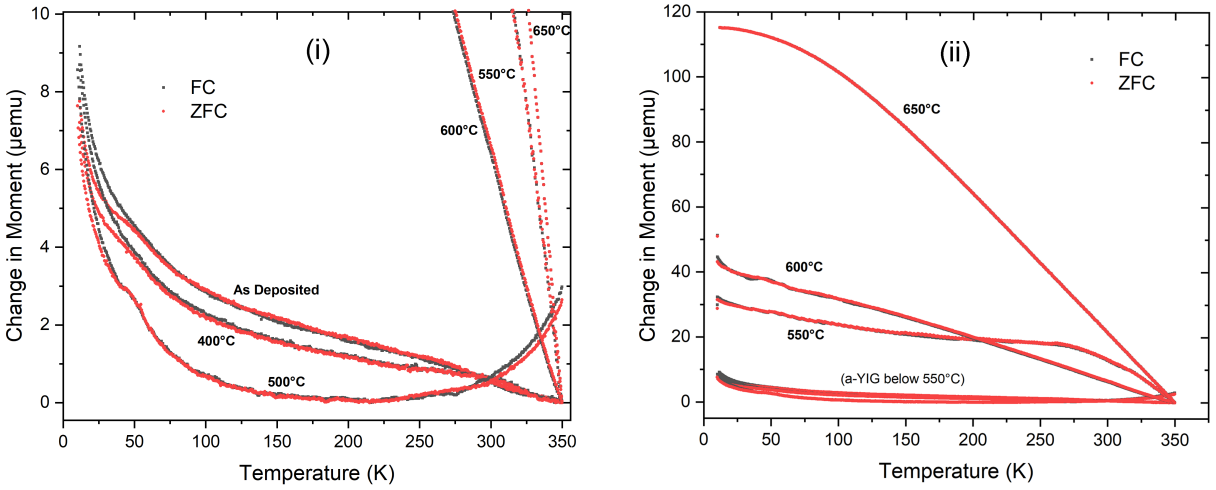

(a)

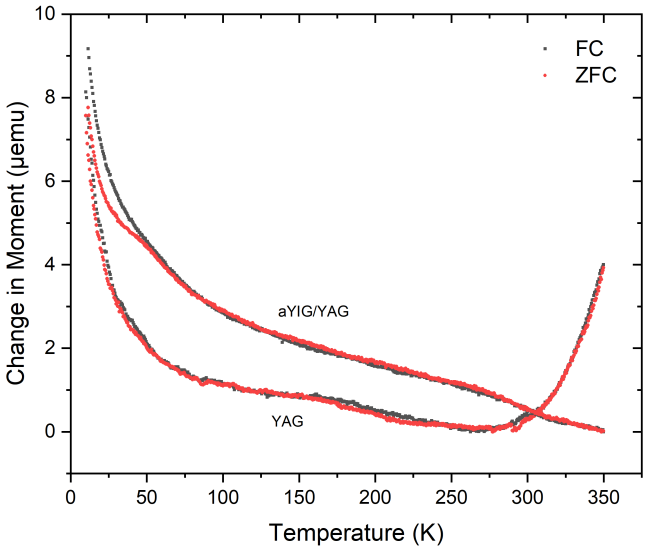

(b)

Figure 5.9: M(T) data for a-YIG on YAG thin films. ZFC and FC curves are shown for (a)(i) As-deposited, and annealed at 400°C or 500°C respectively, and (ii) 550°C, 600°C and 650°C with a wider scale view. (b) M(T) response for as-deposited a-YIG/YAG and YAG substrate only.

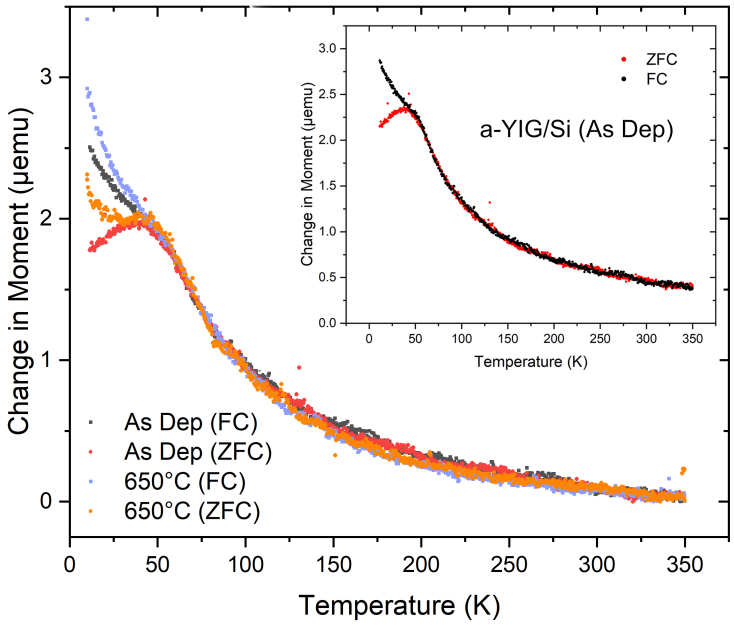

Figure 5.10: M(T) data for a-YIG on Si thin films. ZFC and FC curves are shown for as-deposited and annealed at 650°C respectively. Inset shows as-deposited a-YIG/Si only.

shown in Figure 5.8(b). M(T) behaviour is significantly different for a-YIG/YAG annealed above 550°C, shown in Figure 5.8(a)(ii). A clear transition from spin-glass behaviour to a typical ferrimagnetic M(T) at 650°C is shown. Interestingly, the magnetic moment significantly increases between 500°C and 550°C, despite no YIG crystallisation being detectable by XRD (or EXAFS in Section 5.5) at 550°C, and thus still being an amorphous phase.

In contrast to a-YIG/YAG, the M(T) response for a-YIG/Si is very stable with increased annealing temperature: showing spin-glass behaviour even after 650°C annealing (Figure 5.10). Very little difference in M(T) was observed between as-deposited, 200°C, 400°C, an 650°C. The absolute moment observed at the spin-freezing temperature is also consistent between the a-YIG/Si samples: such that the M(T) almost lie one top of each other above T_F. This reflects the absence of YIG recrystallisation on Si observed in the XRD data.

5.4 XAS and XMCD

Soft x-ray spectroscopy was performed on four a-YIG on YAG samples on the BLADE (beamline I10) at the Diamond Light Source. These samples were the as-deposited a-YIG, and a-YIG ex-situ annealed at 200°C. 400°C and 650°C respectively. A YIG/GGG thin film - grown similarly to YIG/GGG in Chapter 4 and annealed at 650°C - was also measured as a comparison. Soft

x-ray absorption spectroscopy was used to study the Fe in the a-YIG thin films, and assess whether the Fe environment in a-YIG is different to the crystalline YIG state, or altered by ex-situ annealing. The process of spectroscopic magnetometry offered by XMCD is described in Chapter 3. XAS and XMCD measurements were performed on each a-YIG/YAG sample in a field of 5T, and taken at temperatures of 10K, 50K, 100K, 200K, and 300K respectively. A grazing incidence of 65° away from the sample surface normal was initially attempted to provide a larger footprint (and thus XAS signal) and probe in-plane magnetisation. However, this resulted in significant surface charging and made TEY measurement in this arrangement difficult. Consequently, XAS was ultimately performed at normal incidence for all samples. This was deemed suitable, given an applied field of 5T significantly exceeded the $4\pi M_S$ required to bring the YIG magnetisation out of plane: approximately 1750 Oe at room temperature for a bulk YIG M_S [101, 52]. In addition, use of normal incidence reduced the effect of self-absorption on the spectra.

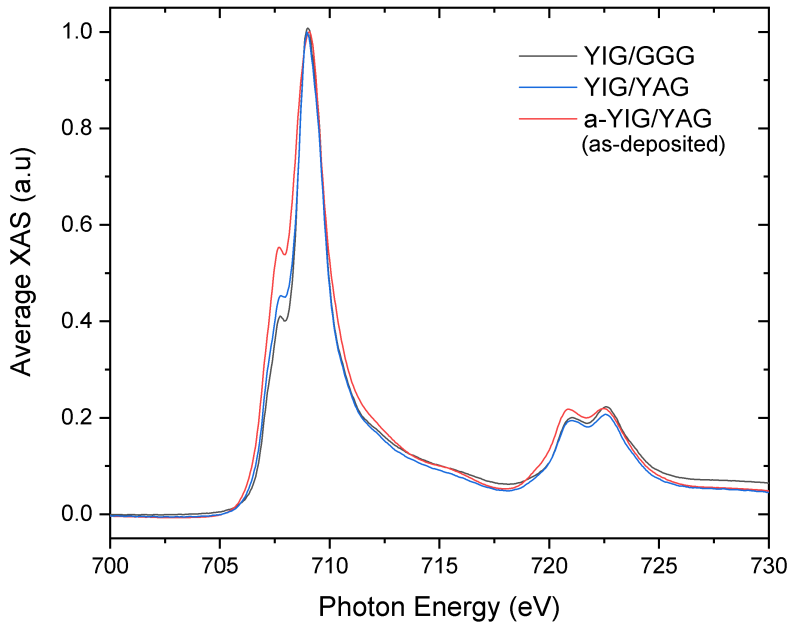

Figure 5.11: Average XAS spectra (experimental) for a-YIG/YAG, YIG/YAG and YIG/GGG.

Averaged XAS data ($\frac{\sigma^+ + \sigma^-}{2}$) for crystalline YIG/GGG, crystalline YIG/YAG and a-YIG/YAG is shown in Figure 5.11. Between the three spectra, the most significant difference is on the 707.7eV shoulder of the L_3 edge, and also at the L_2 edge. Absorption is greater at these points in the a-YIG film than in both crystalline YIG/YAG and YIG/GGG. Minor differences in absorption are also visible between YIG/YAG and YIG/GGG: with higher absorption at 707.7eV by the YIG/YAG, and higher absorption at 722.5eV by the YIG/GGG. XAS spectra for the

a-YIG/YAG also shows a minor shift to lower energy.

XMCD spectra extracted from the crystalline YIG/GGG, YIG/YAG and a-YIG/YAG films across the L_3 and L_2 edges are shown in Figure 5.12. For YIG/GGG in Figure 5.12(a), each of the three L_3 peaks in the XMCD occurs at different energies, centred on the Fe L_3 transition energy expected at 707eV: a strong minimum at 708.8eV, and two maxima at 707.6eV and 709.5eV respectively. A positive structure is also shown between 721-724eV at the Fe L_2 transition. This XMCD lineshape agrees well with YIG XMCD recorded in literature [217, 218]. Integration of the YIG/GGG XMCD in Figure 5.12(a) and application of the XMCD sum rules yields a value for the orbital-to-spin moment ratio, $\mu_L/\mu_S = (0.012 \pm 0.006)$. This was calculated from the integral values of p = (-0.056 ± 0.003) and q = (-0.003 ± 0.001). This value of q in the XMCD integral is proportional to the orbital magnetic moment contribution, almost quenched to zero in the YIG film. This follows the quenching of the orbital magnetic moment expected in 3d transition metals. A corresponding g-factor of (2.02 ± 0.02) is calculated from the XMCD ratio of orbital-to-spin moment. This g-factor is consistent with Vasili *et al.* [218], where a g-factor of 2.01 was obtained via similar XMCD sum rules analysis.

Crystalline YIG/YAG XMCD spectra - Figure 5.12(b) - shows a similar lineshape to that of YIG/GGG: with L_3 peaks occurring at the same respective photon energies and the L_2 edge remaining a positive structure. The biggest difference between YIG/GGG and YIG/YAG XMCD occurs at 709.5eV, where dichroism between positive and negatively circular x-rays is less in YIG/YAG compared to the YIG/GGG. Integration of the YIG/YAG XMCD gives integral values of p = (-0.039 ± 0.002) and q = (-0.007 ± 0.002). Using the XMCD sum rules, a $\mu_L/\mu_S = (0.044 \pm 0.009)$ was calculated, from which a corresponding g-factor of (2.09 ± 0.03) was inferred. The μ_L/μ_S is low, much like the YIG/GGG sample, but does not agree within experimental error. μ_L/μ_S and g of YIG/YAG being slightly larger than measured in the YIG/GGG may reflect the larger lattice mismatch between YIG and YAG limiting recrystallisation and resulting magnetic quality (in comparison to YIG/GGG).

This value of g for YIG/YAG from XMCD cannot be compared directly to that obtained via FMR in Chapter 4: (1.96 ± 0.01). This is because the YIG/YAG film from Chapter 4 was both grown at a reduced thickness (48.8nm compared to 80nm) and annealed at a higher temperature of (850°C instead of 650°C). Given these are different YIG/YAG samples, the value of g is not expected to be the same. Nevertheless, a difference of 6.5% is observed between the two values. Part of this difference may be attributed to the XMCD technique. Values of g obtained from XMCD sum rules analysis are highly sensitive to baseline subtractions. Differences in subtraction procedure become highly significant in materials where the integral value of q tends to zero, such as YIG. Achieving flat baselines near the L_2 edge is critical but also challenging: reflected in Vasili *et al.* (2017) [218].

XMCD spectra for the as-deposited a-YIG/YAG thin film, shown in Figure 5.12(c), is very different. Compared to crystalline YIG, the size of the a-YIG XMCD is almost an order

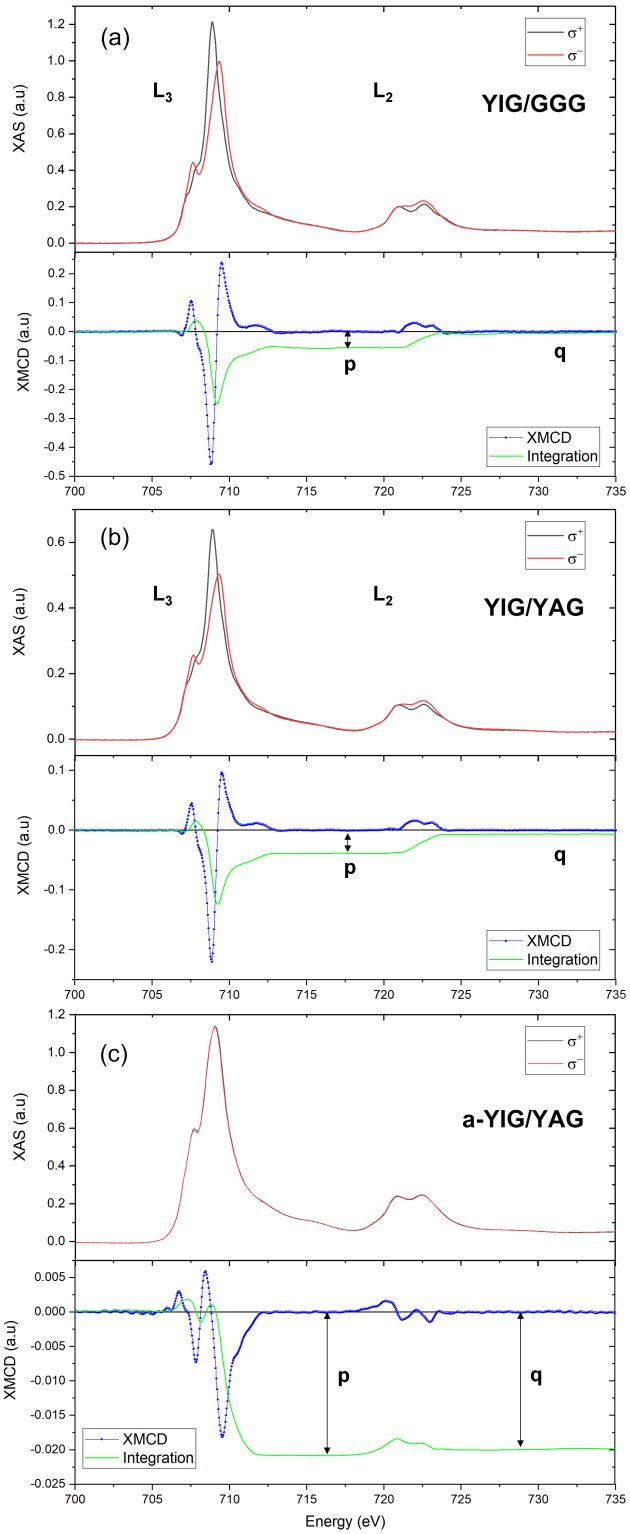

Figure 5.12: Fe XAS and XMCD spectra (experimental) for (a) YIG/GGG, (b) YIG/YAG and (c) a-YIG/YAG. Normal Incidence, TEY, 300K, B = 5T

of magnitude smaller. XAS from left and right circular x-rays overlap significantly over the measured range of photon energy. The most dichroism occurs at very tops of the 707.7eV shoulder and 709.1eV peak over L_3; dichroism over L_2 is very small. The a-YIG XMCD lineshape over the L_3 edge shows three distinct peaks, but significantly the peaks are opposite in orientation compared to those of YIG; a maximum at 708.4eV, and two minima at 707.8eV and 709.5eV respectively (the latter being the strongest peak). A smaller fourth peak is also observed at 706.7eV. At the L_2 edge, a structure consisting of three peaks exists between 718-726eV. Integration and application of the XMCD sum rules yields a large value of μ_L/μ_S = (0.59 ± 0.03), from integrals of p = (-0.021 ± 0.001) and q = (-0.020 ± 0.001). This corresponds to a large non-zero orbital moment (compared to the YIG) with a resulting g-factor of (3.19 ± 0.05).

Contributions to YIG/GGG magnetism (at the film surface) from tetrahedral and octahedral Fe^{3+} sites were evaluated using atomic multiplet calculations, following Cowan's ab-initio Hartree-Fock method with relativistic correction using CTM4XAS software [164]. Following [219], a Slater parameter reduction of 70%, 80%, 80% was used, with a 10Dq of 1.6eV and -0.6eV (for O_h and T_d respectively). A Lorentzian gamma of 0.15eV was used for the L_3 edge and 0.3eV for the L_2, with Gaussian broadening of approximately 0.2eV. Shown in Figure 5.13(a), multiplet calculations agree well with normalised XMCD data from the YIG/GGG film at the L_3 for a relative occupation of Fe sites (Fe^{2+} O_h:Fe^{3+} T_d:Fe^{3+} O_h) of 0:60:40, with a 5% tolerance on each. This is the expected ratio of T_d:O_h Fe^{3+} in stoichiometric YIG. Fe^{2+} contributions are zero - with the maximum at 707.6eV being instead due to Fe^{3+} O_h contributions - indicating magnetism in the YIG sample is produced almost entirely by Fe^{3+} species.

Evaluations of YIG/YAG magnetism from atomic multiplet calculations produce a similar result. Shown in Figure 5.13(b), multiplet calculations agree well with XMCD data for an occupation of Fe sites of 0:64:36, again with a 5% tolerance on each. Minor adjustments from 0:60:40 were necessary to minimise the residual between the multiplet calculation and XMCD at the L_3 edge in YIG/YAG. Nevertheless, this is still in broad agreement with the expected Fe^{3+} T_d:O_h ratio of 3:2, with no Fe^{2+} contributions being present.

a-YIG/YAG Atomic Multiplet Calculations and Discussion

As deposited a-YIG/YAG shown in Figure 5.13(c) is notably different to YIG/GGG and YIG/YAG with respect to atomic multiplet calculations. Fits to the experimental XMCD from multiplet calculations show that surface magnetism in a-YIG is approximately 80% dominated by O_h-coordinated Fe species, in contrast to the crystalline YIG: dominated by T_d-coordinated Fe^{3+}. This domination of O_h-coordinated Fe is reflected in the reversal of the XMCD signal in a-YIG compared to YIG, where the maxima/minima at L_3 are oppositely oriented. Multiplet calculations reproduce the XMCD lineshape at the L_3 edge best with a significant Fe^{2+} O_h con-

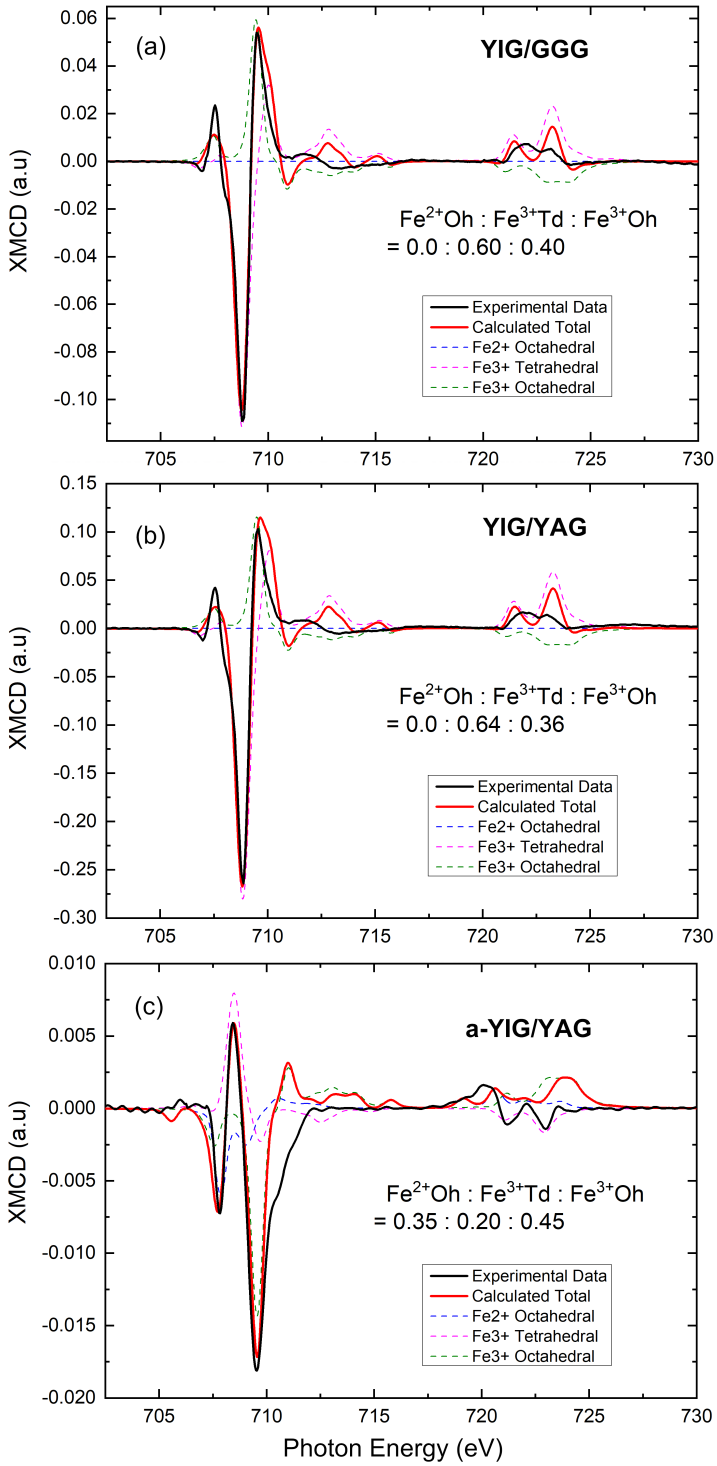

Figure 5.13: Fe XMCD spectra (experimental and atomic multiplet calculations) for (a) YIG/GGG, (b) YIG/YAG and (c) a-YIG/YAG thin films. Normal Incidence, TEY, 300K, B = 5T

tribution of approximately 35%. The presence of Fe^{2+} at the a-YIG surface would potentially allow for hopping conduction to occur between Fe^{2+} and Fe^{3+} sites. The existence of metallic states near the a-YIG surface would provide partial explanation for non-local transport in a-YIG between Pt contacts being the result of charge transfer, as argued by [19]. Electron hopping would corroborate a-YIG resistivity measurements of 10^4 Ωm at room temperature: five to six orders of magnitude lower than room temperature single crystal YIG [220, 114].

However, the presence of Fe^{2+} in the a-YIG according to the atomic multiplet calculation calculations is doubtful for many reasons. XANES measured about the Fe K-edge (discussed in Section 5.5) strongly suggests that Fe^{2+} is diminishingly small (if present at all) in the bulk of both a-YIG and YIG films. The a-YIG calculated XMCD lineshape in Figure 5.13(c) does not perfectly match experimental XMCD, both at the L_3 edge (near 706.7 eV and 711 eV) and the L_2 edge. More significantly, a minima at 706eV shown in the multiplet calculations - a signature pre-edge feature of Fe^{2+} - is not present in the experimental XMCD. These factors provide experimental evidence that Fe^{2+} may not be present in the a-YIG, despite it being needed to produce a reasonable match between XMCD and theoretical multiplet calculations at L_3. It is important to emphasise that atomic multiplet calculations are made to match the observed magnetism in the a-YIG XMCD, and do not necessarily reflect true chemical species and stoichiometry.

The parameters used in the multiplet simulations, despite describing crystalline YIG reasonably well, are likely not valid for a-YIG. Theoretical atomic multiplet calculations can only be used an approximate guide for interpreting XMCD, especially in unknown materials. Atomic multiplet theory assumes a material's stoichiometry to be known *a priori*: including crystal field splitting (Dq) and Slater integral reductions. This is reflected in calculations fitting well to the crystalline YIG XMCD and the expected Fe^{3+} T_d:O_h 3:2 stoichiometry. It is not certain that a-YIG stoichiometry is comparable to the crystalline YIG state, either in terms of Fe species or the $Y_3Fe_5O_{12}$ formula unit. Furthermore, atomic multiplet theory is an ionic model that cannot describe iron oxides in full due to the covalent nature of the oxygen bonds [221]. If not known a priori, different variations of calculation parameters and linear combinations of Fe^{2+} O_h:Fe^{3+} T_d:Fe^{3+} O_h produce equally plausible calculations to match XMCD data. This is a known problem in iron oxides such as Fe_3O_4, where several groups calculate XMCD of stoichiometric Fe_3O_4 differently *ab initio* based on their choice of Dq and Slater parameters [222, 223]. To assess the a-YIG properly, a rigorous study using all known permutations of YIG multiplet calculation parameters to fit to the XMCD would be required; this is far beyond the scope of this work. Additional effects such as charge transfer between Fe^{3+} and oxygen ligands would also require serious consideration in performing such calculations.

The remainder of the XMCD results will only consider atomic multiplet calculations to

experimental XMCD data. Non-linear backgrounds and background subtraction procedures were highly influential on obtained XMCD and integrals. This is especially true for the a-YIG XMCD - an order of magnitude weaker than crystalline YIG samples. As a result, XMCD sum rule analysis to evaluate μ_L/μ_S as a function of sample or annealing temperature was not successful. Beyond comparisons of μ_L/μ_S between a-YIG and YIG at room temperature (shown in Figure 5.12), trends with temperature on individual samples were too highly influenced by background to be considered physical.

5.4.1 Atomic Multiplet Calculations with Sample Temperature

Averaged XAS spectra for as-deposited a-YIG/YAG and crystalline YIG/YAG acquired at different sample temperatures are shown in Figure 5.14(a) and (b) respectively. For both a-YIG and YIG, the most significant temperature-dependence occurs on the 707.7 eV shoulder of the L_3 edge. At all temperatures, absorption is greater at this point in the a-YIG film than in the crystalline YIG. σ^+ and σ^- XAS for the a-YIG and YIG (at 10K and 300K) are shown in Figure 5.14(c) and (d). For the crystalline YIG XAS, the σ^+ and σ^- spectra are similarly shaped at both 10K and 300K. This is reflected in the crystalline YIG/YAG XMCD spectra acquired at different sample temperatures, shown in Figure 5.14(f). The XMCD lineshape for crystalline YIG/YAG remains fairly consistent with temperature, maintaining 3 peaks across the L_3 edge with no notable shifts in photon energy, and a positive L_2 structure. The magnitude of the XMCD signal is observed to decrease with increasing sample temperature. This agrees with the film's ferrimagnetic M(T) response: YIG/YAG (650°C) from Figure 5.9(b).

In contrast, the σ^+ and σ^- XAS spectra in as-deposited a-YIG/YAG show a noticeable temperature dependence. At 10K, the difference between σ^+ and σ^- is greater at the 707.7eV shoulder at the L_3 edge, as well as L_2 edge, than in XAS at 300K. However, other features of the XAS (such as the 708.8eV maxima at L_3) show little temperature dependence, with σ^+ and σ^- being similar. This is reflected in the a-YIG/YAG XMCD lineshape in Figure 5.14(e), varying significantly between 10K to 300K. XMCD spectra and multiplet calculations for a-YIG/YAG at 10K and 300K are also reproduced in Figure 5.15 for direct comparison.

a-YIG XMCD at 10K shows a reduced maximum at the L_3 edge, with the minima at 707.5eV and 709.5eV dominating. Approaching 300K, the now-shifted 707.8eV minimum reduces in magnitude, and the XMCD is instead dominated by the maximum at 708.5eV and the 709.5eV minimum (shown also in Figure 5.13(c)). The reduction of the 707.5eV minimum implies that the O_h Fe species in the a-YIG have an explicit dependence on sample temperature, where larger contributions are observed as the sample is cooled. Other changes in the a-YIG XMCD are noted; at 10K and 50K, the 707.5eV minimum is particularly broad in energy - potentially composed of two peaks - before narrowing significantly at 100K and above. In addition, this minimum shifts by 0.3eV to higher energy with increasing sample temperature, while the other

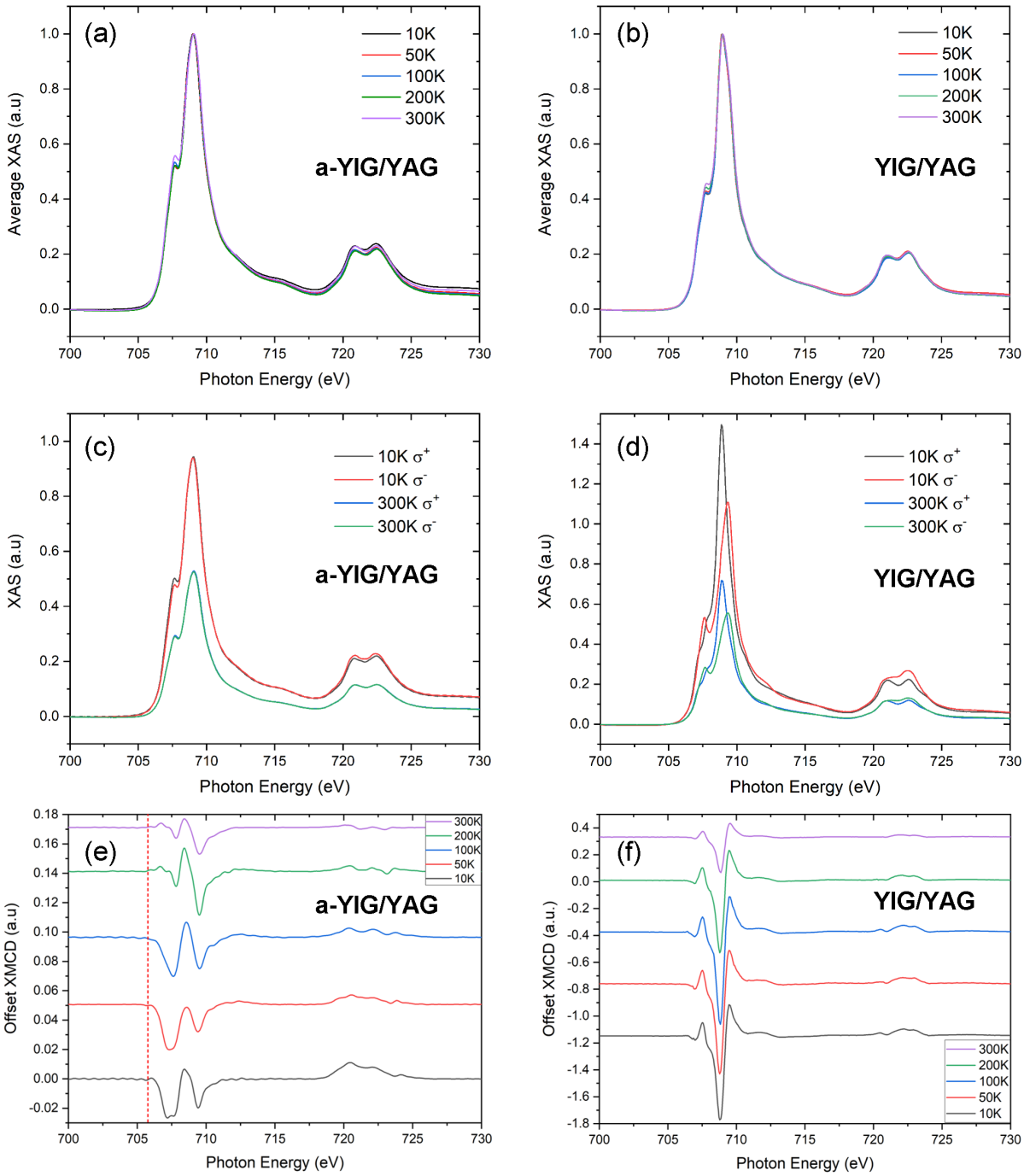

Figure 5.14: Averaged XAS spectra for (a) a-YIG/YAG and (b) YIG/YAG. σ^+ and σ^- XAS for (c) a-YIG/YAG and (d) YIG/YAG. (e) XMCD spectra of a-YIG/YAG and (f) YIG/YAG for different sample temperatures. Normal Incidence, TEY, B = 5T. The red dashed line in (e) indicates the expected energy of the Fe^{2+} O_h pre-edge signature, absent from all experimental XMCD.

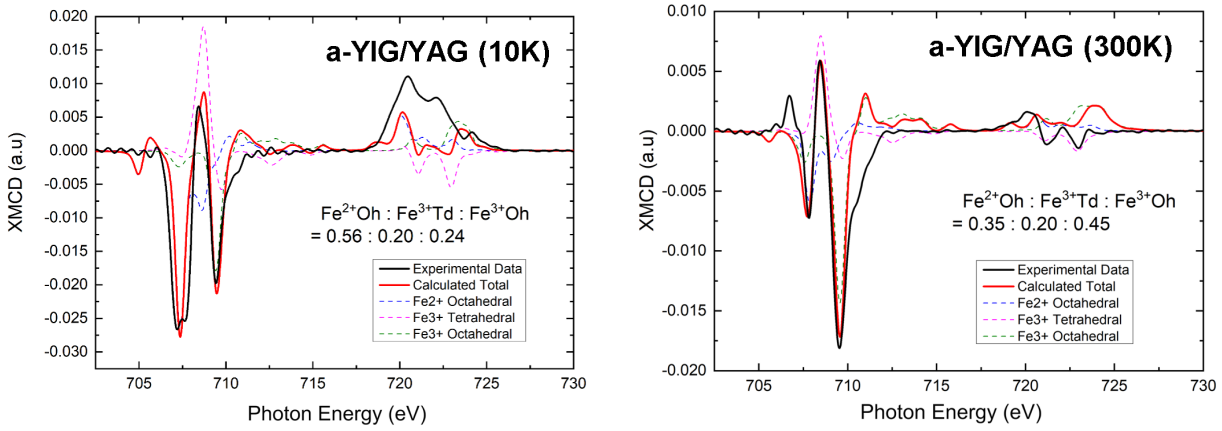

(a) (b)

Figure 5.15: Atomic multiplet calculations for a-YIG/YAG XMCD measured at (a) 10K and (b) 300K - reproduced from Figure 5.13.

peaks remain at fixed energies. The smaller peak at 706.7eV is also seen to emerge in the XMCD lineshape at 200K and 300K.

Temperature dependence seen in Fe $L_{3,2}$ XMCD is typically attributed to Fe^{2+} impurities in XAS studies (for example, in MgO thin films [224]). Atomic multiplet calculations also show that Fe^{2+} O_h and Fe^{3+} O_h have the largest variation with temperature between 707-708eV. However, as discussed in the previous section, the presence of Fe^{2+} in the a-YIG is considered unlikely, given the XANES data and absence of an Fe^{2+} pre-edge feature in the XMCD. This is a significant observation, although the mechanism behind this temperature-dependence cannot be explained at present. This temperature dependence appears similar to the M(T) behaviour measured from the VSM-SQUID, whereby the 707-708eV minimum narrows and shifts to higher-energy above the spin-freezing temperature of 50K. It can be hypothesised that the XMCD broadening at 707.5eV reflects the freezing of spins in the a-YIG to a ground state. Experimentally testing this would require M(T) measurements performed using XMCD.

Fe site contributions from atomic multiplet calculations of a-YIG/YAG and YIG/YAG as a function of sample temperature are shown in Figure 5.16. Calculated spectra were generated at each sample temperature respectively. Multiplet contributions have been grouped to consider T_d Fe^{3+} sites, and O_h (Fe^{2+} and Fe^{3+}) sites respectively. Here, calculated contributions to XMCD are considered in two ways. Firstly, T_d and O_h contributions as a ratio adding to 100% of the total atomic multiplet calculation are shown in Figure 5.16(a)(i) and (b)(i). For YIG/YAG - Figure 5.16(b)(i) - T_d Fe^{3+} sites and O_h (Fe^{2+} and Fe^{3+}) atomic multiplet contributions remain fairly consistent from 10K to 300K: T_d Fe^{3+} ranging from 67% to 64%, and O_h (Fe^{3+}) from 33% to 36% respectively; no Fe^{2+} contributions were required.

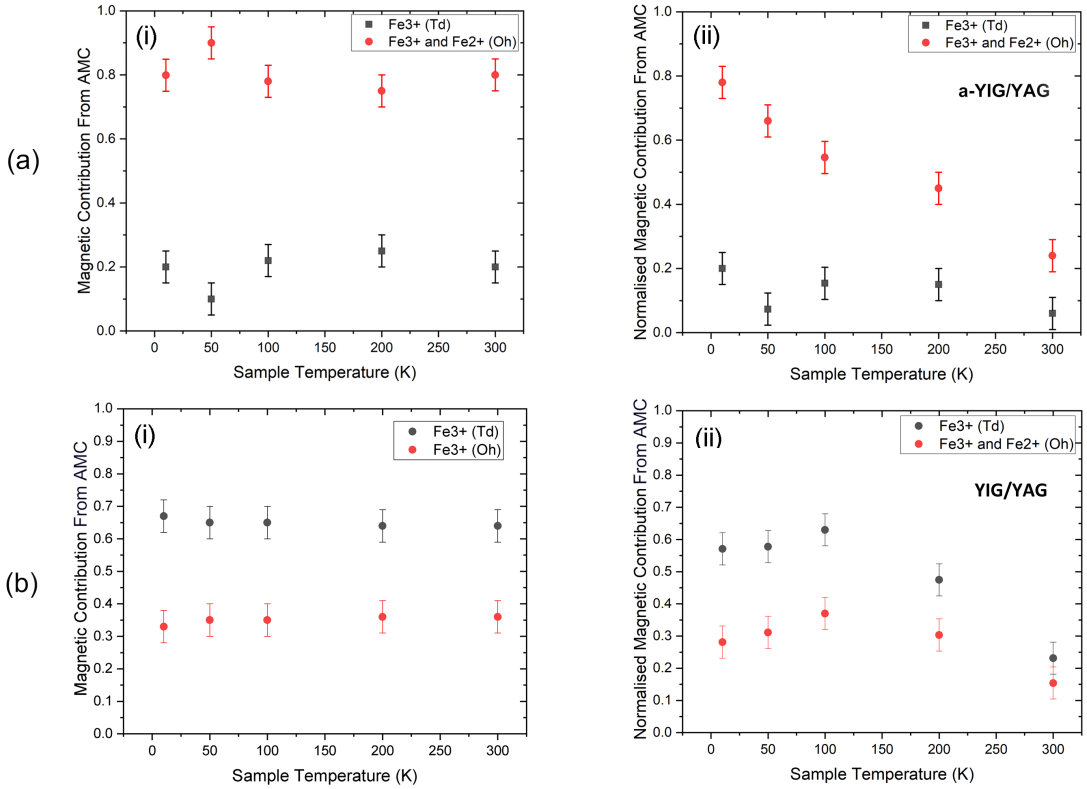

Figure 5.16: Fe site contributions to (a) a-YIG/YAG and (b) YIG/YAG magnetism from atomic multiplet calculations, as a function of sample temperature. Values from atomic multiplet calculations spectrum fitting (i), and normalising calculation contributions to the size of the XMCD signal (ii) are shown.

In contrast, a-YIG/YAG contributions to XMCD are strongly dominated by O_h species at 10K, comprising approximately 80% of the total calculated fit. Despite the presence of Fe^{2+} O_h being unlikely from the experimental XMCD and XANES data, multiplet calculations required a significant contribution of Fe^{2+} O_h at all sample temperatures to reproduce the L_3 edge lineshape in the a-YIG XMCD data. Fe^{2+} O_h contributions are maximal for the 10K spectra (Figure 5.15(a)), at 56% of the total. The required Fe^{2+} O_h contribution decreased with sample temperature to 35% at 300K (Figure 5.15(b)). However, Fe^{3+} O_h instead increased with sample temperature, from 24% to 45% at 10K and 300K respectively; the total contribution from O_h species was seen to be consistent at (80 ± 5)% at most temperatures, as shown in Figure 5.16(a)(i). Contributions from the T_d Fe^{3+} account for between (20 ± 5)% of the total across all temperatures, reflecting the observed XMCD lineshapes for a-YIG/XMCD. 50K, however, is an anomaly. Shown in Figure 5.14(e), the T_d Fe^{3+} peak at 708.8eV unexpectedly drops below zero in the experimental 50K XMCD: producing an anomalously low T_d Fe^{3+} contribution in the multiplet calculations. 50K XMCD anomalies are acknowledged again in Section 5.4.2.

Secondly, atomic multiplet contributions have also been 'normalised' to take into account

the magnitude of the experimental XMCD signal itself: Figure 5.16(a)(ii) and (b)(ii). Following [159], a calculated atomic multiplet fit for XMCD is a sum of contributions from (Fe^{2+} O_h:Fe^{3+} T_d:Fe^{3+} O_h) multiplied by a scalar to match the magnitude of the experimental XMCD. With a series of atomic multiplet fits - e.g. against sample temperature - the largest XMCD spectrum can be used to normalise all others in the series. This normalisation scales atomic multiplet contribution values to reflect the magnitude of the XMCD signal; the difference between the normalised T_d Fe^{3+} and O_h (Fe^{2+} and Fe^{3+}) multiplet values becomes directly proportional to the XMCD magnitude, and thus magnetism of the sample. Shown in Figure 5.16(a)(ii) and (b)(ii), the magnetism of both the as-deposited a-YIG/YAG and YIG/YAG is observed to decrease with temperature, minimal at 300K.

5.4.2 Atomic Multiplet Calculations with Annealing Temperature

T_d Fe^{3+} sites and O_h (Fe^{2+} and Fe^{3+}) site contributions to atomic multiplet XMCD fitting have also been evaluated in a-YIG/YAG as a function of annealing temperature: as-deposited, 200°C, 400°C, and 650°C YIG/YAG respectively. Five separate multiplet contribution against annealing temperature plots are shown in Figure 5.17(a), measured at five different sample temperatures between 10-300K. At most sample temperatures, the magnetic contributions of the Fe^{3+} T_d to the atomic multiplet calculations of a-YIG (between as-deposited and 400°C annealing) either increase slightly from 10% to 20%, or remain consistent at (20 ± 10)% with annealing temperature. This is until recrystallisation of the YIG/YAG occurs at 650°C, where the Fe^{3+} T_d becomes the dominant species, and Fe^{2+} contributions to the O_h Fe species are negligible. 50K, however, is an anomaly, where atomic multiplet fitting to a-YIG XMCD produced a more sizable increase in Fe^{3+} T_d from 10% to 40% with ex-situ annealing between as-deposited and 400°C; O_h (Fe^{2+} and Fe^{3+}) contributions were correspondingly smaller. No explanation for this is given at present. The XMCD being measured near the a-YIG spin-freezing temperature of a-YIG at (45 ± 2)K may be a relevant factor, or otherwise a coincidence.

Normalisation of the atomic multiplet contributions to the magnitude of the XMCD signal - as discussed in the previous section - is shown in Figure 5.17(b). Normalising to XMCD magnitude across the annealing temperature series suggests that magnetic contributions in the a-YIG remain stable with ex-situ annealing across the tested temperature range. Compared to the change upon the YIG recrystallising at 650°C, it is arguable that magnetism in a-YIG/YAG is not significantly affected by ex-situ annealing at 200°C and 400°C, remaining similarly small in all cases. Whether this is true for a-YIG/YAG films ex-situ annealed at 500°C, 550°C and 600°C - whose M(T) differs significantly to a-YIG/YAG annealed to 400°C - is not known in the absence of XMCD data for these samples. This temperature range presents an area of interest for future XMCD work on a-YIG/YAG.

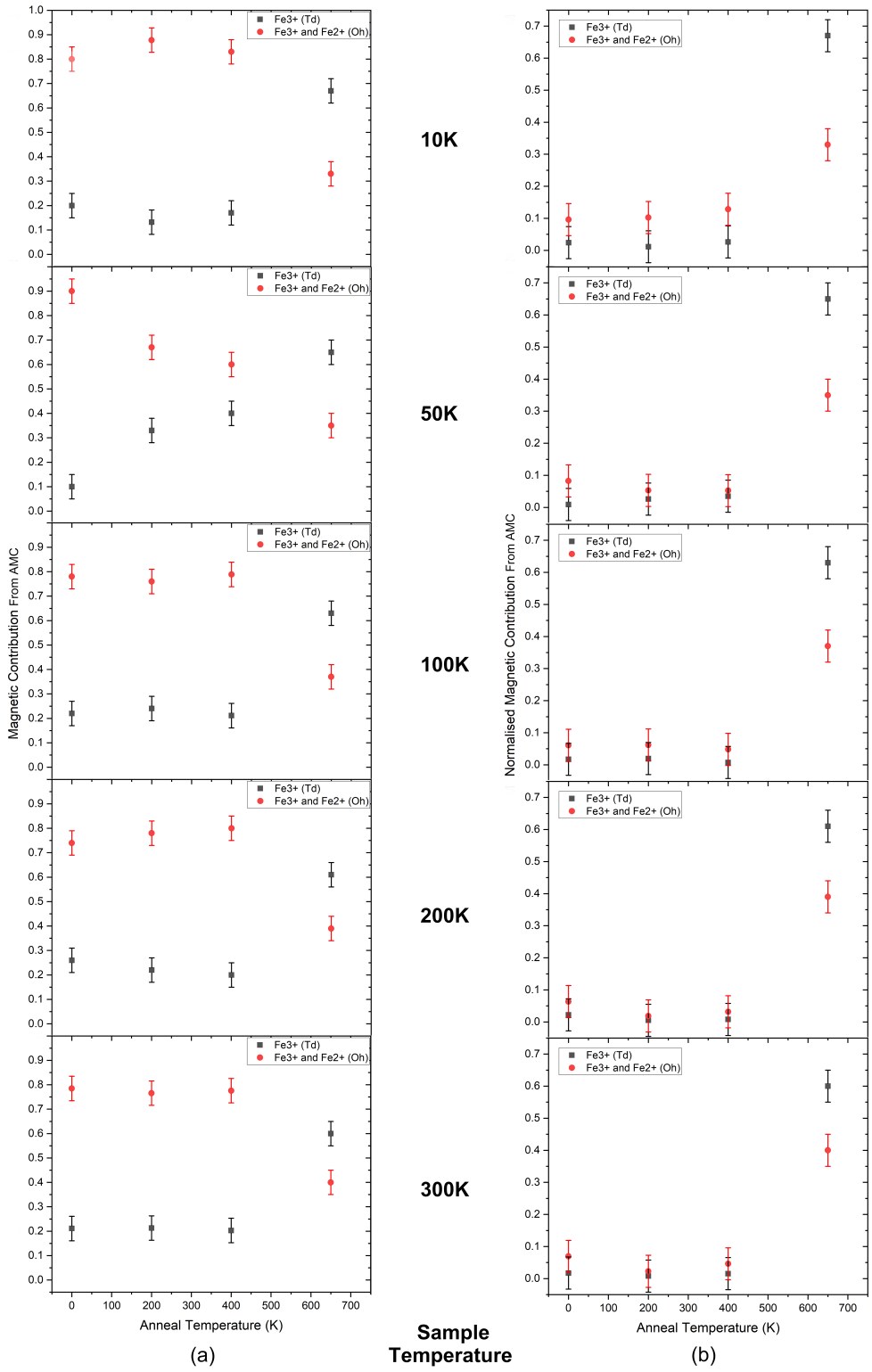

Figure 5.17: Fe site atomic multiplet contributions from XMCD fitting, as a function of annealing temperature. Atomic multiplet values from both (a) spectrum fitting, and (b) normalisation to the size of the XMCD signal are shown.

5.5 EXAFS and XANES

Detailed measurements using XANES/EXAFS at the Fe K edge were performed on the a-YIG/YAG films to assess potential changes in Fe valence or local short range order with annealing temperature. YIG/GGG was also measured as a comparison. The aim was to investigate disorder in amorphous YIG to ascertain if low temperature annealing modifies structural and therefore magnetic interactions, potentially allowing for long spin lifetimes. As the films were amorphous (both as-grown and post low temperature annealed), X-ray diffraction offered no information on the local or long range structure requiring more sophisticated techniques to be used to obtain detailed structural information. By using Fe K–edge XANES and EXAFS, the valence and potential co-ordination peaks of Fe cations as a function of the anneal temperature of a-YIG was investigated. The process of x-ray spectroscopy offered by XANES/EXAFS is described in Chapter 3.

5.5.1 XANES

XAS data over the Fe K-edge from the YIG/GGG is shown in Figure 5.18(a). It is notable that significant substrate reflections are still present in the YIG/GGG XAS, producing spikes at energies above the absorption edge. The dominant Fe valence was inferred from analysis of the 1s to 3d pre-edge XANES feature, following methods similar to [179, 225, 226]. XAS data was normalised using the ATHENA program [182] at the K-edge step. A spline fit to the tail of the absorption edge was subtracted as a background to isolate the 1s to 3d pre-edge feature. The spectral shape of the pre-edge feature was fit to a convolution of two pseudo-Voigt functions to evaluate Fe^{2+} and Fe^{3+} species contributions: initially centred at 7112eV and 7114.5eV respectively, with Gaussian and Lorentzian contributions allowed to vary. All fittings tended towards a single Gaussian of Fe^{3+} species valence with an energy centroid of (7114.2 $\pm$ 0.2)eV. The lack of convolution in the pre-edge spectral shape (and fit) indicates a very high $Fe^{3+}/\Sigma Fe$ ratio; an $Fe^{3+}/\Sigma Fe = 0.87$ shows significant skew from 7114eV towards lower x-ray energies [179]. $Fe^{3+}/\Sigma Fe$ approaching 1 also agrees with the atomic multiplet calculations fit to the YIG/YAG and YIG/GGG XMCD data in Section 5.4, where Fe^{2+} contributions are zero.

K-edge XAS for the a-YIG/YAG thin films is shown in Figure 5.18(b). The effect of substrate reflections is smaller in the YIG/YAG XAS, likely due to the larger mismatch in lattice constants between YIG-YAG (compared to YIG/GGG). For all a-YIG/YAG, the 1s $\rightarrow$ 3d transition feature also tends to a single Gaussian centred at (7114.2 $\pm$ 0.2)eV, indicating a similarly high Fe^{3+}/Fe to the YIG/GGG. This fitting is seen for all tested annealing temperatures. This is in contrast to atomic multiplet calculations fitting of the a-YIG XMCD - Figure 5.12(c) - which suggests a distinct Fe^{2+} contribution to a-YIG surface magnetism. Bulk sensitive XANES exhibiting a Fe^{3+}/Fe approaching 1 suggests that the Fe^{2+} suggested by the XMCD

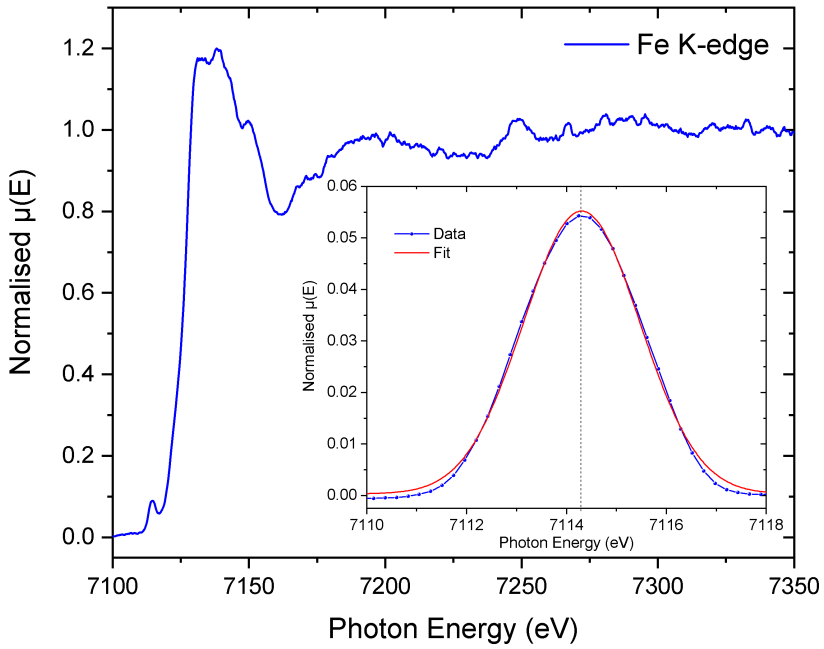

(a)

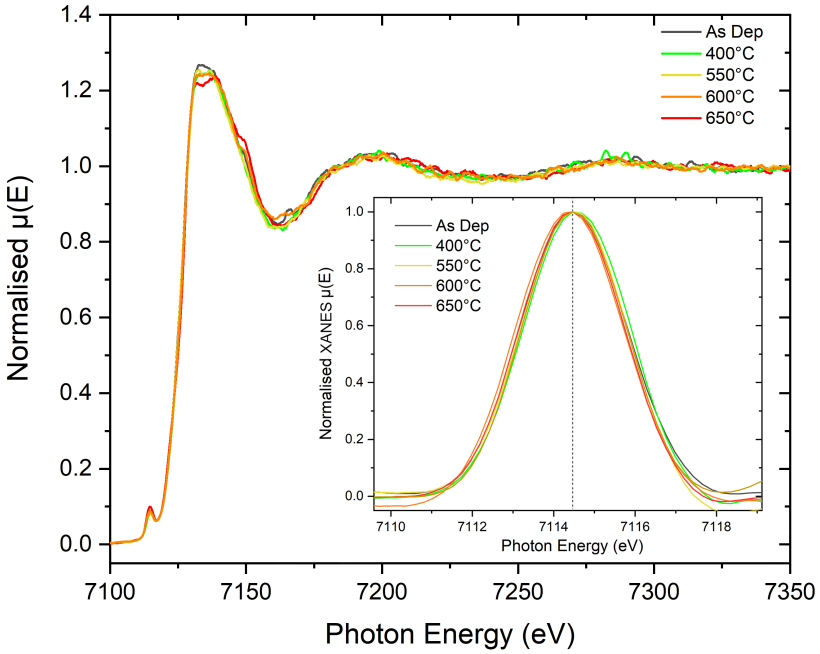

(b)

Figure 5.18: XAS for taken over the Fe K-edge for (a) YIG/GGG and (b) a-YIG/YAG and YIG/YAG films subject to different ex-situ annealing temperatures. Insets show pre-edge XANES of the 1s $\rightarrow$ 3d transition feature, following spline subtraction. Peak fitting tends to a Gaussian centred at 7114.2eV, indicating an Fe^{3+}/Fe approaching 1.

atomic multiplet calculations is not a true chemical species in the a-YIG (not stoichiometric), and instead reflects an attempt to fit to the a-YIG magnetism only.

5.5.2 EXAFS

In addition to the XANES data, structural analysis was performed using the EXAFS data. Background correction and Fourier transforms were performed by the ATHENA program [182]. For all samples, a k-weight of k^3 was found to produce oscillations in k of a similar amplitude to reasonably high k, while avoiding glitches (from 3 to 11 $Å^{-1}$). The magnitude of the forward Fourier transformed EXAFS spectra are shown in Figure 5.19. Shown in Figure 5.19(a), crystalline YIG/GGG and YIG/YAG spectra show two significant peaks in r-space: a first coordination peak centred at (1.5 ± 0.1)Å, and a smaller second coordination peak at (3.4 ± 0.1)Å. A potential third peak also exists at (5.4 ± 0.1)Å for both films. A shouldering peak at 4.9Å is also observed in this third coordination peak in YIG/GGG spectra that does not correlate to YIG/YAG spectra. It is difficult to discern whether 4.9Å or 5.4Å is the true third coordination distance in YIG/GGG for two reasons. Firstly, substrate contributions in the YIG/GGG XAS (Figure 5.18(a)) were difficult to smooth out, and influence high-K components of the fourier transform to r-space. This is evidenced in systematic broadening and shouldering artefacts in all three coordination peaks in YIG/GGG r-space EXAFS (mostly absent in YIG/YAG r-space EXAFS peaks). Secondly, both 4.9Å and 5.4Å correspond to either simulated or reported Fe-Fe distances in YIG, discussed below.

A first-order coordination peak at (1.5 ± 0.1)Å is common to all measured YIG and a-YIG samples, in agreement with EXAFS performed on nanocrystalline YIG powders [227] and correlating to Fe-O distances. Second and third peaks show broad agreement with Fe-Fe distances measured from VESTA simulations of the conventional YIG unit cell; Fe-Fe distances between a central Fe^{3+} O_h cation and its nearest neighbour Fe^{3+} T_d (3.51Å) and Fe^{3+} O_h (5.44Å) were measured. The second-nearest Fe^{3+} O_h to Fe^{3+} T_d distance was also measured to be 5.66Å. These distances are illustrated in Figure 5.20. The second coordination peak also parallels that of nanocrystalline YIG powders [227], observed at 3.3Å. Magnetic neutron scattering distribution functions for amorphous YIG from Chukalkin *et al.* (1989) [228] also appear to broadly reflect the observed coordination peaks in Figure 5.19. Chukalkin *et al.* illustrate spatial distributions of magnetic iron cations that show two positive extrema at r = 0.14nm and 0.48nm, and a negative extrema at r = 0.36nm. These extrema of opposing signs are considered to evidence the nearest-neighbour ferro- and antiferromagnetic orientations of magnetic moments in the amorphous YIG: an (unexpected, direct-exchanged) Fe-Fe moment, and superexchanged Fe^{3+} O_h-Fe^{3+} T_d and Fe^{3+} O_h-Fe^{3+} O_h moments respectively. A minimum superexchanged Fe-Fe distance in crystalline YIG of 0.346nm is calculated by Chukalkin *et al*, in agreement with their magnetic scattering data for a-YIG, as well as both [227] and the

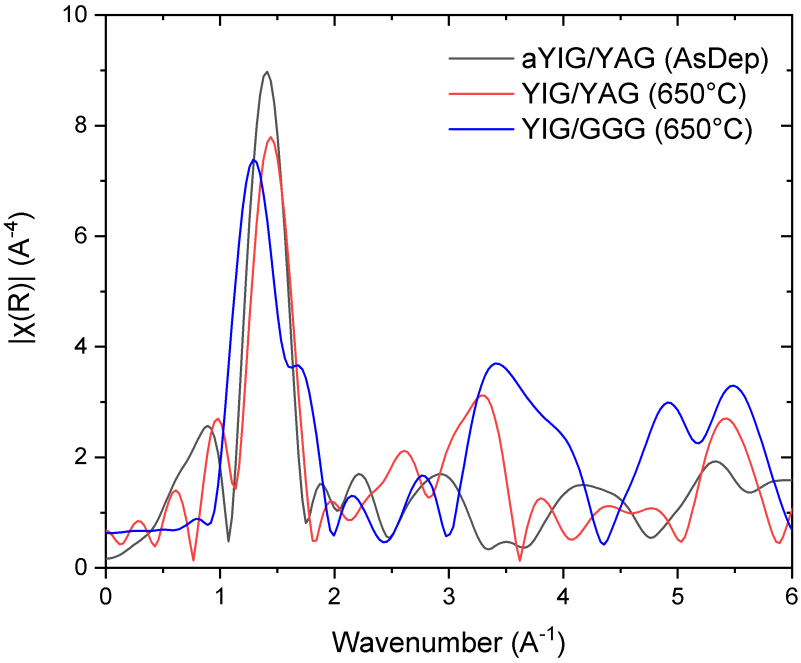

(a)

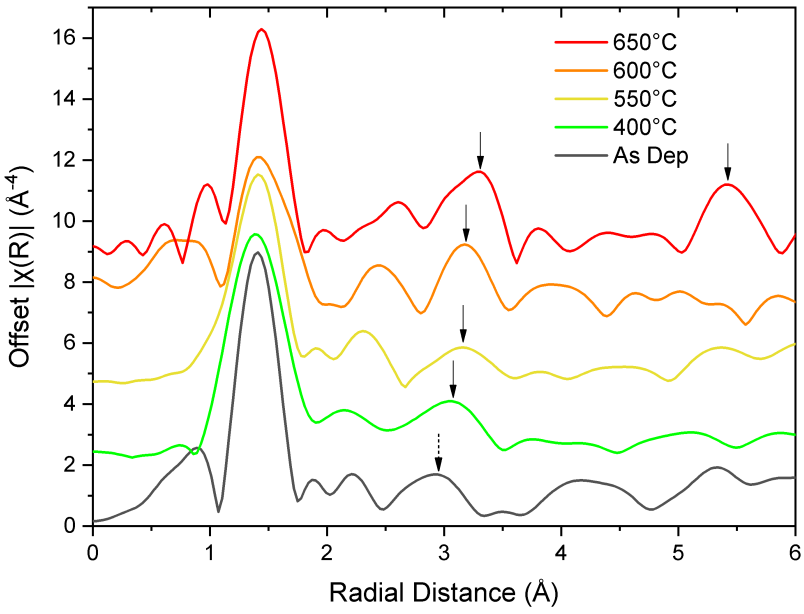

(b)

Figure 5.19: Magnitude of the k^3-weighted Fourier transform of the EXAFS signals at the Fe K-edge for: (a) YIG/GGG, YIG/YAG and as-deposited a-YIG/YAG thin films, and (b) a-YIG/YAG and YIG/YAG films subject to different ex-situ annealing temperatures. Arrows in (b) indicate coordination peaks above first-order.

r-space EXAFS data shown in Figure 5.19(b) (second coordination peaks)..

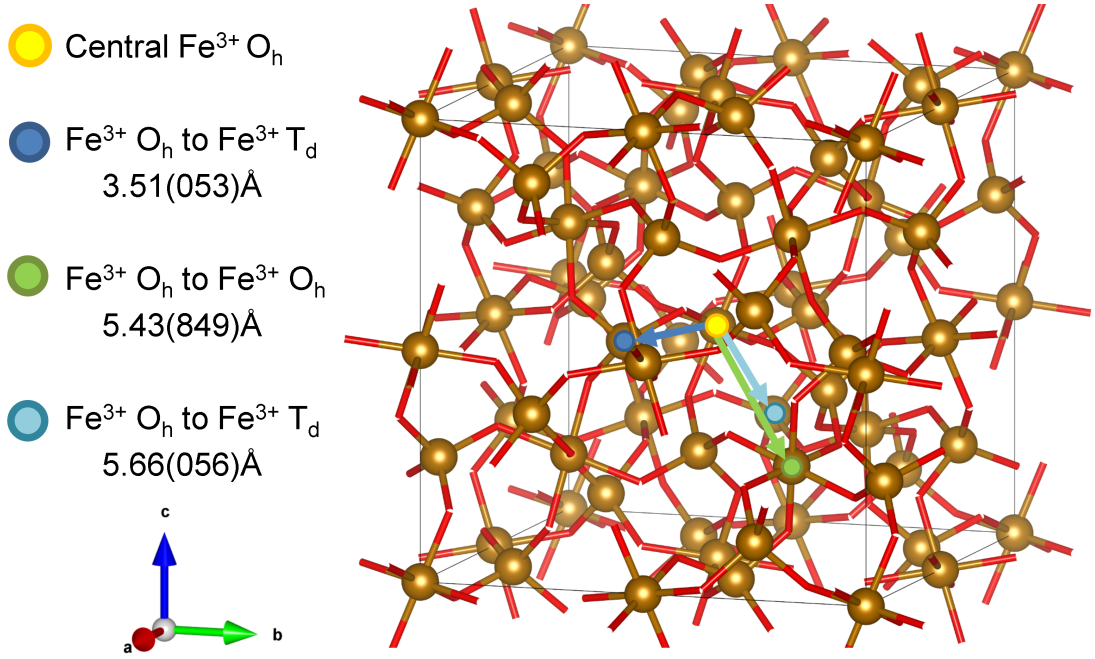

Figure 5.20: VESTA simulation of the conventional YIG unit cell for YIG: generated to show only Fe atoms with Fe-O bonds (red) to indicate coordination. Fe-Fe distances from a central Fe^{3+} O_h ion are shown with coloured arrows. Note, multiple Fe atoms surrounding the central Fe^{3+} O_h exist with these illustrated Fe-Fe distances.

Fourier transformed r-space spectra for the a-YIG/YAG films are shown in Figure 5.19(b). In contrast to crystalline YIG, peaks in the as-deposited a-YIG/YAG spectra are difficult to distinguish from other high-r background fluctuations. An Fe^{3+} O_h-Fe^{3+} T_d coordination peak at (2.9 ± 0.1)Å in the as-deposited a-YIG is arguable. The same was true of a-YIG/YAG ex-situ annealed at 200°C. However, a structure more clearly resembling a second order coordination peak in Figure 5.19 emerges in a-YIG/YAG annealed at 400°C, at a distance of (3.0 ± 0.1)Å. Between 400°C a-YIG/YAG and 650°C YIG/YAG, this second coordination peak shows a potential trend towards higher-r with annealing temperature; this peak reaches (3.3 ± 0.1)Å in crystalline YIG/YAG at 650°C. The second and third coordination peaks are more distinguishable for crystalline YIG/YAG annealed at 600°C and 650°C. This corroborates the XRD measurements from Figure 5.1, whereby obvious structural changes or recrystallisation are only observed in the a-YIG/YAG at and above 600°C ex-situ annealing.

5.6 Summary and Conclusions

In this chapter, four 80nm a-YIG films have been fabricated on YAG substrates by room temperature PLD and annealed ex-situ in air at varying temperatures between as-deposited and 650°C (the threshold for YIG crystallisation). This annealing attempted to modify the chemical and magnetic disorder of the a-YIG: assessing if a-YIG could be made to have differing 'amorphousness' and Fe environments. Normal incidence XAS and XMCD measurements were performed at the Fe $L_{2,3}$-edges, and fitted with atomic multiplet calculations to determine the co-ordination and valences of the Fe sites in both the a-YIG and YIG samples, as well as investigate their contribution to the sample's overall magnetic structure. XAS measurements were performed at the Fe K-edge, from which XANES was analysed to infer the proportion of Fe^{3+}, and EXAFS was used to infer 1st and 2nd coordination distances of iron cations in the XMCD samples: in addition to a-YIG/YAG thin films annealed at 500°C, 550°C and 600°C respectively. Supplementary structural characterisation via XRD and magnetic characterisation using room-temperature and temperature-dependent VSM were attempted on both the a-YIG and YIG films.

Recrystallisation of YIG/YAG was observed at 650°C, and characterisation was successful. X-ray diffraction showed an epitaxial YIG/YAG thim film with compressive out-of-plane strain, similarly to YIG/YAG presented in Chapter 4. Magnetic hysteresis in YIG/YAG annealed above 600°C is clear from VSM, with magnetisation approaching (94 ± 5)emu/cc and coercivity of (47 ± 2)Oe. M(T) data shows the expected ferrimagnetic response. YIG/YAG annealed at 600°C shows similar M(H) and M(T) behaviour, albeit with reduced magnetisation. XMCD measurements over the Fe $L_{3,2}$ edges show a lineshape comparable to both a YIG/GGG (650°C) thin film grown as a comparison, as well as YIG XMCD in literature. Atomic multiplet calculations fit to the YIG/YAG XMCD also suggest an Fe^{3+} T_d:O_h ratio in YIG/YAG of 64:36 (±5 on each), approaching the expected 60:40 (3:2) ratio of stoichiometric YIG, and with no Fe^{2+} contribution being required. XANES measured over the Fe K-edge confirms YIG/YAG is almost entirely composed of Fe^{3+} species, with the pre-edge 1s→3d transition tending to a Gaussian centred at (7114.2 ± 0.2)eV: indicating a very high Fe^{3+}/Fe ratio approaching 1. This is comparable to the YIG/GGG 650°C film, where the expected 60:40 ratio is observed, with near identical XANES. Three Fe coordination distances of (1.5 ± 0.1)Å, (3.4 ± 0.1)Å, and (5.4 ± 0.1)Å are confidently inferred from k-edge EXAFS in YIG/YAG. These distances broadly agree with expected Fe-O and Fe-Fe distances in YIG from EXAFS and magnetic scattering distributions in literature.

Characterisation of a-YIG/YAG as a function of annealing temperature has been only partly successful. a-YIG/YAG annealed below 600°C showed no discernible features for structural analysis; X-ray diffraction showed no clear diffraction peaks of the YIG near the (444) reflection or in broad scans, confirming the a-YIG was amorphous in nature. However, K-edge EXAFS

shows a potential trend in r-space with the Fe^{3+} O_h-Fe^{3+} T_d coordination peak. This Fe-Fe distance increases from (2.9 ± 0.1)Å towards a higher r of (3.3 ± 0.1)Å with annealing temperature. An Fe-O coordination peak at (1.5 ± 0.1)Å is seen at all temperatures. Room temperature VSM measurements of the a-YIG were difficult to perform, due to both unexpected hysteresis in the YAG(111) substrates, and the a-YIG M(H) being similar in size to baseline signal of the quartz rod. M(H) acquired from a-YIG/Si suggests that a-YIG magnetism is extremely weak (below 2emu/cc). M(T) measurements of a-YIG/YAG and a-YIG/Si show characteristic spin-glass behaviour with a spin freezing peak T_F at (44 ± 2)K, below which ZFC and FC are observed to split. Contrary to Wesenberg *et al.* [18], no clear ZFC/FC splitting at high temperature was observed. M(T) was observed to change for a-YIG/YAG annealed at 550°C, where a M(T) response in-between the spin-glass response and ferrimagnetic response is observed (despite no clear structural features at this temperature), before ferrimagnetic YIG/YAG at and above 600°C. In contrast, M(T) of a-YIG/Si remained stable with annealing up to 650°C.

X-ray magnetic spectroscopy performed on a-YIG/YAG has also only been partly successful in characterising the material. a-YIG XMCD measured over the Fe $L_{3,2}$ edges is an order of magnitude smaller than in YIG, owing to significantly weaker magnetism. The XMCD lineshape is an effective reversal of the YIG lineshape, with peaks over the L_3 edge being oppositely oriented. Atomic multiplet calculations indicate that a-YIG magnetism is approximately 80% dominated by O_h Fe species. Theoretical multiplet calculations also suggest a significant Fe^{2+} O_h contribution of 35% in a-YIG at 300K. However, this is contradicted by Fe K-edge XANES indicating a Fe^{3+}/Fe ratio approaching 1 (identically to the crystalline YIG). The absence of a minima at 706eV in the experimental a-YIG XMCD (a signature of Fe^{2+}) also indicates that Fe^{2+} species are ultimately absent from the a-YIG.

Considering the ratio of O_h:T_d Fe species, multiplet calculations suggest that O_h-dominated magnetism in a-YIG is stable with sample temperature. O_h-dominant contributions to a-YIG magnetism are also stable with ex-situ annealing up to 400°C, in comparison to the change observed upon the a-YIG recrystallising at 650°C. It is concluded that a-YIG magnetism is both very weak and not significantly affected by changes in structure due to ex-situ annealing, before recrystallisation occurs. The experimental a-YIG XMCD has also shown an unexpected temperature-dependence, with a particularly broad L_3 edge structure at 707.5eV potentially composed of two peaks appearing below 50K. This structure narrows and shifts by 0.3eV to higher energy, while the other L_3 peaks remain at fixed energy. No explanation for this temperature dependence can be given at present.

Chapter 6

FMR Spin Pumping Study of YIG/a-YIG/Pt Trilayers

The mediation of spin transport through ferromagnetic insulators has become a significant topic of interest in spintronics, since the demonstration of non-local transport by magnons in the ferrimagnetic insulator YIG by Kajiwara *et al.* [3]. More recently, antiferromagnetic insulators have presented exciting new possibilities for magnonic device development, with observable spin transport mediated either via magnons or local magnetic correlations. For amorphous YIG, spin transport was first demonstrated by Wang *et al.* (2015). in an FMR spin-pumping geometry [20]. Non-local transport between Pt contacts was later reported by Wesenberg *et al.* (2017) [18]. These works are described in more detail in Section 2.6.2. However, repeat experiments by other groups have failed to observe similar spin-transport in either geometry. Instead, non-local spin transport in a-YIG is seen to be very small, or entirely absent. Observed non-local signals are considered a result of a-YIG resistivity dropping due to Joule heating, or defects in a-YIG trilayer spacers [19, 21]. It is hypothesised that samples of a-YIG may, in fact, have differing levels of 'amorphousness' and Fe cation distributions, which are highly dependent on growth conditions, leading to differences in reported a-YIG behaviour.

In this chapter, the study of a series of thin-film YIG/a-YIG/Pt trilayers is presented. Six YIG/a-YIG/Pt trilayers have been grown, with a-YIG thickness being the variable of interest. Each trilayer has been structurally and magnetically characterised, with particular attention drawn towards FMR spectroscopy measurements. The dependence of FMR spin-pumping observed in these trilayer structures with a-YIG spacer thickness is presented and analysed. The chapter concludes with a discussion of the FMR spin-pumping observed in these trilayer structures, and its significance in the context of how spin-transport may be mediated in amorphous YIG.

6.1 Trilayer Preparation and Growth

Six samples of amorphous YIG were deposited by room-temperature PLD onto 5x5mm GGG (111) substrates, to a nominal thickness of 45nm. In all cases, the GGG substrate was pre-cleaned in acetone (sonicated for 5 minutes) and then in IPA (sonicated for 5 minutes). The cleaned substrates were then dried using a nitrogen gun to prevent the formation of solvent residue. In-situ outgassing of the GGG with the CO_2 laser was performed at approximately 200°C, in-vacuum at a base pressure of $1x10^{-7}$ mbar for 30 minutes to remove any residual moisture. The substrate was then allowed to cool to room temperature before deposition. The deposition conditions used were identical to the a-YIG/GGG and a-YIG/YAG thin films presented in Chapter 4, given in Table 4.1. The a-YIG layer was then ex-situ annealed in a tube furnace at 850°C (ramping 4°C per minute) in air, for three hours: recrystallising into YIG.

Due to the preparation of YIG on separate GGG substrates via ex-situ annealing, their FMR quality was measured **before** the addition of the subsequent a-YIG and Pt layers. This ensured all the YIG films had comparable Gilbert damping, α, within experimental error, so any observed increases in damping were solely attributed to the layers added thereafter. This layer-by-layer "grow and characterise" approach was taken to the YIG, a-YIG, and eventual Pt layer in all trilayer samples. Advantageously, this allowed changes in damping (if any) resulting from an added a-YIG layer, versus a-YIG and Pt, to be measured independently and compared. However, extra care was taken to ensure minimal surface contamination between growths due to measurements. Consequently, only XRD and FMR measurements were performed layer-by-layer. VSM - requiring adhesive varnish and solvent cleaning - was left until all layers were deposited, and the full YIG/a-YIG/Pt trilayer produced.

After measurement, the YIG film was inspected under optical microscope for potential contamination, before being blown clean by nitrogen gun. In-situ outgassing was used again to remove moisture. However, preliminary tests showed that outgassing YIG/GGG in-vacuum, even for 15 minutes, dramatically worsened its FMR quality and Gilbert damping upon re-measurement by an order of magnitude. Gilbert damping of the YIG increased from $(4.1\pm 0.6)x10^{-4}$ to $(33 \pm 2)x10^{-4}$ following the in-vacuum outgassing. Shown in Figure 6.1(a), Gilbert damping was found to be insignificantly changed within experimental error, if outgassing was instead performed at approximately 300°C (or below) in $1x10^{-1}$ mbar of pure oxygen for 15 minutes. This is a significant observation, highlighting the sensitivity of YIG FMR to preparation conditions when producing trilayers or more sophisticated devices.

Thereafter, room temperature deposition of a-YIG was performed under the same conditions as previously. The thickness of deposited a-YIG layers was varied between 0nm and 30nm, across each of the seven trilayers. The notional thicknesses of a-YIG spacer intended for investigation were: 0nm, 2.5nm, 6nm, 12nm, 20nm and 30nm.

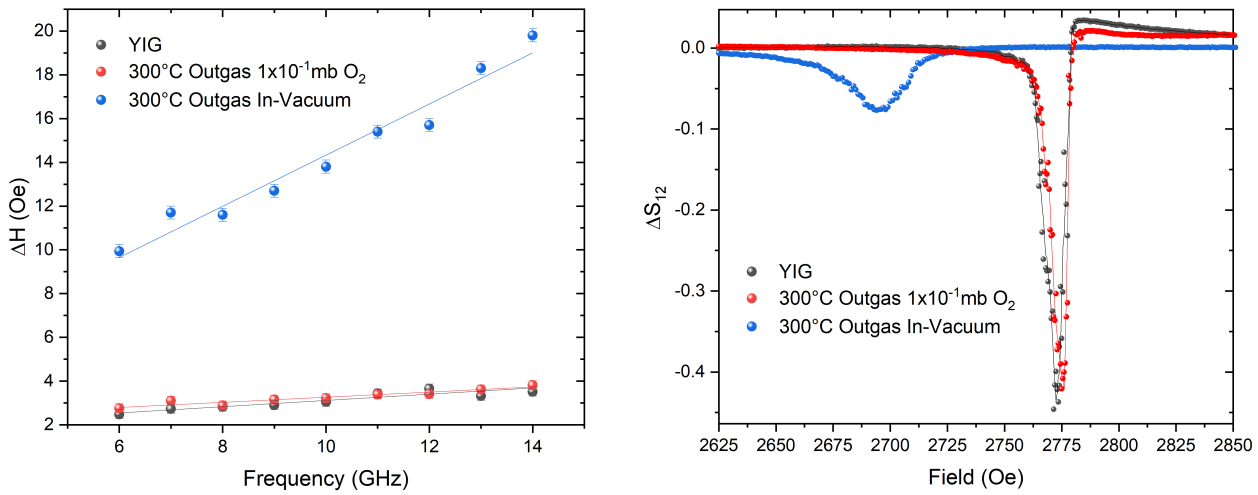

(a) (b)

Figure 6.1: (a) VNA-FMR resonance linewidth versus frequency responses and (b) resonance linescans at 10GHz for a single YIG/GGG thin film: initially as-grown, then after being subjected to in-situ outgassing at 300°C for 15 minutes (at first at 1x10^{-1}mb partial oxygen pressure, and then in vacuum).

The same preparation and outgassing in oxygen procedure was also done to the YIG/a-YIG bilayer before depositing the Pt. Unlike a-YIG, room-temperature Pt deposition is performed in-vacuum at a base pressure of <1x10^{-7} mbar. Pt deposition performed in a background O_2 pressure of 2.5x10^{-3} mbar was found to form an amorphous platinum oxide, instead of platinum. This was evidenced by 4-point electrical resistance vs temperature measurements shown in Figure 6.2(a), and reflects reported Pt thin films from [229, 230], shown in Figure 6.2(b). The room-temperature electrical resistance of (7.5 ± 0.5)nm films of 'platinum' on glass was measured to be (15.0 ± 0.1)Ω for vacuum deposited Pt and (454 ± 1)Ω for oxygen deposited PtO_x. This corresponds to a resistivity of (11.3 ± 0.8)x10^{-8} Ωm for Pt, and (340 ± 20)x10^{-8} Ωm for the PtO_x: highlighting the different composition of the two materials. The vacuum Pt resistivity agrees, within error, with the accepted value of ρ_{Pt} at room-temperature, 10.6x10^{-8} Ωm [109]. All platinum layers for the YIG/a-YIG/Pt trilayers were deposited in-vacuum with a nominal thickness of 5nm. This choice of Pt thickness was based on measurements of spin transport in FM/Pt bilayers performed by Swindells *et al.* (2019), as a function of Pt layer thickness [96]. Swindells *et al.* (2019) show the effective spin-mixing conductance across FM/Pt interfaces increases with Pt thickness, ultimately tending to a maximum, constant value at and above 2nm of Pt. A Pt thickness of 5nm ensures that the YIG/Pt bilayer, and a-YIG/Pt interfaces in the trilayers, are within this regime of spin mixing conductance being independent of Pt thickness. A Pt thickness of 5nm also exceeds values of spin diffusion length for Pt (measured by FMR spin pumping), at approximately 1.2nm at room temperature [231]. Furthermore, 5nm

thick Pt layers were also used for the (ISHE detected) measurements of FMR spin-pumping in YIG(20nm)/a-YIG(t)/Pt(5nm) trilayers performed by Wang *et al.* (2015) [20].

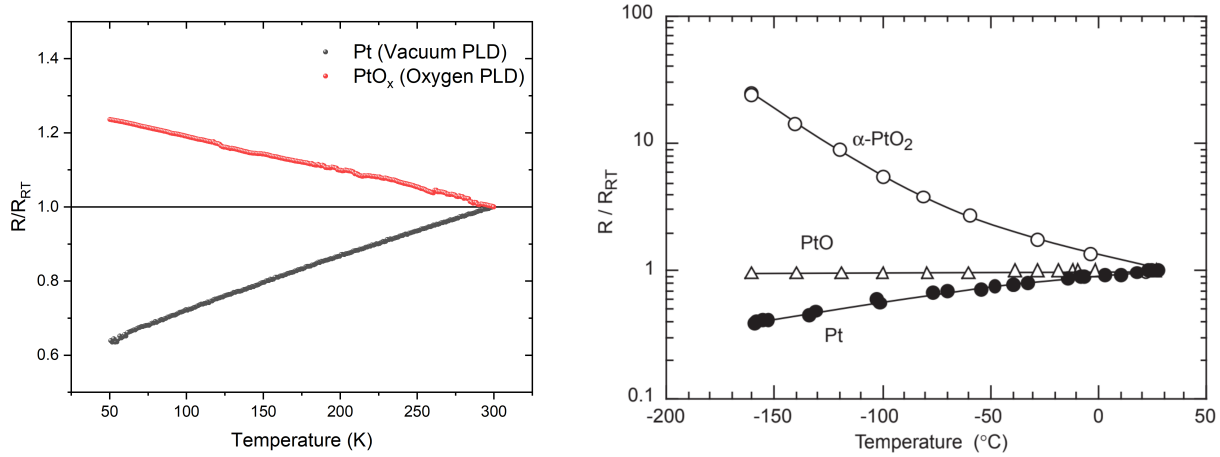

(a) (b)

Figure 6.2: (a) Resistance (normalised by that at room temperature) against sample temperature measured by 4-point PPMS for 7.5nm 'platinum' thin films on glass, deposited in vacuum (Pt) or in 2.5x10^{-3}mbar oxygen partial pressure like a-YIG (PtO$_x$). (b) Temperature dependence of the resistivity (normalised by that measured at room temperature) for Pt, PtO and α-PtO$_2$, reproduced from [230]

6.2 Structural Characterisation

6.2.1 X-Ray Diffraction and Reflectivity

X-ray diffraction was performed on each sample to confirm an epitaxial recrystallisation of the YIG layer on the GGG substrate: reflected by the presence of Pendellösung oscillations about the GGG(444) peak in 2θ-ω. For subsequent a-YIG and Pt layers, no significant changes to the observed (444) reflection were observed. 2θ-ω measurements for each layer of the 21.1nm a-YIG trilayer are shown in Figure 6.3 as an example. The expected GGG substrate peak was observed for all the trilayers, however no discernible film peaks (beyond Pendellösung oscillations) were present.

XRR measurements were performed on all samples in the series to determine the thickness and roughness of each layer in the final trilayer structure. Measurements were performed as described in Section 3.2.1, and reflectivity fringes were fitted to using the GenX and GlobalFit software packages [140]. Each layer of the trilayer had its individual XRR measured after its deposition. This is because the final Pt layer has a much stronger x-ray reflectivity than both the YIG and a-YIG layers beneath it, owing to its higher density. The Pt response ultimately

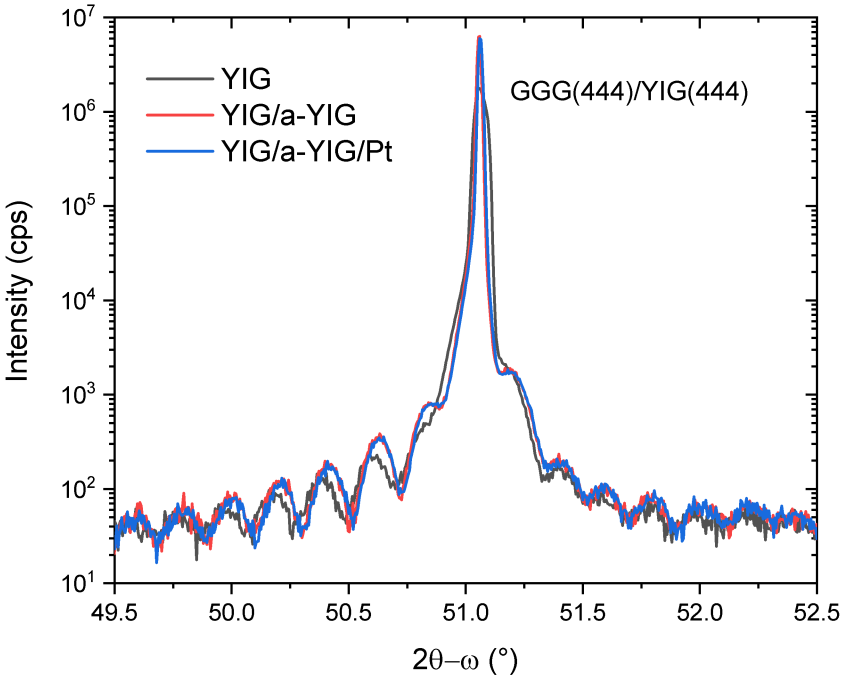

Figure 6.3: Example 2θ-ω XRD measurements about the GGG(444) reflection for the YIG/a-YIG/Pt trilayers. Shown spectra are for the YIG, YIG/a-YIG, and YIG/a-YIG/Pt structure on the 21.1nm a-YIG spacer.[11].

dominates the XRR response, making the YIG and a-YIG layers difficult to characterise from a single XRR measurement of the completed trilayer. Layer-by-layer XRR is advantageous, as thickness and roughness values found for one layer (e.g. YIG) can be held as known constants in fitting the next XRR spectra (e.g. YIG plus a-YIG), improving the accuracy of the a-YIG characterisation. XRR measurements for two of the trilayers are displayed as an example in Figure 6.4, with modelled SLD of the final trilayer. From Figure 6.4, a clear modulation of the YIG fringes occurs following the addition of the a-YIG spacer layer. This indicated that the two layers of YIG produced were not of the same phase, and distinguishable in SLD - reflected in the illustrated SLD simulations.

For the fitting procedure, notional densities for the GGG substrate and YIG film were required. For the GGG and YIG, a density of 7.08 gcm^{-3} and 5.17 gcm^{-3} was used respectively. Across all of the grown trilayers, fitting of the Kiessig fringes to the YIG layer returned an average thickness of (45 $\pm$ 2) nm, with an average RMS roughness of (0.6 $\pm$ 0.1) nm. For the platinum layer, an average thickness of (5.6 $\pm$ 0.2) nm was measured, with an average RMS roughness of (0.5 $\pm$ 0.1) nm. The Pt density was held constant at 21.45 gcm^{-3} for all fittings. The XRR determined thicknesses and roughnesses for the a-YIG spacer layers are shown in

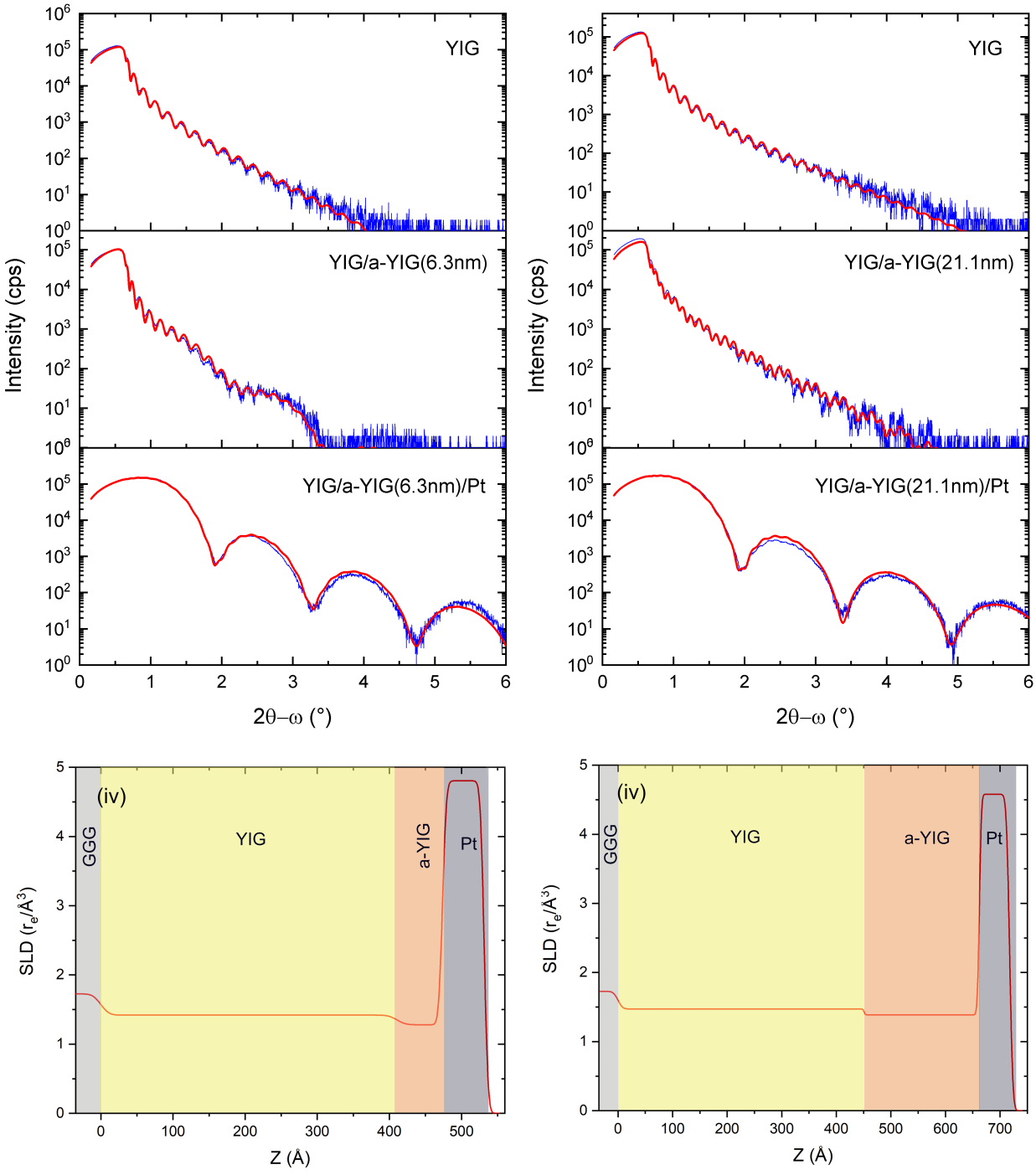

Figure 6.4: XRR measurement (blue) with fitted curve (red) for the YIG/a-YIG/Pt trilayers. Measured spectra for the (i) YIG, (ii) YIG/a-YIG, (iii) YIG/a-YIG/Pt structures are shown for: (a) 6.3nm a-YIG spacer and (b) 21.1nm a-YIG spacer. Simulated scattering length density (SLD) against sample Z from XRR fitting is shown in (iv), for each sample respectively.

Table 6.1, in comparison to the notional thicknesses that were aimed for. XRR fitting also returned an average SLD value for a-YIG approximately 2% lower than YIG. However, this SLD is derived assuming the formula unit stoichiometry of the a-YIG and its scattering length is equivalent to crystalline YIG (i.e. $Y_3Fe_5O_{12}$), and the number of x-ray scatters per unit cell is the only difference. This may not be the case, so this a-YIG SLD value is only notional. Nevertheless, this lower SLD is sensible, reflecting a lack of structural order or non-optimal packing of unit cells.

Notional a-YIG Thickness (nm)	XRR a-YIG Thickness (± 0.2 nm)	XRR a-YIG RMS Roughness (± 0.1 nm)
2.5	2.8	0.7
6	6.3	0.7
12	11.7	0.7
20	21.1	0.6
30	30.6	0.7

Table 6.1: Summary of a-YIG spacer thicknesses and roughnesses, extracted from fitting measured XRR data.

From Table 6.1, the RMS roughness is of a similar magnitude across all deposited a-YIG spacers: coming to an average of (0.7 ± 0.1)nm. Roughnesses of this scale are favourable, being approximately half of the notional unit cell length of crystalline YIG (1.23nm). The consistency in these roughnesses from film to film is encouraging, suggesting that the inferfaces formed between either the YIG/a-YIG or a-YIG/Pt layers are comparable in quality between all trilayers produced and studied: given their identical preparation technique.

6.2.2 Cross-Sectional TEM

The 21.1nm a-YIG trilayer was prepared for HAADF-STEM imaging via focused ion beam milling, to assess the structural quality of the interfaces being produced in the trilayer series, particularly the YIG/a-YIG interface. The cross-sectional TEM images shown in Figure 6.5(a) confirms that the thickness of the a-YIG spacer is (21 ± 1)nm, consistent with the values obtained from XRR fitting. The interfaces observed between the a-YIG and YIG are also very smooth, with roughness on the order of (if not smaller than) 1nm, also in agreement with fitting to XRR data. No obvious mixing region between the YIG and a-YIG is present. The a-YIG/Pt interface is also similarly smooth. However, TEM images acquired from this cross-section cannot be guaranteed to be representative of interface quality across all of the sample. Nevertheless, agreement with roughnesses from XRR data averaged across the entire sample supplements the layer quality indicated by the TEM imaging.

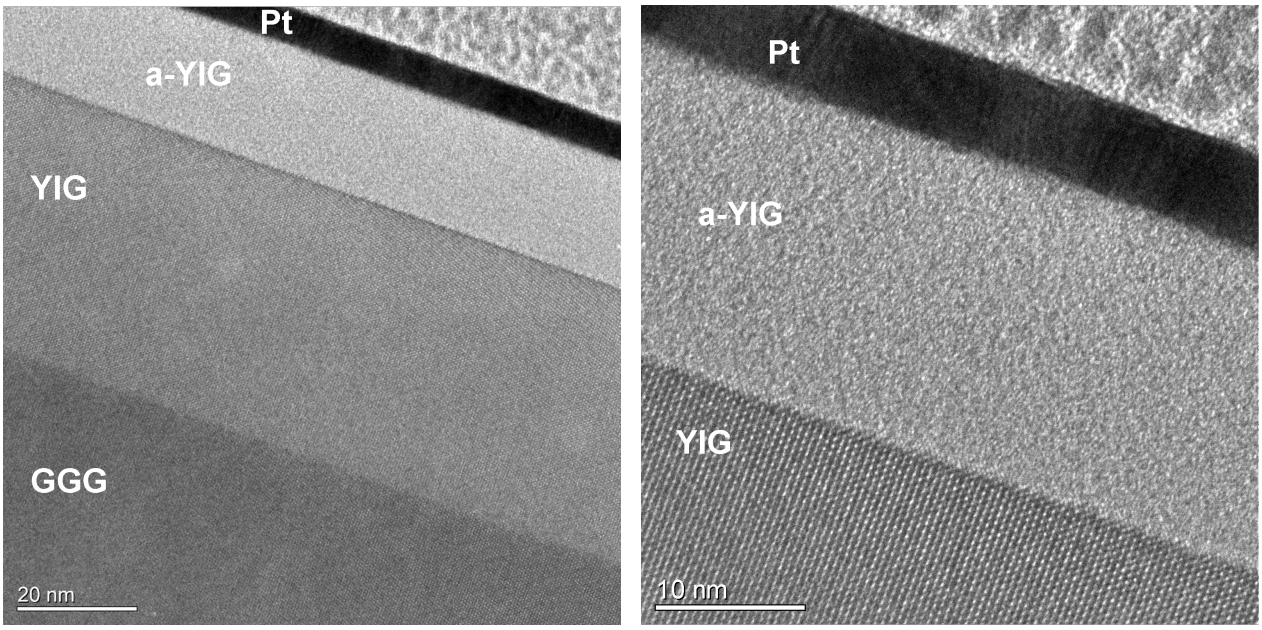

Figure 6.5: Cross-sectional TEM images of the YIG(111)/a-YIG (21 nm)/Pt trilayer grown on GGG, with a TEM zone axis of [$\bar{1}$10]. The YIG and a-YIG layers are clearly distinguishable. Smooth interfaces are present between all layers with roughness below 1nm.

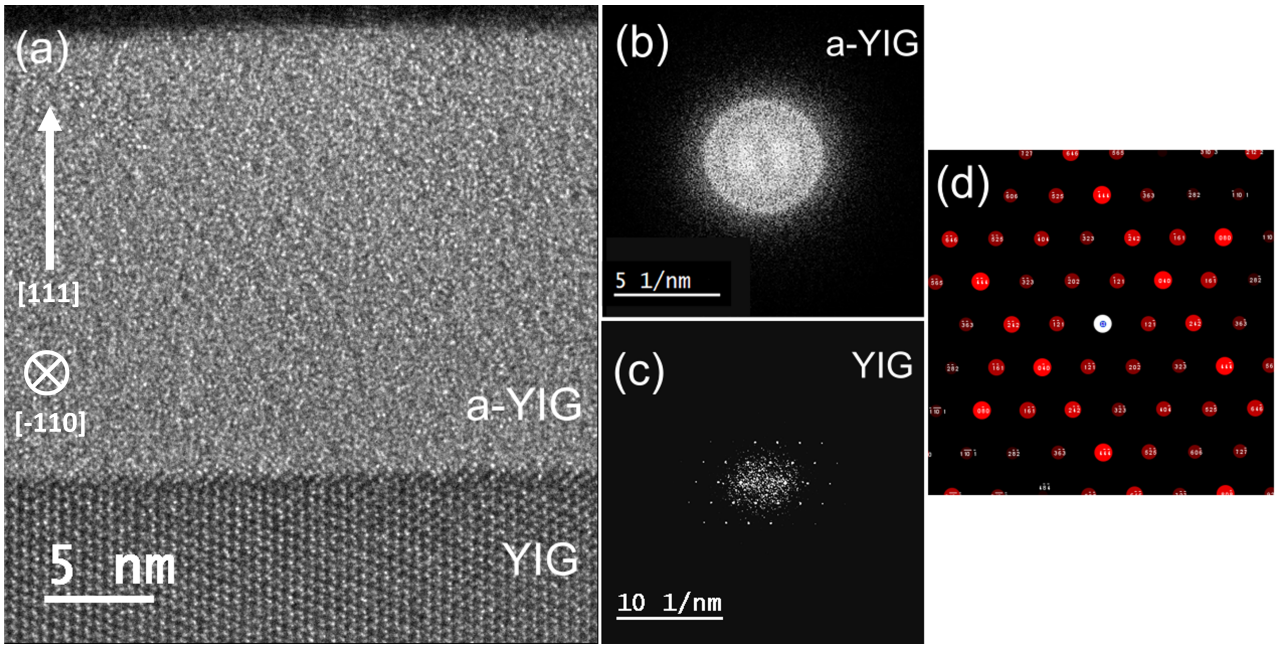

Figure 6.6: (a) Magnified cross-sectional TEM image of the YIG/a-YIG interface for the YIG(111)/a-YIG (21 nm)/Pt trilayer. (b) FFT pattern acquired from the a-YIG layer and (c) electron diffraction pattern from the YIG layer. (d) Diffraction pattern for YIG [$\bar{1}$10] simulated using the JEMS software [190], matching observed YIG diffraction.

Growth of the YIG on the GGG substrate is confirmed to be highly crystalline from electron diffraction in Figure 6.6(c), and similarly epitaxial to the recrystallised YIG/GGG films shown in Chapter 4. No obvious structural defects or intermixing between the YIG/GGG layers is observed. This suggests that any potential magnetic dead layers formed at the YIG/GGG interface, as reported in YIG/GGG thin films by Mitra *et al.* [116] are either very small or absent. The a-YIG is confirmed to be amorphous both in BF imaging, and from FFT patterns in Figure 6.6(b).

6.3 Magnetic Characterisation

6.3.1 VSM

Vibrating sample magnetometry was performed on all samples in the series, once the entire trilayer structure was deposited. This was to assess both the magnetic quality of the YIG, and to evaluate any trends in coercivity or saturation magnetisation due to the presence of the a-YIG spacer (in comparison to the YIG/Pt 0nm a-YIG bilayer). In-plane VSM measurements were performed using the LakeShore 8600 VSM. A magnetic bias field between ±100 Oe was sufficient to saturate the magnetically soft YIG and show clear hystersis. Measured in-plane M(H) loops - following removal of the paramagnetic GGG background - are shown in Figure 6.7, and extracted values for coercivity and M_S are plotted as a function of a-YIG spacer thickness in Figure 6.8. For all measured VSM loops, magnetisation was compared between trilayer samples to account for any small differences in YIG film volume. YIG film volume was obtained using thickness extracted from XRR in Section 6.2.1, and multiplying by the sample area. Sample area was measured using a travelling optical microscope. Using this calculated volume, raw magnetic moment (emu) was converted into magnetisation (emu/cc) in plotted M(H) loops.

For all measured trilayers, the in-plane VSM data shows narrow hysteresis loops similar to those for YIG/GGG in Chapter 4. Rotation of the samples in-plane by 90° showed no significant changes to either coercivity or loop squareness, reflecting the weak in-plane anisotropy seen in FMR. Shown in Figure 6.8(a), saturation magnetisation of the trilayer YIG films are observed to be between 117 - 127 emu/cc (84 - 91% of the expected value of 140 emu/cc for YIG [52]). The average M_S and standard deviation comes to (124 ± 5)emu/cc (neglecting the 30nm a-YIG spacer). The final 30nm a-YIG trilayer was seen to have an unexpectedly increased M_S compared to other a-YIG thicknesses, approximately 96% of bulk YIG. Coercivity is similarly small in all trilayers. At most, a coercivity of (1.5 ± 0.2) Oe is seen for the YIG/Pt bilayer (0nm a-YIG): suggesting the absence of an a-YIG spacer layer systematically broadens H_c compared to typical values of below 0.5 Oe for our YIG/GGG. Repeat growths of YIG/Pt(5nm) bilayers show similar broadenings of coercivity by approximately (1.0 ± 0.3)Oe (compared to an average YIG H_C of 0.25Oe). However, shown in Figure 6.8(b), no clear correlation between a-YIG

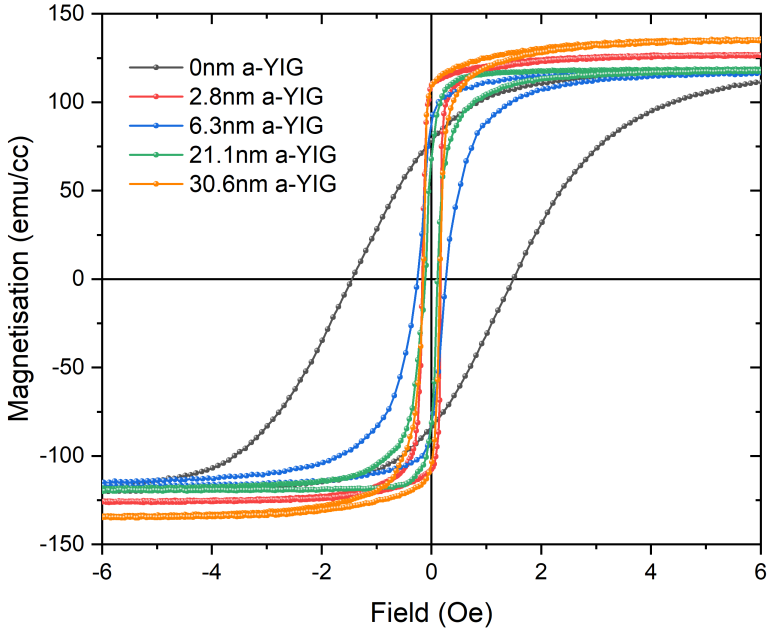

Figure 6.7: Example hysteresis M(H) loops measured with in-plane VSM performed on the YIG/a-YIG/Pt trilayer samples: magnetisation against applied field. Applied field swept between ±100 Oe.

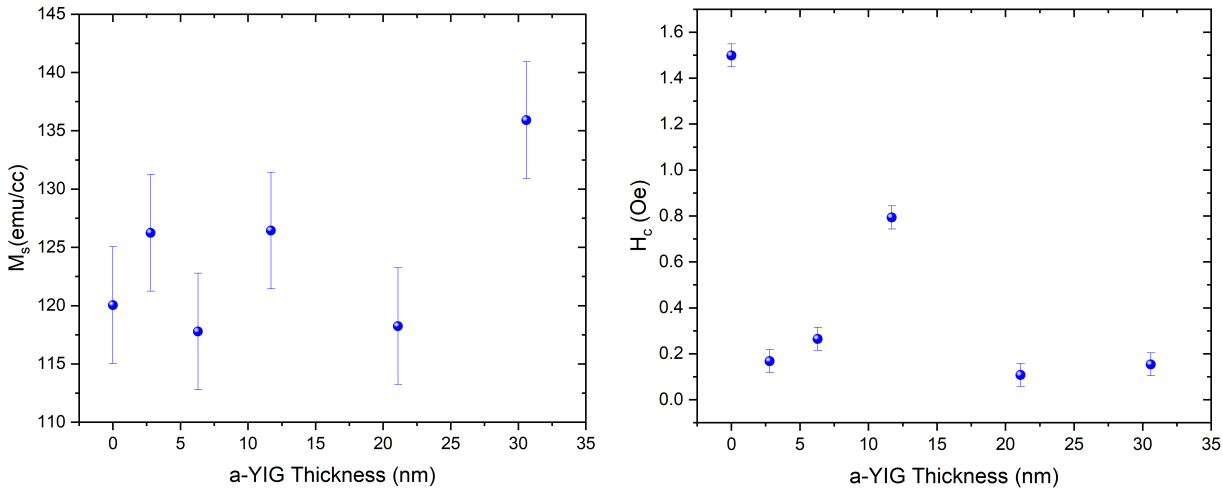

(a) (b)

Figure 6.8: Comparison of (a) saturation magnetisation and (b) coercivity for YIG/a-YIG/Pt trilayer samples, measured from in-plane VSM.

thickness and coercivity is shown for the trilayer series. An explanation for this is coercivity on this scale (1Oe or less) may be highly sensitive to the interfaces formed between the YIG and a-YIG, or a-YIG and Pt layers during deposition. Alternatively, uncontrollable differences in the nanostructure between separately deposited YIG layers - resulting from the PLD process or ex-situ annealing - may also be to blame. This would also explain the variability in M_S despite both growth and annealing being repeated as similarly as possible.

6.3.2 FMR Spectroscopy

VNA-FMR spectroscopy was performed on the trilayers as described in Chapters 3 and 4, to measure the Gilbert damping of the YIG in the trilayer, and its dependence with a-YIG thickness, in comparison to a YIG/Pt bilayer (0nm a-YIG spacer). VNA-FMR was performed on all samples over a field range of 0-4.5kOe in steps of 0.5Oe, and a frequency range of 10kHz-15GHz in 1601 equally spaced frequency steps. All the VNA-FMR measurements discussed were performed at an RF power of +7dBm. For FMR measurements where the final Pt layer had been deposited, a thin layer of PTFE tape was placed between the co-planar waveguide and the platinum surface of the trilayer. This was to prevent conduction from the waveguide to the platinum metal which could create systematic errors in measured Kittel curves or damping.

The easy axis in-plane Kittel curves measured for the 21.1 nm trilayers are shown in Figures 6.9(a),(b) as an example. Resonance linescans taken at 10GHz for the YIG/Pt bilayer, 2.8nm trilayer, and 21.1nm trilayer are also shown in Figure 6.9(c). An easy axis Kittel curve following Equation 2.48 was fitted to each of these frequency field maps to extract magnetic parameters of interest. Extracted values for effective magnetisation (M_{eff}) and the gyromagnetic ratio γ - from which an effective g-factor was found following Equation 2.33 - are summarised in Table 6.2. Values for M_{eff} obtained from Kittel curve fitting are systematically larger than M_S values quoted from in-plane VSM from Section 6.3, as expected. Removing the magnetic anisotropy correction ($-\frac{K_1}{M_S}$) of approximately (4 ± 1)emu/cc from M_{eff}, an average saturation magnetisation M_S for YIG of (134 ± 5)emu/cc is obtained from FMR. This value agrees with the average YIG M_S of (124 ± 5) emu/cc from VSM, within error. An average of the two techniques was taken, giving an average YIG M_S of (129 ± 5) emu/cc, consistent with M_S values for recrystallised YIG/GGG from Chapter 4 and Hauser *et al.* [11].

Shown in Figure 6.9(b), the Kittel curves measured for the YIG, YIG/a-YIG, and YIG/a-YIG/Pt structures almost lie on top of one another, with resonant fields within 10Oe of each other. Extracted magnetic parameters in Table 6.2 reflect this, with all fit values agreeing with each other within 5%. This similarity between the Kittel curves suggests that the addition of either a-YIG, or a-YIG plus Pt to the YIG layer does not significantly impact the YIG's magnetisation. Any changes to YIG magnetisation induced by the deposition of subsequent layers (for example, by resputtering or impaction by the PLD plume) would cause a corresponding

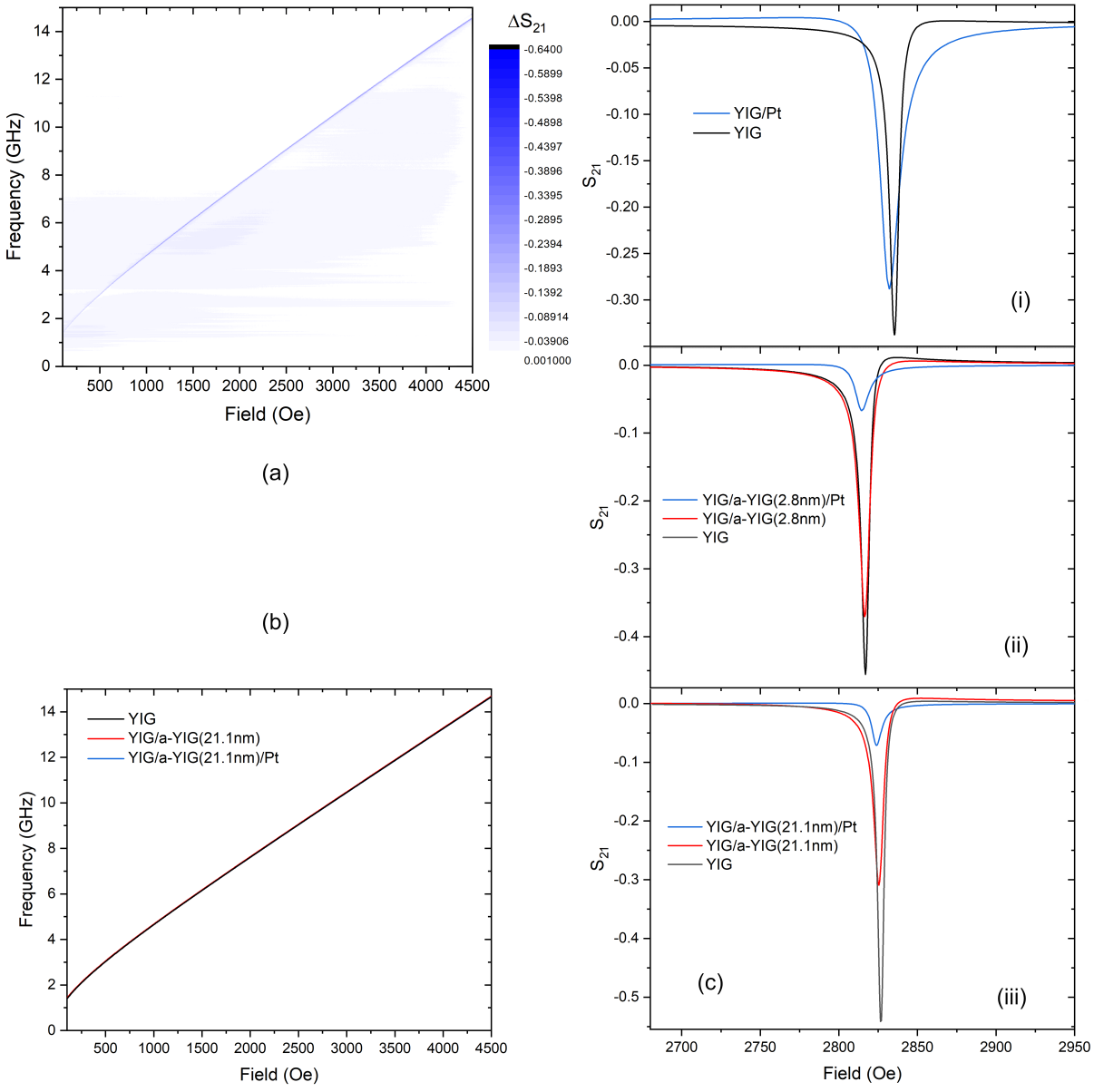

Figure 6.9: (a) Exemplar VNA-FMR frequency-field map measured from the 21.1nm a-YIG spacer trilayer. (b) Easy axis in-plane Kittel curves extracted from the 21.1nm a-YIG spacer trilayer. (c) Resonance linescans at 10GHz for the YIG, YIG /a-YIG, and YIG/a-YIG/Pt structures are shown for the (i) 0nm, (ii) 2.8nm and (iii) 21.1nm a-YIG spacers.

Layer(s)	a-YIG (nm)	Gyromagnetic Ratio ($\pm$0.01x10^{11}rad/T)	g-factor ($\pm$0.01)	M_{eff} ($\pm$5emu/cc)
YIG	0	1.73	1.97	134
	2.8	1.72	1.96	138
	6.3	1.72	1.96	139
	11.7	1.72	1.96	139
	21.1	1.73	1.97	136
	30.6	1.74	1.98	141
YIG/a-YIG	0	-	-	-
	2.8	1.73	1.97	136
	6.3	1.73	1.97	133
	11.7	1.72	1.96	139
	21.1	1.73	1.97	136
	30.6	1.74	1.98	142
YIG/a-YIG/Pt	0	1.72	1.96	139
	2.8	1.73	1.97	136
	6.3	1.74	1.98	135
	11.7	1.73	1.97	134
	21.1	1.73	1.97	134
	30.6	1.73	1.97	142

Table 6.2: Summary of magnetic parameters for YIG/a-YIG/Pt trilayers, extracted by easy-axis Kittel curve fitting: gyromagnetic ratio and g-factor and effective magnetisation (M_{eff}).

shift in the Kittel curve resonant field, following Equation 2.48. Shifts in resonant field that are seen in 10GHz linescans from Figure 6.9(c) are minor and attributed to the accuracy of the magnet power supply. One change that is more clear, is the broadening of the Kittel curve produced following the addition of the final Pt layer. The 10GHz linescans for YIG/a-YIG/Pt all show that the resonance is both reduced in intensity and, more importantly, possesses a larger linewidth. This indicates a successful pumping of spin from the YIG layer, through the a-YIG and into the Pt.

Anisotropy Measurements

VNA-FMR measurements were also performed at different azimuthal angles, to probe the in-plane anisotropy (if any) of each stage of the trilayers. For these angular FMR measurements, the azimuthal angle was rotated in steps of 5° over a 180° range between -90 to 90° centred around the 0° position. However, a larger field step of 2.5 Oe (or 5Oe with the final Pt layer) was used in comparison to the 0° case, to allow each azimuthal angle scan to proceed at a reasonable speed. The GGG(111) substrates on which the trilayers were fabricated were pre-cut with diagonal corners to indicate the [1$\bar{1}$0] edge. It was therefore possible to consistently mount the trilayers in the same relative sample orientation during all VNA-FMR measurements. The orientation used is illustrated as an inset in Figure 6.10. Linescans at a constant frequency

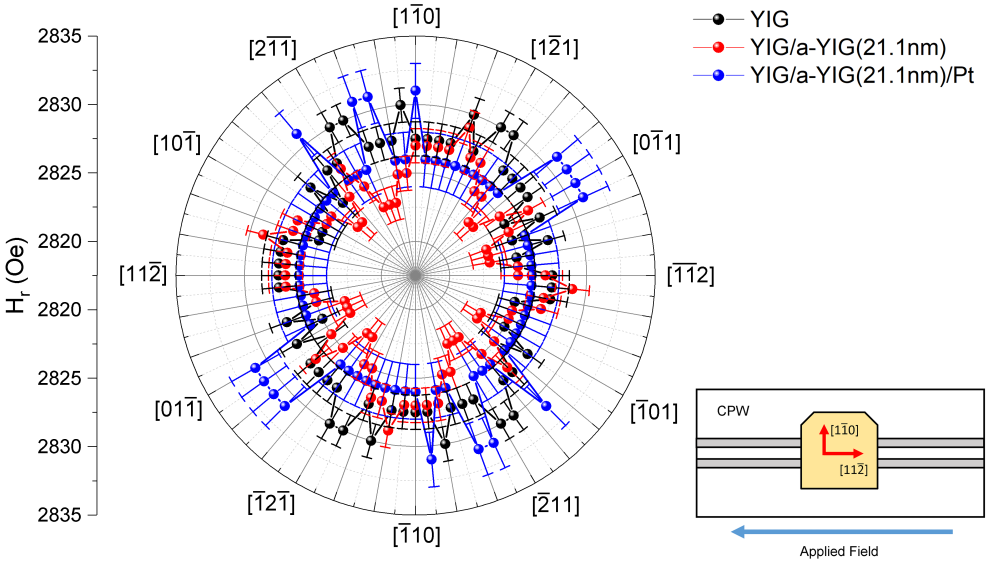

Figure 6.10: H_r data extracted from azimuthal VNA-FMR performed on the 21.1nm a-YIG spacer. Measured data for the YIG, YIG/a-YIG, and YIG/a-YIG/Pt structure all show an effectively isotropic dependence on azimuthal angle, within 8 Oe. Relative orientation of the clipped corners indicating the [11$\bar{0}$] of the sample to the CPW at the '0 degrees' position is shown as an inset.

of 10GHz were extracted from FMR measured at each azimuthal angle, and then fitted using an asymmetric Lorentzian function to determine the corresponding resonance field (H_r). These values of H_r were plotted as a function of azimuthal angle to measure the anisotropy. The anisotropy data from each stage of the 21.1 nm trilayer is plotted in Figure 6.10 as an example. At each stage, the anisotropy observed is essentially isotropic to within a H_r range of 8Oe. No preferred in-plane easy axis directions can be inferred. This is consistent with the YIG/GGG and YIG/YAG thin films presented in Chapter 4. The addition of either a-YIG or a-YIG plus Pt does not apparently alter or change the initial isotropy of the YIG layer significantly, within error.

Damping Measurements

The damping behaviour of each stage of the trilayers was also measured from the in-plane VNA-FMR spectroscopy data. From each of the in-plane Kittel curves measured (such as those in Figure 6.9), a series of resonance linescans were extracted at fixed frequencies. Following the subtraction of any non-linear background, an asymmetric Lorentzian function was fitted, from which the FMR linewidth (the Lorentzian's HWHM) was extracted. This was repeated with a frequency interval of 1GHz, and the obtained linewidths (ΔH) were plotted as a function of their corresponding resonance frequency. Fitting the frequency dependence of ΔH, according to Equation 2.50 allowed the extraction of the ΔH_0 from the offset, and the Gilbert damping

parameter, α, from the gradient.

Plots of ΔH against resonance frequency from the YIG/Pt bilayer and 6.3nm and 11.7nm spaced trilayers are shown as an example in Figure 6.11. It is found that the frequency dependence of the FMR linewidth is strongly linear for each stage of the trilayers. In all cases, two-magnon scattering like behaviour is absent. This indicates that the initial YIG layer does not possess a significantly high defect or impurity density due to the PLD or diffusion from the GGG substrate. Across all of the tested samples, an average value for the initial YIG α of $(4.7 \pm 0.9)\text{x}10^{-4}$ was measured (error from standard deviation). In the YIG/Pt bilayer, a clear increase in α is observed with the addition of the Pt layer. This indicates successful pumping of spins from the YIG layer and into the Pt.

For the trilayers, the addition of a-YIG to the YIG produces only a minor increase in Gilbert damping. However, measured values for YIG/a-YIG damping are within one standard deviation of the average YIG damping, within error. No clear correlation between YIG/a-YIG damping and a-YIG thickness is observed. This does not reflect behaviour seen in spin-pumping experiments performed by Wang *et al.* (2015) on permalloy/a-YIG structures [20], where a significant change in damping is observed with the addition of a-YIG alone. The more significant difference seen between the linewidth-frequency response (Figure 6.11) of YIG and YIG/a-YIG is an increase in extrinsic damping, with a larger offset in FMR linewidth (ΔH_0) being observed, increasing by an average of (1.7 ± 0.3)Oe. This is likely due to structural defects or magnetic inhomogeneities produced at the YIG/a-YIG interface. Such effects would produce a systematic broadening of FMR linewidth at all frequencies, as seen with the addition of the a-YIG layer. With the addition of the final Pt layer, a much larger change in Gilbert damping is produced in the YIG/a-YIG/Pt trilayer; indicating successful spin-pumping through the a-YIG spacer into the Pt.

The Gilbert damping measured for the YIG/a-YIG and YIG/a-YIG/Pt stages from all of the trilayers is plotted as a function of the a-YIG spacer layer thickness in Figure 6.12. The average YIG damping (α_{YIG}) and its standard deviation is also shown. From the observed increases in Gilbert damping, the effective spin mixing conductance $g_{\text{eff}}^{\uparrow\downarrow}$ was calculated for each trilayer respectively following Equation 2.59.

Relevant parameters of YIG layer thickness (t_{YIG}) were obtained from XRR measurements, and the average YIG saturation magnetisation (M_{S}) of (129 ± 5) emu/cc. For the YIG/Pt bilayer structure (0nm a-YIG), a $g_{\text{eff}}^{\uparrow\downarrow}$ of $(4.4 \pm 0.5)\text{x}10^{18}$ m^{-2} is calculated. This $g_{\text{eff}}^{\uparrow\downarrow}$ in good agreement with other YIG/Pt bilayers in the literature [232, 21, 233].

For YIG/a-YIG/Pt, the change in Gilbert damping between the final YIG/a-YIG/Pt trilayer and the **average** YIG damping (as shown in Figure 6.12) is considered. Calculated values for $g_{\text{eff}}^{\uparrow\downarrow}$ are plotted against a-YIG thickness in Figure 6.13. It is very important to note that Equation 2.59 for calculating $g_{\text{eff}}^{\uparrow\downarrow}$ is strictly valid for spin pumping across a single interface: discussed in Chapter 2. The trilayer has two interfaces, separated by a finite a-YIG volume across which spin

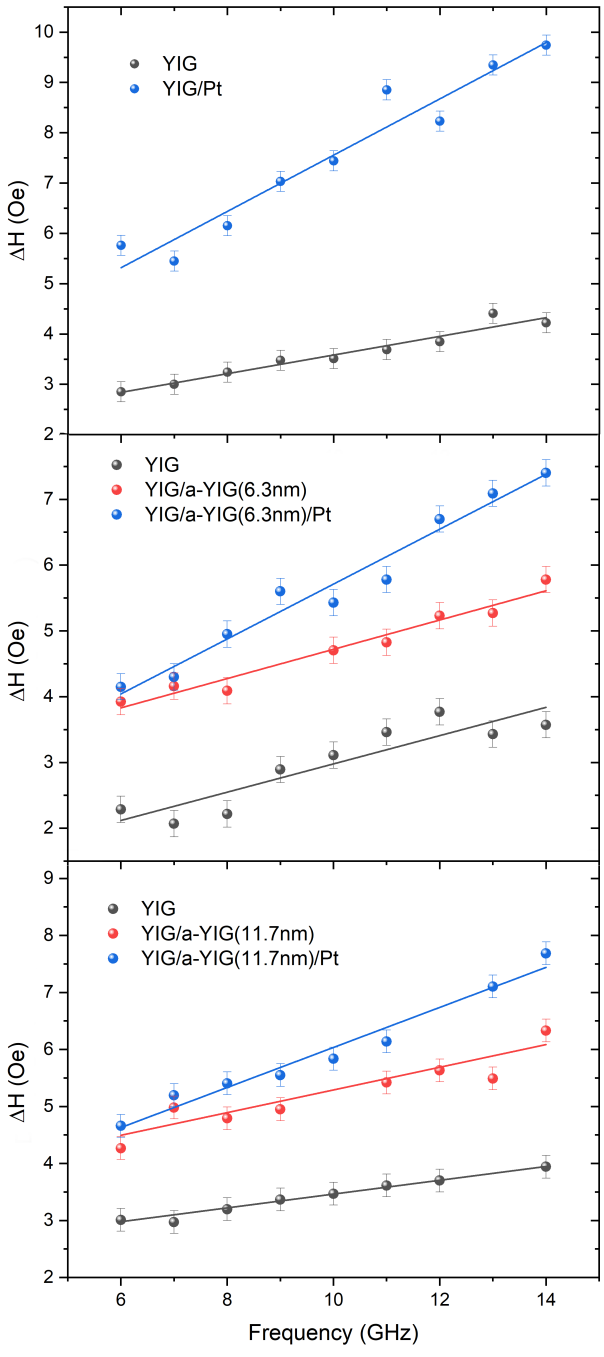

Figure 6.11: A comparison of ΔH(f) in the (a) YIG/Pt bilayer, (b) 6.3nm YIG/a-YIG/Pt trilayer and (c) 11.7nm YIG/a-YIG/Pt spacer. Individual ΔH(f) responses of YIG, YIG/a-YIG, and YIG/a-YIG/Pt structures are shown.

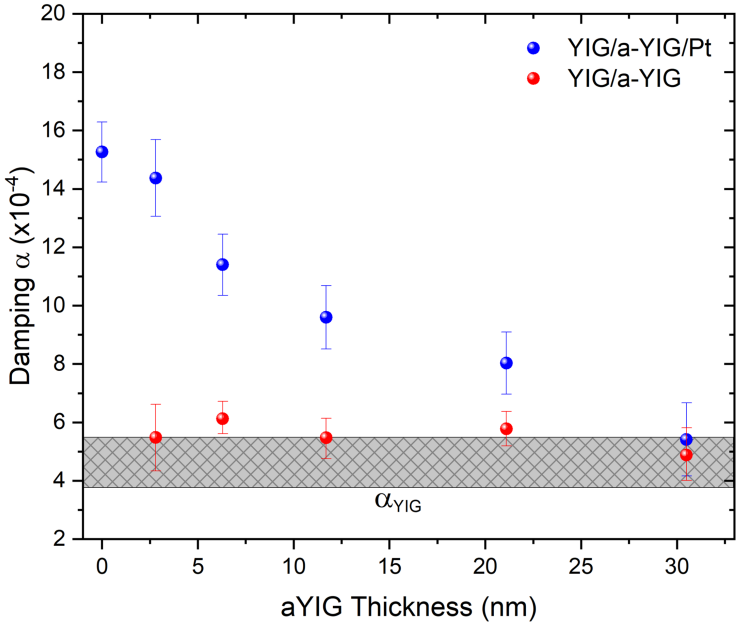

Figure 6.12: Gilbert damping, α, measured in YIG(45nm)/a-YIG(t nm)/Pt(5.5nm) trilayers as a function of a-YIG spacer thickness (t), showing average YIG damping and standard deviation.

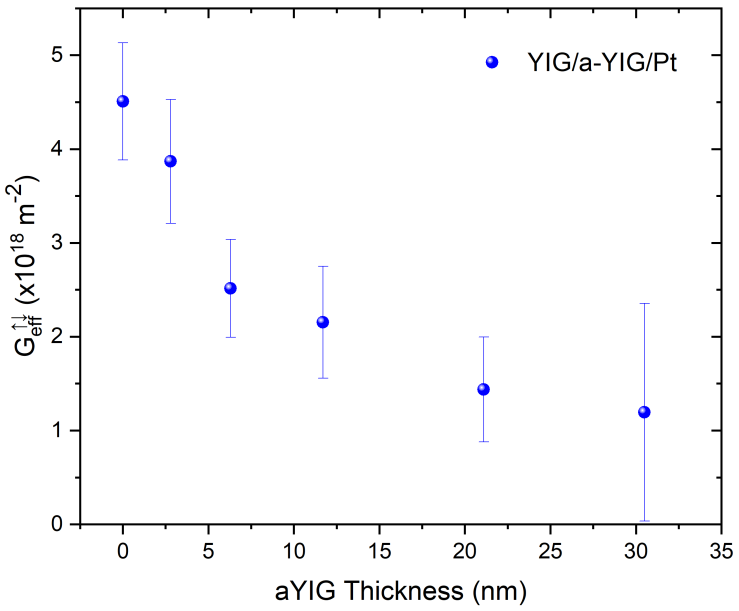

Figure 6.13: Effective spin mixing conductance, $g_{\text{eff}}^{\uparrow\downarrow}$, estimated from the measured change in Gilbert damping in YIG(45nm)/a-YIG(t nm)/Pt(5.5nm) trilayers as a function of a-YIG spacer thickness (t).

memory losses may occur, making an accurate calculation of $g_{\text{eff}}^{\uparrow\downarrow}$ more complex. Nevertheless, Equation 2.59 can provide a first order approximation for trilayer $g_{\text{eff}}^{\uparrow\downarrow}$ and act as a quality indicator between samples. It is also noted that, as the difference in damping approaches zero (as a-YIG approached 30nm thick), the associated error in $g_{\text{eff}}^{\uparrow\downarrow}$ from quadrature becomes very large. Given $g_{\text{eff}}^{\uparrow\downarrow}$ is directly proportional to the change in damping due to spin pumping [85], the thickness dependence shown in Figure 6.13 has broadly the same form as that in Figure 6.12. Across the series, values of $g_{\text{eff}}^{\uparrow\downarrow}$ on the order of 1x10^{18} m^{-2} are seen. This is unlike Py/Pt [21], where a $g_{\text{eff}}^{\uparrow\downarrow}$ of 2.25x10^{19} m^{-2} was observed to immediately drop to zero with any added thickness of a-YIG. Values of $g_{\text{eff}}^{\uparrow\downarrow}$ for our trilayers are comparable to those for YIG/Cu (20nm)/Pt trilayers studied by Du *et al.* [232].

As the thickness of the a-YIG layer is increased, the additional Gilbert damping due to spin pumping into the Pt is reduced. From Figures 6.12 and 6.13, the additional damping broadly follows an exponential dependence and drop-off with a-YIG thickness. Shown in Figure 6.14, the change in Gilbert damping ($\Delta\alpha$) due to the addition of a-YIG plus Pt is calculated. $\Delta\alpha$ is calculated from the measured trilayer α minus the average YIG α of (4.7 $\pm$ 0.9)x10^{-4}, both shown in Figure 6.12. The natural logarithm, ln$\Delta\alpha$, shown in 6.15 follows a linear trend against a-YIG spacer thickness. This is a signature that suggests that diffusive magnon transport is sustained within the a-YIG: allowing spin pumping from the YIG layer, through the a-YIG and into the Pt. Applying a linear fit to ln$\Delta\alpha$ and taking the reciprocal of the gradient gives an estimate for the magnon diffusion length of the a-YIG. The YIG/Pt bilayer (0 nm a-YIG) is excluded from the linear trend fitting. From Figure 6.15, a magnon diffusion length of (16 $\pm$ 2)nm is estimated, on the basis that the decay in Gilbert damping is exponential and the observed magnon transport is diffusive.

Comparison to Metallic Multilayers

The Gilbert damping data of the YIG/a-YIG/Pt trilayers and YIG/a-YIG bilayers were compared to the model used by Mizukami *et al.* (2002) to evaluate spin pumping measured in metallic Py/Cu(L)/Pt trilayers and Py/Cu(L) bilayers [97, 85] (discussed in detail in Section 2.5.3). The model for the dependence on Gilbert damping - expressed as a damping parameter, $G = \gamma M_S \alpha$ - for metallic trilayers (Equation 6.1) and bilayers (Equation 6.2) is given below.

$$G(L) = G_0 + \left[1 + g^{\uparrow\downarrow}\frac{\tau_{\text{SF}}\delta_{\text{SD}}}{h}\frac{1+\tanh\left(L/\lambda_{\text{SD}}\right)g\tau_{\text{SF}}\delta_{\text{SD}}/h}{\tanh\left(L/\lambda_{\text{SD}}\right)+g\tau_{\text{SF}}\delta_{\text{SD}}/h}\right]^{-1} \times \frac{\left(g_L\mu_B\right)^2}{2h}\frac{g^{\uparrow\downarrow}S^{-1}}{d} \tag{6.1}$$

$$G(L) = G_0 + \left[1 + \frac{g^{\uparrow\downarrow}\tau_{\text{SF}}\delta_{\text{SD}}/h}{\tanh\left(L/\lambda_{\text{SD}}\right)}\right]^{-1} \frac{\left(g_L\mu_B\right)^2}{2h}\frac{g^{\uparrow\downarrow}S^{-1}}{d} \tag{6.2}$$

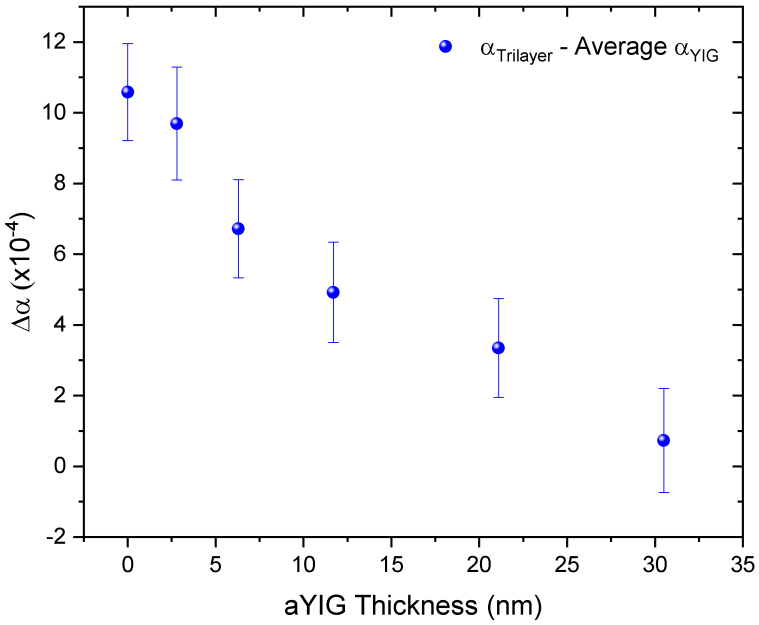

Figure 6.14: Change in Gilbert damping, $\Delta\alpha$, measured in YIG(45nm)/a-YIG(t nm)/Pt(5.5nm) trilayers as a function of a-YIG spacer thickness (t).

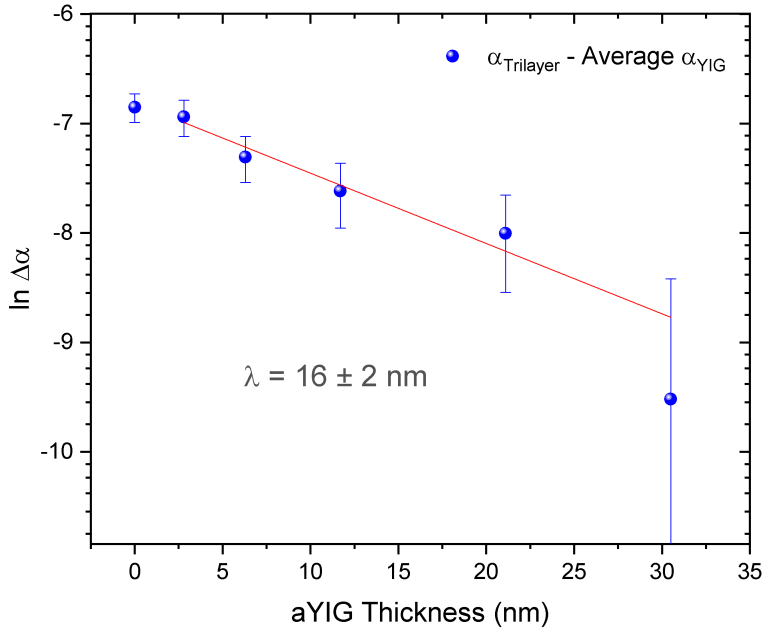

Figure 6.15: Natural logarithm of the change in Gilbert damping, ln$\Delta\alpha$, measured in YIG(45nm)/a-YIG(t nm)/Pt(5.5nm) trilayers as a function of a-YIG spacer thickness (t).

Initial values for fitting parameters were determined from values given by Mizukami *et al.* [97], and using the available G(L) data to empirically calculate the remaining parameters the authors left undefined: $g\tau_{SF}\delta_{SD}/h$ and $g^{\uparrow\downarrow}\frac{\tau_{SF}\delta_{SD}}{h}$. These were calculated to be approximately 25.286 and 11.598 respectively with a 12% uncertainty. With these values and the Py/Cu/Pt parameters summarised in Section 2.5.3, the fits by Mizukami *et al.* are reproduced reasonably well, as shown in Figure 6.16(a). However, a small difference in G(L) of 5% for L > 5000Å was noted.

Attempting to apply the same model to the YIG/a-YIG/Pt and YIG/a-YIG data, the YIG/Pt bilayer data point was omitted and a $\log_{10}$ scale used, similarly to Mizukami *et al.* G_0 was calculated from the average YIG α in Figure 6.12 to be (1.03 ± 0.06)x10^6 s^{-1}. The spin-diffusion length, λ_{SD}, followed the value estimated from Figure 6.15 as (160 ± 20)Å. The average FM YIG thickness, d, was defined as (450 ± 20)Å from the XRR data, held constant for all fitting. All other fitting parameters were restricted within bounds of being either two orders of magnitude larger or smaller than their initial values inferred from Mizukami *et al.*.

Shown in Figure 6.16(b), the model for spin-pumping in metallic trilayers ultimately does not fit the YIG/a-YIG/Pt or YIG/a-YIG Gilbert damping data. For constant G_0 and λ_{SD}, lineshapes were only able to broadly follow the data if one or more of the floating parameters - $g^{\uparrow\downarrow}S^{-1}$, $g^{\uparrow\downarrow}\frac{\tau_{SF}\delta_{SD}}{h}$, and $g\tau_{SF}\lambda_{SD}/h$ - reached the maximum imposed bounds with unrealistic error margins. Alternatively, if G_0 and λ_{SD} are not fixed, the resulting fits suggest the spin diffusion length in the a-YIG exceeds a 40nm bound; such diffusion lengths do not agree either with the value extracted from the FMR ln$\Delta\alpha$ data, or a reasonable $\frac{1}{e}$ estimate of λ_{SD} from the drop-off in ln$\Delta\alpha$, shown in Figure 6.15. In addition, the trilayer and bilayer curves do not show any sign of overlapping at higher values of a-YIG spacer thickness, emphasising disagreement with the model further.

Disagreement between the metallic multilayer model and the FMR data may be for several reasons. Compared to the Py/Cu/Pt and Py/Cu data from Mizukami *et al.* [97], the range of a-YIG spacer thicknesses measured is small, with only five available points to fit to. In addition, the largest (30.6nm) a-YIG spacer in Figures 6.12 and 6.14 shows a more rapid drop-off towards the YIG α compared to the other trilayers in the series. However, fitting was similarly poor when excluding this point. Additional G(L) data for trilayers, at both smaller and larger L than in this trilayer series, is likely necessary for effective fitting with this highly-parameterised model. However, more fundamentally, it could be argued that this metallic layer, diffusive spin-pumping model is not applicable to insulating a-YIG and YIG oxides. The dependence of $\Delta\alpha$ on a-YIG thickness in Figures 6.14 and 6.15 is not perfectly exponential (or perfectly linear in ln). This presents the possibility that spin-transport through the a-YIG is instead 'diffusive-like', rather than truly diffusive.

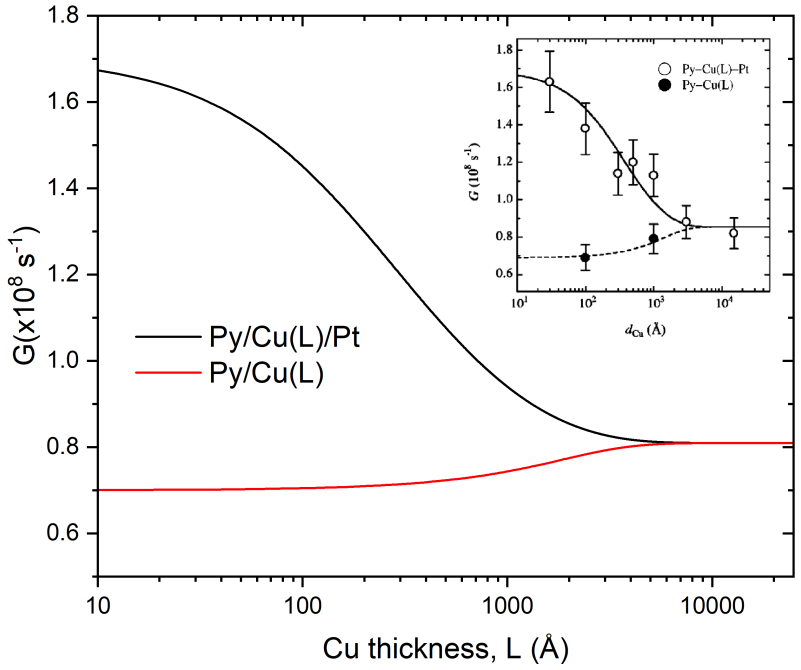

(a)

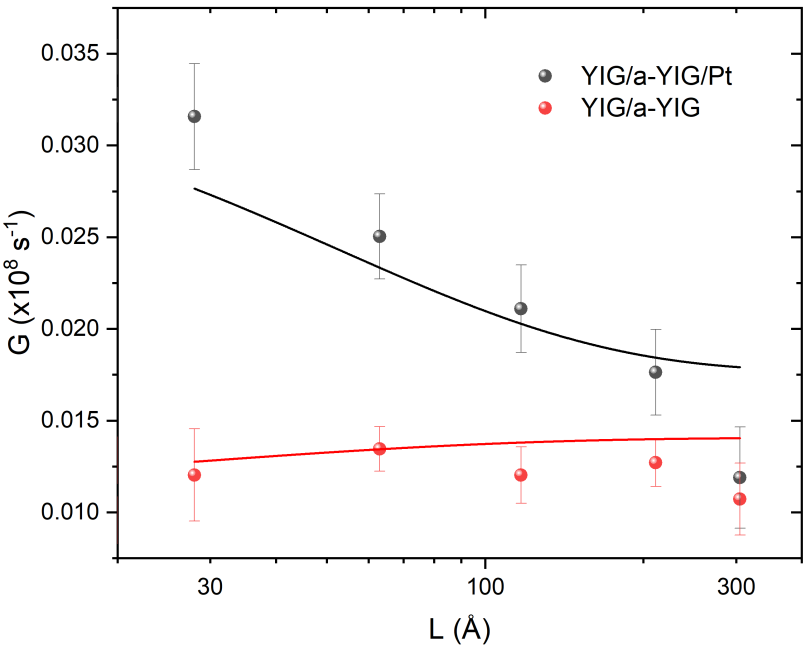

(b)

Figure 6.16: (a) Simulated G(L) for Py/Cu/Pt parameters from Mizukami *et al.* (2002). Original data and trends shown in inset [97]. (b) Fitting of metallic G(L) model to YIG(45nm)/a-YIG(L Å)/Pt(5.5nm) trilayers and YIG(45nm)/a-YIG(L Å) bilayers, for fixed G_0 and λ_{SD}.

6.4 Summary and Conclusions

In this chapter, a series of six PLD-grown YIG/a-YIG/Pt trilayer structures have been fabricated by PLD and characterised structurally with XRD/XRR and magnetically using in-plane VNA-FMR spectroscopy, following a layer-by-layer approach. Upon depositing the final Pt layer, magnetic characterisation using VSM was also performed. In addition, cross-sectional TEM imaging of the 21.1nm trilayer was performed to evaluate the quality of the YIG/a-YIG and a-YIG/Pt interfaces formed within the deposited trilayers.

All trilayers possessed a linear relationship in the FMR linewidth as a function of frequency, indicating dominant intrinsic Gilbert damping behaviour. This is true for the YIG/GGG thin film alone, the YIG/a-YIG and finally YIG/a-YIG/Pt trilayer structures. A significant change in Gilbert damping was observed with the addition of platinum, either directly to the YIG as a bilayer, or to the YIG plus a-YIG spacer as a trilayer. Effective spin mixing conductance $g_{\text{eff}}^{\uparrow\downarrow}$ was calculated to be (4.4 ± 0.5)x10^{18} m^{-2} for the YIG/Pt bilayer. $g_{\text{eff}}^{\uparrow\downarrow}$ for the YIG/a-YIG/Pt trilayers was also evaluated as a function of a-YIG thickness. However this can only be treated as a first order approximation. Surprisingly, unlike Wang *et al.* [20], the addition of a-YIG alone to YIG does not produce a significant additional Gilbert damping (within experimental error) when grown for thicknesses between 0nm and 30nm.

As the thickness of the a-YIG layer is increased the additional damping due to spin pumping into the Pt is reduced. A clear relationship between damping and a-YIG thickness emerges and resembles one described by diffusive magnon transport. However, a significantly longer magnon diffusion length of (16 ± 2)nm for a-YIG is observed; this diffusion length is approximately 4 times larger than that observed in previous spin-pumping studies by Wang *et al.* (at 3.6nm), and comparable to crystalline NiO where diffusion lengths of 9.6nm or more have been measured [20]. The acquired Gilbert damping, G(L), against a-YIG thickness data ultimately did not agree with the theory for diffusive spin-pumping, modelled for metallic trilayers.

Chapter 7

Conclusions and Future Work

7.1 Summary of Work

The work presented in this thesis was undertaken with three main objectives. The first was to successfully produce high quality YIG thin films on literature-relevant substrates of GGG(111) and YAG(111). This followed a recrystallisation PLD approach by ex-situ annealing in air for 3 hours at 850°C. Epitaxial YIG/GGG and YIG/YAG thin films have been achieved with magnetic quality comparable to high-quality films in literature. The effect of lattice mismatch from each substrate on the structural and magnetic quality of the recrystallised YIG has been investigated. YIG/GGG thin films show extremely strong FMR, with narrow linewidths of (2.0 ± 0.3)Oe at 10GHz being measured and intrinsic Gilbert damping on the order of (4.2 ± 0.5)x10^{-4}. YIG/YAG, in contrast, shows poorer FMR with a dominant extrinsic damping behaviour: non-linear and negative in $\Delta H(f)$. This is considered a result of inhomogeneous strain in the YIG/YAG film, as reflected in the literature. From this work, a recipe for attaining high quality YIG films via recrystallisation-PLD was been established: used both to produce other films analysed in this thesis and for future research at the University of York.

The second objective of this work was to characterise thin films of PLD-grown amorphous YIG on YAG(111) substrates, via soft polarised x-ray magnetic spectroscopy (XMCD) and hard x-ray absorption (XANES/EXAFS). Such characterisation presented a visible gap in existing a-YIG literature, and was pursued to investigate the magnetism of the Fe sites in a-YIG (in comparison to crystalline YIG). The a-YIG/YAG films were subjected to ex-situ annealing at varying temperatures, approaching recrystallisation at 650°C, in an attempt to modify magnetic (or structural) correlation lengths in the a-YIG. The a-YIG remained amorphous with XRD showing only substrate reflections until being ex-situ annealed at 600°C. Fe K-edge EXAFS has suggested a possible Fe^{3+} O_h-Fe^{3+} T_d coordination distance of (2.9 ± 0.1)Å in the a-YIG. This distance follows an apparent trend with annealing temperature, increasing to a higher r of (3.3 ± 0.1)Å at 650°C. VSM measurements have confirmed that a-YIG magnetism is very weak,

and a spin-glass signature has been observed in M(T). a-YIG/YAG M(T) has been observed to transition towards a ferrimagnetic response with ex-situ annealing performed at 550°C (despite no measurable structural changes in XRD). a-YIG XMCD measured over the Fe $L_{3,2}$ edges has been shown to be an order of magnitude smaller than in YIG, owing to significantly weaker magnetism. Atomic multiplet calculations indicate that a-YIG magnetism is approximately 80% dominated by O_h Fe species. However, the a-YIG Fe^{2+}:Fe^{3+} stoichiometry could not be determined with certainty from multiplet calculations performed in this work. Fe K-edge XANES indicates a Fe^{3+}/Fe ratio approaching 1, identically to the crystalline YIG. An XMCD minima at 706eV (a signature of Fe^{2+}) is absent from all experimental a-YIG XMCD. An unexpected temperature-dependence in the as-deposited a-YIG XMCD is also reported, though not explained at present. O_h-dominant contributions to a-YIG magnetism are considered stable with ex-situ annealing up to 400°C. It is concluded that a-YIG magnetism is both very weak and not significantly affected by ex-situ annealing before recrystallisation occurs.

The final objective was to perform an FMR spin-pumping investigation of the a-YIG by fabricating a series of YIG/a-YIG/Pt trilayers, with varying a-YIG spacer layer thickness. Successful spin pumping has been observed, with a large measurable enhancement in YIG Gilbert damping with the addition of platinum; either directly to the YIG as a bilayer, or to the YIG plus a-YIG spacer as a trilayer. Unlike Wang *et al.*[20], no significant enhancement in damping is observed when only a-YIG is grown on YIG for thicknesses between 0 and 30nm, without the Pt layer. As the thickness of the a-YIG layer is increased, the additional damping due to spin pumping into the Pt is reduced. The relationship between damping and a-YIG thickness resembles that described by diffusive magnon transport. However, a significantly longer magnon diffusion length of (16 ± 2)nm for a-YIG is observed; approximately four times larger than that observed in previous spin-pumping studies [20, 21].

7.2 Further Work

The results achieved in this work present a number of directions and open questions for future research into both YIG recrystallisation and amorphous YIG. This body of further work is outlined and discussed below, with reference to each results chapter presented in this thesis.

7.2.1 Recrystallisation of YIG

Although the recrystallisation-PLD approach used throughout this thesis produces YIG thin films with literature quality FMR, the recipe used cannot be justified as optimal for our growth system. A number of growth parameter optimisation studies are required to produce YIG films with the lowest possible FMR linewidths and Gilbert damping. Parameter spaces to be investigated include the effect of background oxygen pressure and UV laser power on deposited a-YIG

films (to then be recrystallised). However, with a recrystallisation-PLD approach, these growth parameters may have little impact on the quality of the YIG film, compared to the final ex-situ annealing step. There are also open questions regarding seemingly minor steps of the growth procedure that may have importance. For example, with the discussion of YIG outgassing in Section 6.1, outgassing the GGG substrate before growth in partial oxygen pressure (instead of vacuum) may influence the YIG/GGG interface or final YIG film roughness.

Changes to the ex-situ annealing step could also be investigated. Unlike Hauser *et al.* [11], YIG films produced in this work were annealed in air instead of a pure oxygen atmosphere. Repeat growths and characterisation of a-YIG recrystallised in pure oxygen warrants a comparison to the in-air YIG films presented. Annealing in oxygen is predicted to produce YIG films with lower damping, with an oxygen excess during the recrystallisation process (compared to 20% of an atmosphere, in air) encouraging better YIG oxide stoichiometry. Another important direction to pursue would be performing the recrystallisation of YIG *in-situ* in the PLD chamber, with the use of the CO_2 laser and background oxygen pressure. Such work would provide a means for growing YIG films and trilayer structures with minimal contamination potential. Alternatively, development of a new growth recipe for in-situ YIG PLD with substrate heating **during** growth would be equally valuable.

Beyond optimisation, gaps in literature surrounding YIG recrystallisation present viable future work. Following Gage *et al.* [120] reporting that 'double annealed' YIG films (400°C then 800°C) produce higher magnetisation than YIG films directly annealed at 800°C, no studies regarding the effect of such annealing on YIG FMR have been published to date. Double annealing would be easily applicable to our own films and recrystallisation-PLD approach. Following in-situ TEM imaging of YIG recrystallisation on SiO_2 membranes by Gage *et al.* (and our own a-YIG/SiN imaging in Chapter 4), TEM imaging of in-situ recrystallisation of an a-YIG/GGG cross-section would provide valuable insights; the mechanism behind YIG/GGG recrystallisation (or nucleation) is currently unknown. In-situ imaging would be possible by mounting an a-YIG/GGG cross-section onto a MEMS-based sample heating chip, with available FIB apparatus [234]. The recrystallisation of YIG/YAG also presents open questions. Detailed characterisation of inhomogenous strain in YIG/YAG using XRD - with emphasis on reciprocal space mapping and rocking curves - could be performed and ideally correlated to observed FMR linewidths (broadened and negative/non-linear in $\Delta H(f)$). Such analysis of YIG/YAG, as a function of annealing temperature between 650°C to 850°C (and above) may show the dependence of the FMR on strain more clearly. Similarly to YIG/GGG above, MEMS-based X-TEM imaging of the recrystallisation process may aid in understanding the mechanism behind unexpected interfacial tensile strain seen in YIG/YAG thin films.

7.2.2 Studies of Amorphous YIG

Further measurements of XMCD are required to complete the characterisation of a-YIG/YAG as a function of annealing temperature presented in Chapter 5. Specifically, the a-YIG/YAG films annealed at 500°C, 500°C and 600°C respectively are the temperature range of interest. 500°C and 550°C a-YIG/YAG films showed a notable change in magnetic response - both in M(H) and M(T) - despite no clear structural changes being observed in XRD. This could potentially indicate a change in magnetic correlation in the a-YIG without recrystallisation. Measurements of XMCD spectra indicating a change in lineshape could confirm this theory. Atomic multiplet calculations may also provide an approximate guide to any change in the observed O_h-dominant magnetism for a-YIG annealed at these temperatures. However, significant theoretical work is required to improve the accuracy of atomic multiplet calculations used in this thesis. Discussed in Chapter 5, reproducing a-YIG XMCD lineshapes without the use of Fe^{2+} would require a rigorous exploration of Slater and crystal-field parameters used in the CTM4XAS software. Repeat XMCD studies of a-YIG ex-situ annealed on GGG and Si substrates also warrant investigation. However, paramagnetic contributions from the GGG would be a limiting factor to other methods of a-YIG characterisation (such as VSM).

Using alternative magnetic characterisation techniques to probe a-YIG magnetism also presents viable future work. Polarised neutron reflectivity (PNR) measurements of a-YIG films, as a function of annealing temperature, would provide a means of probing the a-YIG magnetisation as a function of film depth. Unlike XMCD where magnetism can only be probed near the surface, PNR is sensitive to the entire thickness of the a-YIG film, and allows the depth to which a-YIG magnetisation extends into the bulk to be examined. Photoemission electron microscopy from XMCD (XMCD-PEEM) could also provide supplemental information of the a-YIG surface magnetism, following [16]: allowing for imaging and analysis of domain structure (if any is present).

7.2.3 Spin Transport in Amorphous YIG

In light of successful magnon transport being observed in the YIG/a-YIG/Pt trilayers via FMR-driven spin-pumping, a variety of spin transport experiments warrant being performed on our PLD-grown a-YIG. These experiments should focus on using different spin-transport geometries and detection techniques to the work presented in this thesis. Magnon diffusion lengths inferred from each can be compared, and any differences evaluated. Crucially, these spin transport measurements would concern a-YIG produced from the same growth technique and apparatus to allow direct comparison with (notionally) the same a-YIG material. This potentially eliminates the problem of 'differently amorphous' a-YIG between different groups in literature (discussed in Chapter 1 and Section 2.6.2). Repeat measurements of spin pumping

in YIG/a-YIG(t)/Pt trilayers, but instead using an inverse spin Hall effect (ISHE) detection technique (similar to Wang *et al.* [20]), would provide a direct comparison to Gilbert damping measurements performed in this work. This is significant as reported values of spin/magnon diffusion length are considered to be sensitive to both measurement method and assumptions used to derive them in subsequent analysis [95, 96, 94].

Lateral spin transport experiments in our a-YIG using lithographed electrical Pt (and/or Cu) contacts, following Wesenberg *et al.* [18] and Gomez-Perez *et al.* [19], form a logical next step following spin-pumping. In addition to spin transport, electrical resistivity may also be evaluated with appropriate contact design. However, a number of control experiments require consideration to assess potential effects due to Pt contacts that may influence spin transport measured in a-YIG. Measurements of spin transport through YIG should be pursued first: both as a comparison, and evaluation of the quality of lithographed contacts. Further characterisation work of YIG and a-YIG, both before and after the addition of a Pt layer, would also be advisable.

Measurement of spin transport through a-YIG subjected to ex-situ annealing (before the addition of Pt) could provide insight into whether magnetic correlations in a-YIG can be modified to influence or enhance magnon diffusion lengths; this could be investigated in a spin-pumping and/or lateral contact geometry. Based on XMCD and M(T) VSM presented in Chapter 5, a sensible temperature range to investigate initially would be between 500-550°C, where M(T) of a-YIG is observed to change without visible structural change in XRD. For a spin-pumping geometry with YIG/a-YIG/Pt trilayers, control experiments regarding whether the ex-situ annealing of YIG/a-YIG bilayers at such temperatures produces any notable change in Gilbert damping (prior to the addition of Pt) would require consideration.

Lists of Abbreviations and Symbols

Abbreviations

a-YIG	Amorphous Yttrium Iron Garnet
AF	Antiferromagnetic
BLADE	Beamline for Advanced Dichroism Experiments
CPW	Co-planar Waveguide
EDX	Energy Dispersive X-Ray Spectroscopy
EXAFS	Extended X-ray Absorption Fine Structure
FC	Field Cooled
FIB	Focused Ion Beam
FMR	Ferromagnetic Resonance
FM	Ferromagnetic
FWHM	Full-width at Half Maximum
FY	Fluorescence Yield (detection)
GGG	Gadolinium Gallium Garnet, $Gd_3Ga_5O_{12}$
GKA	Goodenough-Kanamori-Anderson
HAADF-STEM	High-angle Annular Dark Field Scanning Transmission Electron Microscopy
LCP	Left-hand Circular Polarised (X-rays)
LINAC	Linear Accelerator
LLG	Landau-Lifshitz-Gilbert (equation)
MCA	Magnetocrystalline Anisotropy
ME	Magnetoelastic
O_h	Octahedral (lattice site coordination)

PEEM	Photoemission Electron Microscopy
PF	Pole Figure
PLD	Pulsed Laser Deposition
RCP	Right-hand Circular Polarised (X-rays)
RC	Rocking Curve
RF	Radio Frequency
RT	Room Temperature
SEM	Scanning Electron Microscopy
SLD	Scattering Length Density
SOT	Spin Orbit Torque
SQUID	Superconducting Quantum Interference Device
STT	Spin Transfer Torque
$\mathbf{T_d}$	Tetrahedral (lattice site coordination)
TEM	Transmission Electron Microscopy
TEY	Total Electron Yield (detection)
UHV	Ultra High Vacuum
UV	Ultra-violet
VNA-FMR	Vector Network Analyser Ferromagnetic Resonance
VNA	Vector Network Analyser
VSM	Vibrating Sample Magnetometer/Magnetometry
XANES	X-ray Absorption Near Edge Structure
XAS	X-ray Absorption Spectrum/Spectroscopy
XMCD	X-ray Magnetic Circular Dichroism
XRD	X-ray Diffraction/Diffractometer
XRR	X-ray Reflectivity
YAG	Yttrium Aluminium Garnet, $Y_3Al_5O_{12}$
YIG	Yttrium Iron Garnet, $Y_3Fe_5O_{12}$
ZA	Zone Axis
ZFC	Zero Field Cooled

Symbols

α	Gilbert damping parameter (intrinsic damping of FMR linewidth)
χ	Magnetic Susceptibility
χ_{XRD}	Tilt angle in XRD
ΔH	Resonance linewidth in magnetic field
$\Delta\mathrm{H}_0$	Extrinsic damping component of FMR linewidth
$\Delta\mathrm{H}_{\mathrm{PP}}$	Peak-to-peak FMR linewidth
δ_{SD}	Spin-flip scattering state energy spacing
ϵ	Spin-flip probability
γ	Gyromagnetic ratio
$\hbar$	Reduced Planck's constant
λ	Wavelength
λ_{SD}	Spin diffusion length
$\mathbf{I}_S$	Spin current
μ(E)	X-ray absorption coefficient
$\mu_{\mathrm{L}}/\mu_{\mathrm{S}}$	Orbital and spin magnetic moment
μ_0	Magnetic Permeability of Free Space
μ_0H	Magnetic Field
μ_{B}	Bohr Magneton ($\frac{e\hbar}{2m_e}$)
ω	Angular Frequency
ω_{XRD}	Incident X-ray angle in XRD
ϕ	Azimuthal angle in FMR
Ψ	Wavefunction
$\sigma^{+/-}$	Positively (right)/negatively (left) circularly polarised x-rays
τ_{SF}	Spin-flip rate
Θ	Weiss constant
θ	Polar angle in FMR
$g_{\mathrm{eff}}^{\uparrow\downarrow}$	Effective spin mixing conductance

g_J or g_L	Landé g-factor
$\mathbf{M}$	Magnetisation
$\mathbf{m}$	Unit Vector of Magnetisation
C	Curie constant
d_{hkl}	Spacing of (hkl)-oriented crystal lattice planes
Dq	Crystal Field Splitting Parameter
f_r	Resonant Frequency
g	Spectroscopic g-factor
H_{cubic}	Cubic anisotropy magnetic field component
H_c	Coercive magnetic field
H_{eff}	Effective Magnetic Field
H_r	Resonant magnetic field
H_u	Uniaxial anisotropy magnetic field
hkl	Miller Indices in XRD
J	Exchange Integral
$K_\perp$	Perpendicular magnetic anisotropy density
k_B	Boltzmann constant
$K_{c1,2}$	First/second order magnetocrystalline anisotropy constant
M_{eff}	Effective Magnetisation
M_S	Saturation Magnetisation
$S_{x,y}$	S-parameter measured between ports x and y of the VNA
T_C	Curie Temperature
T_f	Spin Freezing Temperature
U	Magnetic (Helmholtz) Free Energy Density

References

[1] A. V. Chumak, V. I. Vasyuchka, A. A. Serga, and B. Hillebrands. "Magnon spintronics". In: *Nature Physics* 11.6 (June 2015), pp. 453–461. ISSN: 1745-2473.

[2] B. Lenk, H. Ulrichs, F. Garbs, and M. Münzenberg. "The building blocks of magnonics". In: *Physics Reports* 507.4-5 (2011), pp. 107–136. ISSN: 03701573.

[3] Y. Kajiwara et al. "Transmission of electrical signals by spin-wave interconversion in a magnetic insulator". In: *Nature* 464.7286 (Mar. 2010), pp. 262–266. ISSN: 0028-0836.

[4] A. V. Chumak, A. A. Serga, and B. Hillebrands. "Magnonic crystals for data processing". In: *Journal of Physics D: Applied Physics* 50.24 (2017), aa6a65. ISSN: 13616463.

[5] A. A. Serga, A. V. Chumak, and B. Hillebrands. "YIG magnonics". In: *Journal of Physics D: Applied Physics* 43.26 (2010). ISSN: 00223727.

[6] M. Sparks, R. Loudon, and C. Kittel. "Ferromagnetic Relaxation. I. Theory of the Relaxation of the Uniform Precession and the Degenerate Spectrum in Insulators at Low Temperatures". In: *Physical Review* 122.3 (May 1961), pp. 791–803. ISSN: 0031-899X.

[7] A. Gurevich and G. Melkov. "Magnetic Oscillations and Waves". In: *CRC Press* (1996).

[8] A. J. Lee et al. "Metallic ferromagnetic films with magnetic damping under 1.4x10-3". In: *Nature Communications 2017 8:1* 8.1 (Aug. 2017), pp. 1–6. ISSN: 2041-1723.

[9] S. Husain, S. Akansel, A. Kumar, P. Svedlindh, and S. Chaudhary. "Growth of Co2FeAl Heusler alloy thin films on Si(100) having very small Gilbert damping by Ion beam sputtering". In: *Scientific Reports 2016 6:1* 6.1 (June 2016), pp. 1–11. ISSN: 2045-2322.

[10] K. Kobayashi et al. "Damping constants for permalloy single-crystal thin films". In: *IEEE Transactions on Magnetics* 45.6 (2009), pp. 2541–2544. ISSN: 00189464.

[11] C. Hauser et al. "Yttrium Iron Garnet Thin Films with Very Low Damping Obtained by Recrystallization of Amorphous Material". In: *Scientific Reports* 6 (Feb. 2016), p. 20827.

[12] H. Chang et al. "Nanometer-Thick Yttrium Iron Garnet Films With Extremely Low Damping". In: *IEEE Magnetics Letters* 5.August (2014), pp. 1–4. ISSN: 1949-307X.

[13] S. M. Rezende, A. Azevedo, and R. L. Rodríguez-Suárez. "Introduction to antiferromagnetic magnons ". In: *J. Appl. Phys* 126 (2019), p. 151101.

[14] A. Barman et al. "The 2021 Magnonics Roadmap". In: *Journal of Physics: Condensed Matter* 33.41 (Aug. 2021), p. 413001. ISSN: 0953-8984.

[15] R. Lebrun et al. "Tunable long-distance spin transport in a crystalline antiferromagnetic iron oxide". In: *Nature 2018 561:7722* 561.7722 (Sept. 2018), pp. 222–225. ISSN: 1476-4687.

[16] A. Ross et al. "Propagation Length of Antiferromagnetic Magnons Governed by Domain Configurations". In: *Nano Letters* (2019). ISSN: 15306992.

[17] H. Ochoa, R. Zarzuela, and Y. Tserkovnyak. "Spin hydrodynamics in amorphous magnets". In: *Physical Review B* 98.5 (2018), pp. 1–8. ISSN: 24699969.

[18] D. Wesenberg, T. Liu, D. Balzar, M. Wu, and B. L. Zink. "Long-distance spin transport in a disordered magnetic insulator". In: *Nature Physics* 13.10 (2017), pp. 987–993. ISSN: 17452481.

[19] J. M. Gomez-Perez et al. "Absence of evidence of spin transport through amorphous Y3Fe5O12". In: *Applied Physics Letters* 116.3 (Jan. 2020), p. 032401. ISSN: 00036951.

[20] H. Wang, C. Du, P. C. Hammel, and F. Yang. "Spin transport in antiferromagnetic insulators mediated by magnetic correlations". In: *Physical Review B - Condensed Matter and Materials Physics* 91.22 (June 2015), pp. 1–5. ISSN: 1550235X.

[21] L. Yang et al. "Absence of spin transport in amorphous YIG evidenced by nonlocal spin transport experiments". In: *Physical Review B* 104.14 (Oct. 2021), p. 144415. ISSN: 24699969.

[22] J. M. D. Coey. *Magnetism and magnetic materials*. Cambridge University Press, 2009, p. 628. ISBN: 0521816149.

[23] A. I. M. Rae and J. Napolitano. *Quantum Mechanics, Sixth Edition*. Taylor & Francis, 2017. ISBN: 9781482299182.

[24] S. Blundell. *Magnetism in condensed matter*. Oxford University Press, 2001, p. 238. ISBN: 9780198505914.

[25] D. Jiles. *Introduction to magnetism and magnetic materials*, p. 588. ISBN: 9781482238877.

[26] C. Kittel. *Introduction to solid state physics*. Wiley, 2005, p. 680. ISBN: 9780471415268.

[27] G. F. Dionne. *Magnetic Oxides*. Boston, MA: Springer US, 2009. ISBN: 978-1-4419-0053-1.

[28] K. M. Krishnan. *Fundamentals and Applications of Magnetic Materials*. Oxford University Press, Dec. 2016.

[29] L. Néel. "Antiferromagnetism and ferrimagnetism". In: *Proceedings of the Physical Society. Section A* 65.11 (Nov. 1952), pp. 869–885. ISSN: 03701298.

[30] A. B. Lidiard. "Antiferromagnetism". In: *Reports on Progress in Physics* 17.1 (Jan. 1954), pp. 201–244. ISSN: 00344885.

[31] J. C. Slater. "Atomic shielding constants". In: *Physical Review* 36.1 (July 1930), pp. 57–64. ISSN: 0031899X.

[32] A. Sommerfeld and H. Bethe. "Elektronentheorie der Metalle". In: *Aufbau Der Zusammenhängenden Materie*. Springer Berlin Heidelberg, 1933, pp. 333–622.

[33] K. Moorjani and J. M. D. Coey. *Magnetic glasses*. Elsevier, 1984, p. 525. ISBN: 0444416404.

[34] B. D. Cullity and C. D. Graham. "Introduction to Magnetic Materials". In: *Introduction to Magnetic Materials* (Nov. 2008).

[35] P. W. Anderson. "New approach to the theory of superexchange interactions". In: *Physical Review* 115.1 (1959), pp. 2–13. ISSN: 0031899X.

[36] J. Kanamori. "Superexchange interaction and symmetry properties of electron orbitals". In: *Journal of Physics and Chemistry of Solids* 10.2-3 (July 1959), pp. 87–98. ISSN: 00223697.

[37] S. V. Streltsov and D. I. Khomskii. "Orbital physics in transition metal compounds: new trends". In: *Physics-Uspekhi* 60.11 (Nov. 2017), pp. 1121–1146. ISSN: 1063-7869.

[38] P. W. Anderson and H. Hasegawa. "Considerations on double exchange". In: *Physical Review* 100.2 (Oct. 1955), pp. 675–681. ISSN: 0031899X.

[39] P. G. De Gennes. "Effects of double exchange in magnetic crystals". In: *Physical Review* 118.1 (1960), pp. 141–154. ISSN: 0031899X.

[40] G. Gubbiotti, G. Carlotti, and B. Hillebrands. "Spin waves and magnetic anisotropy in ultrathin (111)-oriented cubic films". In: *J. Phys. C* 10 (1998), p. 2171.

[41] E. R. Callen, A. E. Clark, B. Desavage, W. Coleman, and H. B. Callen. "Magnetostriction in Cubic Néel Ferrimagnets, with Application to YIG". In: *Physical Review* 130.5 (June 1963), p. 1735. ISSN: 0031899X.

[42] W. Strauss. "Magnetoelastic Properties of Yttrium-Iron Garnet". In: *Physical Acoustics* 4.PB (Jan. 1968), pp. 211–268. ISSN: 0893-388X.

[43] L. R. Bickford. "Ferromagnetic Resonance Absorption in Magnetite Single Crystals". In: *Physical Review* 78.4 (May 1950), p. 449. ISSN: 0031899X.

[44] C. Vittoria. *Magnetics, dielectrics, and wave propagation with MATLAB® codes*. CRC Press, Jan. 2010, pp. 1–445. ISBN: 9781439894804.

[45] R. G. Burns. *Mineralogical Applications of Crystal Field Theory*. Cambridge University Press, Sept. 1993. ISBN: 9780521430777.

[46] B. Figgis. *Introduction to ligand fields*. New York: Interscience Publishers, 1966.

[47] R. Skomski. *Simple Models of Magnetism*. Oxford University Press, 2008, pp. 1–366.

[48] C. Kittel. "On the Gyromagnetic Ratio and Spectroscopic Splitting Factor of Ferromagnetic Substances". In: *Physical Review* 76.6 (Sept. 1949), p. 743. ISSN: 0031899X.

[49] M. Blume, S. Geschwind, and Y. Yafet. "Generalized Kittel-Van Vleck Relation between g and g'; Validity for Negative g Factors". In: *Phys. Rev.* 181.2 (May 1969), pp. 478–487.

[50] J. M. Shaw, H. T. Nembach, T. J. Silva, and C. T. Boone. "Precise determination of the spectroscopic g-factor by use of broadband ferromagnetic resonance spectroscopy". In: *Journal of Applied Physics* 114.24 (Dec. 2013). ISSN: 0021-8979.

[51] J. M. Shaw et al. "Quantifying Spin-Mixed States in Ferromagnets". In: *Physical Review Letters* 127.20 (2021), p. 207201. ISSN: 10797114.

[52] D. D. Stancil and A. Prabhakar. *Spin waves : theory and applications*. Springer, 2009. ISBN: 9780387778655.

[53] Y. Sun, Y. Y. Song, and M. Wu. "Growth and ferromagnetic resonance of yttrium iron garnet thin films on metals". In: *Applied Physics Letters* 101.8 (2012), pp. 8–11. ISSN: 00036951.

[54] G. S. Abo et al. "Definition of magnetic exchange length". In: *IEEE Transactions on Magnetics* 49.8 (2013), pp. 4937–4939. ISSN: 00189464.

[55] C. Kittel. "On the theory of ferromagnetic resonance absorption". In: *Physical Review* 73.2 (1948), pp. 155–161. ISSN: 0031899X.

[56] O. Yalcin. *Ferromagnetic Resonance - Theory and Applications*. Ed. by O. Yaln. InTech, July 2013. ISBN: 978-953-51-1186-3.

[57] J. Smit and H. Beljers. "Ferromagnetic resonance absorption in BaFe12O19, a highly anisotropic crystal". In: *Philips Research Reports* 10 (1955), pp. 113–130.

[58] T. L. Gilbert. "A phenomenological theory of damping in ferromagnetic materials". In: *IEEE Transactions on Magnetics* 40.6 (Nov. 2004), pp. 3443–3449. ISSN: 00189464.

[59] K. Zakeri et al. "Spin dynamics in ferromagnets: Gilbert damping and two-magnon scattering". In: *Physical Review B* 76.10 (Sept. 2007), p. 104416. ISSN: 1098-0121.

[60] P. Pincus. "Excitation of spin waves in ferromagnets: eddy current and boundary condition effects". In: *Physical Review* 118.3 (May 1960), pp. 658–664. ISSN: 0031899X.

[61] P. Dai et al. "Magnon damping by magnon-phonon coupling in manganese perovskites". In: *Physical Review B* 61.14 (Apr. 2000), p. 9553.

[62] A. Barman and J. Sinha. *Spin dynamics and damping in ferromagnetic thin films and nanostructures*. Springer International Publishing, Dec. 2017, pp. 1–156. ISBN: 9783319662961.

[63] S. Zhang and Z. Li. "Roles of Nonequilibrium Conduction Electrons on the Magnetization Dynamics of Ferromagnets". In: *Physical Review Letters* 93.12 (Sept. 2004), p. 127204.

[64] Y. Tserkovnyak, A. Brataas, G. E. Bauer, and B. I. Halperin. "Nonlocal magnetization dynamics in ferromagnetic heterostructures". In: *Reviews of Modern Physics* 77.4 (Oct. 2005), pp. 1375–1421.

[65] B. Heinrich, R. Urban, and G. Woltersdorf. "Magnetic relaxation in metallic films: Single and multilayer structures". In: *Journal of Applied Physics* 91.10 I (May 2002), pp. 7523–7525.

[66] H. Suhl. "Theory of the magnetic damping constant". In: *IEEE Transactions on Magnetics* 34.4 (1998), pp. 1834–1838. ISSN: 00189464.

[67] B. Heinrich, J. F. Cochran, and K. Myrtle. "The exchange splitting of phonon assisted microwave transmission at 9.5 GHz". In: *Journal of Applied Physics* 53.3 (June 1998), p. 2092. ISSN: 0021-8979.

[68] N. Mazumder and B. Roy. "Effect of phonon viscosity on dislocation motion in yttrium iron garnet". In: *Journal of Applied Physics* 50 (1979), p. 6549.

[69] V. Kamberský. "Spin-orbital Gilbert damping in common magnetic metals". In: *Physical Review B* 76.13 (Oct. 2007), p. 134416.

[70] V. Kamberský. "On ferromagnetic resonance damping in metals". In: *Czechoslovak Journal of Physics* 26.12 (1976), pp. 1366–1383. ISSN: 15729486.

[71] J. Kuneš and V. Kamberský. "First-principles investigation of the damping of fast magnetization precession in ferromagnetic 3d metals". In: *Physical Review B - Condensed Matter and Materials Physics* 65.21 (June 2002), pp. 1–3. ISSN: 1550235X.

[72] O. Eriksson, A. Bergman, L. Bergqvist, and J. Hellsvik. *Atomistic Spin Dynamics: Foundations and Applications*. 1st. Oxford University Press, May 2017.

[73] D. Thonig and J. Henk. "Gilbert damping tensor within the breathing Fermi surface model: anisotropy and non-locality". In: *New Journal of Physics* 16.1 (Jan. 2014), p. 013032. ISSN: 1367-2630.

[74] K. Gilmore, M. D. Stiles, J. Seib, D. Steiauf, and M. Fähnle. "Anisotropic damping of the magnetization dynamics in Ni, Co, and Fe". In: *Physical Review B - Condensed Matter and Materials Physics* 81.17 (May 2010), p. 174414. ISSN: 10980121.

[75] G. Schmidt, C. Hauser, P. Trempler, M. Paleschke, and E. T. Papaioannou. "Ultra Thin Films of Yttrium Iron Garnet with Very Low Damping: A Review". In: *physica status solidi (b)* 257.7 (July 2020), p. 1900644. ISSN: 1521-3951.

[76] R. Arias and D. L. Mills. "Extrinsic contributions to the ferromagnetic resonance response of ultrathin films". In: *Physical Review B* 60.10 (Sept. 1999), p. 7395.

[77] K. Lenz et al. "Two-magnon scattering and viscous Gilbert damping in ultrathin ferromagnets". In: *Physical Review B* 73.14 (Apr. 2006), p. 144424.

[78] Y. Niimi and Y. Otani. "Reciprocal spin Hall effects in conductors with strong spin–orbit coupling: a review". In: *Reports on Progress in Physics* 78.12 (2015), p. 124501.

[79] K. S. Das, W. Y. Schoemaker, B. J. Van Wees, and I. J. Vera-Marun. "Spin injection and detection via the anomalous spin Hall effect of a ferromagnetic metal". In: *Physical Review B* 96.22 (Dec. 2017), p. 220408. ISSN: 24699969.

[80] A. Hirohata, J. Sagar, L. R. Fleet, and S. S. Parkin. "Heusler Alloy films for spintronic devices". In: *Springer Series in Materials Science* 222.2013 (2016), pp. 219–248. ISSN: 0933033X.

[81] J. C. Slonczewski. "Current-driven excitation of magnetic multilayers". In: *Journal of Magnetism and Magnetic Materials* 159.1-2 (June 1996), pp. L1–L7. ISSN: 0304-8853.

[82] A. Mahmoud et al. "Introduction to Spin Wave Computing". In: *TechRxiv Preprint (IEEE)* (Sept. 2021).

[83] F. Yang and P. Chris Hammel. "FMR-driven spin pumping in Y3Fe5O12-based structures". In: *Journal of Physics D: Applied Physics* 51.25 (June 2018), p. 253001. ISSN: 0022-3727.

[84] A. Brataas, Y. Tserkovnyak, G. E. Bauer, and P. J. Kelly. "Spin pumping and spin transfer". In: *Spin Current* (Dec. 2017), pp. 93–142.

[85] Y. Tserkovnyak, A. Brataas, and G. E. W. Bauer. "Spin pumping and magnetization dynamics in metallic multilayers". In: *Physical Review B* 66.22 (Dec. 2002), p. 224403.

[86] B. Heinrich and J. A. C. Bland. *Ultrathin Magnetic Structures III: Fundamentals of Nanomagnetism*. Berlin: Springer-Verlag, 2005.

[87] Y. Sun et al. "Growth and ferromagnetic resonance properties of nanometer-thick yttrium iron garnet films". In: *Applied Physics Letters* 101.15 (2012). ISSN: 00036951.

[88] C. Swindells and D. Atkinson. "Interface enhanced precessional damping in spintronic multilayers: A perspective ". In: *J. Appl. Phys* 131 (2022), p. 170902.

[89] M. Weiler et al. "Experimental test of the spin mixing interface conductivity concept". In: *Physical Review Letters* 111.17 (Oct. 2013), p. 176601. ISSN: 00319007.

[90] K. Xia, P. J. Kelly, G. E. Bauer, A. Brataas, and I. Turek. "Spin torques in ferromagnetic/normal-metal structures". In: *Physical Review B* 65.22 (May 2002), p. 220401. ISSN: 01631829.

[91] A. Kapelrud and A. Brataas. "Spin Pumping and Enhanced Gilbert Damping in Thin Magnetic Insulator Films". In: *Physical Review Letters* 111.9 (Aug. 2013), p. 097602.

[92] X. Jia, K. Liu, K. Xia, and G. E. Bauer. "Spin transfer torque on magnetic insulators". In: *Europhysics Letters* 96.1 (Sept. 2011), p. 17005. ISSN: 0295-5075.

[93] S. Mizukami, Y. Ando, and T. Miyazaki. "Ferromagnetic resonance linewidth for NM/80NiFe/NM films (NM=Cu, Ta, Pd and Pt)". In: *Journal of Magnetism and Magnetic Materials* 226-230.PART II (May 2001), pp. 1640–1642. ISSN: 0304-8853.

[94] C. Swindells et al. "Magnetic damping in ferromagnetic/heavy-metal systems: The role of interfaces and the relation to proximity-induced magnetism". In: *Physical Review B* 105.9 (Mar. 2022), p. 094433. ISSN: 2469-9950.

[95] J. Bass and W. P. Pratt. "Spin-diffusion lengths in metals and alloys, and spin-flipping at metal/metal interfaces: an experimentalist's critical review". In: *Journal of Physics: Condensed Matter* 19.18 (Apr. 2007), p. 183201. ISSN: 0953-8984.

[96] C. Swindells, A. T. Hindmarch, A. J. Gallant, and D. Atkinson. "Spin transport across the interface in ferromagnetic/nonmagnetic systems". In: *Physical Review B* 99.6 (Feb. 2019), pp. 5–9. ISSN: 24699969.

[97] S. Mizukami, Y. Ando, and T. Miyazaki. "Effect of spin diffusion on Gilbert damping for a very thin permalloy layer in Cu/permalloy/Cu/Pt films". In: *Physical Review B* 66.10 (Sept. 2002), p. 104413. ISSN: 01631829.

[98] S. Yakata, Y. Ando, T. Miyazaki, and S. Mizukami. "Temperature dependences of spin-diffusion lengths of Cu and Ru layers". In: *Japanese Journal of Applied Physics, Part 1: Regular Papers and Short Notes and Review Papers* 45.5 A (May 2006), pp. 3892–3895. ISSN: 00214922.

[99] F. Bertaut and F. Forrat. "Structure des ferrites ferrimagnetiques des terres rares". In: *Comptes Rendus de l' Academie des Sciences* 242 (1956), pp. 382–4.

[100] P. E. Wigen, R. D. McMichael, and C. Jayaprakash. "Route to chaos in the magnetic garnets". In: *Journal of Magnetism and Magnetic Materials* 84.3 (1990), pp. 237–246.

[101] G. Winkler. *Magnetic garnets*. Vieweg, 1981, p. 736. ISBN: 3528084871.

[102] A. J. Princep et al. "The full magnon spectrum of yttrium iron garnet". In: *NPJ Quantum Materials* 2.1 (Nov. 2017), pp. 1–5. ISSN: 23974648.

[103] F. Hansteen. *Ultrafast Optical Control of Magnetization in Ferrimagnetic Garnets*. Tech. rep. Nijmegen: Radboud University, 2006.

[104] B. Lax and K. J. Button. *Microwave Ferrites and Ferri-magnetics*. New York: McGraw-Hill, 1962.

[105] M. A. Gilleo and S. Geller. "Magnetic and Crystallographic Properties of Substituted Yttrium-Iron Garnet, Y2O3.xM2O3.(5-x)Fe2O3". In: *Phys. Rev.* 110.1 (Apr. 1958), pp. 73–78.

[106] M. Wu. "Nonlinear Spin Waves in Magnetic Film Feedback Rings". In: *Solid State Physics - Advances in Research and Applications* 62 (Jan. 2010), pp. 163–224. ISSN: 0081-1947.

[107] S. Geller and M. A. Gilleo. "The crystal structure and ferrimagnetism of yttrium-iron garnet, Y3Fe2(FeO4)3". In: *Journal of Physics and Chemistry of Solids* 3.1-2 (1957), pp. 30–36. ISSN: 00223697.

[108] T. Fujii and Y. Sakabe. "Growth and Magnetic Properties of YIG Films". In: *Encyclopedia of Materials: Science and Technology* (Jan. 2001), pp. 3666–3670.

[109] R. C. Weast. *CRC Handbook of Chemistry and Physics*. 64. ed. Boca Raton: CRC Press, 1983.

[110] M. B. Park and N. H. Cho. "Structural and magnetic characteristics of yttrium iron garnet (YIG, Ce : YIG) films prepared by RF magnetron sputter techniques". In: *Journal of Magnetism and Magnetic Materials* 231.2-3 (June 2001), pp. 253–264. ISSN: 0304-8853.

[111] P. J. Besser, J. E. Mee, P. E. Elkins, and D. M. Heinz. "A Stress Model For Heteroepitaxial Magnetic Oxide Films Grown By Chemical Vapor Deposition". In: *Mat. Res. Bull* 6 (1971), pp. 1111–1124.

[112] S. Mino, A. Tate, T. Uno, T. Shintaku, and A. Shibukawa. "Structure and Lattice Deformation of Ce-Substituted Yttrium Iron Garnet Film Prepared by RF Sputtering". In: *Japanese Journal of Applied Physics* 32.7 R (July 1993), pp. 3154–3159. ISSN: 13474065.

[113] O. I. Gorbatov et al. "Magnetic exchange interactions in yttrium iron garnet: A fully relativistic first-principles investigation". In: *Physical Review B* 104.17 (Nov. 2021). ISSN: 24699969.

[114] R. Metselaar and P. K. Larsen. "Electrical Properties of Yttrium Iron Garnet". In: *Proc. Int. Sch. Phys. Enrico Fermo* 70.417 (1978).

[115] S. Emori and P. Li. "Ferrimagnetic insulators for spintronics: Beyond garnets". In: *Journal of Applied Physics* 129.2 (Jan. 2021). ISSN: 0021-8979.

[116] A. Mitra et al. "Interfacial Origin of the Magnetisation Suppression of Thin Film Yttrium Iron Garnet". In: *Scientific Reports* 7.1 (Sept. 2017), pp. 1–8. ISSN: 2045-2322.

[117] E. M. Gyorgy et al. "The magnetic properties of amorphous Y3Fe5O12". In: *Journal of Applied Physics* 50.4 (1979), pp. 2883–2886. ISSN: 00218979.

[118] A. W. Simpson and J. M. Lucas. "Temperature Variation of Susceptibility of Some Amorphous Antiferromagnetic Oxides". In: *Journal of Applied Physics* 42.6 (May 1971), pp. 2181–2185. ISSN: 0021-8979.

[119] Y. G. Chukalkin, V. R. Shtirts, and B. N. Goshchitskii. "Structural and Magnetic Transformations in Y3Fe5O12 under Neutron Irradiation". In: *Physica Status Solidi (a)* 125.1 (1991), pp. 301–311. ISSN: 1521396X.

[120] T. E. Gage, P. Dulal, P. A. Solheid, D. J. Flannigan, and B. J. Stadler. "Si-integrated ultrathin films of phase-pure Y3Fe5O12 (YIG) via novel two-step rapid thermal anneal". In: *Materials Research Letters* 5.6 (2017), pp. 379–385. ISSN: 21663831.

[121] R. Eason et al. "Current state-of-the-art of pulsed laser deposition of optical waveguide structures: Existing capabilities and future trends". In: *Applied Surface Science* 255.10 (Mar. 2009), pp. 5199–5205. ISSN: 01694332.

[122] P. R. Willmott and J. R. Huber. "Pulsed laser vaporization and deposition". In: *Reviews of Modern Physics* 72.1 (Jan. 2000), pp. 315–328. ISSN: 00346861.

[123] Robert Eason. *Pulsed Laser Deposition of Thin Films*. Ed. by R. Eason. Hoboken, NJ, USA: John Wiley & Sons, Inc., Nov. 2006. ISBN: 9780470052129.

[124] H. M. Christen and G. Eres. "Recent advances in pulsed-laser deposition of complex oxides". In: *Journal of Physics: Condensed Matter* 20.26 (July 2008), p. 264005. ISSN: 0953-8984.

[125] R. W. Eason et al. "Multi-beam pulsed laser deposition for advanced thin-film optical waveguides". In: *Journal of Physics D: Applied Physics* 47.3 (Jan. 2014), p. 034007. ISSN: 00223727.

[126] B. D. Cullity and S. R. Stock. *Elements of x-ray diffraction*. 3rd. Prentice Hall, 2001, p. 664. ISBN: 0131788183.

[127] W. Clegg et al. *Crystal Structure Analysis: Principles and Practice*. Oxford University Press, Sept. 2009, pp. 1–408. ISBN: 9780199219469.

[128] K. Inaba. "X-Ray Thin-Film Measurement Techniques I. Overview". In: *The Rigaku Journal* 24.1 (2008).

[129] H. Toraya. "Introduction to X-Ray Analysis Using the Diffraction Method". In: *The Rigaku Journal* 32.2 (2016).

[130] T. Mitsunaga. "X-ray thin-film measurement techniques II. Out-of-plane diffraction measurements". In: *The Rigaku Journal* 25.1 (2009).

[131] R. Roof. "INDX: X-Ray Diffraction Powder Pattern Indexing, Trial Unit Cell Testing". In: *Organisation for Economic Co-Operation and Development, Nuclear Energy Agency* 41.26 (1989).

[132] M. Birkholz. *Thin Film Analysis by X-Ray Scattering*. WILEY-VCH Verlag GmbH & Co. KGaA, 2006. ISBN: 978-3-527-31052-4.

[133] S. A. Speakman. "Introduction to High Resolution X-Ray Diffraction of Epitaxial Thin Films". In: *Massachusetts Institute of Technology* (2010).

[134] M. Ohring. *The Materials Science of Thin Films*. New York: Academic Press, 2001. ISBN: 012524990X.

[135] R. Jenkins and R. L. Snyder. *Introduction to X-ray Powder Diffractometry*. New York: John Wiley & Sons, Inc., June 1996. ISBN: 0471513393.

[136] K. Nagao and E. Kagam. "X-ray thin film measurement techniques VII. Pole figure measurement". In: *The Rigaku Journal* 27.2 (2011).

[137] S. Kobayashi. "X-ray thin-film measurement techniques IV: In-plane XRD measurements". In: *The Rigaku Journal* 26.1 (2010).

[138] M. Yasaka. "X-ray thin-film measurement techniques V. X-ray reflectivity measurement". In: *The Rigaku Journal* 26.2 (2010).

[139] A. Gibaud. "Specular Reflectivity from Smooth and Rough Surfaces". In: *X-ray and Neuron Reflectivity: Principles and Applications*. Springer Berlin Heidelberg, July 2007, pp. 87–120.

[140] M. Björck and G. Andersson. "GenX: an extensible X-ray reflectivity refinement program utilizing differential evolution". In: *Journal of Applied Crystallography* 40.6 (Nov. 2007), pp. 1174–1178. ISSN: 0021-8898.

[141] M. Yasaka. "Integrated Thin Film Analysis Software GlobalFit (Reflectivity Analysis)". In: *The Rigaku Journal* 26.1 (2010).

[142] D. B. Williams and C. B. Carter. *Transmission electron microscopy: A textbook for materials science*. Second. Springer US, 2009, pp. 1–760.

[143] K. E. MacArthur. "The use of annular dark-field scanning transmission electron microscopy for quantitative characterisation". In: *Johnson Matthey Technology Review* 60.2 (2016), pp. 117–131. ISSN: 20565135.

[144] L. A. Giannuzzi and F. A. Stevie. "A review of focused ion beam milling techniques for TEM specimen preparation". In: *Micron* 30.3 (June 1999), pp. 197–204. ISSN: 0968-4328.

[145] S. Foner. "Versatile and Sensitive Vibrating-Sample Magnetometer". In: *Review of Scientific Instruments* 30.548 (Dec. 1959). ISSN: 0034-6748.

[146] "User's Manual 7300 VSM System." In: *Lake Shore Cryotronics, Inc.* (2001).

[147] P. A. Joy, P. S. Anil Kumar, and S. K. Date. "The relationship between field-cooled and zero-field-cooled susceptibilities of some ordered magnetic systems". In: *Journal of Physics Condensed Matter* 10.48 (Dec. 1998), pp. 11049–11054. ISSN: 09538984.

[148] R. W. Chantrell, N. S. Walmsley, J. Gore, and M. Maylin. "Theoretical studies of the field-cooled and zero-field cooled magnetization of interacting fine particles". In: *Journal of Applied Physics* 85.8 II A (Apr. 1999), pp. 4340–4342. ISSN: 00218979.

[149] J. Clarke. "SQUIDs". In: *Scientific American* 271.2 (Aug. 1994), pp. 46–53. ISSN: 0036-8733.

[150] M. Elfresh. *Fundamentals of Magnetism and Magnetic Measurements Featuring Quantum Design's Magnetic Property Measurement System*. Tech. rep. Purdue University, 1994, pp. 1–34.

[151] M. Buchner, K. Höfler, B. Henne, V. Ney, and A. Ney. "Tutorial: Basic principles, limits of detection, and pitfalls of highly sensitive SQUID magnetometry for nanomagnetism and spintronics". In: *Journal of Applied Physics* 124.16 (Oct. 2018), p. 161101. ISSN: 0021-8979.

[152] C. Swindells et al. "Proximity-induced magnetism and the enhancement of damping in ferromagnetic/heavy metal systems". In: *Applied Physics Letters* 119.15 (Oct. 2021), p. 152401. ISSN: 0003-6951.

[153] L. F. Chen. *Microwave electronics: measurement and materials characterization*. Wiley, 2004, p. 537. ISBN: 978-0-470-84492-2.

[154] N. Instruments. "Introduction to Network Analyser Measurements". In: *National Instruments RF Academy* (2012).

[155] G. Woltersdorf. "Spin Pumping and Two-Magnon Scattering In Magnetic Multilayers". PhD thesis. Halle: Martin-Luther-Universitat, 2004.

[156] A. Krysztofik et al. "Characterization of spin wave propagation in (1 1 1) YIG thin films with large anisotropy". In: *Journal of Physics D: Applied Physics* 50.23 (May 2017), p. 235004. ISSN: 0022-3727.

[157] C. Dubs et al. "Sub-micrometer yttrium iron garnet LPE films with low ferromagnetic resonance losses". In: *Journal of Physics D: Applied Physics* 50.20 (Apr. 2017), pp. 1–8. ISSN: 13616463.

[158] I. S. Maksymov and M. Kostylev. "Broadband stripline ferromagnetic resonance spectroscopy of ferromagnetic films, multilayers and nanostructures". In: *Physica E: Low-dimensional Systems and Nanostructures* 69 (May 2015), pp. 253–293. ISSN: 1386-9477.

[159] G. van der Laan and A. I. Figueroa. "X-ray magnetic circular dichroism - A versatile tool to study magnetism". In: *Coordination Chemistry Reviews* 277 (Oct. 2014), pp. 95–129. ISSN: 00108545.

[160] F. de Groot and A. Kotani. *Core level spectroscopy of solids*. CRC Press, Jan. 2008, pp. 1–491. ISBN: 9781420008425.

[161] M. L. Baker et al. "K- and L-edge X-ray Absorption Spectroscopy (XAS) and Resonant Inelastic X-ray Scattering (RIXS) Determination of Differential Orbital Covalency (DOC) of Transition Metal Sites". In: *Coordination chemistry reviews* 345 (Aug. 2017), pp. 182–208. ISSN: 0010-8545.

[162] N. A. Dyson. *X-rays in atomic and nuclear physics*. London: Longman, 1973, pp. 180–196. ISBN: 0582462185.

[163] G. van der Laan and A. I. Figueroa. "X-ray magnetic circular dichroism—A versatile tool to study magnetism". In: *Coordination Chemistry Reviews* 277-278 (Oct. 2014), pp. 95–129. ISSN: 00108545.

[164] E. Stavitski and F. M. de Groot. "The CTM4XAS program for EELS and XAS spectral shape analysis of transition metal L edges". In: *Micron* 41.7 (Oct. 2010), pp. 687–694. ISSN: 09684328.

[165] R. D. Cowan and D. C. Griffin. "Approximate relativistic corrections to atomic radial wave functions*". In: *JOSA, Vol. 66, Issue 10, pp. 1010-1014* 66.10 (Oct. 1976), pp. 1010–1014. ISSN: 0030-3941.

[166] R. D. Cowan. *The theory of atomic structure and spectra*. 3. Univ of California Press, 1981.

[167] F. De Groot. "Multiplet effects in X-ray spectroscopy". In: *Coordination Chemistry Reviews* (2004).

[168] G. Van Der Laan. "Applications of soft x-ray magnetic dichroism". In: *Journal of Physics: Conference Series* 430.1 (Apr. 2013), p. 012127.

[169] C. T. Chen et al. "Experimental Confirmation of the X-Ray Magnetic Circular Dichroism Sum Rules for Iron and Cobalt". In: *Physical Review Letters* 75.1 (July 1995), p. 152. ISSN: 00319007.

[170] B. T. Thole, P. Carra, F. Sette, and G. Van Der Laan. "X-ray circular dichroism as a probe of orbital magnetization". In: *Physical Review Letters* 68.12 (Mar. 1992), p. 1943. ISSN: 00319007.

[171] G. Materlik, T. Rayment, and D. I. Stuart. "Diamond Light Source: Status and perspectives". In: *Philosophical Transactions of the Royal Society A: Mathematical, Physical and Engineering Sciences* 373.2036 (Mar. 2015). ISSN: 1364503X.

[172] C. Abraham et al. *Diamond-II Conceptual Design Report With contributions from Diamond-II: Conceptual Design Report*. Tech. rep. Diamond Light Source Ltd, 2019.

[173] *I10 Technique Information: I10-Beamline for Advanced Dichroism Experiments (BLADE)*. Tech. rep. Diamond Light Source Ltd, 2016.

[174] H. Wang et al. "Complete polarization analysis of an APPLE II undulator using a soft X-ray polarimeter". In: *Journal of Synchrotron Radiation* 19.6 (Nov. 2012), pp. 944–948. ISSN: 09090495.

[175] D. H. Bilderback, P. Elleaume, and E. Weckert. "Review of third and next generation synchrotron light sources". In: *J. Phys. B: At. Mol. Opt. Phys* 38 (2005), pp. 773–797.

[176] C. Schmitz-Antoniak. "X-ray absorption spectroscopy on magnetic nanoscale systems for modern applications". In: *Reports on Progress in Physics* 78.6 (June 2015). ISSN: 00344885.

[177] R. Nakajima, J. Stöhr, Y. U. Idzerda, J. Stö, and Y. U. Idzerda. "Electron-yield saturation effects in l-edge x-ray magnetic circular dichroism spectra of fe, co, and ni". In: *Physical Review B - Condensed Matter and Materials Physics* 59.9 (1999), pp. 6421–6429. ISSN: 1550235X.

[178] G. S. Henderson, F. M. F. De Groot, and B. J. A. Moulton. "X-ray Absorption Near-Edge Structure (XANES) Spectroscopy". In: *Spectroscopic Methods in Mineralogy and Geology* 78 (2014), pp. 75–138.

[179] A. J. Berry, H. S. C. O'Neill, K. D. Jayasuriya, S. J. Campbell, and G. J. Foran. "XANES calibrations for the oxidation state of iron in a silicate glass". In: *American Mineralogist* 88.7 (2003), pp. 967–977. ISSN: 0003004X.

[180] W. T. Chen, C. W. Hsu, J. F. Lee, C. W. Pao, and I. J. Hsu. "Theoretical Analysis of Fe K-Edge XANES on Iron Pentacarbonyl". In: *ACS Omega* 5.10 (Mar. 2020), pp. 4991–5000. ISSN: 24701343.

[181] M. Newville. "Fundamentals of XAFS". In: *Consortium for Advanced Radiation Sources* (2004).

[182] B. Ravel and M. Newville. "ATHENA, ARTEMIS, HEPHAESTUS: data analysis for X-ray absorption spectroscopy using IFEFFIT". In: *Journal of synchrotron radiation* 12.Pt 4 (July 2005), pp. 537–541. ISSN: 0909-0495.

[183] J. A. Clarke. *The Science and Technology of Undulators and Wigglers*. Oxford University Press, Sept. 2007.

[184] S. Ramos et al. "B18: A core XAS spectroscopy beamline for Diamond XAFS on minerals". In: *Article in Journal of Physics Conference Series* 190 (2009), p. 12039.

[185] A. J. Dent et al. "B18: A core XAS spectroscopy beamline for Diamond". In: *Journal of Physics: Conference Series* 190 (2009). ISSN: 17426596.

[186] A. Sposito, G. B. Stenning, S. A. Gregory, P. A. De Groot, and R. W. Eason. "Compositional tuning of yttrium iron garnet film properties by multi-beam pulsed laser deposition". In: *Thin Solid Films* 568.1 (2014), pp. 31–37. ISSN: 00406090.

[187] C. Hahn et al. "Measurement of the intrinsic damping constant in individual nanodisks of Y3Fe5O12 and Y3Fe5O12—Pt". In: *Applied Physics Letters* 104.15 (Apr. 2014), p. 152410. ISSN: 0003-6951.

[188] M. Lammel et al. "Atomic layer deposition of yttrium iron garnet thin films". In: *Physical Review Materials* 6.4 (Apr. 2022), p. 044411. ISSN: 2475-9953.

[189] B. Ferrand, J. Daval, and J. C. Joubert. "Heteroepitaxial growth of single crystal films of YIG on GdGaG substrates by hydrothermal synthesis". In: *Journal of Crystal Growth* 17.C (Dec. 1972), pp. 312–314. ISSN: 0022-0248.

[190] P. A. Stadelmann. *JEMS - A Java-based EMS software package for Electron Diffraction Analysis and Simulation. https://www.jems-swiss.ch.* 2004.

[191] G. Vertesy and I. Tomas. "Survey of the dependence on temperature of the coercivity of garnet films". In: *Journal of Applied Physics* 77.12 (1995). ISSN: 0021-8979.

[192] T. Nomura, Y. H. Matsuda, and T. C. Kobayashi. "Solid and Liquid Oxygen under Ultrahigh Magnetic Fields". In: *Oxygen 2022, Vol. 2, Pages 152-163* 2.2 (May 2022), pp. 152–163. ISSN: 2673-9801.

[193] A. A. Jalali-Roudsar, V. P. Denysenkov, and S. I. Khartsev. "Determination of magnetic anisotropy constants for magnetic garnet epitaxial films using ferromagnetic resonance". In: *Journal of Magnetism and Magnetic Materials* 288 (Mar. 2005), pp. 15–21. ISSN: 03048853.

[194] T. Liu et al. "Ferromagnetic resonance of sputtered yttrium iron garnet nanometer films". In: *Journal of Applied Physics* 115.17 (Jan. 2014), pp. 1–4. ISSN: 00218979.

[195] A. Mitra. "Structural and magnetic properties of YIG thin films and interfacial origin of magnetisation suppression". PhD thesis. Leeds: University of Leeds, 2017.

[196] M. C. Onbasli et al. "Pulsed laser deposition of epitaxial yttrium iron garnet films with low Gilbert damping and bulk-like magnetization". In: *APL Materials* 2.10 (2014). ISSN: 2166532X.

[197] H. Qin, S. J. Hämäläinen, K. Arjas, J. Witteveen, and S. Van Dijken. "Propagating spin waves in nanometer-thick yttrium iron garnet films: Dependence on wave vector, magnetic field strength, and angle". In: *Physical Review B* 98.22 (Dec. 2018), p. 224422. ISSN: 24699969.

[198] B. M. Howe et al. "Pseudomorphic Yttrium Iron Garnet Thin Films With Low Damping and Inhomogeneous Linewidth Broadening". In: *IEEE Magnetics Letters* 6 (2015), pp. 1–4. ISSN: 1949-307X.

[199] O. A. Kelly et al. "Inverse Spin Hall Effect in nanometer-thick YIG / Pt system". In: *ArXiv* arXiv:1308 (2013), pp. 1–12.

[200] A. Talalaevskij et al. "Magnetic properties of spin waves in thin yttrium iron garnet films". In: *Physical Review B* 95.6 (Feb. 2017), p. 064409. ISSN: 24699969.

[201] J. Lustikova et al. "Spin current generation from sputtered Y3Fe5O12 films". In: *Journal of Applied Physics* 116.15 (Oct. 2014), p. 153902. ISSN: 0021-8979.

[202] N. Beaulieu et al. "Temperature Dependence of Magnetic Properties of an 18-nm-thick YIG Film Grown by Liquid Phase Epitaxy: Effect of a Pt Overlayer". In: (Aug. 2018).

[203] P. Pirro et al. "Spin-wave excitation and propagation in microstructured waveguides of yttrium iron garnet/Pt bilayers". In: *Applied Physics Letters* 104.1 (Jan. 2014), p. 012402. ISSN: 0003-6951.

[204] C. Hahn et al. "Comparative measurements of inverse spin Hall effects and magnetoresistance in YIG/Pt and YIG/Ta". In: *Physical Review B* 87.17 (May 2013), p. 174417. ISSN: 1098-0121.

[205] A. Krysztofik, S. Özoğlu, R. D. McMichael, and E. Coy. "Effect of strain-induced anisotropy on magnetization dynamics in Y3Fe5O12 films recrystallized on a lattice-mismatched substrate". In: *Scientific Reports 2021 11:1* 11.1 (July 2021), pp. 1–10. ISSN: 2045-2322.

[206] Materials Technology International (MTI Corporation). *Undoped YAG Crystal and Substrate Properties (Product Data Sheet). Available at https://www.mtixtl.com/xtlflyers/yag.pdf.*

[207] A. Krysztofik et al. "Ultra-low damping in lift-off structured yttrium iron garnet thin films". In: *Applied Physics Letters* 111.19 (2017). ISSN: 00036951.

[208] S. A. Manuilov, S. I. Khartsev, and A. M. Grishin. "Pulsed laser deposited Y3Fe5O12 films: Nature of magnetic anisotropy i". In: *Journal of Applied Physics* 106.12 (2009). ISSN: 00218979.

[209] H. Wang, C. Du, P. C. Hammel, and F. Yang. "Strain-tunable magnetocrystalline anisotropy in epitaxial Y3Fe5 O12 thin films". In: *Physical Review B - Condensed Matter and Materials Physics* 89.13 (Apr. 2014), p. 134404. ISSN: 1550235X.

[210] G. Li et al. "Tunable perpendicular magnetic anisotropy in epitaxial Y3Fe5O12 films". In: *APL Materials* 7.4 (Apr. 2019), p. 041104. ISSN: 2166532X.

[211] Y. G. Chukalkin, V. R. Shtirts, and B. N. Goshchitskii. "Amorphization of Neutron-Irradiated Yttrium Iron Garnet". In: *Physica Status Solidi (a)* 79.2 (1983), pp. 361–366. ISSN: 1521396X.

[212] P. D. Esquinazi et al. "Defect-Induced Magnetism in Nonmagnetic Oxides: Basic Principles, Experimental Evidence, and Possible Devices with ZnO and TiO2". In: *physica status solidi (b)* 257.7 (July 2020), p. 1900623. ISSN: 1521-3951.

[213] A. Ney. "Magnetic properties of semiconductors and substrates beyond diamagnetism studied by superconducting quantum interference device magnetometry". In: *Semiconductor Science and Technology* 26.6 (Apr. 2011), p. 064010. ISSN: 0268-1242.

[214] M. A. Garcia et al. “Sources of experimental errors in the observation of nanoscale magnetism”. In: *Journal of Applied Physics* 105.1 (Jan. 2009), p. 013925. ISSN: 0021-8979.

[215] M. Sawicki, W. Stefanowicz, and A. Ney. “Sensitive SQUID magnetometry for studying nanomagnetism”. In: *Semiconductor Science and Technology* 26.6 (Apr. 2011), p. 064006. ISSN: 02681242.

[216] C. Uyeda, A. Yamagishi, H. Hori, and M. Date. “Magnetic properties of liquid oxygen in high magnetic fields”. In: *Physica B: Physics of Condensed Matter* 155.1-3 (1989), pp. 421–424. ISSN: 09214526.

[217] B. B. Krichevtsov et al. “Magnetization reversal in YIG/GGG(111) nanoheterostructures grown by laser molecular beam epitaxy”. In: *Science and Technology of Advanced Materials* 18.1 (Jan. 2017), pp. 351–363. ISSN: 18785514.

[218] H. B. Vasili et al. “Direct observation of multivalent states and 4f→3d charge transfer in Ce-doped yttrium iron garnet thin films”. In: *Physical Review B* 96.1 (2017), pp. 1–10. ISSN: 24699969.

[219] P. Kuiper, B. G. Searle, L. C. Duda, R. M. Wolf, and P. J. Van Der Zaag. “Fe L2,3 linear and circular magnetic dichroism of Fe3O4”. In: *Journal of Electron Spectroscopy and Related Phenomena* 86.1-3 (Aug. 1997), pp. 107–113. ISSN: 03682048.

[220] N. Thiery et al. “Electrical properties of epitaxial yttrium iron garnet ultrathin films at high temperatures”. In: *Physical Review B* 97.6 (Feb. 2018), p. 064422. ISSN: 24699969.

[221] P. S. Miedema and F. M. De Groot. “The iron L edges: Fe 2p X-ray absorption and electron energy loss spectroscopy”. In: *Journal of Electron Spectroscopy and Related Phenomena* 187.1 (Apr. 2013), pp. 32–48. ISSN: 03682048.

[222] S. Matzen et al. “Epitaxial growth and ferrimagnetic behavior of MnFe2O 4(111) ultrathin layers for room-temperature spin filtering”. In: *Physical Review B - Condensed Matter and Materials Physics* 83.18 (May 2011), p. 184402. ISSN: 1550235X.

[223] F. Schedin, E. W. Hill, G. Van Der Laan, and G. Thornton. “Magnetic properties of stoichiometric and nonstoichiometric ultrathin Fe3O4(111) films on AI2O3(0001)”. In: *Journal of Applied Physics* 96.2 (July 2004), pp. 1165–1169. ISSN: 00218979.

[224] T. Haupricht et al. “Local electronic structure of Fe2+ impurities in MgO thin films: Temperature-dependent soft x-ray absorption spectroscopy study”. In: *Physical Review B - Condensed Matter and Materials Physics* 82.3 (July 2010). ISSN: 10980121.

[225] F. Galdenzi, G. D. Ventura, G. Cibin, S. Macis, and A. Marcelli. “Accurate Fe3+/Fetot ratio from XAS spectra at the Fe K-edge”. In: *Radiation Physics and Chemistry* 175 (Oct. 2020), p. 108088. ISSN: 0969-806X.

[226] T. E. Westre et al. “A multiplet analysis of Fe K-edge 1s → 3d pre-Edge features of iron complexes”. In: *Journal of the American Chemical Society* 119.27 (1997), pp. 6297–6314. ISSN: 00027863.

[227] P. Kidkhunthod, S. Phumying, and S. Maensiri. “X-ray absorption spectroscopy study on yttrium iron garnet (Y3Fe5O12) nanocrystalline powders synthesized using egg white-based sol–gel route”. In: *Microelectronic Engineering* 126 (Aug. 2014), pp. 148–152. ISSN: 0167-9317.

[228] Y. G. Chukalkin, V. R. Shtirz, and B. N. Goshchitskii. “The Structure and Magnetism of Amorphous Y3Fe5O12”. In: *physica status solidi (a)* 112.1 (Mar. 1989), pp. 161–174. ISSN: 1521396X.

[229] R. E. Leuchtner, D. B. Chrisey, J. S. Horwitz, and K. S. Grabowski. “The preparation of epitaxial platinum films by pulsed laser deposition”. In: *Surface and Coatings Technology* 51.1-3 (Apr. 1992), pp. 476–482. ISSN: 02578972.

[230] Y. Abe, M. Kawamura, and K. Sasaki. “Preparation of PtO and α-PtO2 thin films by reactive sputtering and their electrical properties”. In: *Japanese Journal of Applied Physics, Part 1: Regular Papers and Short Notes and Review Papers* 38.4 A (1999), pp. 2092–2096. ISSN: 00214922.

[231] W. Zhang et al. “Determination of the Pt spin diffusion length by spin-pumping and spin Hall effect”. In: *Applied Physics Letters* 103.24 (Dec. 2013), p. 242414. ISSN: 0003-6951.

[232] C. Du, H. Wang, F. Yang, and P. C. Hammel. “Enhancement of Pure Spin Currents in Spin Pumping Y3Fe5 O12/Cu/Metal Trilayers through Spin Conductance Matching”. In: *Physical Review Applied* 1.4 (2014), pp. 1–6. ISSN: 23317019.

[233] M. Haertinger et al. “Spin pumping in YIG/Pt bilayers as a function of layer thickness”. In: *Physical Review B - Condensed Matter and Materials Physics* 92.5 (2015), pp. 1–6. ISSN: 1550235X.

[234] A. Minenkov et al. “Advanced preparation of plan-view specimens on a MEMS chip for in situ TEM heating experiments”. In: *MRS Bulletin* (Mar. 2022), pp. 1–12. ISSN: 08837694.